A Method to Measure Flame Index in Turbulent Partially-Premixed Flames

by

David Ari Rosenberg

A dissertation submitted in partial fulfillment
of the requirements for the degree of
Doctor of Philosophy
(Aerospace Engineering)
in the University of Michigan
2014

Doctoral Committee:

Professor James F. Driscoll, Chair
Professor Arvind Atreya
Assistant Professor Mirko Gamba
Assistant Professor Benjamin Wesley Longmier

To my parents, brothers, and Jessica
for reminding me there is world outside engineering.

Acknowledgments

I would first like to thank my advisor, Professor James F. Driscoll, for his help and support throughout my time in the PhD program. Jim has been an excellent advisor, and I feel privileged to have worked with him. Of all the possible advisors and universities, I think Jim and the University of Michigan were not only the best option, but the ideal one as well. I would also like to express appreciation for my committee members—Professors Arvind Atreya, Mirko Gamba, and Benjamin Longmier—whose comments and suggestions have been very helpful.

I have so much thanks for my fellow graduate students in the Propulsion and Combustion Engineering Laboratory who taught me how to set up the piping system for a combustor and the optics for laser diagnostics. My interactions with Matt Fotia, Jacob Temme, Patton Allison, Yuntao Chen, Aaron Skiba, and Tim Wabel have taught me how to be an experimental researcher, and have been very helpful. Interactions with Jim's computational students, Sean Torrez and Derek Dalle, have taught me how to properly construct the long code I developed for this dissertation; how to produce attractive papers and graphics; and more about Russia, Kazakhstan, Mongolia, and the rest of Central Asia than I ever thought I would be interested in (I turn out to be very interested.). I would also like to further acknowledge Derek for condensing and improving the files that govern the formatting of this dissertation.

The staff of the Department of Aerospace Engineering—Denise Phelps and Cindy Enoch—has offered invaluable help. The department's technical staff—Dave McLean, Terry Larrow, Eric Kirk, Chris Chartier, Aaron Borgman, and Tom Griffin—has offered immense aid, as well.

I would like to thank my parents, Julian and Zella, for their love and support. When I was two years old, my mom took me on monthly trips to the National Gallery of Art after dropping off my older brother, Evan, at nursery school. We rode the Metro every time, and I have to assume that this started a life-long interest in transportation—anything related to bikes, trains, airplanes, or spacecraft. (However, the trips, and living near DC, probably instilled a sense of entitlement that no museum was worth paying for.) Without my dad's suggestion, while I was in high school, that I look into studying mechanical engineering in college, there's a good chance I would have simply reverted to my

original career plan—being a garbage man who rides on the back of the truck. This job seems to no longer exist, and seems to have been outsourced mostly to robot arms, so I would likely be unemployed . Meanwhile my brothers, Evan and Michael, have helped to remind me that a world outside engineering exists.

Finally, I would like to thank my finacée, Jessica Young. Your presence and support has made this all so much happier, and I hope that it continues for the rest of our lives.

Funding for this research was provided by the National Science Foundation award CBET 0852910, which was monitored by Dr. Arvind Atreya and Dr. Ruey Hung Chen. The use of the GTMC was funded by the Office of Naval Research under grant N00014-10-10561 and by the DOE-UTSR program under grant FE0007060. I would like to thank Dr. Wolfgang Meier of DLR Stuttgart for the permission to use the GTMC design.

TABLE OF CONTENTS

LIST OF FIGURES

LIST OF TABLES

LIST OF APPENDICES

LIST OF ABBREVIATIONS

CCD Charge-Coupled Device

DDG Digital Delay Generator

DNS Direct Numerical Simulation

FIMM Flame Index Measurement Method

GTMC Gas Turbine Model Combustor

ICCD Intensified Charge-Coupled Device

LIF Laser-Induced Fluorescence

NADF Non-linear Anisotropic Diffusion Filter

PLIF Planar Laser-Induced Fluorescence

PVC Precessing Vortex Core

PDF Probability Density Function

PMF Probability Mass Function

SNR Signal-to-Noise Ratio

TTL Transistor-Transistor Logic

NOMENCLATURE

A	=	probability of a non-premixed flamelet
B	=	probability of no flamelet
C	=	probability of a premixed flamelet
e	=	normal strain rate $\left[\mathrm{s}^{-1}\right]$
f_{B}	=	Boltzmann fraction
G_{FO}	=	Takeno flame index
I_{ν}^{0}	=	normalized laser spectral irradiance $\left[\mathrm{MW}/(\mathrm{cm}^2\,\mathrm{cm}^{-1})\right]$
L	=	laser sheet intensity distribution
$\dot{m}_i$	=	mass flowrate of species i [kg/s]
n_i	=	number density of species i $\left[\mathrm{m}^{-3}\right]$
S_{back}	=	background signal
S_{dark}	=	camera dark noise
S_{e}	=	true laser-induced fluorescence signal
S_i	=	laser-induced fluorescence signal of species i
S_{tot}	=	total signal acquired
t_i	=	camera exposure time [s]
t_{ro}	=	camera readout time [s]
V_{c}	=	collection volume $\left[\mathrm{m}^3\right]$
w_R	=	uncertainty of the measurement result
Y_i	=	mass fraction of species i

Greek

β_p	=	probability that flamelet is premixed, if a flamelet is present
Γ	=	dimensionless spectral overlap function
$\delta_{i,j}$	=	separation distance between locations of $\left(\nabla Y_i\right)_{\max}$ and $\left(\nabla Y_j\right)_{\max}$ [m]
Δs	=	flamelet searching distance [m]
ϵ_{pp}	=	degree of partial-premixing
η_{det}	=	transmission efficiency of the detector
η_{opt}	=	transmission efficiency of the collection optics

ξ = flame index

σ = standard deviation

Φ_F = fluorescence quantum efficiency

ϕ_{global} = fuel-air equivalence ratio for the overall mixture

χ_i = mole fraction of species i

Ω = collection solid angle [sr]

Subscripts

a = air

ace = acetone

f = fuel

FL = flame luminosity

FLnT = flame luminosity with no tracer gas added

FLnT,L = flame luminosity with no tracer gas added, and lasers on

(i, j) = matrix indices for evaluated acetone PLIF signal gradient pixel

(i', j') = matrix indices for evaluated NO_2 PLIF signal gradient pixel

(i^*, j^*) = matrix indices for pixel marked in ξ matrix

Mathematical Operators

$\langle \cdots \rangle$ = ensemble/temporal average

$\langle \cdots | \cdots \rangle$ = conditional ensemble/temporal average

∇^2 = Laplacian

$\Pr(\cdots)$ = probability

$\overline{\cdots}$ = spatial average

∇ = spatial gradient

ABSTRACT

A Method to Measure Flame Index in Turbulent Partially-Premixed Flames

by

David Ari Rosenberg

Chair: James F. Driscoll

This dissertation describes the development of a diagnostic technique and data processing routine to measure the flame index in partially-premixed flames, called the Flame Index Measurement Method. Many modern combustion applications involve conditions in which the fuel and oxidizer are only partially mixed prior to entering the flame. These partially-premixed flames contain some regions of premixed and some regions of non-premixed flamelets. New computational approaches use the flame index concept: premixed regions are identified and a premixed model is applied; non-premixed regions are also identified and a non-premixed model is applied. The flame index is defined as the normalized dot product of the gradients of the fuel and oxidizer mass fractions; it is $+1$ in premixed flamelets and is -1 in non-premixed flamelets. Previously there had been no experimentally measured values of flame index available to assess the modeling approaches.

A new method has been developed to measure the flame index using Planar Laser-Induced Fluorescence tracers to indicate the sign and direction of the fuel and oxygen gradients. Through the modeling of premixed and non-premixed flamelets, acetone was selected as a fuel tracer and nitrogen dioxide was

selected as an oxygen tracer. The fluorescence properties of both acetone and nitrogen dioxide were studied. With acetone seeded into the fuel, and nitrogen dioxide seeded into the air, the Flame Index Measurement Method was evaluated in laminar premixed and non-premixed methane/acetone/air flames, as well as in a well-defined turbulent partially-premixed burner, the Gas Turbine Model Combustor (GTMC). The flame index was measured in the GTMC with methane, propane, and syngas flames.

Statistics (mean, variance, and probability mass functions) of the flame index are reported for the highly-turbulent partially-premixed GTMC flames. Two new statistical quantities were developed that describe the probability for the occurrence of premixed flamelets and the degree of partial-premixing. Aspects of the new measurement technique are discussed, including: signal-to-noise ratio, tracer gas seeding levels, data analysis/gradient identification methods, and uncertainty.

CHAPTER 1

Introduction

This dissertation will focus on the classification of flames depending on how the fuel and oxidizer interact, or don't interact, before burning.

1.1 Motivation

Flames can be considered to exist in one of three regimes depending on how the fuel and oxidizer interact before burning. The regimes are premixed, non-premixed, and partially-premixed flames. The first regime, premixed flames, is characterized by the mixing of the fuel and oxidizer to within their flammability limits prior to burning. The second regime, non-premixed flames, is characterized by the fuel and oxidizer approaching the flame front from opposite sides. The third regime, partially-premixed flames, is characterized by some regions of the flame containing premixed flamelets and some regions containing non-premixed flamelets [1]. Many modern combustion applications—gas turbines in particular—involve combustion in which the fuel and oxidizer are not completely mixed prior to entering the flame, and exhibit partially-premixed flames.

When studying partially-premixed flames, computational modelers want to easily identify the premixed and non-premixed regions of the flame, so they can apply the appropriate models. The Takeno flame index [2] has been suggested as an indicator of which regions are premixed and which regions are non-premixed, and the degree to which they are pre-

mixed or non-premixed. The flame index is defined as:

$$G_{\mathrm{FO}} = \nabla Y_{\mathrm{F}} \cdot \nabla Y_{\mathrm{O}}, \tag{1.1}$$

where G_{FO} is the flame index and Y_{F} and Y_{O} are the fuel and oxidizer mass fractions, respectively. A flame is locally premixed the flame index is positive, and where a flame is locally non-premixed the flame index is negative. The absolute value of G_{FO} is indicative of the supplying rate of the fuel and oxidizer to the flame by molecular diffusion.

New computational approaches of Bray et al. [3], Mizobuchi et al. [4], and Knudsen and Pitsch [5, 6] have used a normalized flame index concept, ξ, defined as:

$$\xi = \frac{\nabla Y_{\mathrm{F}} \cdot \nabla Y_{\mathrm{O}}}{|\nabla Y_{\mathrm{F}} \cdot \nabla Y_{\mathrm{O}}|}, \tag{1.2}$$

where $\xi = +1$ in premixed flamelets and $\xi = -1$ in non-premixed flamelets. The definition of flame index in Eq. (1.2) forms the basis for how flame index was measured in this dissertation.

A new method had been developed to measure the flame index using planar laser-induced fluorescence (PLIF) of fuel and oxygen tracers. Through the modeling of premixed and non-premixed flamelets, acetone (CH_3COCH_3) was selected as a fuel tracer and nitrogen dioxide (NO_2) was selected as an oxygen tracer. The fluorescence properties of both acetone and NO_2 have been studied. With acetone seeded into the fuel, and NO_2 seeded into the air, the Flame Index Measurement Method (FIMM) has been evaluated in a laminar premixed and a laminar non-premixed methane/acetone/air flame, as well as in a well-defined turbulent partially-premixed burner, the Gas Turbine Model Combustor (GTMC). The flame index has been measured in the GTMC with methane, propane, and syngas flames.

1.2 Background

1.2.1 Flame Index

In computational models the flame index concept is useful in allowing the modeler to divide a partially-premixed flame into premixed and non-premixed reaction zones, where the appropriate combustion model can be applied. There have been several studies that modeled the subgrid flame index to be a function of the resolved scale gradients of fuel and oxygen concentrations [3–10], however no study has been performed to experimentally verify these models by measuring the fuel and oxidizer gradient. Models of partially-premixed flames need to correctly predict the flame index, so measurements are needed to assess the models.

1.2.2 Planar Laser-Induced Fluorescence

The fluorescence signal of some species i, S_i, is related to the species' number density, n_i by [11, 12]:

$$S_i = \eta_{\text{opt}} \frac{\Omega}{4\pi} V_c \eta_{\text{det}} n_i f_B I_\nu^0 \Gamma \Phi_F, \tag{1.3}$$

where η_{opt} is the transmission efficiency of the collection optics, Ω is the collection solid angle, V_c is the collection volume, η_{det} is the efficiency of the detector, n_i is the number density of species i, f_B is the Boltzmann fraction, and $I_\nu^0 \left[\text{MW}/(\text{cm}^2\,\text{cm}^{-1})\right]$ is the normalized laser spectral irradiance. Γ is the dimensionless spectral overlap function defined by Partridge and Laurendeau [13]; and Φ_F is the fluorescence quantum efficiency, which is dependent on the incident laser wavelength, pressure, and temperature.

The form of Planar Laser-Induced Fluorescence (PLIF) used in this dissertation is that of tracer-PLIF, where an extra species is added to the flow to indicate the location of either the fuel or the oxygen in the flow. Oftentimes tracers are used to measure the concentrations of the fuel or oxygen. In this case, both the fuel and oxygen were tracked with their own

tracers. The fuel and oxygen concentrations were not measured, but the sign and locations of their gradients were measured.

1.2.2.1 Nitrogen Dioxide Laser-Induced Fluorescence

Laser-Induced Fluorescence (LIF) of NO_2 has been used in several previous studies of reacting and non-reacting flows. Cold flow mixing has been investigated using an argon-ion laser at 488 nm [14]. NO_2 has been shown to decompose in the reaction zone of a flame [15], so it can be used as a marker of the reaction interface between unburned reactants and combustion products [16, 17].

Spectroscopy of NO_2 has been well studied for two reasons. NO_2 is an important atmospheric pollutant, so it is of interest to environmentalists [18, 19]; and NO_2 has a very dense and complex electronic spectrum that is difficult to study, so it is of interest to chemists and physicists [20–25]. NO_2 is known to absorb radiation in the UV and visible wavelengths from 250 nm to 700 nm, with an absorption cross section at 532 nm (the wavelength used in this dissertation) of $16 \times 10^{-20}\,\mathrm{cm}^2$ [25–28]. Agarwal et al. [15] showed that NO_2 will fluoresce from 540 nm to 675 nm when excited by a 488 nm argon-ion laser, while Donnelly et al. [29–32] showed that NO_2 will fluoresce from 550 nm to wavelengths longer than 800 nm when excited by a 532 nm Nd:YAG laser.

The linearity of NO_2 fluorescence was studied by Gulati and Warren [14], at an excitation wavelength of 488 nm, with respect to the laser power up to 2.0 W (much lower than the laser power in this dissertation) and with respect to NO_2 concentration in N_2 up to 5000 ppm (the same concentration used in this dissertation, although in air). Gulati and Warren [14] found the response of NO_2 to be linear in both cases. Agarwal et al. [15] studied NO_2 fluorescence with respect to its concentration in air, with an excitation wavelength of 488 nm, and found that it began to saturate at about 600 ppm, although Agarwal et al. had only a single data point in this non-linear regime, and all others were in the linear regime (concentration from 150 ppm to 500 ppm).

The rapid disappearance of the NO_2 fluorescence signal when crossing from the unburned side to the burned side of a flame is the result of chemical reactions with O and H atoms and thermal dissociation through the collisions with M, the combustion products. These reactions were described by Cattolica [16] as:

$$H + NO_2 \xrightarrow{k_{NO_2,1}} NO + OH \tag{R 1.1}$$

$$O + NO_2 \xrightarrow{k_{NO_2,2}} NO + O_2 \tag{R 1.2}$$

$$NO_2 + M \xrightarrow{k_{NO_2,3}} NO + O + M\cdot \tag{R 1.3}$$

The reaction rates $k_{NO_2,1}$, $k_{NO_2,2}$, and $k_{NO_2,3}$ can be found in Baulch et al. [33].

1.2.2.2 Acetone Laser-Induced Fluorescence

Acetone has frequently been used as a fuel tracer and its fluorescence properties are well known [34–37]. Acetone will absorb light with wavelengths from 200 nm to 325 nm, with an absorption cross section at 266 nm—the wavelength used in this dissertation—of about 4.4×10^{-20} cm^2, at room temperature [35, 37]. Acetone will emit in the wavelength range between 320 nm and 550 nm when excited by a 266 nm laser [38].

Acetone fluorescence linearity has been studied with respect to laser energy [36–38] and acetone concentration [36–39], and was found to respond linearly in both cases.

The breakdown of acetone is through both thermal decomposition at high temperatures by collisions with combustion products M, and reactions with combustion radicals such as H, O, OH, and CH_3. These reactions can be described as [40–43]:

$$CH_3COCH_3 + M \xrightarrow{k_{acetone,1}} CH_3CO + CH_3 + M \tag{R 1.4}$$

$$H + CH_3COCH_3 \xrightarrow{k_{acetone,2}} H_2 + CH_2COCH_3 \tag{R 1.5}$$

$$O + CH_3COCH_3 \xrightarrow{k_{acetone,3}} OH + CH_2COCH_3 \quad \text{(R 1.6)}$$

$$OH + CH_3COCH_3 \xrightarrow{k_{acetone,4}} H_2O + CH_2COCH_3 \quad \text{(R 1.7)}$$

$$CH_3 + CH_3COCH_3 \xrightarrow{k_{acetone,5}} CH_4 + CH_2COCH_3 \cdot \quad \text{(R 1.8)}$$

The reaction rates $k_{acetone,1}$, $k_{acetone,2}$, $k_{acetone,3}$, $k_{acetone,4}$, and $k_{acetone,5}$ can be found in Chong and Hochgreb [43].

1.3 A Plan to Measure Flame Index

In the development of the Flame Index Measurement Method several important decisions were made. The first question was how many spatial dimensions would be appropriate for the measurement. As the flame index involves the spatial gradients of the fuel and oxidizer mass fractions, zero-dimensional and one-dimensional measurements would exclude a significant amount of information. To be useful, zero-dimensional and one-dimensional measurements would also require tomography to give a full picture of what is occurring in the flame, and would require either an extremely complicated setup, or be unable to provide instantaneous measurements. Three-dimensional measurements would be possible using the technique described by Aldén et al. [44], but would be extremely complicated and expensive to implement. It was finally decided that the use of the Planar Laser-Induced Fluorescence (PLIF) technique would be appropriate because two dimensions would be sufficient to characterize an axisymmetric flame, and the technique provides instantaneous measurements.

The next research issue arose because the direct observation of oxygen (O_2) and simple fuels, such as methane (CH_4), has not been performed using PLIF. Instead the LIF measurement of fuel and oxygen tracers was utilized. The selection of these tracers will be described in Chapter 3.

A burner in which to develop the measurement method along with the flame conditions

would need to be selected. For the initial calibration of the method, an enclosed laminar co-flow burner was selected because of its simple flow conditions, and because of its ability to burn both premixed and non-premixed flames. It was decided that a CH_4/air flame would be studied because the chemistry is well known. A turbulent flame would later need to be studied to ensure the method functions in the real-world partially-premixed flames that are of interest to both computational modelers and experimentalists.

Finally, an optical system that would allow for the simultaneous PLIF imaging of the fuel and oxygen tracers would need to be set up, and a method to process the data and determine the flame index would need to be developed.

1.4 Goals

The overall goal of this dissertation was fairly simple: to determine whether it would be possible to measure the flame index in a turbulent partially-premixed flame. The other goals were then derived from this. The selection of good fuel and O_2 tracers was needed. Once selected, the tracers would need to be detected with good Signal-to-Noise Ratios (SNRs). This was fairly easy for the fuel tracer, acetone, but difficult for the O_2 tracer, NO_2, so the majority of time was spend improving the SNR of the NO_2 PLIF images. Involved in this was the need to set up a laboratory capable of simultaneous PLIF, as well as the alignment of all necessary optics, and the design of a gas flow and metering system. Finally, the selection of flow conditions to study was needed.

Once the data was captured, the methods for processing the data would need to be developed. These methods would have to include procedures for correcting the raw PLIF images for the camera's white-field, the background signal, and the non-uniformities in the laser sheets. Despite the efforts to improve the SNR of the PLIF images through the design of the experiment, procedures for improving the SNR during the post-processing of the images was needed as well. Finally, the computational methods by which the flame index

would be measured needed to be developed. Likewise, statistical quantities that could be derived from the acquired data sets were identified.

1.5 Contributions

The most important contribution is the Flame Index Measurement Method itself. The computational components of the method will be described in Section 4.2.1. Also important in the development of the Flame Index Measurement Method, and a contribution that stands on its own, was the selection of NO_2 as a fluorescence tracer for the identification of the sign and location of O_2 gradients in both turbulent and laminar flames.

As will be described in Chapter 3, acetone (CH_3COCH_3) was selected as a fuel tracer and nitrogen dioxide (NO_2) was selected as an O_2 tracer. Using these two tracers, a LIF-based flame index was defined as:

$$\xi_{LIF} = \frac{\left(\nabla S_{\text{acetone}}\right)_{\max} \cdot \left(\nabla S_{NO_2}\right)_{\max}}{\left|\left(\nabla S_{\text{acetone}}\right)_{\max} \cdot \left(\nabla S_{NO_2}\right)_{\max}\right|}, \tag{1.4}$$

where ξ_{LIF} is the flame index based on the LIF signals, S_{acetone} is the acetone fluorescence signal, and S_{NO_2} is the NO_2 fluorescence signal. Like with ξ in Eq. (1.2), $\xi_{LIF} = +1$ in premixed flamelets and $\xi_{LIF} = -1$ in non-premixed flamelets.

If the acetone and NO_2 fluorescence signal gradients are correctly measured:

$$\xi = \xi_{LIF}. \tag{1.5}$$

There are some uncertainties in the measurement of the fluorescence signals. These uncertainties will be discussed in Section 5.2.

The two quantities $\overline{\beta_p}$ and ϵ_{pp} were newly defined. The quantity $\overline{\beta_p}$ is the average probability, for an entire data set, that a flamelet is premixed ($\xi = +1$) if a flamelet is present. So, $\overline{\beta_p} = +1$ if all flamelets are premixed, 0.5 if all flamelets are fully partially-premixed

(meaning they are premixed just as often as they are non-premixed), and 0 if all flamelets are non-premixed. The degree of partial-premixing, ϵ_{pp}, is a re-normalization of $\overline{\beta_p}$ to simplify it somewhat. The quantity ϵ_{pp} is defined such that it only indicates if all flamelets are fully partially-premixed ($\epsilon_{pp} = 1$) or are entirely premixed or non-premixed ($\epsilon_{pp} = 0$), but does not say whether the flame is leaning more toward premixed or non-premixed flamelets.

As a note, the inverse of $\overline{\beta_p}$, the probability for a non-premixed flamelet if a flamelet exists, $\overline{\beta_{np}}$, was not introduced and will not be discussed in this dissertation because it is simply defined as $\overline{\beta_{np}} = 1 - \overline{\beta_p}$.

1.6 Outline of the Dissertation

This thesis will describe the development of the Flame Index Measurement Method in the following manner. Chapter 2 will describe the experimental setup used in the development of the method. Section 2.1 will describe the burners and gas-flow system used. Section 2.2 will describe the conditions studied in each burner such as the mass flowrates, the fuel-air equivalence ratios, and the tracer seeding levels. Section 2.3 will describe the setup of the optics system including a description of the laser beam paths, dimensions of the laser sheets, the cameras used, the spatial resolution of the cameras, and how the synchronization of the system was achieved. Section 2.4 will describe the procedure for capturing a single data set. Section 2.5 will describe the methods used to correct the raw PLIF images for the background signal, the camera's white-field, and the non-uniformities in the laser sheet. Finally, Section 2.6 will describe the methods used during the processing of the corrected PLIF images to improve their Signal-to-Noise Ratios (SNRs), and to determine the locations of the maximum tracer signal gradients.

Chapter 3 will describe the selection of the fuel and O_2 tracers as well as their fluorescence properties. Section 3.1 will describe the computational modeling of flamelets used

to select NO_2 as an O_2 tracer and acetone as a fuel tracer, as well as an evaluation of their performance. Section 3.2 will describe a study of the linearity and possible saturation of both NO_2 and acetone fluorescence with respect to laser energy and tracer concentration in air, for NO_2, or in CH_4, for acetone. Section 3.3 will describe the proof of concept study of these fluorescence tracers in a laminar premixed and a laminar non-premixed flame.

Chapter 4 will describe the Flame Index Measurement Method itself. Section 4.1 will describe how the PLIF images were processed to improve their SNRs, as well as demonstrate the need for the processing. Section 4.2 will describe the core of the Flame Index Measurement Method, the Flamelet Searching Method, as well as show the results of the method, and the statistical post-processing of the method. The new quantities, $\overline{\beta_p}$ and ϵ_{pp}, will be defined in Section 4.2 as well.

Chapter 5 will show and discuss the results of the turbulent flame data sets as well as discuss the uncertainties in the Flame Index Measurement Method. Section 5.1 will show the results of the GTMC cases we well as discuss the variation between the cases. Section 5.2 will discuss the uncertainties in both the flame conditions studied as well as uncertainties in the Flame Index Measurement Method.

Finally, Chapter 6 will summarize and provide conclusions for the dissertation, as well as discuss the possibilities for future work. Section 6.1 will provide the summary, while Section 6.2 will provide the conclusions. Section 6.3 will discuss the possibilities for future work involving the Flame Index Measurement Method.

CHAPTER 2

Experimental

2.1 Experimental Facilities

The Flame Index Measurement Method (FIMM) was developed using combustion experiments conducted in two separate burners. The initial calibration of FIMM was performed using a laminar enclosed co-flow burner. FIMM was then refined using the turbulent partially-premixed Gas Turbine Model Combustor (GTMC). When selecting which burners to use, the primary concern was safety. Nitrogen dioxide (NO_2) is a highly toxic gas and is considered Immediately Dangerous to Life or Health (IDLH) at 20 ppm [45]. To maintain safety an exhaust with a strong suction was installed in the laboratory, the gas bottle containing NO_2 was kept in a well-ventilated gas-bottle cabinet, only enclosed combustion chambers were used, and an NO_2 detector was worn whenever NO_2 was flowing through the tubing system.

2.1.1 Enclosed Co-Flow Burner

The laminar flame cases were conducted in an enclosed co-flow burner, shown in Fig. 2.1, with methane (CH_4) / acetone (CH_3COCH_3) / air flames. Acetone was added to the fuel stream through the use of an acetone bubbler, described in Section 2.1.3, while the NO_2 seeding was achieved by using a gas cylinder pre-mixed with air and NO_2 at 5000 ppm, by volume.

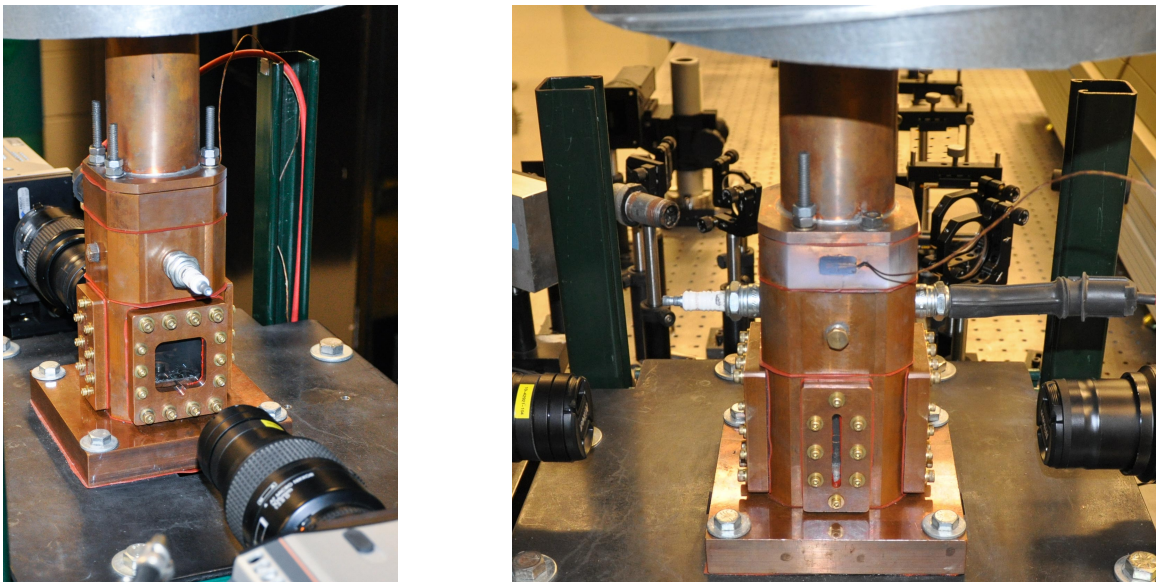

(a) Side View.

(b) Back View.

Figure 2.1: Back and side views of enclosed co-flow burner.

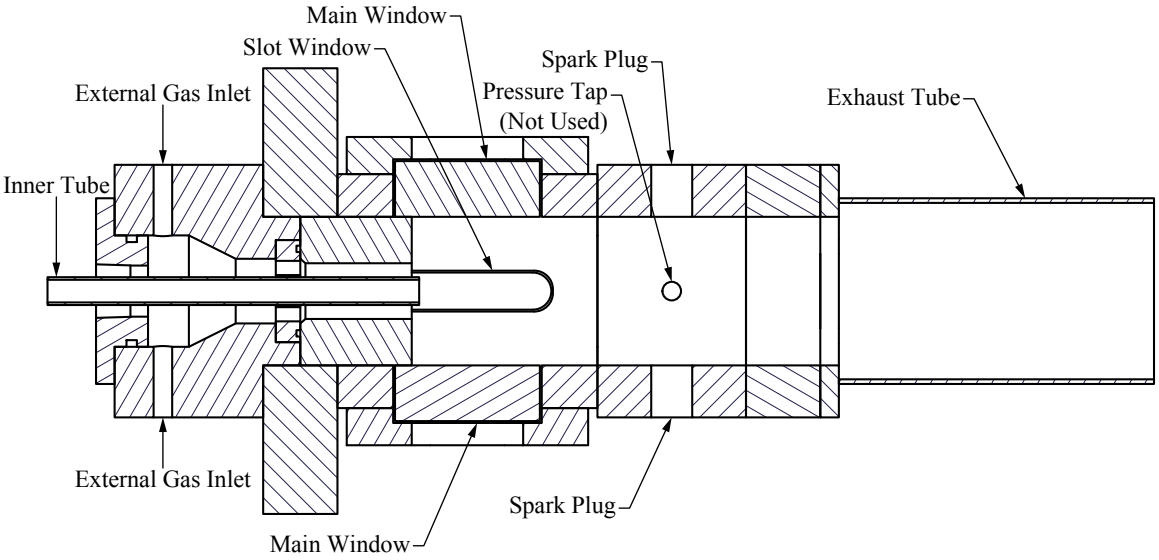

Figure 2.2: Cross-sectional view of the enclosed co-flow burner.

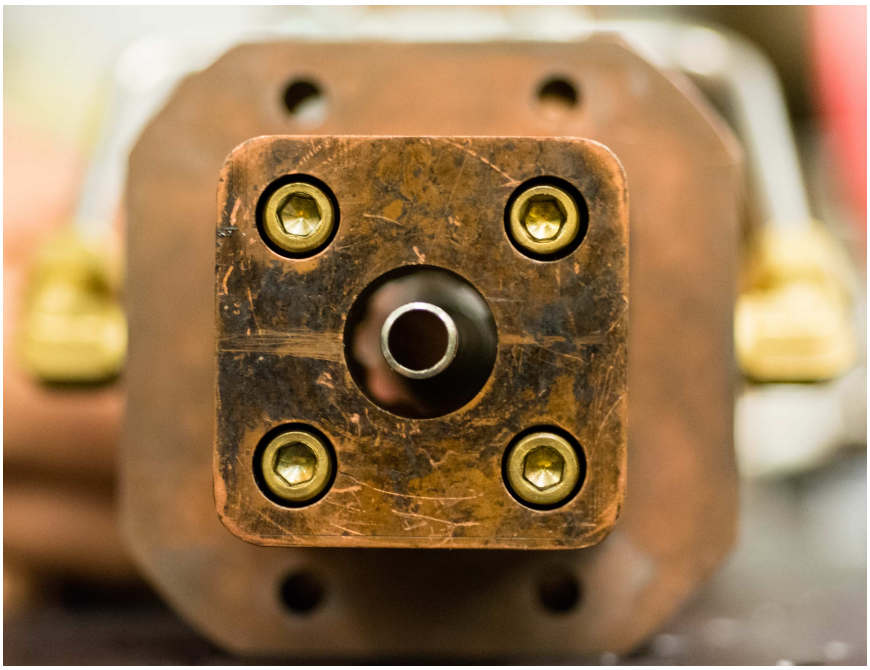

Figure 2.3: Enclosed co-flow burner injector face.

A cross-sectional view of the burner can be seen in Fig. 2.2, while a close-up of the injector face can be seen in Fig. 2.3. The burner's outer tube had a diameter of 19 mm; the inner tube had a diameter of 8 mm, had a wall thickness of 0.9 mm, and protruded 3 mm above the lip of the outer tube. The burner was operated with four fused silica windows, with a thickness of 19.05 mm, for flame visualization. The burner was modified from the Michigan Single Element Injector Experiment [46], with the nozzle removed, the length of the burner shortened, a long exhaust tube added, and both the inner and outer injectors widened. This was an ideal combustor to modify as it was designed to be well sealed, and operated with an inner tube and outer tube.

A piping diagram for the flow system used while running the enclosed co-flow burner is shown in Fig. 2.4. The burner was set up so that it could be operated in either a premixed or non-premixed configuration. When running in the premixed configuration, both the air/NO_2 mixture and the CH_4/acetone mixture flowed through the inner tube, and nothing flowed through the outer tube. In the non-premixed configuration, the air/NO_2 mixture flowed through the outer tube, while the CH_4/acetone mixture flowed through the inner

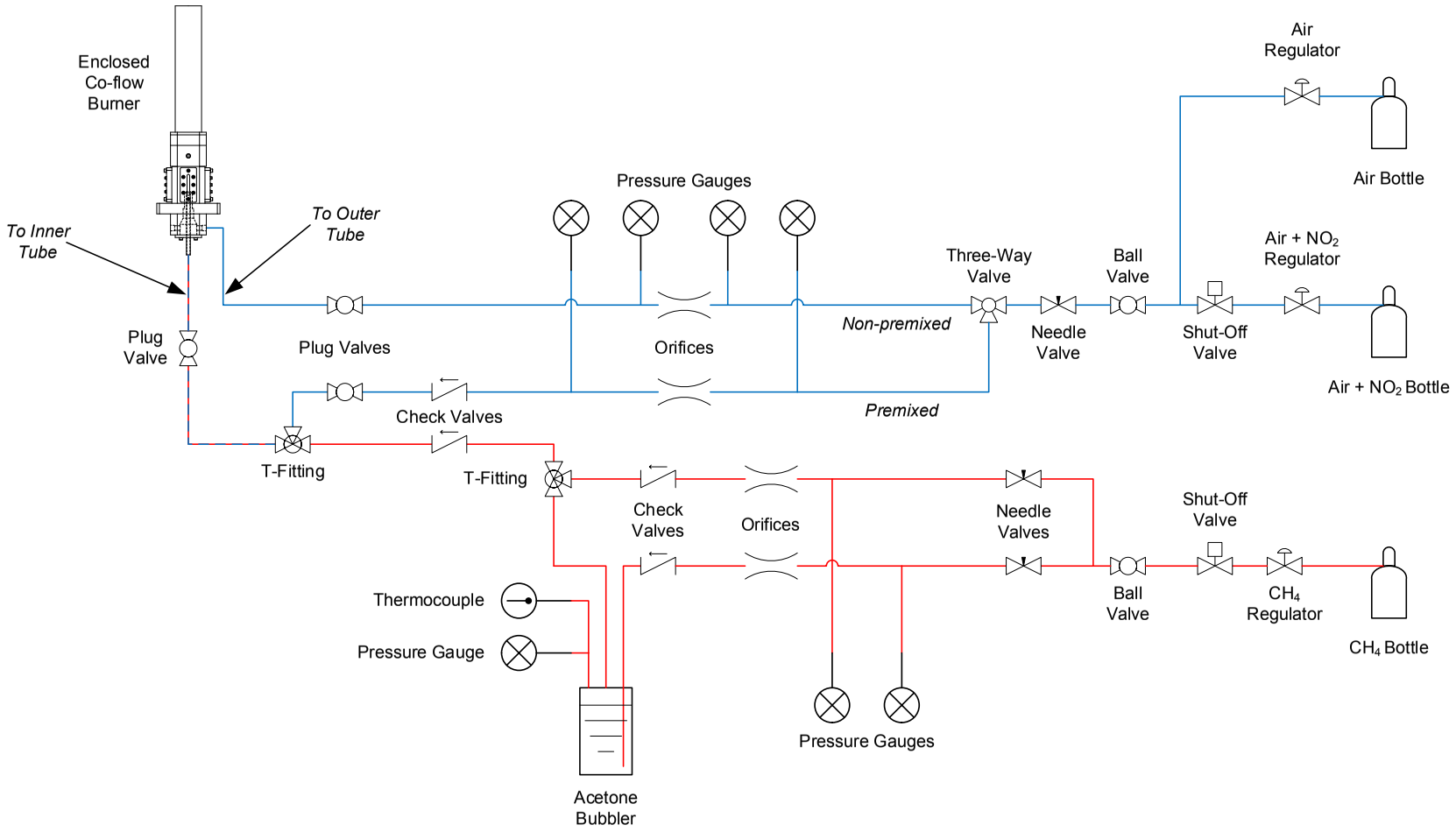

Figure 2.4: Piping diagram of the system used with the enclosed co-flow burner.

tube. Switching between the two configurations was accomplished with a three-way valve. The acetone concentration was controlled by diluting the CH_4 line that passed through the acetone bubbler with a bypass line that was pure CH_4. The mixing between the bubbler and bypass lines was achieved by using a T-fitting and long pipe. When running the experiment in the premixed configuration, a second T-fitting was used to mix the air/NO_2 line with the CH_4/acetone line. The flowrates for the gases were controlled using choked-flow orifices.

One major problem with the enclosed co-flow burner was the windows. The burner had originally been designed to operate at high pressure, so the windows were very thick. This created problems because the laser sheets were both thin, as will be discussed in greater detail in Section 2.3.1, leading to a high concentration of energy over a small area. Frequently cracks would form in the middle of the window, not compromising its structural integrity, but reducing the transmitted energy of the laser and adding more non-uniformities to the laser sheet. Unfortunately there was no way to correct for this. The laser energies were turned low to try minimize the occurrence and severity of these cracks.

2.1.2 Gas Turbine Model Combustor

The majority of flame index measurements were taken on a dual-swirl burner, known as the Gas Turbine Model Combustor (GTMC) and pictured in Fig. 2.5, which was developed by Meier and colleagues at DLR Stuttgart [47–49]. The injector consisted of a central air nozzle, an annular fuel nozzle, and a co-annular air nozzle. The disassembled and assembled fuel and both air nozzles can be seen in Fig. 2.6. Both air nozzles supplied swirling air at atmospheric pressure and temperature from a common plenum. The inner air nozzle had an outer diameter of 15 mm and the annular nozzle had an inner diameter of 17 mm and an outer diameter of 25 mm. The measured swirl number was approximately 0.55. Non-swirling fuel was provided through three exterior ports fed through the annular nozzle, which was subdivided into 72 channels with a $0.5\,\text{mm} \times 0.5\,\text{mm}$ cross section. The exit plane of the central air nozzle and fuel nozzle lay 4.5 mm below the exit plane of the

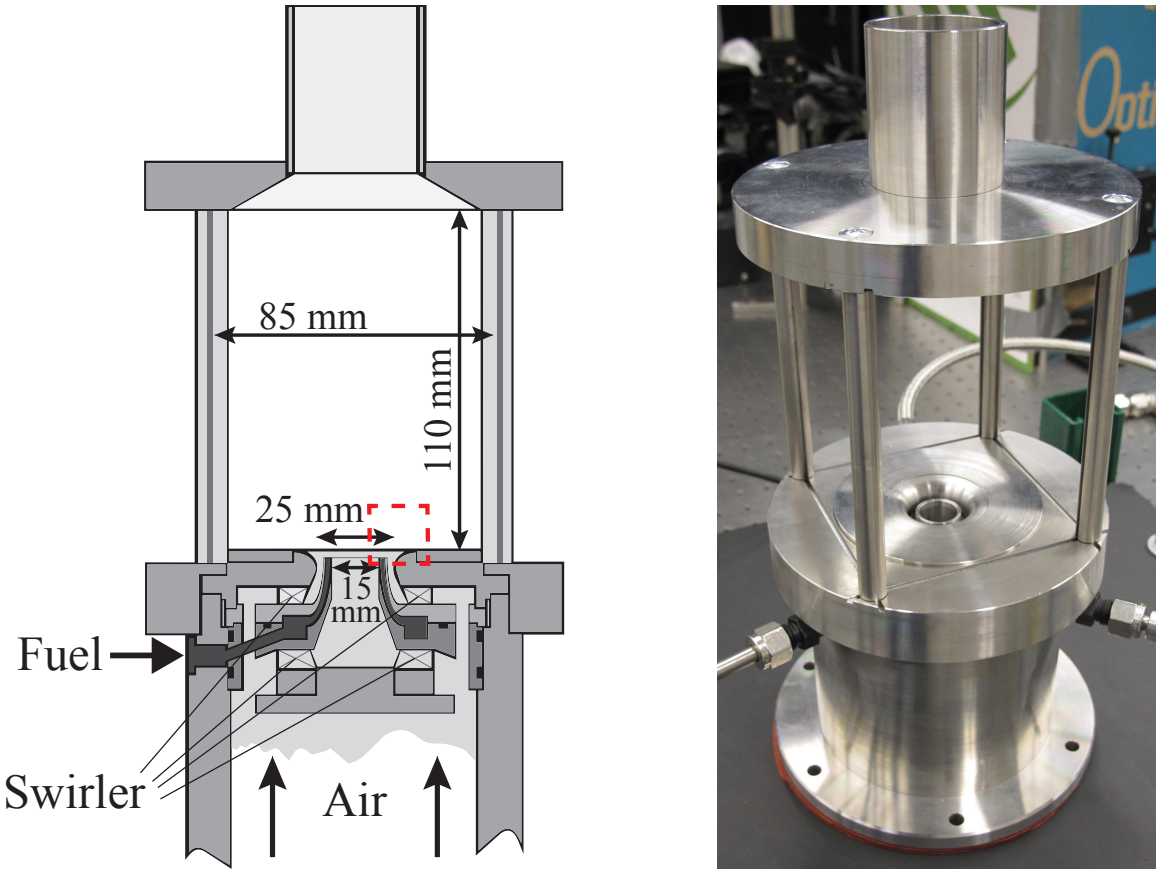

(a) Cross-sectional view of the Gas Turbine Model Combustor [47]. The dashed box shows the field of view used in the experiments.

(b) Photograph of the Gas Turbine Model Combustor

Figure 2.5: Cross-sectional and photographic views of the Gas Turbine Model Combustor developed by Meier and colleagues at DLR Stuttgart.

outer air annulus. The exit plane of the outer air annulus will be referred to as the injector face. The combustion chamber had a square cross section of 85 mm in width and 110 mm in height. The exit of the combustion chamber was an exhaust tube with a diameter of 40 mm and a height of 50 mm. In the present investigation, the burner was operated with four fused silica windows, each with a thickness of 1.5 mm, for flame visualization.

Fortunately, the problems with the enclosed co-flow burner's windows cracking from the lasers were not present in the GTMC due to the thin windows. Windows would occasionally crack after the flame had been extinguished, but never while data was being taken. These cracks were not caused by the lasers, but were caused by the heating and expan-

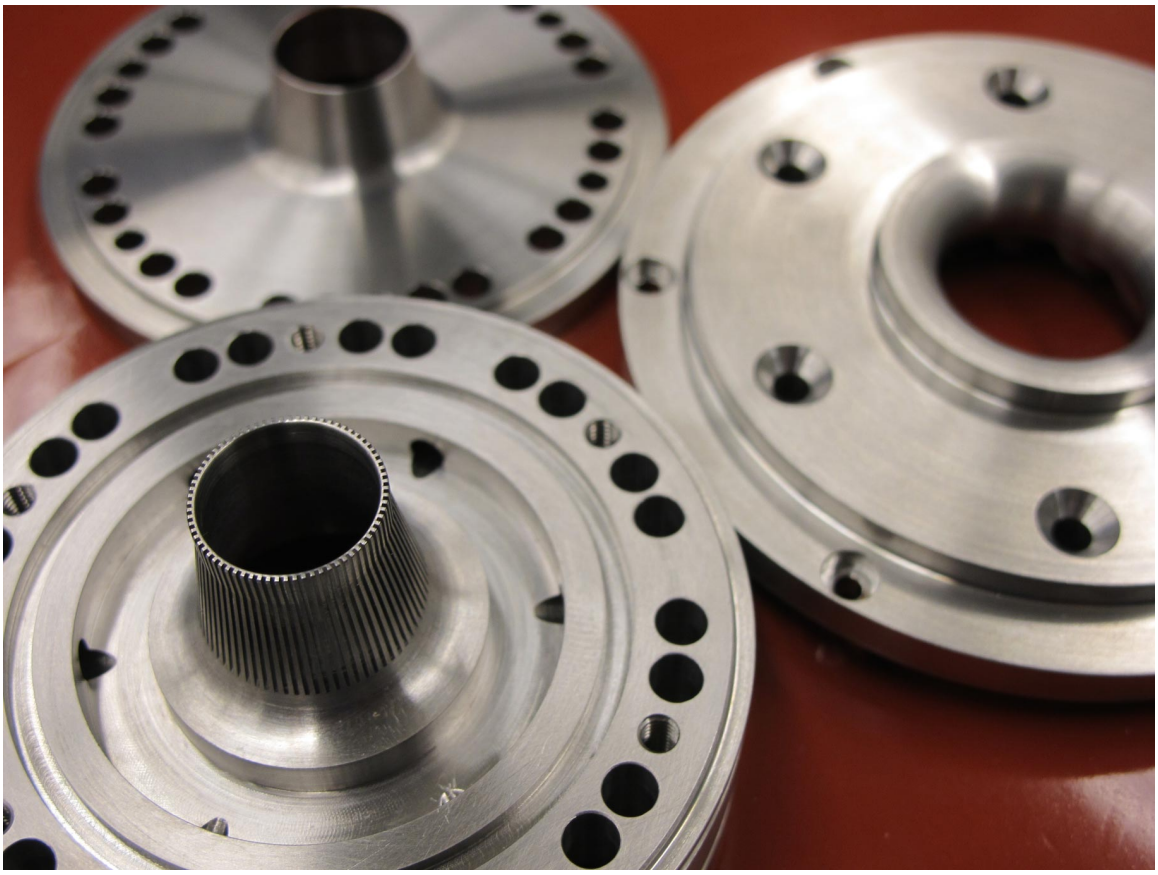

(a) View of the disassembled GTMC nozzle components.

(b) View of the GTMC inner air nozzle and fuel channels.

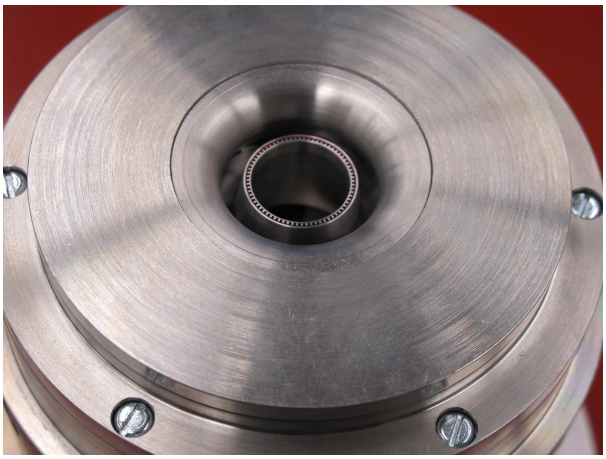

(c) View of the assembled GTMC with injector face ring in place.

Figure 2.6: Views of the GTMC injector face and both fuel and air nozzles. Holes pointing toward center are for fuel flow, holes aligned vertically are for outer air nozzle or screw holes.

sion and subsequent contraction of the GTMC and its windows after the flame had been extinguished.

As with the enclosed co-flow burner, acetone was added to the fuel stream through the use of an acetone bubbler, described in Section 2.1.3, while the NO_2 seeding was achieved by using a a gas cylinder pre-mixed with air and NO_2 at 5000 ppm, by volume. Due to the higher fuel flowrates used during the GTMC experiments—excluding acetone, it was between 12 and 155 times the fuel flowrates used during the enclosed co-flow burner experiments—the acetone seeding system was redesigned to use separate fuel bottles for the bubbler and bubbler bypass lines. At the higher flowrates, independently controlling the flowrates of the bubbler and bypass lines was extremely difficult when they were split off from the same gas bottle.

A diagram of the piping system used while running the GTMC is shown in Fig. 2.7. The system was set up to run the acetone bubbler with two fuel bottles—one for the bubbler and one for the bypass line—and to allow for a third fuel bottle, which would also bypass the acetone bubbler, to be added. Rather than relying on a T-fitting and long pipe to mix the fuel lines, a mixing chamber was used. The chamber was filled with glass marbles and a cone to direct the fuel flows toward the center of the chamber. While not shown in Fig. 2.7, the outlet of the mixing chamber was three separate fuel lines, which were directed to the three fuel ports on the GTMC leading to the annular fuel nozzle. When only two fuel bottles were used, which was typical, the third fuel line was capped off at the mixing chamber. The low pressure (about 100 psi or 670 kPa) building air line was added to the system to use when neither NO_2 nor clean air was needed, to avoid using up the pure air or air with NO_2 gas bottles. (The building air line contained a lot of water and dirt.) Like with the enclosed co-flow burner piping system, the flowrates of the various gases were controlled by choked-flow orifices—except for the building air line, which was left uncontrolled.

Unfortunately, unlike the enclosed co-flow burner, the GTMC was not designed to seal very well. However, with the strong exhaust system installed in the laboratory no NO_2

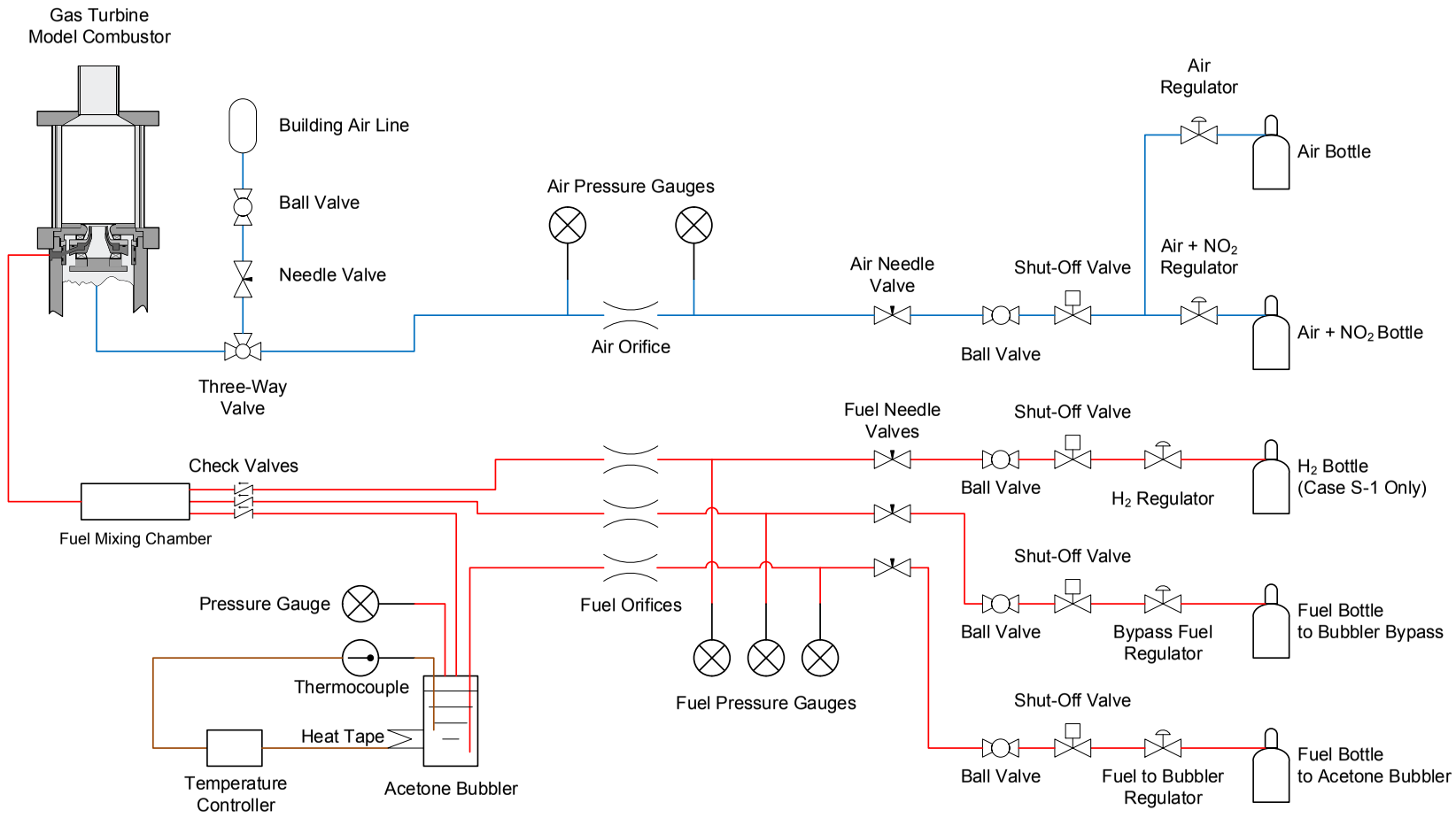

Figure 2.7: Piping diagram of the system used with the Gas Turbine Model Combustor.

escaped and the NO_2 detector never went off.

Previous studies of the GTMC have shown that a combustion instability exists with resonations taking place between 300 Hz and 400 Hz, depending on the fuel, equivalence ratio, and air flowrate [47, 50].

2.1.3 Acetone Bubbler

Controllable acetone seeding for both burners was achieved through the use of an acetone bubbler and a bypass fuel line. The bubbler, pictured in Fig. 2.8, consisted of a stainless steel chamber through which the fuel flowed. It was assumed that the exiting mixture was saturated with acetone. During the enclosed co-flow burner experiments, the bubbler was not temperature controlled, as the fuel flowrates through the bubbler were low enough that they did not cool the bubbler. However, during the GTMC experiments it was found that the fuel flowrates through the bubbler—which were between 13 and 230 times that of the co-flow burner, depending on the case—were high enough to rapidly cool the bubbler. Two actions were implemented to remedy this: first, the temperature of the bubbler was monitored throughout a given experiment so that average acetone flowrates, rather than only beginning or ending flowrates, would be known; second, the bubbler was altered to be temperature controlled through the use of a PID controller and heat tape so that wide ranges of acetone flowrates, and subsequent variations in the fuel-air equivalence ratio, during a single experiment would be avoided.

The bubbler was temperature controlled during the GTMC experiments through the use of PID controller (Omega Engineering CN9121A with SSR330DC25 solid-state relay) with a K-type thermocouple and heat tape (Barnstead/Thermolyne BriskHeat BS0051040) wrapped around the outside of the bubbler. The temperature was set to slightly above room temperature, at 26.0 °C. When running an experiment the bubbler temperature varied from 20 °C to 28 °C, although within a given run the temperature never varied by more than 2.7 °C.

(a) Left View.

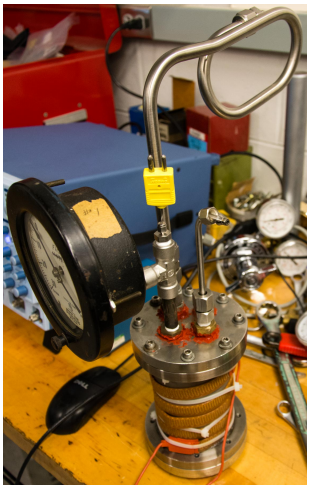

(b) Back View.

(c) Back view of acetone bubbler with tubing connected.

Figure 2.8: Multiple views of the acetone bubbler from the sides and back with heat tape. The smaller inlet tube extends to the bottom of the bubbler, while the larger exit tube begins at the top flange.

The acetone bubbler operated on the principle that the region above the liquid acetone in the bubbler was filled with gaseous acetone at acetone's vapor pressure for the temperature of the bubbler. For example, at 26.0 °C, the vapor pressure of acetone is 0.317 atm (32.1 kPa) [51]. So when a fuel was bubbled through the bubbler, which was at atmospheric pressure, the mixture exiting the bubbler would be 31.7 % acetone by volume. To more precisely control the acetone concentration, a second line of the same fuel that passed through the bubbler was routed to bypass the bubbler and mix with the bubbler line downstream of the acetone bubbler.

The acetone concentration in the fuel/acetone mixture exiting the bubbler (before combining with the bypass line) was determined by first calculating the vapor pressure of the acetone in the bubbler:

$$p_{\mathrm{ace}_{\mathrm{bub}}} = \exp\left(A + \frac{B}{T} + C\ln(T) + D * T^{F}\right), \tag{2.1}$$

where $p_{\mathrm{ace}_{\mathrm{bub}}}$ is the vapor pressure of acetone in Pa; A, B, C, D, and F are curve-fitting

coefficients acquired from DIPPR Project 801 [51]; and T is the temperature of the bubbler, measured about an inch off of the bottom of the bubbler, in the liquid acetone. The acetone concentration in the mixture exiting the bubbler, $\chi_{\mathrm{ace}_{\mathrm{bub}}}$, is then the same as $p_{\mathrm{ace}_{\mathrm{bub}}}$, converted to atm (the pressure of the bubbler was at 1 atm, as it was open to the room, through the burner). The molecular weight of the fuel/acetone mixture exiting the bubbler, $M_{\mathrm{f/ace}_{\mathrm{bub}}}$, can them be determined to be:

$$M_{\mathrm{f/ace}_{\mathrm{bub}}} = M_{\mathrm{f}} + \frac{\chi_{\mathrm{ace}_{\mathrm{bub}}}}{1-\chi_{\mathrm{ace}_{\mathrm{bub}}}} M_{\mathrm{ace}}, \tag{2.2}$$

where M_{f} is the molecular weight of the fuel and M_{ace} is the molecular weight of acetone (58.08 g/mol). The acetone mass fraction in this mixture, $Y_{\mathrm{ace}_{\mathrm{bub}}}$, can be found to be:

$$Y_{\mathrm{ace}_{\mathrm{bub}}} = \frac{M_{\mathrm{ace}}}{\left(1-\chi_{\mathrm{ace}_{\mathrm{bub}}}\right) M_{\mathrm{f/ace}_{\mathrm{bub}}}} \chi_{\mathrm{ace}_{\mathrm{bub}}}. \tag{2.3}$$

Next, the flowrate of acetone out of the bubbler, $\dot{m}_{\mathrm{acetone}}$, can be found to be:

$$\dot{m}_{\mathrm{acetone}} = \frac{Y_{\mathrm{ace}_{\mathrm{bub}}}}{1-Y_{\mathrm{ace}_{\mathrm{bub}}}} \dot{m}_{\mathrm{f}_{\mathrm{bub}}}, \tag{2.4}$$

where $\dot{m}_{\mathrm{f}_{\mathrm{bub}}}$ is the flowrate of the fuel to the acetone bubbler, which is known based on the orifice size and pressure upstream of the orifice. The mass fraction of acetone after the bubbler and bypass fuel lines combine, Y_{acetone} is determined as:

$$Y_{\mathrm{acetone}} = \frac{\dot{m}_{\mathrm{acetone}}}{\dot{m}_{\mathrm{f}_{\mathrm{bypass}}} + \dot{m}_{\mathrm{f}_{\mathrm{bub}}} + \dot{m}_{\mathrm{acetone}}}, \tag{2.5}$$

where $\dot{m}_{\mathrm{f}_{\mathrm{bypass}}}$ is the flowrate of the fuel which bypasses the bubbler, and is used to control the acetone concentration in the final fuel/acetone mixture. The molecular weight of the

final mixture, $M_{\mathrm{f/ace}}$, can be determined to be:

$$M_{\mathrm{f/ace}} = \left(\frac{Y_{\mathrm{acetone}}}{M_{\mathrm{acetone}}} + \frac{1 - Y_{\mathrm{acetone}}}{M_{\mathrm{f}}} \right)^{-1}. \tag{2.6}$$

Finally, the mole fraction of acetone in the final mixture, χ_{acetone}, can be found to be:

$$\chi_{\mathrm{ace}} = Y_{\mathrm{acetone}} \frac{M_{\mathrm{f/ace}}}{M_{\mathrm{acetone}}}. \tag{2.7}$$

Typically, to ensure the mixture exiting the acetone bubbler was saturated with acetone, a series of bubblers in ice water baths were used [35]. This was not done in the experiments in this dissertation largely because controlling the precise concentration of the acetone was not important. It was easier and more practical to monitor and record the temperature of the bubbler and determine the average fuel-air equivalence ratio for a given run. In addition, whether or not the mixture exiting the bubbler was fully saturated with acetone was unimportant, as long as there was enough acetone for its fluorescence to be observed with a good SNR.

2.2 Flame Conditions

Using the enclosed co-flow burner and the GTMC, seven flame configurations, shown in Table 2.1, were studied. The first two cases, L-1 and L-2, were laminar methane (CH_4) / acetone (CH_3COCH_3) / air flames conducted on the enclosed co-flow burner. Case L-1 was a premixed flame, while case L-2 was a non-premixed flame.

The remaining cases (M-1, P-1, P-2, P-3, and S-1) were turbulent flames conducted on the GTMC. Case M-1 was a CH_4/acetone/air flame, similar to case B studied by Weigand et al. [47]. Cases P-1, P-2, and P-3 were propane (C_3H_8) / acetone / air flames. Case P-1 is similar to case M-1, but with methane switched out for propane. Case P-2 is similar to case P-1, but fuel-rich rather than fuel-lean. Case P-3 is similar to case P-2, but

Table 2.1: Flame conditions. NO_2 and acetone mole fractions are given for the pure fuel and pure air streams. The syngas mixture was 25.0 % H_2 and 75.0 % CO, by volume.

Case	Fuel	$\dot{m}_a$, g/min	$\dot{m}_f$, g/min	ϕ_{global}	$\chi_{NO_2} \times 10^{-3}$	$\chi_{acetone}$
L-1	CH_4	3.23	0.28	1.17	2.09	0.18
L-2	CH_4	7.71	1.38	2.42	5.03	0.18
M-1	CH_4	303.89	17.44	0.76	4.90	0.21
P-1	C_3H_8	299.61	16.91	0.77	5.09	0.22
P-2	C_3H_8	301.78	26.57	1.21	5.11	0.21
P-3	C_3H_8	172.53	14.99	1.20	5.08	0.20
S-1	syngas	304.02	36.71	0.64	5.08	0.17

a flowrate that was 60 % that of case B. In addition, the outer air swirler of the GTMC was blocked while running case P-3, as shown in Fig. 2.9 in an attempt to reduce the level of mixing in the flame (it did not). Finally, case S-1 was a syngas/acetone/air flame at conditions similar to cases M-1 and P-1, but with a syngas mixture consisting of 25.0 % hydrogen (H_2) and 75.0 % carbon monoxide (CO), by volume.

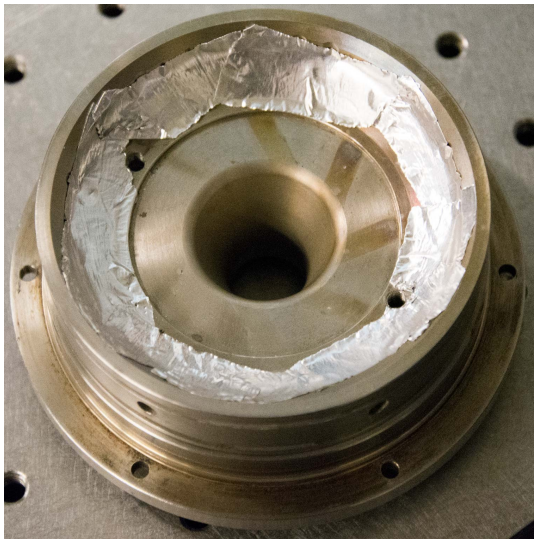

Figure 2.9: View of the GTMC's blocked outer air swirler during case P-3. The two holes not covered by tape were screw holes, not for air passage.

As a note, the NO_2 concentration was lower for case L-1 because a bottle of pure air, connected to the same line as the bottle with air and NO_2, was left open during the

experiment. The strong exhaust on the enclosed co-flow burner made stabilizing laminar premixed flames difficult. Leaving the air bottle open was initially accidental, but was allowed to remain when it was realized that it helped to stabilize the premixed flame. The resulting NO_2 concentration was determined based on the flow coefficients, C_v, provided by the manufacturers of the gas bottle regulators (the lines from the two bottles merged upstream of the flow-controlling orifice).

2.3 Optics

2.3.1 Simultaneous PLIF System

A diagram of the layout of the lasers, cameras, and burner for the simultaneous acetone and NO_2 PLIF system during the GTMC experiments can be seen in Fig. 2.10. The NO_2 PLIF was achieved with a frequency-doubled Nd:YAG laser (Spectra Physics LAB-150, Laser #1) operated at a wavelength of 532 nm. The acetone PLIF was achieved with a frequency-quadrupled Nd:YAG laser (Spectra Physics GCR-130, Laser #2) operated at a wavelength of 266 nm. Both lasers had a linewidth of approximately 1.0 cm^{-1}. The 266 nm laser had a pulse width of about 6 ns, while the 532 nm laser had a pulse width of approximately 8 ns. The 266 nm laser was operated at an energy of 20 mJ/pulse during the enclosed co-flow burner experiments, and 30 mJ/pulse during the GTMC experiments. The 532 nm laser was operated at 50 mJ/pulse during case L-1, 30 mJ/pulse during case L-2, and 110 mJ/pulse during the GTMC experiments. At the enclosed co-flow burner, the 266 nm laser energy had been reduced to 9 mJ, a normalized spectral irradiance of 100 MW/(cm^2 cm^{-1}). At the GTMC, the 266 nm laser energy had been reduced to 11 mJ, a normalized spectral irradiance of 174 MW/(cm^2 cm^{-1}). At the enclosed co-flow burner, during case L-1, the 532 nm laser energy had been reduced to 27.5 mJ, a normalized spectral irradiance of 714 MW/(cm^2 cm^{-1}). During case L-2, the 532 nm laser energy had been reduced to 17 mJ, a normalized spectral irradiance of 448 MW/(cm^2 cm^{-1}). At the

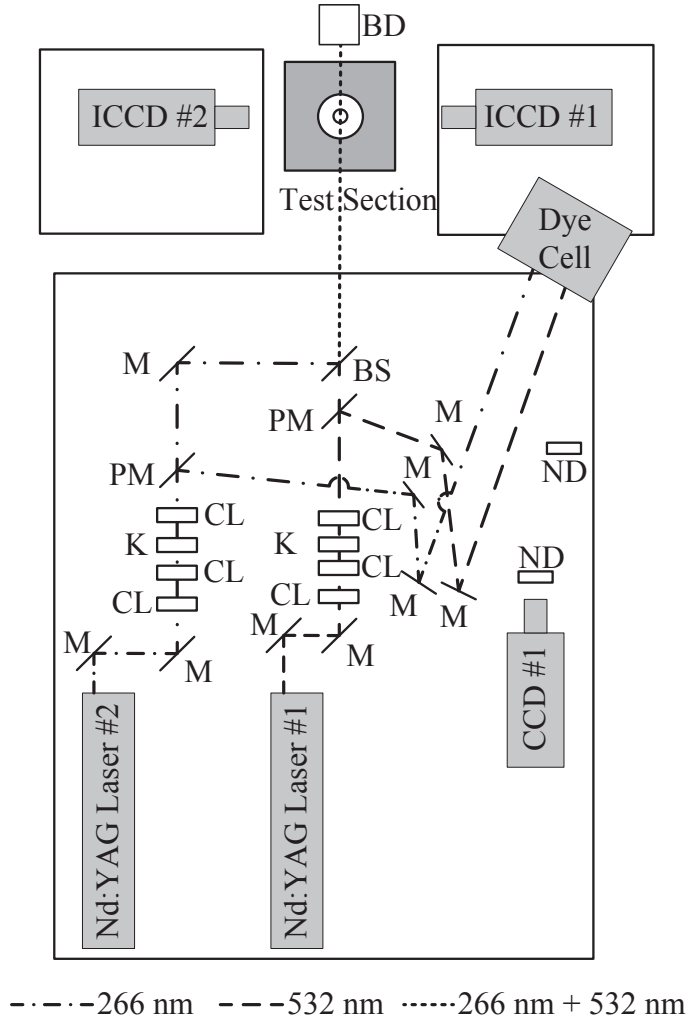

Figure 2.10: Diagram of laser and camera setup for simultaneous PLIF during the GTMC cases. BD - beam dump, BS - beam splitter, CL - cylindrical lens, K - knife edge, M - mirror, ND - neutral density filter, PM - partial mirror.

GTMC, the 532 nm laser energy had been reduced to 33 mJ, a normalized spectral irradiance of 426 MW/(cm^2 cm^{-1}). Both lasers were pulsed at a rate of 10 Hz. Laser energies were measured daily at the laser head by a calibrated pyroelectric energy meter (Scientech PHDX50UV and S310).

The internal harmonic generator of Laser #2 (266 nm) needed to be re-tuned daily to maximize the energy output of the laser. From one day to the next, the tuning could be slightly different, and the shape of the 266 nm laser beam could vary. For this reason, and because the power and shape of the 266 nm laser beam tended to degrade over time, it was

decided to correct for the non-uniformities in the laser sheet on a shot-to-shot basis using a dye cell.

The laser beams were formed into laser sheets by passing through two cylindrical lenses to expand the laser beams into laser sheets, and then collimate the sheets. The 532 nm laser beam first passed through a concave cylindrical lens with a focal length of −100 mm (Lattice Electro Optics UF-CC-1611-100) to expand the laser beam vertically, then a convex cylindrical lens with a focal length of 300 mm (Melles Griot 01 LCP 019) to collimate the laser sheet vertically. At the same time, the 266 nm laser beam passed first through a concave cylindrical lens with a focal length of −125 mm (CVI RCC-40.0-25.4-63.6-UV), then through a convex cylindrical lens with a focal length of 250 mm (CVI Melles Griot SCX-50.8-127.1-UV). The laser sheets then passed between two knife edges, set 10 mm apart, to chop the top and bottom of the laser sheets. After the knife edges, the laser sheets were focused using convex cylindrical lenses with focal lengths of 500 mm (Lattice Electro Optics B-CX-2020-500-532 for the 532 nm laser sheet, CVI Melles Griot SCX-50.8-254.3-UV for the 266 nm laser sheet). The laser sheets next passed through 10 % pick-off mirrors to a dye cell with an optically thick Rhodamine 6G solution to correct for the non-uniformity of the laser sheet. The distances were set up such that the laser sheets would be focused inside the dye cell. The remaining 90 % of the laser sheets were then combined using a dichroic beam splitter (CVI Melles Griot BSR-25-2025) and passed through the burner. At the test section the 266 nm laser sheet had a height of 8 mm and a $1/e^2$ thickness of 128 µm at its focal point. At the same location the 532 nm laser sheet had a height of 8 mm and a $1/e^2$ thickness of 115 µm. The knife edge was used to create a sharp edge in the observed PLIF signals and the fluorescence observed in the dye cell, so that the two images could later be aligned, as suggested by Clemens [52].

The optical setup was slightly different during the enclosed co-flow burner experiments, and is shown in Fig, 2.11. The knife edges and the two cylindrical lenses used to expand the 532 nm sheet vertically were not used. The rest of the setup was the same. The 266 nm

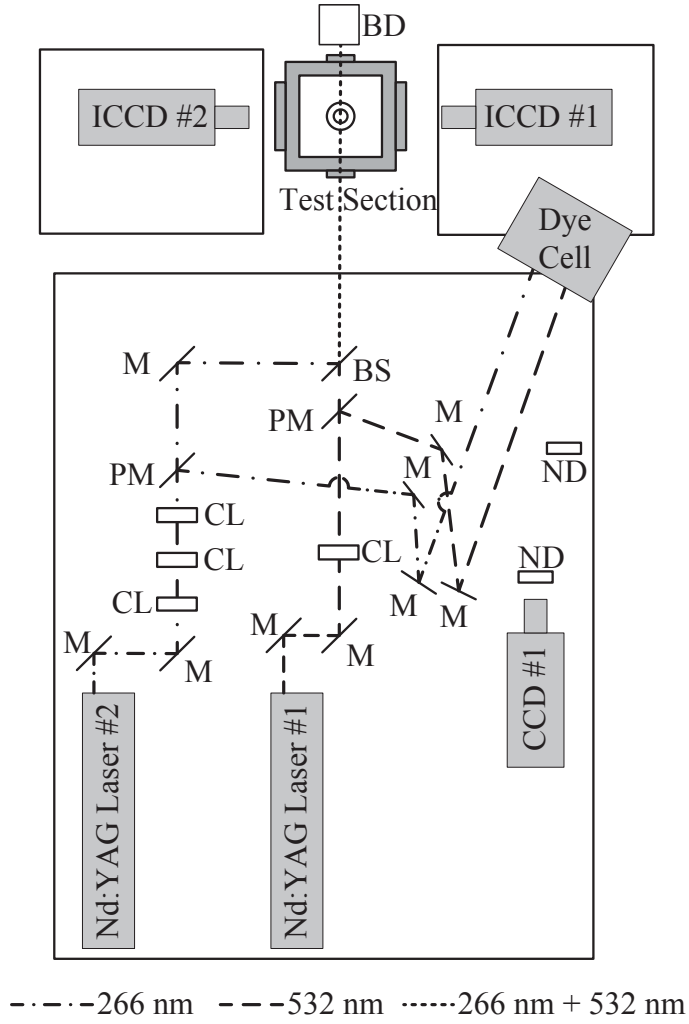

Figure 2.11: Diagram of laser and camera setup for simultaneous PLIF during the enclosed co-flow burner cases. BD - beam dump, BS - beam splitter, CL - cylindrical lens, M - mirror, ND - neutral density filter, PM - partial mirror.

laser sheet had a height of 11 mm, and the 532 nm laser sheet had a height of 4 mm.

NO_2 fluorescence was observed by a red-sensitive Intensified Charge-Coupled Device (ICCD) camera (Andor iStar DH334T-18U-A3, ICCD #1) with an interference filter (CVI Melles Griot LPF-600) and two 3 mm-thick color filters (Schott OG-550) to allow light with wavelengths 600 nm and longer to pass through. Observing the NO_2 fluorescence using a red-sensitive ICCD, with a third generation intensifier, was necessary to achieve the maximum possible Signal-to-Noise Ratio (SNR). The acetone fluorescence was also observed by an ICCD camera (Andor iStar DH734-25F-03, ICCD #2) with an interference

filter (Omega Optical 500ASP) to allow light at wavelengths of 400 nm to 500 nm to pass through. Each ICCD was fitted with a Micro-Nikkor 105 mm f/2.8D lens. A CCD camera (Sony XCD-X710, CCD #1) was fitted with a 50 mm f/1.8 Nikkor lens. CCD #1 imaged the dye cell for shot-to-shot corrections to the non-uniformity of the laser sheets. A neutral density (ND) filter, with an optical density of 2, was placed to cover only the half of the dye cell that the 532 nm laser sheet hit. A second ND filter, with an optical density of 1, was placed to cover the entire dye cell image. The dye cell camera had an exposure time of 3 ms, and it captured the fluorescence from both of the laser sheets in that time.

To ensure that the NO_2 camera's gate was fully open, the intensifier was gated to turn on 50 ns before the arrival of the 532 nm laser pulse. The intensifier gain on the NO_2 camera was turned up to the maximum possible level. The acetone camera's intensifier was gated to turn on 50 ns before the arrival of the 266 nm laser pulse, except for cases L-1 and L-2 where the intensifier gated on 30 ns before the arrival of the 266 nm laser pulse. The acetone camera's intensifier gain was off for cases L-1 and L-2, and at 70 % for the GTMC cases. For case L-1 the NO_2 camera operated with an intensifier gate width of 200 ns, while the acetone camera operated with a gate width of 100 ns. For all other cases both cameras operated with a 100 ns gate width. The reason for the differences between the GTMC cases and the enclosed co-flow burner cases is that during the enclosed co-flow burner cases, various timing combination were being tested for maximum SNR, and those timings had been selected by the time the GTMC cases were run.

There was some overlap between the fluorescence spectra of acetone and the wavelengths observable by ICCD #1 that the optical filters on the camera did not filter out. If nothing had been done, some of the acetone fluorescence would have been seen by the NO_2 camera. As a result, the lasers were timed such that the 266 nm laser pulse reached the burner 500 ns before the 532 nm laser pulse.

The ICCDs each had an array of 1024×1024 pixels, with each pixel having an effective area of $169\,\mu m^2$. During the enclosed co-flow burner experiments, the resolu-

tion of the NO_2 camera was 23.5 ± 4.0 µm/pixel and the acetone camera's resolution was 23.6 ± 4.0 µm/pixel. During the GTMC experiments, the resolution of the NO_2 camera was 21.5 ± 1.2 µm/pixel while the acetone camera's resolution was 21.6 ± 1.3 µm/pixel. However, during the image processing, which will be discussed in Section 4, the images are aligned to have the same size as the acetone image and binned 8×8 for the enclosed co-flow burner, leading to a resolution of 189.2 ± 11.4 µm/pixel. For the GTMC experiments, the images were aligned before binning 4×4 for a resolution of 86.3 ± 2.5 µm/pixel. The binning of the images reduces the resolution while increasing the SNR.

The images output by the ICCDs were 16-bit *sif* files (a format proprietary to the camera manufacturer), and were converted to *tiff* files. CCD #1 output its images as 8-bit *tiff* files.

A total of 450 images were taken by each camera for the GTMC experiments, all of which were usable. For case L-1 on the enclosed co-flow burner, 222 images usable were captured, and 300 usable images were captured for case L-2. For cases L-1, L-2, and M-1, images were captured in sets of 150, as this was the maximum number that the computers controlling the cameras could store in memory at a single time. A spooling feature in the software controlling the ICCDs was discovered after running those cases, but 450 frames had been captured for case M-1, so that number was used for the remaining cases. Case L-1 is an anomaly here because the premixed flame was not very stable, and kept blowing out. While running case L-1, four sets of images were captured—the first two having 100 frames, the last two having 150 frames—and only in 222 frames was the flame attached. After all processing of the images (binning and filtering, which is described in Section 4.1) was complete, the average SNR of the acetone images from the GTMC cases was 24, and for the enclosed co-flow burner cases the acetone SNR was 73. The SNR in the NO_2 images from the GTMC cases was 14, and for the enclosed co-flow burner cases the NO_2 SNR was 15.

The higher SNR in during the enclosed co-flow burner cases is likely because the cameras were slightly closer to the burner. Also, because of the design of the windows

black cloths were draped such that what was essentially a tunnel was created between each ICCD's lens and the window it observed the flame through. These cloths were used to block as much stray light in the laboratory as possible. The design of the GTMC did not allow the cloths to be draped over its windows, and the exterior of the GTMC was much hotter than the exterior of the enclosed co-flow burner, making it a concern that the cloth might burn if they were draped over the top of the GTMC. The GTMC had to be lit with a blowtorch at the exhaust tube, making it a concern that the cloth could be lit as well.

2.3.2 Spatial Resolution

After 4×4 binning, the resolution during the GTMC cases was $86.3 \pm 2.5\,\mu$m/pixel, the 266 nm laser sheet has a $1/e^2$ thickness of $128 \pm 14\,\mu$m, while the 532 nm laser sheet had a $1/e^2$ thickness of $115 \pm 12\,\mu$m. The thermal thickness of a premixed flame, δ_{PF}, can be evaluated as:

$$\delta_{\mathrm{PF}} = 7.4\frac{\alpha_0}{s_L}, \tag{2.8}$$

where α_0 is the thermal diffusivity of the unburned gas mixture at 300 K, and s_L is the flame speed [53]. The mass fractions of all the species upstream of the flame are negligible when compared to that of air, so it can be assumed that $\alpha_0 = \alpha_{\mathrm{air}}$. At a temperature of 300 K, $\alpha_{\mathrm{air}} = 0.225\,\mathrm{cm}^2/\mathrm{s}$ [54]. The equation used here is for premixed flamelets, which are thinner than non-premixed flamelets, so the estimates given are conservative.

The flame speed, s_L, was determined computationally as a part of the flamelet modeling described in Chapter 3. These models were run at fuel-lean and fuel-rich equivalence ratios of $\phi = 0.75$ and $\phi = 1.20$. The actual equivalence ratio at which premixed flamelets burned in the experiments is unknown, so the average s_L will be used. This works out to $s_L = 27.9\,\mathrm{cm}^2/\mathrm{s}$ for a CH_4/acetone flame, $s_L = 36.8\,\mathrm{cm}^2/\mathrm{s}$ for a C_3H_8/acetone flame, and $s_L = 48.4\,\mathrm{cm}^2/\mathrm{s}$ for a syngas/acetone flame with 25 % H_2 and 75 % CO. This gives $\delta_{\mathrm{PF}} = 596\,\mu$m for a CH_4/acetone flame, $\delta_{\mathrm{PF}} = 452\,\mu$m for a C_3H_8/acetone flame, and $\delta_{\mathrm{PF}} = 344\,\mu$m for

a syngas/acetone flame. Finally, in terms of how many pixels exist across a premixed flamelet, it is 7 pixels for a CH_4/acetone flamelet, 5 pixels for a C_3H_8/acetone flamelet, and 4 pixels for a syngas/acetone flamelet. All these resolutions are sufficient for detecting a flamelet.

2.3.3 Simultaneous PLIF Timing

As mentioned previously, there was some overlap in the fluorescence spectrum of acetone and the wavelengths observable by ICCD #1. To deal with this cross-talk the lasers and cameras were set to fire and gate-on 500 ns apart, with the 266 nm laser and acetone camera (Laser #2 and ICCD #2) going first. While the PLIF system was not literally simultaneous, if the time separation, Δt, was short enough such that $\Delta t \ll \tau$, where τ is the fluid mechanic time scale, the flow can be considered "frozen" and the measurement can be considered simultaneous. For the jet flames considered in this study, the characteristic fluid time scale is:

$$\tau = \frac{\Delta x}{U}, \tag{2.9}$$

where Δx is the smallest displacement measurable by the camera and U is the highest velocity seen by the camera. Since sub-pixel movements cannot be detected by a camera, a value of one-half the camera's resolution (41.9 µm/pixel, to be conservative and use the low estimate from the uncertainty) is appropriate for Δx. The most stringent estimate of τ would use the highest flow velocity for U, in this case the jet exit velocity. The mean velocity has been measured to have a maximum value of 10 m/s at a distance of 10 mm above the injector face [55], and 14 m/s at 5 mm [56], so the velocity at the injector face is likely on the order of 20 m/s or less. This gives $\tau = 2.1$ µs, with is much larger than the selected Δt of 500 ns, meaning that the flow can be considered "frozen" during that time period.[1]

[1]For completeness, if the lower speed, enclosed co-flow burner is considered, $\Delta x = 88.9$ µm/pixel and $U = 1.1$ m/s, so $\tau = 81.9$ µs making the flow "frozen." If the unbinned resolution is considered, $\tau = 9.0$ µs for

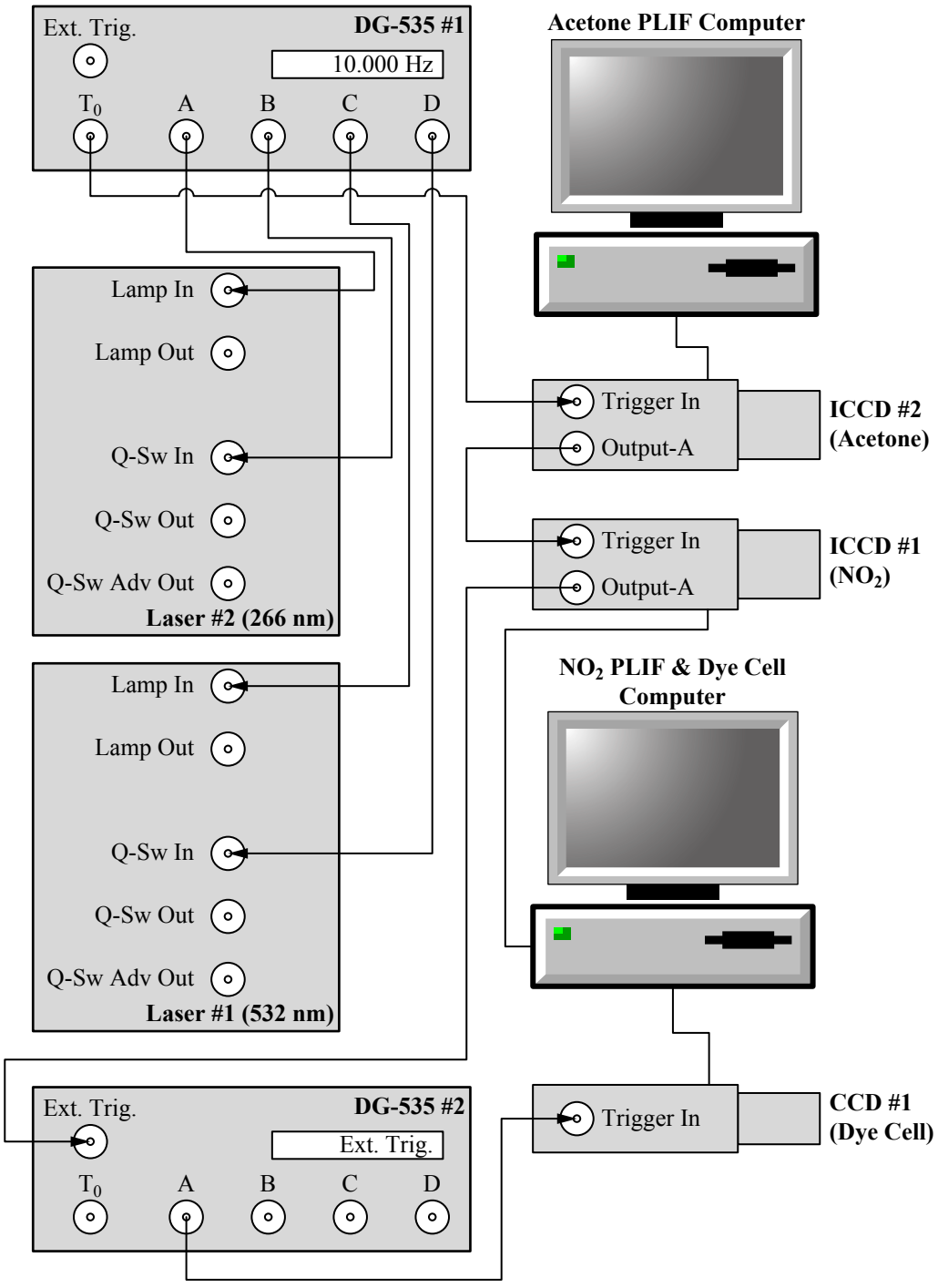

Figure 2.12: Diagram of the wiring used to synchronize the simultaneous acquisition of acetone and NO_2 PLIF signals.

The timing of the lasers and camera was controlled through a combination of two Digital Delay Generators (DDGs) (Stanford Research Systems DG-535) and the digital delay generators built in to ICCDs #1 and #2. The wiring of the system is shown in Fig. 2.12, and a diagram of the timing events is shown in Fig. 2.13. The first delay generator, DG-535 #1, was the primary time keeper of the system at a rate of 10 Hz, which was internally triggered. At a time of $t = 0\,\mu s$ DG-535 #1 would send a trigger signal through output T_0 to the External Trigger of ICCD #2 (the acetone-sensing camera) to start the clock on the camera's internal DDG. All the other outputs of DG-535 #1 were devoted to the timing of the lasers. Outputs A and B of DG-535 #1 were used to control Laser #2 (266 nm). Output A would trigger the flash-lamp on Laser #2 at $t = T_0 + 100\,\mu s$, while output B would trigger the Q-switch at $t = A + 168\,\mu s$. Outputs C and D were then used to control Laser #1 (532 nm). Output C would trigger the flash-lamp of Laser #1 at $t = A - 19.950\,\mu s$, while output D would trigger the Q-switch at $t = C + 189\,\mu s$. The use of a DDG to control the lasers helped to keep consistent timing from day to day. However, slight variations in exactly when the laser beams were emitted would occur because the time depends somewhat on the energy level to which the laser is set, and that is controlled by a continuously variable knob. From one day to the next, although the laser energy was measured with a calibrated energy meter daily, the pulse-to-pulse jitter was on the order of ±3 mJ, so operating at exactly the same energy was hard with Laser #1, and very difficult with Laser #2 due to the need to re-tune its internal harmonic generator every day. The 500 ns time separation between the lasers was verified through the use of two Si-photodiodes (ThorLabs DET10A and DET210) and a high-resolution digital oscilloscope (LeCroy WaveRunner 6100A).

The timing of the cameras was controlled through ICCD #2 (the acetone-sensing camera) which, as mentioned previously, has its internal DDG triggered at $t = 0\,\mu s$ through its External Trigger input. After an insertion delay of approximately 20 ns Output A on ICCD #2 would send a signal to the External Trigger input on ICCD #1 (the NO_2-sensing

the enclosed co-flow burner, and $\tau = 0.5\,\mu s$. for the GTMC experiments.

camera). After an insertion delay of similar length to that of ICCD #2, Output A ICCD #1 would trigger the External Trigger input on DG-535 #2, which was set to output a single pulse on each channel for each external trigger pulse. Output A on DG-535 #2 would then trigger the external trigger of CCD #1 (the dye cell imaging camera) at a time of $t = T_0 + 5\,\mu s$. (On the DG-535 model DDG, Output T_0 would always trigger at the time $t = 0\,\mu s$, if the DG-535 was internally triggered. When the DG-535 was externally triggered, T_0 would still fire at the time $t = 0\,\mu s$, but there would have been an 85 ns insertion delay between the external trigger pulse and the time $t = 0\,\mu s$.) The insertion delay of CCD #1 is unknown, but likely on the order of 20 ns to 100 ns, which has CCD #1 triggering about 260 µs before the arrival of the 266 nm laser pulse. Immediately after this insertion delay, CCD #1 was set to capture an image with a 3 ms exposure, capturing both laser pulses in the image. A DDG was used to trigger CCD #1 rather than triggering directly from Output A on ICCD #1, because the camera model that CCD #1 is, a Sony XCD-X710, is triggered off the falling edge of an inverted Transistor-Transistor Logic (TTL) pulse rather than the rising edge of a normal TTL pulse. Before it was discovered that an ICCD with a red-sensitive third generation intensifier was needed to observe NO_2 fluorescence, a different ICCD was in the same position. This ICCD was the same model as ICCD #2 (Andor iStar DH734-25F-03), which was an older model and dated from mid-2006, and the model output a normal TTL pulse from its Output A. The newer model ICCD that was eventually used for this research had the option to output an inverted TTL pulse, but DG-535 #2 was already in place and offered more control of the output signal.

When the ICCDs received their trigger signals, their CCDs turned on, but the intensifier tube photocathode remained off until a specified delay had passed. The internal DDG in ICCD #2 was set to "gate on" the photocathode (which would allow light to reach the CCD) approximately 268.6 µs after receiving an external trigger, plus a slightly longer insertion delay of about 35 ns. The internal DDG of ICCD #1 was set to gate on the photocathode approximately 269.02 µs after receiving its external trigger, plus an insertion delay of about

135 ns. For all cases the internal DDGs would gate off the photocathodes 100 ns after they gated on, except for case L-1 where the gate width for ICCD #1 was 200 ns. The CCDs on both ICCDs were set for an exposure of 2 ms, the minimum possible on ICCD #2.

The times given for the gate pulse delays for ICCDs #1 and #2 were approximate because they varied from day to day. As a result of the day-to-day variations in laser energy mentioned previously, to ensure that the ICCDs gated on 50 ns before the arrival of their respective laser pulses (30 ns for ICCD #2 during cases L-1 and L-2), the gate pulse delays were measured and adjusted daily after the laser energies had been set and the lasers were warmed up. The timing was measured using a Si-photodiode (ThorLabs DET10A) and the previously mentioned oscilloscope. The ICCDs both had a gate monitor pin, which can be connected to an oscilloscope, and shows when the internal DDG triggers the photocathode to gate on and off. The variation in gate pulse delays was, as expected, small for ICCD #1 at about ± 1.5 ns, while the variation for ICCD #2 was larger at about ± 20 ns. The larger variations for ICCD #2 are likely due to the need to re-tune the internal harmonic generator of Laser #2.

DG-535 #1 was internally triggered at 10 Hz, which means that not only did the lasers fire at that rate, but ICCD #2 would receive a trigger pulse from DG-535 #1 at that rate. (10 Hz was selected because it is the native pulse rate of both lasers.) Due to the slow readout times of CCDs, by the time DG-535 #1 would pulse ICCD #2 for the second laser pulse, ICCD #2 was in the process of reading out the analog charges on the CCD one pixel at a time, converting them into digital signals, and storing the image in memory. ICCD #2 would be unable to capture the LIF occurring as a result of that second laser pulse. In addition, during the time period that ICCD #1 was reading out an image, ICCD #2 would not send a signal pulse through its Output A when an external trigger was received from DG-535 #1, meaning ICCD #2 and CCD #1 would not receive a trigger. ICCD #1 was a newer model than ICCD #2, and was able to read out the charges on its CCD faster than ICCD #2. With the 800×600 pixel, 8-bit images CCD #1 was set to record, it was capable

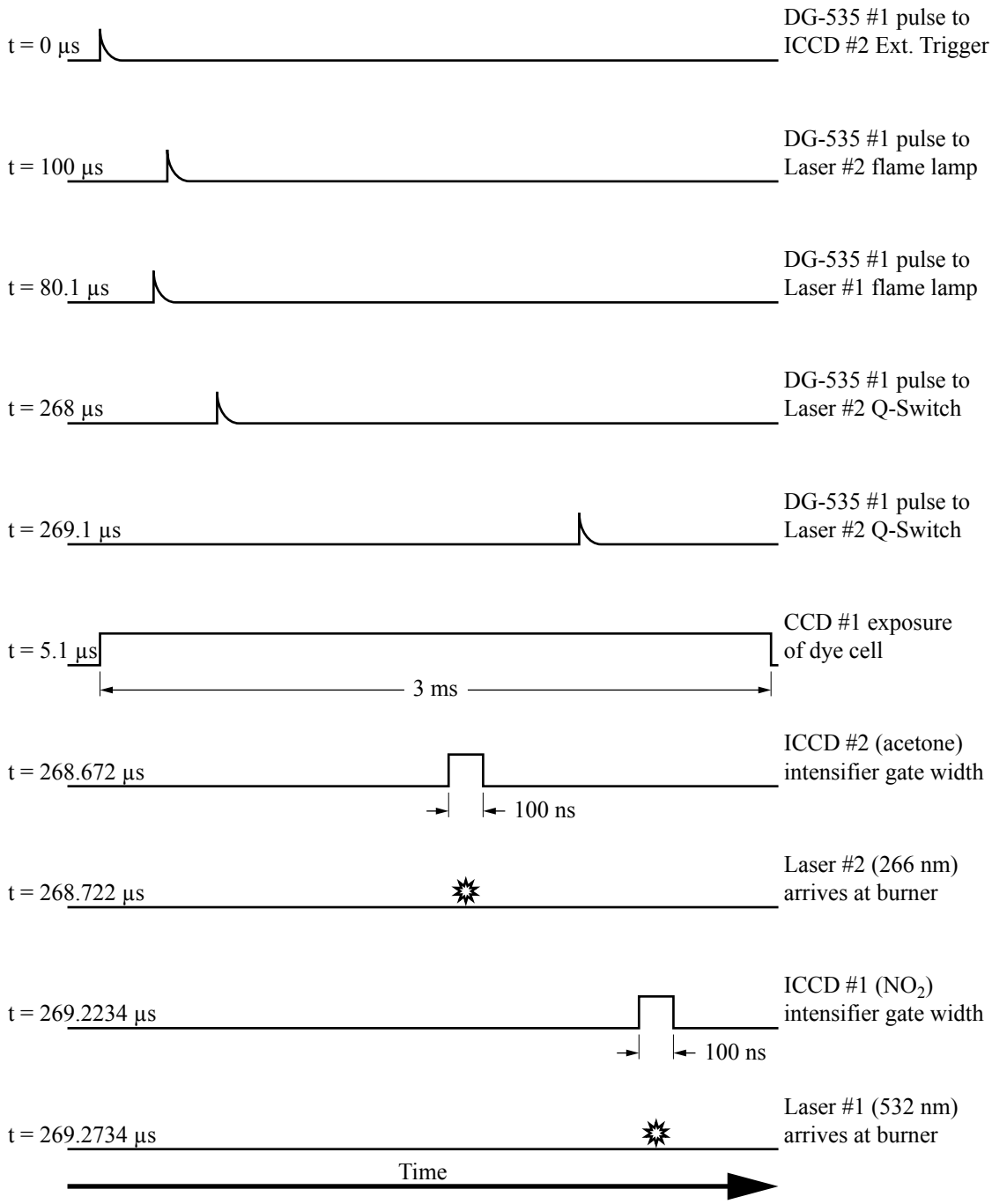

Figure 2.13: Timing of events during one image acquisition cycle. Times given are the start times for each event. Lasers fired at 10 Hz, while cameras captured images every 12^{th} laser pulse. The specific times shown are for case P-1. Diagram is not to scale, except for DDG pulses to Q-Switches, ICCD intensifier gate widths, and laser pulse arrivals.

of a frame rate of 15 fps. This is to say, ICCD #2 was the slowest of the cameras, so it was used as a gatekeeper. It was a safe assumption that by the time ICCD #2 was ready to capture another image, ICCD #1 and CCD #1 would be ready as well. In terms of the cameras, when a data set was acquired, the procedure was that with the flame on and the lasers firing, ICCD #1 and CCD #1 were set to wait for a trigger, and only when the "Take Signal" button on the computer controlling ICCD #2 was clicked would the cameras begin acquiring data. The effect of all of this was that for each laser pulse and fluorescence signal acquired by the cameras, they would miss 11 pulses. It was every 12^{th} laser pulse and fluorescence signal that were actually acquired—a data acquisition rate of roughly 0.83 Hz.

2.4 Experimental Procedure

On a daily basis, several calibration steps had to be taken. Laser #2 (266 nm) required several hours to warm up enough that the internal harmonic generator for the 4^{th} harmonic would no longer drift. This required a re-tuning of the harmonic generating crystals several times during the warm-up period. The laser sheets were checked to be sure they overlapped and passed through the center of the burner. The ICCD camera timing was adjusted to be sure both the NO_2 and acetone PLIF cameras gated on 50 ns before the arrival of their respective laser pulses (30 ns for ICCD #2 during cases L-1 and L-2). This was accomplished through the use of a fast photodiode (ThorLabs DET10A), a digital oscilloscope, and the gate monitor pin on the ICCDs.

Finally, the cameras were both focused on a targeting grid, which had been aligned with the laser sheets, and field of view images of the target were taken with each camera so that the images could later be registered. The images of the target were also used to determine the resolution of the images. For the GTMC experiments, a ring that surrounded the outer air nozzle was removed so that the edge of the nozzle was visible. The distance between that edge and the center of the burner was known, so the location of the center of the burner

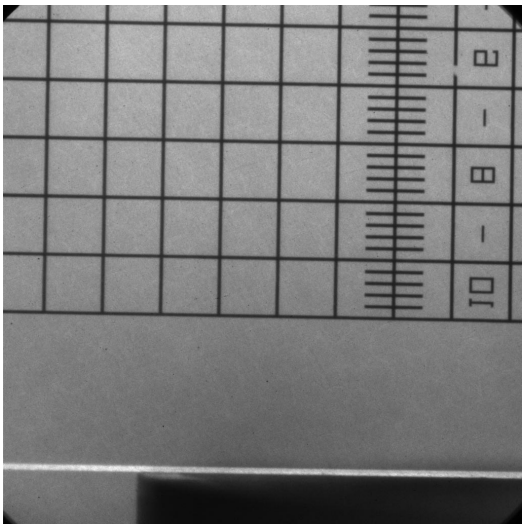

(a) Sample field of view from ICCD #1 (NO_2 camera).

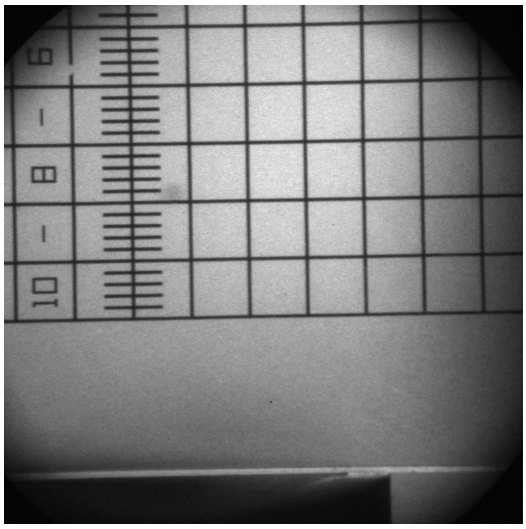

(b) Sample field of view from ICCD #2 (acetone camera).

Figure 2.14: Field of view from ICCDs #1 and #2. Field of view images were used for image registration and resolution calculations. The edge of the outer air nozzle is visible at the bottom of both images. The edge was used to determine the location of the center of the GTMC.

could be determined. Example field of view images for both ICCDs are shown in Fig. 2.14, with the edge of the outer air nozzle visible near the bottom of both images. The setup for capturing a field of view image from the perspective of ICCD #1 is shown in Fig. 2.15. The lamp used to light the target as well as the corner near the outer air nozzle, used to find the location of the center of the burner, are visible. The targeting grid was a fused silica flat, 1 mm thick and 50 mm × 50 mm in size. The lines on the grid were 150 µm thick. A schematic of the targeting grid is shown in Fig. 2.16 at a 240:1 scale.

As was described in Section 2.3.3, ICCD #2 acted as a gatekeeper in allowing the trigger signals downstream to pass or not to pass. So before the burner was lit, the computer controlling both ICCD #1 and CCD #1 was set to initialize both cameras and wait for their respective trigger signals. The computer controlling ICCD #2 was set up so that only the "Take Signal" button needed to be clicked. Both lasers were left firing the entire time.

When it came time to actually run the experiment, great care had to be taken to avoid

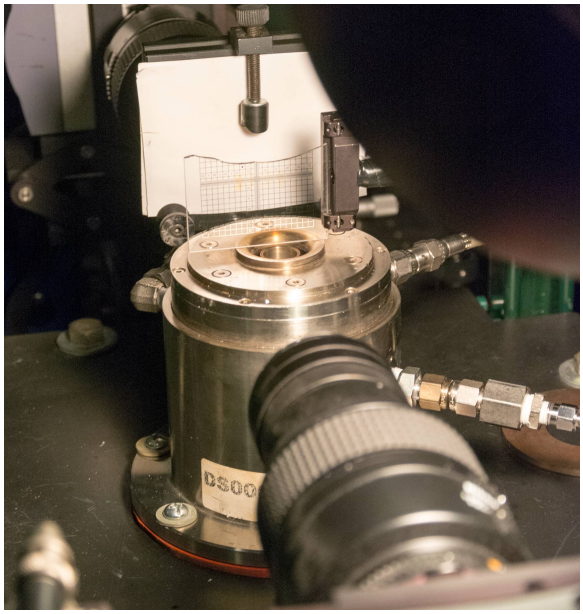

Figure 2.15: Targeting grid set up for capturing field of view image with ICCD #1 (NO_2 camera) during a GTMC experiment. The lamp used to light the target is visible in the upper right corner. The corner near the outer air nozzle, used to determine the location of the center of the burner, is visible as well.

the release of NO_2 during the GTMC experiments. The GTMC was lit at the burner using a blow torch with the exhaust partially closed, the full fuel flowrate, and a low flowrate of pure air (no NO_2). The exhaust was then opened completely, the gas bottle containing the air and NO_2 mixture was opened and the pure air bottle closed. The flowrates on all the fuel and air lines were fine tuned to whatever was called for, and then ICCD #2 was set to run, allowing the other cameras to acquire data simultaneously. The pressures on all the fuel lines, the air lines, and the temperature of the acetone bubbler were recorded every 150 frames so that the average flowrates, acetone concentration, and fuel-air equivalence ratio could be determined.

In addition to the PLIF data, each day a series of background images was taken during the GTMC experiments to account for the CCD dark current, any laser light reflected by the burner's windows or walls that was not blocked by the filters on the ICCD's camera lens, flame luminescence, and any possible fluorescence from the other tracer species seen by an ICCD. One series of images recorded the flame seeded with NO_2 and acetone but

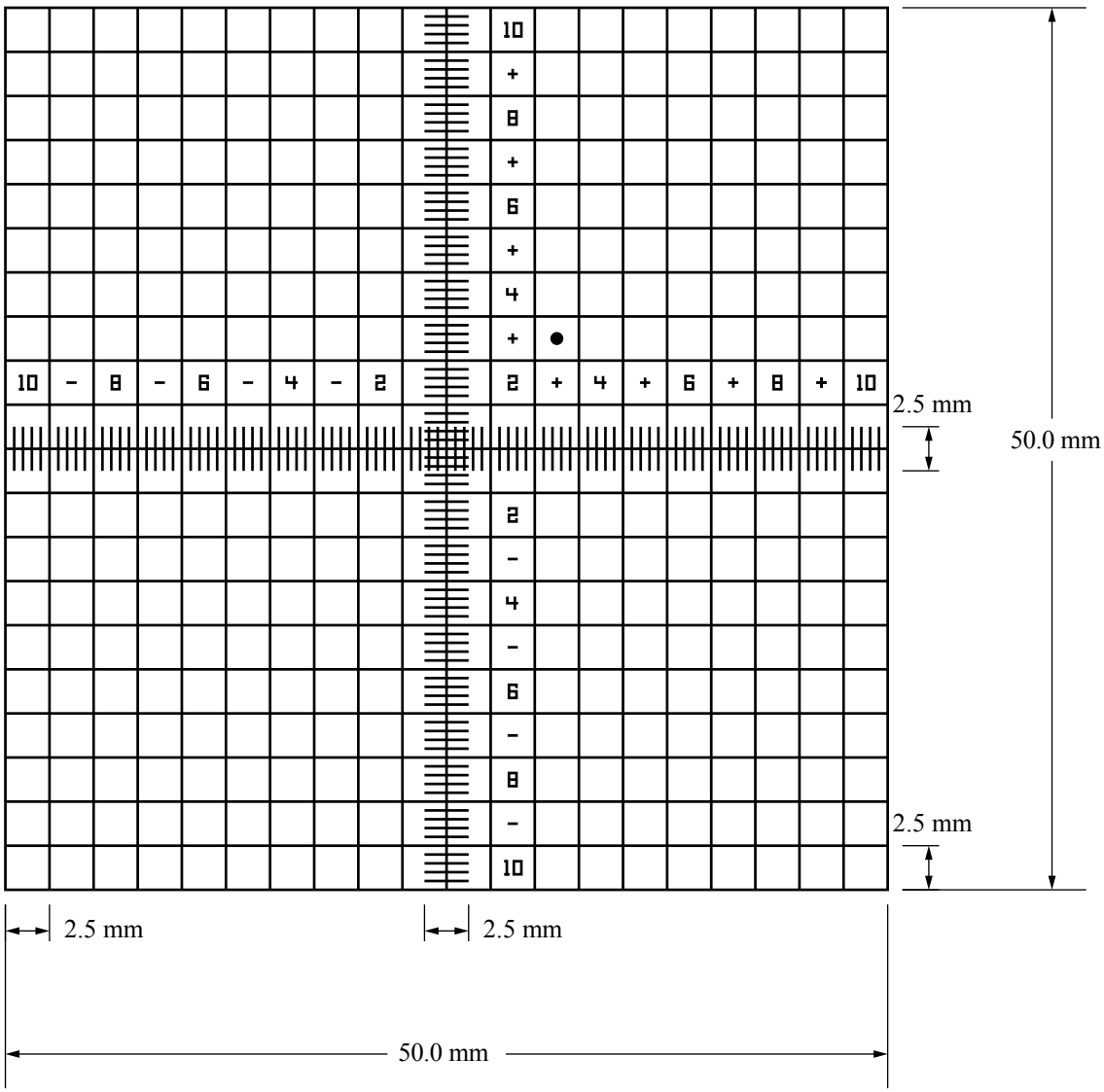

Figure 2.16: Diagram of the intact focusing and image registration target grid. Lines on the target were 150 µm thick. Scale 240:1.

with the lasers turned off. Additional images recorded the flame without the tracer gas a given camera looks for but with the other tracer gas present (e.g., a flame without NO_2 seeding but with acetone seeding, imaged by the NO_2 camera), with the lasers on. A final set of images recorded the same flame without the lasers. Typically, each camera would capture 20 images for each of the background conditions. (For the enclosed co-flow burner experiments, only a background image with the lasers on and no flame was captured.) The theory behind the image corrections that require the background and dye cell images is described in Section 2.5. Typically, and images requiring for there to be no acetone in the flow were acquired before taking the PLIF data, because some residual acetone would remain in the fuel-carrying tubes even with the acetone bubbler removed. Unfortunately, at the flow rates used during the majority of GTMC experiments, a bottle of air mixed with NO_2 would only last for about 15 min, as it contained about 4.7 kg of the mixture. This was slightly longer than the time it took to capture the flame luminosity image—flame with both tracers but without the lasers running—and the PLIF data set. After this the data would be analyzed and the FIMM would be applied.

2.5 Image Corrections

The PLIF signal captured by the cameras includes contributions from multiple sources other than the PLIF signal itself. Clemens [52] provides a method to isolate the PLIF signal from the other signals. If $S_e(x,y)$ is considered to be the signal for a given pixel that is to be evaluated, S_e can be related to the total signal acquired, S_{tot}, through the relationship:

$$S_{tot}(x,y,t_i,t_{ro}) = w(x,y)\left[L(y)S_e(x,y) + S_{back}(x,y,t_i)\right] + S_{dark}(x,y,t_{ro}), \tag{2.10}$$

where $w(x,y)$ is the white-field response function, $L(y)$ is the laser sheet intensity distribution, S_{back} is the background signal, S_{dark} is the camera's dark noise, t_i is the exposure time, and t_{ro} is the array readout time. Rearranging Eq. (2.10) and solving for $S_e(x,y)$ gives a re-

lation for the actual PLIF signal, which can be obtained through relatively straightforward processing:

$$S_{\mathrm{e}}(x,y) = \frac{S_{\mathrm{tot}}(x,y,t_{\mathrm{i}},t_{\mathrm{ro}}) - \left[w(x,y)\,S_{\mathrm{back}}(x,y,t_{\mathrm{i}}) + S_{\mathrm{dark}}(x,y,t_{\mathrm{ro}})\right]}{w(x,y)\,L(y)}. \tag{2.11}$$

The pixels on a CCD array do not have a uniform response to a given source of light, so $w(x,y)$ accounts for this non-uniformity. The white-field response was obtained by imaging a pane of frosted glass illuminated by fluorescent room lights, then rotating the camera 180° so that the pixels that imaged the bottom of the pane of glass, which was not as brightly lit as the top of the pane of glass, then imaged the top of the pane of glass. For each of these two conditions, 30 images were taken, and all 60 images were averaged. Taking the images under these two conditions corrected for any non-uniformity in the lighting of the pane of glass. The images were taken with the intensifier off and an exposure time of 2 ms on both of the Andor cameras. (A white-field correction was not performed on the camera that imaged the dye cell.) A white-field image acquired in this manner would have a lower signal at the edges of the image due to imaging with a circular aperture. This variation was corrected through the equation $I(\beta)/I(0) = \cos^4\beta$, where β is the angle between the optical axis and a line connecting the center of the lens aperture to a given point on the object plane [57]. Prior to this correction, the dark-field response—obtained with the same exposure time as its respective white-field response—had to be subtracted from the white-field response.

The background signal, S_{back}, has contributions from the flame luminosity and from scattered laser light. However, when simultaneous PLIF is employed, fluorescence from both species may contribute. In this experiment the flame luminosity changed when acetone and NO_2 were present. So a method had to be devised that would provide a background image of the flame with acetone and NO_2, of when both the 532 nm and 266 nm lasers were operating, and of any possible fluorescence from the other tracer species.[2] In order

[2]The phrase "the other tracer species" is used to describe the tracer species the other camera was observ-

to factor in these three contributions, three different background images were recorded for each camera. To obtain the luminosity of the flame with acetone and NO_2 present, a series of images was taken of the flame seeded with acetone and NO_2 but no lasers firing; this is called $S_{\mathrm{back_{FL}}}$ (**Back**ground, **F**lame **L**uminosity). Ideally, a series of images could be captured that would include the fluorescence of the other tracer species and the laser light, but this was impossible without a flame also being present. (If no flame were present and the other tracer species were simply flowed into the burner, its fluorescence would exist in regions where if a flame had been present, the species would have been consumed.) In order obtain the needed conditions, a series of images was captured of the flame with the other tracer species present (e.g., a flame without NO_2 but with acetone, imaged by the NO_2 camera), and with both lasers on; this is called $S_{\mathrm{back_{FLnT,L}}}$ (**Back**ground, **F**lame **L**uminosity with **n**o Tracer**, L**asers on). Then a third series of images was captured of the flame with only the other tracer species present (the same flame used to measure $S_{\mathrm{back_{FLnT,L}}}$), with the lasers off; this signal is called $S_{\mathrm{back_{FLnT}}}$ (**Back**ground, **F**lame **L**uminosity with **n**o Tracer). An averaged $S_{\mathrm{back_{FLnT}}}$ is then subtracted from an averaged $S_{\mathrm{back_{FLnT,L}}}$ so that the resulting image would only have contributions from the scattered laser light and the fluorescence of the other tracer species (e.g., scattered 532 nm and 266 nm laser light as well as acetone fluorescence, for the NO_2 camera). The final background signal can be represented by:

$$S_{\mathrm{back}} = S_{\mathrm{back_{FL}}} + S_{\mathrm{back_{FLnT,L}}} - S_{\mathrm{back_{FLnT}}}. \tag{2.12}$$

It should be noted, however, that because the flow is unsteady, the luminosity from shot to shot is different. So each of the three background images was actually the average of 20 images taken under those conditions.

Except in the case of fully saturated fluorescence, the intensity of the fluorescence is dependent on spatial variations in the intensity of the laser sheet. These variations are accounted for by measuring $L(y)$, which is the profile of light intensity in the dye cell, and

ing. In this case, acetone fluorescence for the NO_2 camera, and NO_2 fluorescence for the acetone camera.

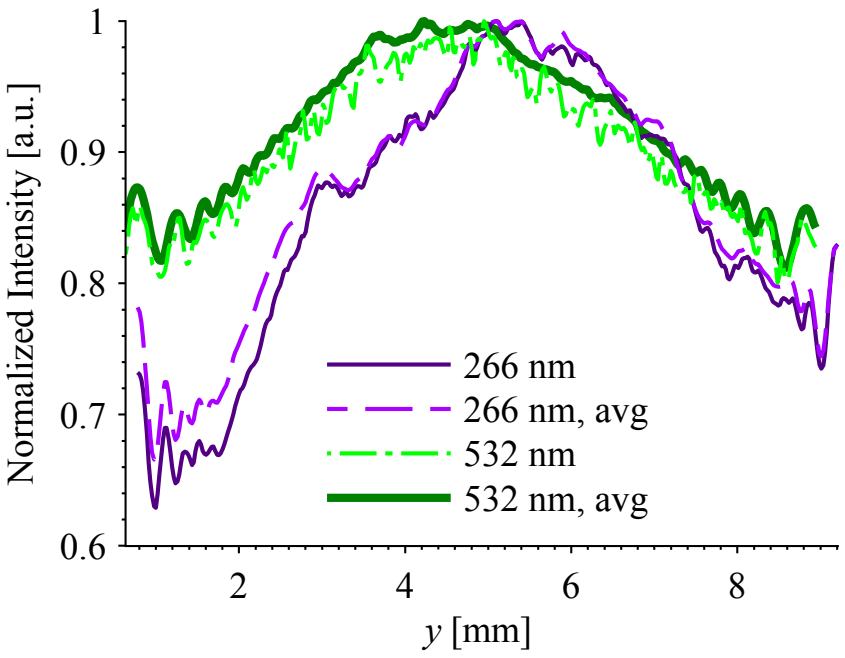

Figure 2.17: Variations in the intensity of both the 266 nm and 532 nm laser sheets in a single pulse are shown, as well as the laser sheet intensities averaged over 450 images. This particular frame and average are from case P-1.

y is the vertical direction. L is considered to be a function only of y because the laser sheet was collimated upstream of both the dye cell and test section. In this experiment, a portion of the laser sheet was picked off and directed to a dye cell filled with an optically thick Rhodamine 6G solution, which was imaged for every laser pulse. A shot-to-shot laser sheet intensity correction was performed, rather than averaging the intensity over several images to obtain the correction. Examples of the profiles of laser sheet intensity are shown in Fig. 2.17. A knife edge was used to chop the edges of the laser sheet before the pick-off mirror to help align the laser sheet intensity correction with the PLIF signal. Both had a sharp drop-off in the signal at their edges.

S_{dark} is the dark-field response of the camera. It is the background signal count that exists with no light source. The dark-field response is dependent on the exposure time and readout time of the CCD. Dark-field images were taken with the same exposure time and readout time as the data image.

If the background image was obtained with the same camera as the S_{tot}, then Eq. (2.11) can be rewritten as:

$$S_{\text{e}} = \frac{S_{\text{tot}} - S_{\text{correction}}}{wL}, \tag{2.13}$$

where $S_{\text{correction}} = wS_{\text{back}} + S_{\text{dark}}$. The background images already take into account the contributions due to the white-field and dark-field found in the numerator of Eq. (2.11) because w and S_{dark} remain constant for different images with the same exposure time and readout time. Technically, $S_{\text{correction}}$ is the background image itself, while S_{back} is one component of that correction. The other components are the white-field and dark-field signals.

Due to the fact that a shot-to-shot correction was used, the laser sheet intensity correction for the PLIF image, S_{tot}, and for the background image, $S_{\text{back}_{\text{FLnT,L}}}$, were different. From Eq. (2.12) and Eq. (2.11), we obtain the full relation for the corrected PLIF signal:

$$S_{\text{e}} = \frac{S_{\text{tot}}}{wL_1} - \frac{wS_{\text{back}_{\text{FL}}} + S_{\text{dark}}}{w} - \frac{wS_{\text{back}_{\text{FLnT,L}}} + S_{\text{dark}}}{wL_2} + \frac{wS_{\text{back}_{\text{FLnT}}} + S_{\text{dark}}}{w}, \tag{2.14}$$

where L_1 is the laser sheet intensity corrections for the acquired PLIF image. L_2 is the sheet correction for the background signal obtained with the flame seeded only with the tracer species that the other camera was observing. It should also be noted that there is no laser sheet intensity correction on the other two background correction terms. This is because those images were acquired without the lasers firing, so there was no laser sheet to correct for.

Equation (2.14) can be simplified if it is rewritten in terms of the background images that were actually acquired:

$$S_{\text{e}} = \frac{S_{\text{tot}}}{wL_1} - \frac{S_{\text{FL}}}{w} - \frac{S_{\text{FLnT,L}}}{wL_2} + \frac{S_{\text{FLnT}}}{w}, \tag{2.15}$$

where S_{FL}, $S_{\text{FLnT,L}}$, and S_{FLnT} are the acquired background images that include the back-

ground signals $S_{\text{back}_{\text{FL}}}$, $S_{\text{back}_{\text{FLnT,L}}}$, and $S_{\text{back}_{\text{FLnT}}}$, respectively.

Finally, Eq. (2.15) can be simplified if the background terms are combined as:

$$S_{\text{B}} = \frac{S_{\text{FL}}}{w} + \frac{S_{\text{FLnT,L}}}{wL_2} - \frac{S_{\text{FLnT}}}{w}, \tag{2.16}$$

where S_{B} is the combined background image.

So, if Eq. (2.16) is combined with Eq. (2.15), we obtain the final equation used to correct the acquired PLIF images in this experiment,

$$S_{\text{e}} = \frac{S_{\text{tot}}}{wL_1} - S_{\text{B}}. \tag{2.17}$$

2.6 Data Processing Methods

To process the PLIF images after the corrections described above, three major operations were performed. The corrected PLIF images were binning, a Non-linear Anisotropic Diffusion Filter (NADF) was applied, and an edge detection algorithm was used to find the locations of minimax acetone and NO_2 PLIF signal gradient. The binning and NADF served to increase the SNR of the image and to improve the edge detection.

2.6.1 Binning

A binned image is one where each pixel is a super-pixel composed of the sum of several pixel values from an original image. When an image is binned 4×4, it means that each super-pixel in the binned image is composed of the sum of the 16 pixel values over a 4×4 grid. The images from the enclosed co-flow burner cases were binned 8×8 (to a resolution of 189 µm/pixel), while the images from the GTMC cases were binned 4×4 (to a resolution of 86 µm/pixel). For the experiments described in this dissertation, the binning of the images was always square, but there is no reason the amounts by which the

images were binned horizontally and vertically have to be the same. In fact, some binning of the flame index matrix, conducted during the post processing of the flame index, was not square. Although this binning was not the summing of sub-pixels, but the statistical analysis of flame index in each super-pixel.

The process of binning was used to increase the SNR of the images. Of course, as is always the case with life, there is no free lunch. The increase in SNR from binning is countered by a decrease in the resolution of the images. For an intensified camera the shot noise depends on statistical fluctuations in the number of photoelectrons, and it may be described by Poisson statistics, where the variance is equal to the mean [58]. The shot noise dominates over the read noise, which occurs during the process of converting the charge on a pixel to a voltage that can be read by an analog-to-digital converter [52]. After binning, the signal in an image can be expected to increase by an amount on the order of the bin-size squared—a factor of 16 for 4×4 binning, and a factor of 64 for 8×8 binning, etc. Typically the amount is less because the image is rarely uniform. The shot noise is proportional $\sqrt{S}$, and SNR is proportional to $\sqrt{S}$ as well. This means that the SNR of a binned image should increase by an amount proportional to the bin-size—a factor of 4 for 4×4 binning, and a factor of 8 for 8×8 binning, etc.

Unless the size of the binning grid happened to align exactly with the size of the image, some pixels would have to be thrown away to avoid super-pixels with too many or too few sub-pixels or super-pixels that share sub-pixels. The binning function which was used was constructed so that it would begin creating super-pixels composed of the sub-pixels in the bottom-right corner of the image, and if left-over pixels had to be thrown away, they would be from the left-most columns and the top-most rows of pixels. Binning began with the bottom-right corner because the majority of detected LIF structures existed toward the bottom and toward the right-side of the images. At an earlier point in the development of the FIMM, the images were cropped to the size of the laser sheet before binning, so selecting which pixels were thrown away was important. Later it was decided to crop several stages

after binning, but the convention was maintained.

The ICCDs used in the LIF experiments were capable of binning directly on the CCD. The idea behind binning directly on the CCD is that the charges from one or more rows of pixels, depending on the bin-size, are shifted onto the CCD's shift register (a row of pixels, shielded from light but equal in length to all other rows of pixels, where the row of pixels currently being read out is shifted down to, then shifted across the shift register to the output amplifier that converts the analog signal on each pixel to a digital one) and then the shift register pixels are shifted over by one or more pixels, depending on the bin-size, onto the output amplifier, where they are read out, converting the analog charge on the amplifier to a digital one. Through this process, the output amplifier may be reading the charge originally contained on one or more pixels. Each time an analog charge is converted to a digital, the amplifier and electronics of the CCD and the camera add some noise, called the read noise, which is roughly the same for each charge converted [59]. So if the charges from several pixels are read out together on the CCD, the noise will be lower than if the signals from those pixels are later combined in software.

The PLIF images in these experiments were software-binned rather than hardware-binned. This was done primarily to allow flexibility with the data. While the SNR might be lower, the possibility of seeing very small LIF structures was desirable. On-camera binning can decrease the CCD readout time, but a faster time was not needed.

As was mentioned earlier, prior to binning, the images during the enclosed co-flow burner had a resolution of 23.6 ± 4.0 µm/pixel, which decreased to 189.2 ± 11.4 µm/pixel after the images were binned 8×8. The images during from the GTMC experiments had a resolution of 21.6 ± 1.3 µm/pixel, which was reduced to 86.3 ± 2.5 µm/pixel after the images were binned 4×4.

2.6.2 Non-linear Anisotropic Diffusion Filter

The noise inherent in a captured image can exist over scales as small as a single pixel. This means that even a slight variation in the signal intensity from one pixel to the next can give very large gradients. There are several techniques to deal with this noise. Frequently a filter will be used to smooth the image, reducing the noise. Oftentimes, these filters are mean filters that set the value of a given pixel to the average value of several surrounding pixels. While these filters are effective at reducing the large gradients due to noise, these filters will often smooth the gradients that exist over large scales due to the consumption of fluorescing species in a flame. These gradients must remain large so that they are easily detected with an edge detection algorithm. If these gradients are smoothed, the edge detection will be difficult.

Perona and Malik [60] developed a Non-linear Anisotropic Diffusion Filter (NADF) that is iterative and intended to smooth an image within a given region, but which resists smoothing the image across large gradients, so that edges are maintained. The NADF is excellent at preserving edges within an image, while it helps an edge detection algorithm to avoid detecting false edges in the uniform regions. Essentially, Perona and Malik developed a smart filter that is aware of the natural boundaries within an image. The filtering process is described by the anisotropic diffusion equation:

$$\frac{\partial}{\partial t} I(x,y,t) = \nabla \cdot \Big(c(x,y,t) \nabla I(x,y,t) \Big) = c(x,y,t) \nabla^2 I + \nabla c \cdot \nabla I, \tag{2.18}$$

where I is the noisy image, c is the diffusion coefficient, x and y are simply the image axes, t is the iterative time step, ∇ is the gradient operator, and ∇^2 is the Laplacian operator. Equation (2.18) can be discretized on a square lattice as:

$$I_{i,j}^{t+1} = I_{i,j}^{t} + \lambda \left[c_N \cdot \Delta_N I + c_S \cdot \Delta_S I + c_E \cdot \Delta_E I + c_W \cdot \Delta_W I \right]_{i,j}^{t}, \tag{2.19}$$

where λ controls the speed of diffusion should be $0 \geq \lambda \leq 0.25$ for stability. N, S, E, and W represent the directions North, South, East, and West, and the operator Δ indicates the nearest-neighbor differences:

$$\Delta_N I_{i,j} \equiv I_{i-1,j} - I_{i,j} \tag{2.20a}$$

$$\Delta_S I_{i,j} \equiv I_{i+1,j} - I_{i,j} \tag{2.20b}$$

$$\Delta_E I_{i,j} \equiv I_{i,j+1} - I_{i,j} \tag{2.20c}$$

$$\Delta_W I_{i,j} \equiv I_{i,j-1} - I_{i,j}. \tag{2.20d}$$

The diffusion coefficient, c is defined as:

$$c(x,y,t) = f\Big(|\nabla I(x,y,t)|\Big), \tag{2.21}$$

where f is the diffusion function, which Perona and Malik developed. c can be discretized, as is needed for Eq. (2.19), as:

$$c^t_{N_{i,j}} = f\left(\left|(\nabla I)^t_{i+(1/2),j}\right|\right) \tag{2.22a}$$

$$c^t_{S_{i,j}} = f\left(\left|(\nabla I)^t_{i-(1/2),j}\right|\right) \tag{2.22b}$$

$$c^t_{E_{i,j}} = f\left(\left|(\nabla I)^t_{i,j+(1/2)}\right|\right) \tag{2.22c}$$

$$c^t_{W_{i,j}} = f\left(\left|(\nabla I)^t_{i,j-(1/2)}\right|\right). \tag{2.22d}$$

This can be rewritten in terms of Eq. (2.20) as:

$$c^t_{N_{i,j}} = f\left(\left|\Delta_N I^t_{i,j}\right|\right) \tag{2.23a}$$

$$c^t_{S_{i,j}} = f\left(\left|\Delta_S I^t_{i,j}\right|\right) \tag{2.23b}$$

$$c^t_{E_{i,j}} = f\left(\left|\Delta_E I^t_{i,j}\right|\right) \tag{2.23c}$$

$$c^t_{W_{i,j}} = f\left(\left|\Delta_W I^t_{i,j}\right|\right). \tag{2.23d}$$

Perona and Malik defined several criteria for what would be a good function for f, and defined two different diffusion functions. The first function was defined as:

$$f(\nabla I) = \exp\left[-\left(\frac{|\nabla I|}{\kappa}\right)^2\right], \tag{2.24}$$

while the second function was defined as:

$$f(\nabla I) = \frac{1}{1+\left(\frac{|\nabla I|}{\kappa}\right)^2}, \tag{2.25}$$

where κ is the conduction coefficient, and should be set to approximately the magnitude of the gradients in image I due to noise. The function in Eq. (2.24) prefers high contrast edges over low contrast edges, while the function in Eq. (2.25) prefers wide regions over smaller ones. It was found that the edge detection was more accurate when the function in Eq. (2.24) was used, so that function was incorporated into the data processing scheme. Other NADFs were developed based on Perona and Malik's [61–63], one with PLIF in mind, however Perona and Malik's is the most vetted and easiest to implement as many algorithms for it have been written.

2.6.3 Edge Detection

The practice of edge detection is a category of mathematical tools for locating regions of either high gradients or discontinuities in images. Typically these regions of high gradients or discontinuities are the *edges* of an object in the image. For this research, the detection of two kinds of edges was desirable. The first kind of edge is the outer edge of a fluorescing species, characterized by a large gradient. The second kind of edge is that of internal structures of a fluorescing species.

Several edge detection algorithms were evaluated, but the Canny algorithm was selected [64]. The Canny method works by looking for local maxima of the image's gradient, and setting an upper and lower threshold to detect strong and weak edges. The weak edges are then only included in the final image if they are connected to stronger edges (leading to more continuous lines than other methods). The use of an upper threshold helps to filter out the large gradients that are typical in noise. Figure 2.18 demonstrates six different edge detection methods on an acetone PLIF image from case M-1 after it has been binned and filtered with an NADF. When compared to other edge detection algorithms the Canny method provides not only the most detected edges, but the most continuous edges as well. Many other methods are either too liberal and detect a lot of false edges, or are too conservative and detect far too few edges.

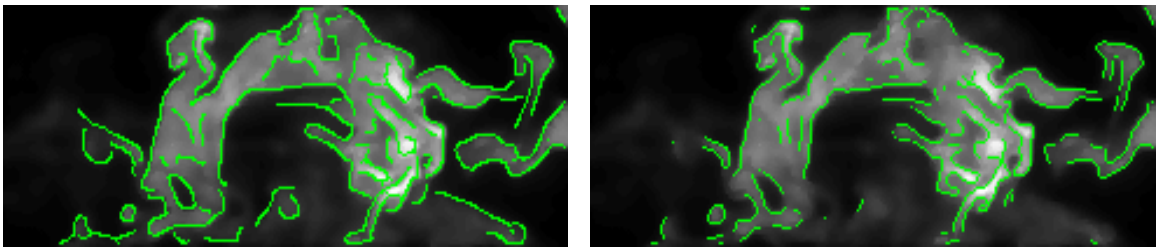

(a) Canny edge detection.

(b) Marr-Hildreth edge detection.

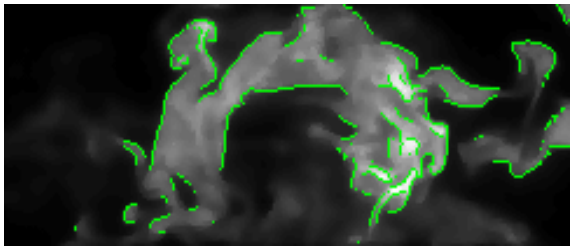

(c) Sobel edge detection.

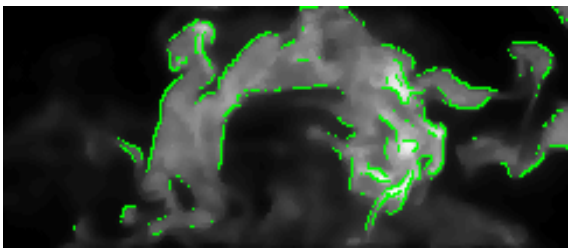

(d) Roberts cross edge detection.

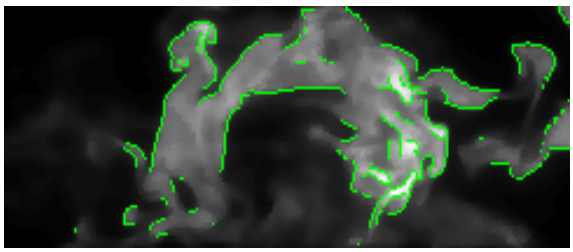

(e) Prewitt edge detection.

Figure 2.18: Comparison of edge detection algorithms showing why the Canny edge detection algorithm was selected. The Canny algorithm provides not only the most detected edges, but the most continuous edges as well.

CHAPTER 3

Tracer Selection

3.1 Modeling

Acetone is well established as a fuel tracer [34], however there was a need to find an effective tracer for O_2. While NO_2 is not traditionally thought of as a fluorescence tracer for O_2, it will function as such, in that when seeded into the air stream, NO_2 is a good indicator of the sign and location of O_2 gradients in laminar and turbulent flames. As was discussed previously, NO_2 has previously been used as a marker of the reaction interface between unburned reactants and combustion products [16, 17], but the use of NO_2 to mark O_2 gradients has not been done. To guide the experiments, flamelet calculations were performed to determine if NO_2 disappears (due to reaction and diffusion) in a manner similar to O_2. These calculations were performed using CHEMKIN 10112 and the GRI-Mech 3.0 [65] chemical reaction mechanism for premixed and non-premixed methane (CH_4) / air flames.

For the purpose of this study an O_2 tracer was considered to be acceptable if the sign of the spatial gradient of the tracer's mass fraction, ∇Y_i, was the same as that of ∇Y_{O_2}. In addition, the tracer cannot be created in the flame; and δ_{i,O_2}, the separation distance between the locations of the maximum gradients of the tracer and O_2 mass fractions, $\left(\nabla Y_i\right)_{\max}$ and $\left(\nabla Y_{O_2}\right)_{\max}$, must be no greater than 1.0 mm.

To elaborate on why an acceptable tracer could not be created in the flame: if the tracer were created in the flame, presumably it would also be consumed in the flame. This would

mean that both positive and negative gradients of the tracer exist in the flame. Identifying which side of the gradient is the consumption of the species in the flame—and closer to where the fuel or oxidizer is consumed—would be very difficult, and may only be possible in flames that are well understood, like laminar flames. The goal of the Flame Index Measurement Method (FIMM) was to measure the flame index in a turbulent flame, and to develop a method that could be applied to flames that are being studied, not flames that are already completely known. For this reason, it was decided that the tracers could only be consumed in the flame, and would have to be seeded into the fuel and air streams.

3.1.1 An Effective Oxygen Tracer

One of the new concerns in combustion science is the development of accurate methods to measure the location and direction of spatial gradients in O_2 concentrations. Oxygen gradients indicate where flamelets are located as well as their type. In the past, several tracer species have been employed in PLIF studies to mark the flame-front location, such as OH and CH_2O [66–70]. However, no tracer has been tested that would indicate the sign of the spatial gradient of the oxidizer, which is needed for the FIMM. As such, the development of the Flame Index Measurement Method began with the search for effective fuel and O_2 tracer gases. This section will describe the selection of an O_2 tracer.

3.1.1.1 Nitric Oxide as an Ineffective Tracer

Initially, nitric oxide (NO) was studied as an O_2 tracer by seeding it at 1000 ppm, by volume, into the air stream. It was found that in both premixed and non-premixed CH_4/air flames ∇Y_{NO} did not follow ∇Y_{O_2}. Too much NO was naturally produced in the flame, as can be seen in Fig. 3.1 for fuel-lean (equivalence ratio, ϕ, of 0.75) and fuel-rich (ϕ = 1.20) premixed CH_4/air flames, and in Fig. 3.2 for a opposed-flow non-premixed CH_4/air flames with a low strain rate of $e = 160\,s^{-1}$ and a high strain rate of $e = 380\,s^{-1}$. NO makes for a bad tracer particularly in the premixed cases as it is consumed at the same time it is be-

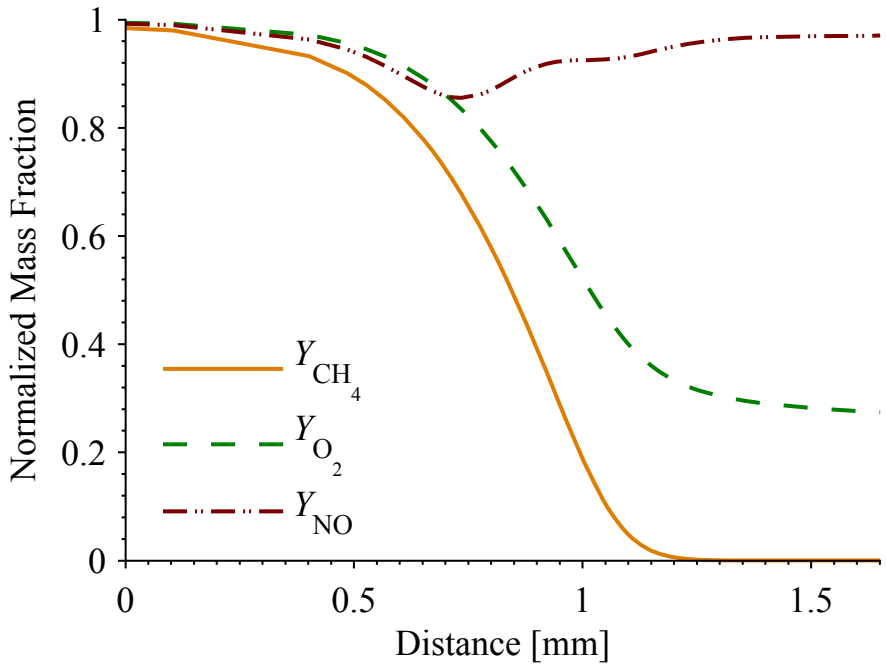

(a) Fuel-lean ($\phi = 0.75$) premixed CH_4/air flame.

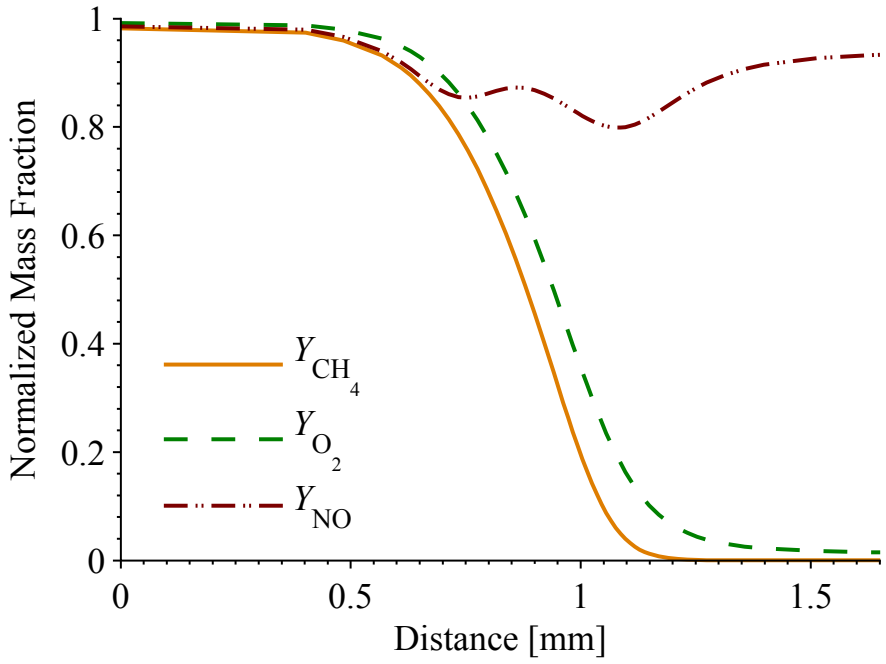

(b) Fuel-rich ($\phi = 1.20$) premixed CH_4/air flame.

Figure 3.1: Computed fuel, oxidizer, and NO tracer normalized mass fractions showing that NO is not a good tracer for O_2. Determined using CHEMKIN for premixed CH_4/air flames that are (a) fuel-lean ($\phi = 0.75$) and (b) fuel-rich ($\phi = 1.20$). NO seeded at 1000 ppm by volume in both cases.

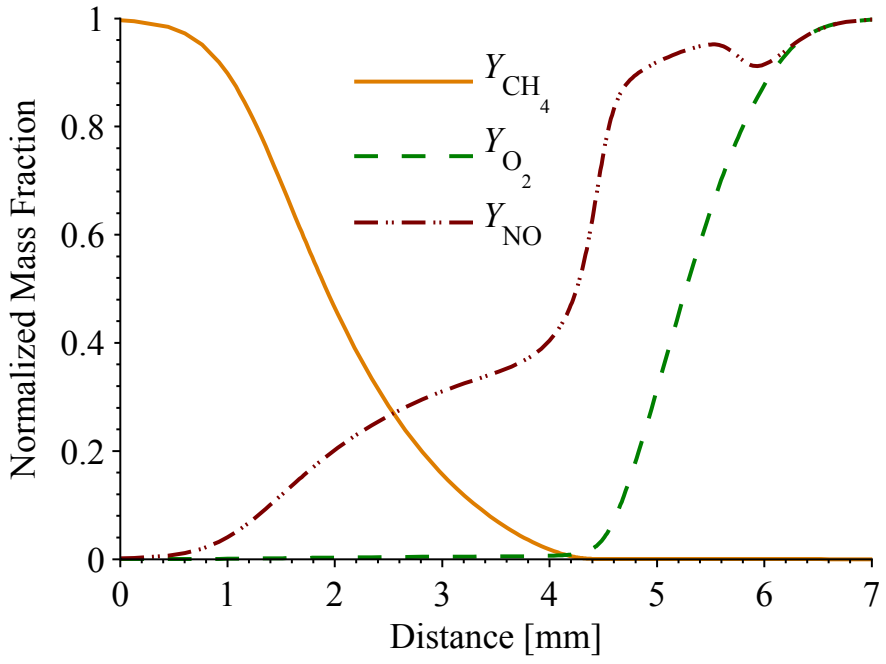

(a) Low strain rate ($e = 160\,\mathrm{s}^{-1}$) CH_4/air flame.

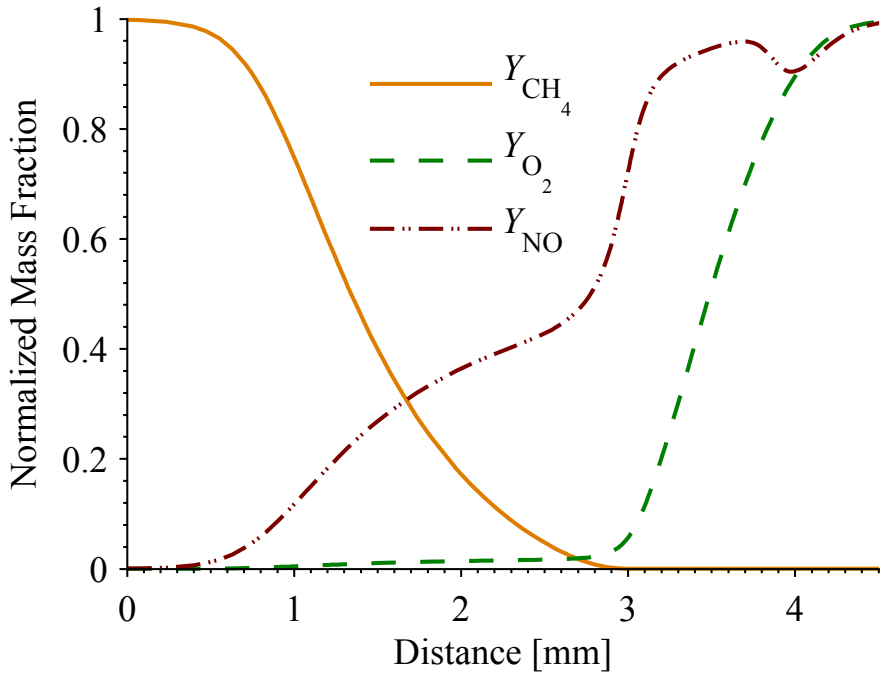

(b) High strain rate ($e = 380\,\mathrm{s}^{-1}$) CH_4/air flame.

Figure 3.2: Computed fuel, oxidizer, and NO tracer normalized mass fractions showing that NO is not a good tracer for O_2. Determined using CHEMKIN for opposed-flow non-premixed CH_4/air flames with (a) a low strain rate ($e = 160\,\mathrm{s}^{-1}$) and (b) a high strain rate ($e = 380\,\mathrm{s}^{-1}$). NO seeded at 1000 ppm by volume in both cases.

ing created in the flame, giving very small gradients that would likely be difficult to detect through PLIF. Therefore NO is not acceptable as an O_2 tracer. OH was also considered as a marker of the oxygen concentration profile, but since it is created in the flame the OH profile is an ambiguous indicator of the O_2 profile.

3.1.1.2 Nitrogen Dioxide as a Good Tracer

After modeling several tracer gases, it was decided that NO_2 is the most effective tracer for O_2. The results of the CH_4/air flamelet models are shown in Fig. 3.3 for fuel-lean ($\phi = 0.75$) and fuel-rich ($\phi = 1.20$) premixed flames, and in Fig. 3.4 for opposed-flow non-premixed flames with low ($e = 160\,s^{-1}$) and high ($e = 550\,s^{-1}$) strain rates. It is seen in both Figs. 3.3 and 3.4 that NO_2 meets all three criteria for a reasonably good tracer of O_2. The signs of the gradients of the O_2 and NO_2 mass fractions remained the same throughout the flame, no NO_2 was created in the flame, and the separation distances between the maximum gradients of the O_2 and NO_2 mass fractions never exceeded 1.0 mm. To be more precise, the separation distances between the maximum gradients were 0.75 mm in the low strain opposed-flow case, 0.45 mm in the high strain opposed-flow case, 0.15 mm in the fuel-lean premixed case, and 0.16 mm in the fuel-rich premixed case. It is emphasized that NO_2 is not an exact tracer for O_2 because of the differences between the NO_2 and O_2 curves in Fig. 3.3. However it is an acceptable way to locate the gradient of O_2 and its direction, and this is what is needed for the FIMM.

Based on the coefficients of diffusivity recommended by Massman [71], at a temperature of 293 K and a pressure of 1 atm, the diffusivity of NO_2 into N_2, D_{NO_2,N_2}, is 1.54 mm/s. At the same temperature and pressure, the diffusivity of O_2 into N_2, D_{O_2,N_2} is 2.05 mm/s. At a pressure of 1 atm and a temperature of 700 K—where NO_2 breakdown occurs and the LIF signal disappears [16]—$D_{NO_2,N_2} = 7.46$ mm/s and $D_{O_2,N_2} = 9.94$ mm/s.

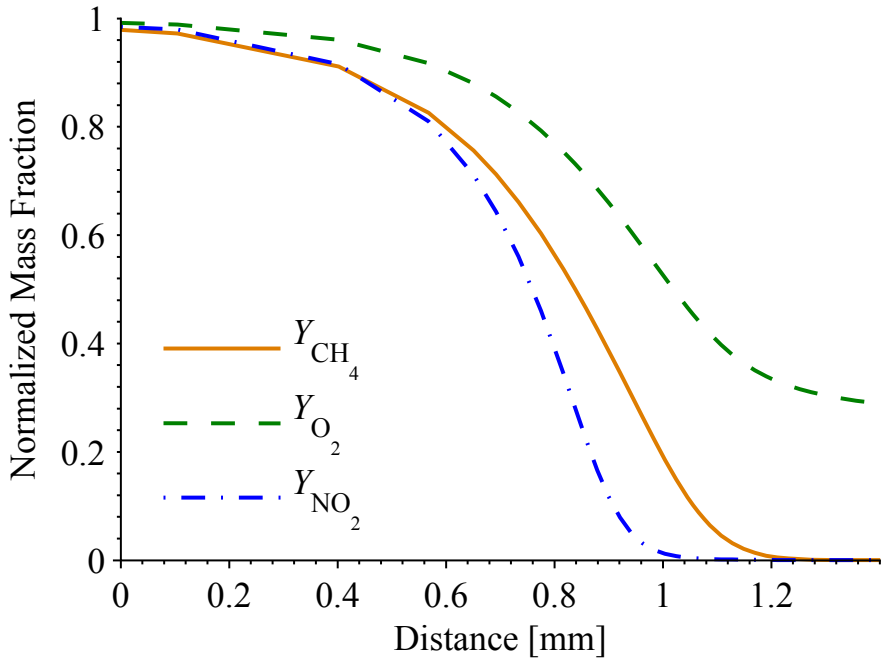

(a) Fuel-lean ($\phi = 0.75$) premixed CH_4/air flame.

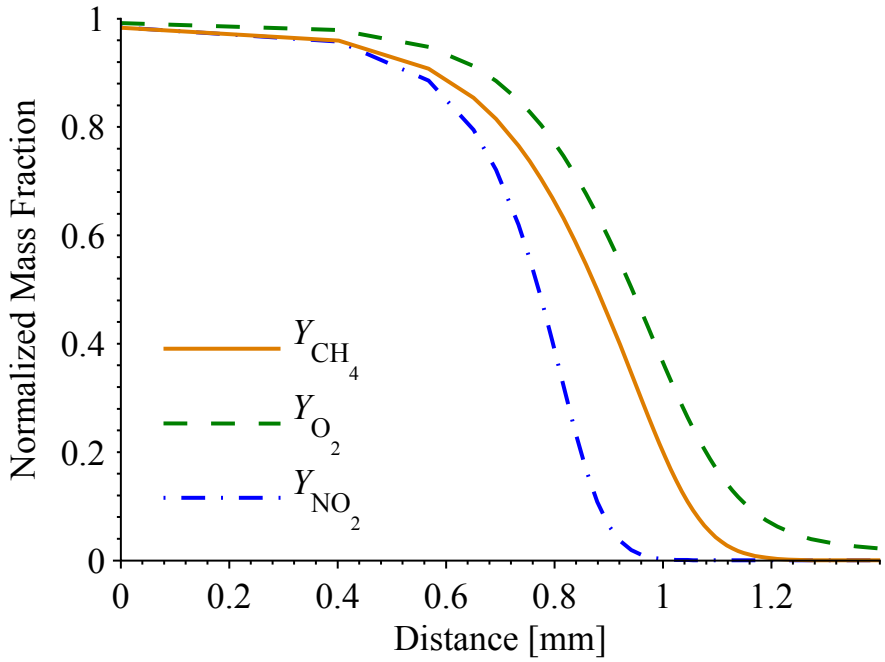

(b) Fuel-rich ($\phi = 1.20$) premixed CH_4/air flame.

Figure 3.3: Computed fuel, oxidizer, and NO_2 tracer normalized mass fractions showing that NO_2 is an acceptable tracer for O_2. Determined using CHEMKIN, for premixed CH_4/air flames with NO_2 seeded at 5000 ppm by volume, at (a) lean ($\phi = 0.75$) and (b) rich ($\phi = 1.20$) equivalence ratios.

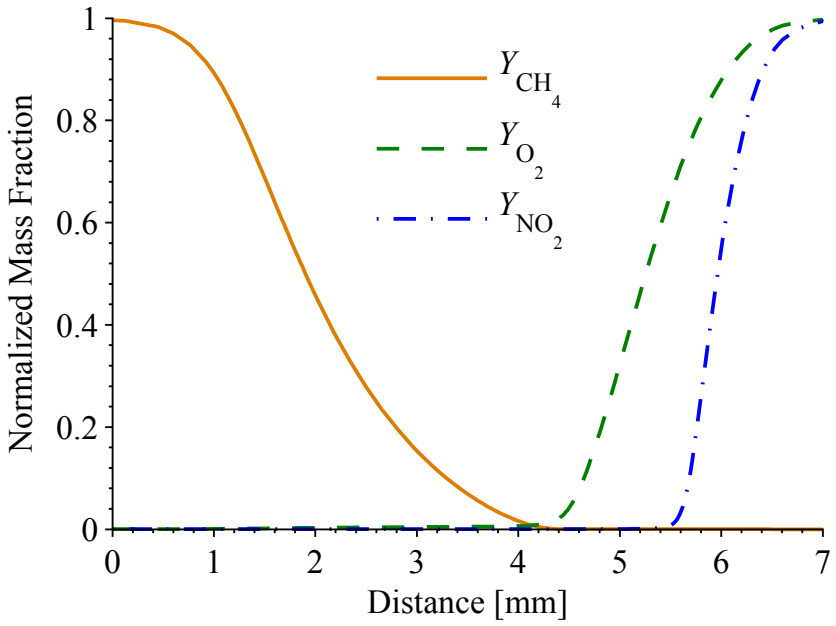

(a) Low strain rate ($e = 160\,\mathrm{s}^{-1}$) CH_4/air flame.

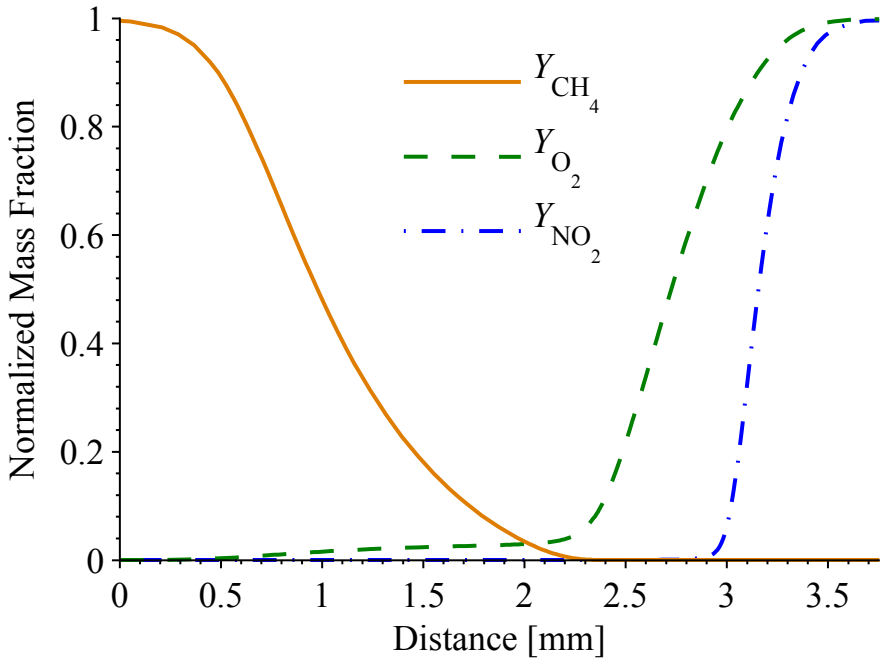

(b) High strain rate ($e = 550\,\mathrm{s}^{-1}$) CH_4/air flame.

Figure 3.4: Computed fuel, oxidizer, and NO_2 tracer normalized mass fractions showing that NO_2 is an acceptable tracer for O_2. Determined using CHEMKIN, for opposed-flow non-premixed CH_4/air flames with NO_2 seeded at 5000 ppm by volume, at (a) low ($e = 160\,\mathrm{s}^{-1}$) and (b) high ($e = 550\,\mathrm{s}^{-1}$) strain rates.

3.1.2 Simultaneous Fuel and Oxygen Tracing

Acetone is already known to be a good fuel tracer, so its selection was not difficult. However, flames with all necessary elements had to be evaluated. A CH_4/acetone/air flame with acetone and nitrogen dioxide as fuel tracers was modeled. The GRI-Mech reaction mechanism does not currently support acetone reactions, so a new mechanism had to be found. Several reaction mechanisms were tried, including that of Pichon et al. [72]. However, because the Pichon mechanism was designed primarily for acetone flames (rather than CH_4/acetone flames), is was not successful. In the end, a modified version of GRI-Mech, similar to the mechanism developed by Chong and Hochgreb [43] was used. After modeling several fuel and oxidizer tracers, it was decided that acetone, seeded at 20 % by volume, would function as a good tracer for CH_4. Likewise NO_2, seeded at 5000 ppm by volume, would function as a good tracer for O_2.

These computational models were run for three different fuels—CH_4; propane (C_3H_8); and two syngas mixtures, one 25 % H_2 and 75 % CO by volume, shown in this section, and the other 20 % H_2 and 80 % CO by volume, shown in Appendix A—under premixed and non-premixed conditions at two different fuel-air equivalence ratios and strain rates. One particularly important result of the models is the separation distance between the locations of maximum mass fraction gradient for a tracer and the species it is tracking, δ_{NO_2,O_2} and $\delta_{ace,f}$, as shown in Table 3.1. The separation distance between the locations of maximum mass fraction gradient for NO_2 and acetone, δ_{ace,H_2}, are shown as well. The uncertainties shown are based on the grid size.

To show that acetone and NO_2 would act as tracers for CH_4 and O_2, respectively, the results of the CHEMKIN models are shown in Fig. 3.5 for non-premixed flames, and in Fig. 3.6 for premixed flames. It can easily be seen in both Figs. 3.5 and 3.6 that the acetone tracks the CH_4, and that the NO_2 tracks the O_2, meaning acetone and NO_2 are good fuel and oxidizer tracers. It is noted that it is not necessary that the profile of the tracer gas fall exactly on top of the fuel or the O_2 profile. The primary goal is to measure whether

Table 3.1: Computed separation distances between the locations of the fluorescence tracers' maximum mass fraction gradients and that of the tracer and fuel or O_2. Determined using CHEMKIN. For the syngas case, fuel refers to CO. Premixed flames have the equivalence ratio (ϕ) provided, while non-premixed flames have the strain rate (e) provided. Uncertainties are based on the grid size. The syngas mixture was 25 % H_2 and 75 % CO, by volume.

Fuel	ϕ	e, s^{-1}	δ_{ace,NO_2}, µm	δ_{NO_2,O_2}, µm	$\delta_{ace,f}$, µm	δ_{ace,H_2}, µm
CH_4	0.75	—	77 ± 31	140 ± 21	50 ± 32	—
	1.20	—	93 ± 15	137 ± 11	44 ± 14	—
	—	179	3632 ± 197	790 ± 197	474 ± 169	—
	—	441	395 ± 177	395 ± 177	197 ± 71	—
C_3H_8	0.75	—	78 ± 26	89 ± 21	42 ± 26	—
	1.20	—	81 ± 15	106 ± 15	13 ± 18	—
	—	186	3000 ± 142	790 ± 213	0 ± 168	—
	—	456	2092 ± 56	592 ± 125	40 ± 56	—
Syngas	0.75	—	77 ± 19	120 ± 15	194 ± 21	131 ± 21
	1.20	—	75 ± 11	113 ± 11	158 ± 14	120 ± 14
	—	182	3434 ± 198	750 ± 337	711 ± 177	1540 ± 163
	—	438	2368 ± 142	632 ± 112	592 ± 125	1066 ± 125

the gradient is a positive or a negative number and its location, and not to measure the absolute value of the gradient with high accuracy. It is seen that acetone pyrolyzes earlier than methane, and that NO_2 also decomposes earlier than O_2. What is encouraging is that the slopes of the tracer gases are monotonic and have the same signs as the fuel and O_2 profiles.

After studying CH_4/acetone/air flames, it was thought that acetone would perform better as a tracer in a C_3H_8/acetone/air flame due to their more similar molecular weights (acetone has a molecular weight of 58.08 g/mol, CH_4 has a molecular weight of 16.04 g/mol, and C_3H_8 has a molecular weight of 44.10 g/mol). This turned out to be the case, as shown in Fig. 3.7 for non-premixed flames, and in Fig. 3.8 for fuel-lean and fuel-rich premixed flames.

Finally, the use of syngas as a fuel was evaluated in non-premixed and premixed syngas/acetone/air flames, shown in Figs. 3.9 and 3.10. The syngas mixture was 25 % H_2 and

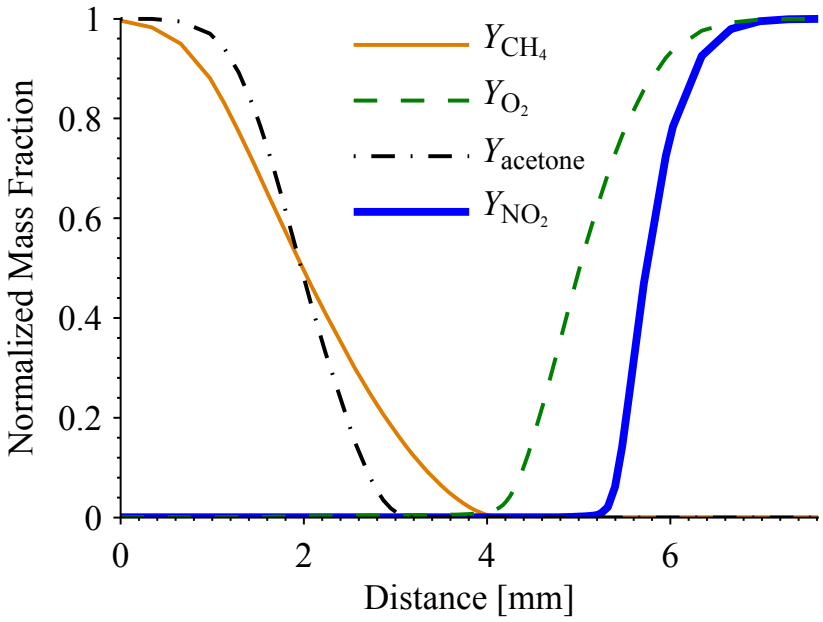

(a) Low strain rate ($e = 180\,\mathrm{s}^{-1}$) CH_4/acetone/air flame.

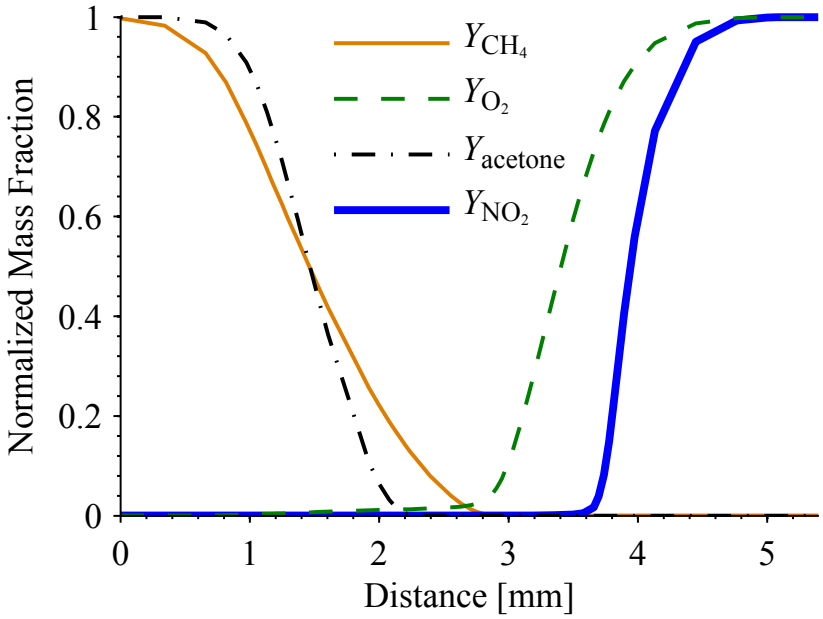

(b) High strain rate ($e = 445\,\mathrm{s}^{-1}$) CH_4/acetone/air flame.

Figure 3.5: Computed fuel and oxidizer, NO_2 and acetone tracer normalized mass fractions showing that NO_2 and acetone are acceptable tracers for O_2 and CH_4. Determined using CHEMKIN, for opposed-flow non-premixed CH_4/acetone/air flames with NO_2 seeded at 5000 ppm by volume and acetone seeded at 20 % by volume. Shown at (a) a low strain rate of $e = 180\,\mathrm{s}^{-1}$ and (b) a high strain rate of $e = 445\,\mathrm{s}^{-1}$.

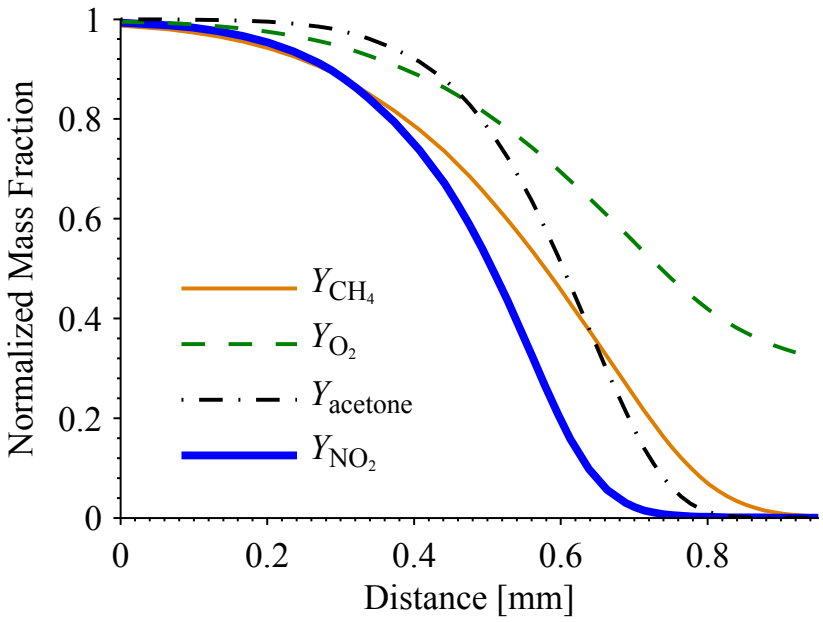

(a) Fuel-lean (ϕ = 0.75) premixed CH_4/acetone/air flame.

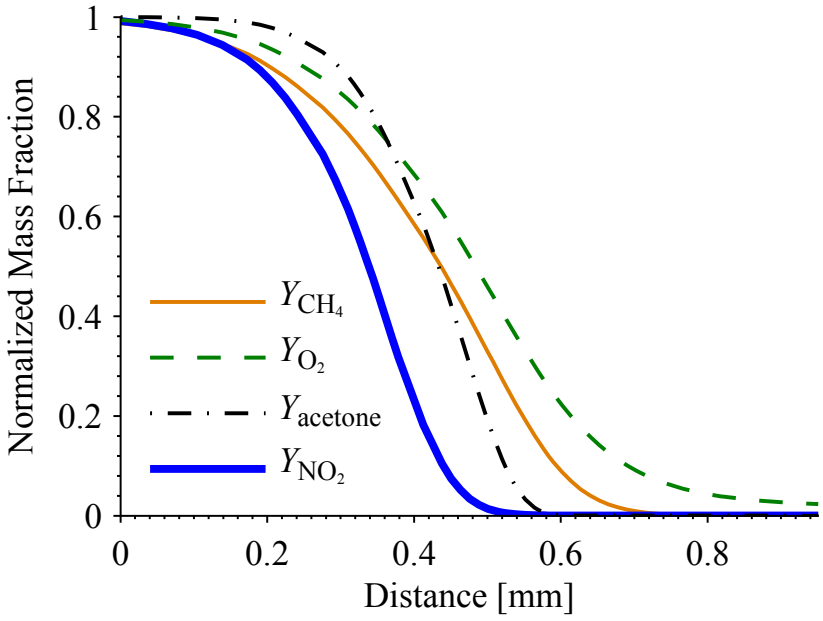

(b) Fuel-rich (ϕ = 1.20) premixed CH_4/acetone/air flame.

Figure 3.6: Computed fuel and oxidizer, NO_2 and acetone tracer normalized mass fractions showing that NO_2 and acetone are acceptable tracers for O_2 and CH_4. Determined using CHEMKIN, for premixed CH_4/acetone/air flames with NO_2 seeded at 5000 ppm by volume and acetone seeded at 20 % by volume, at (a) lean (ϕ = 0.75) and (b) rich (ϕ = 1.20) equivalence ratios.

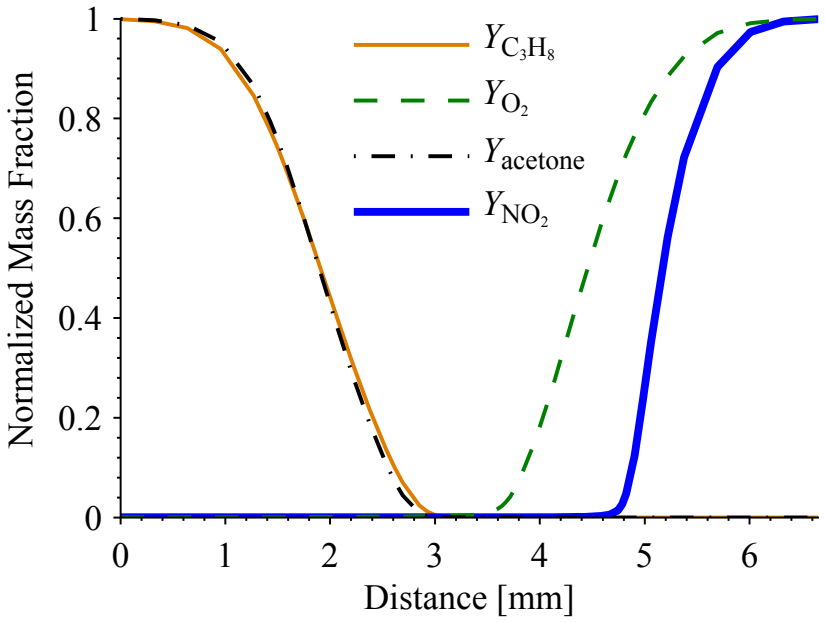

(a) Low strain rate ($e = 185\,s^{-1}$) C_3H_8/acetone/air flame.

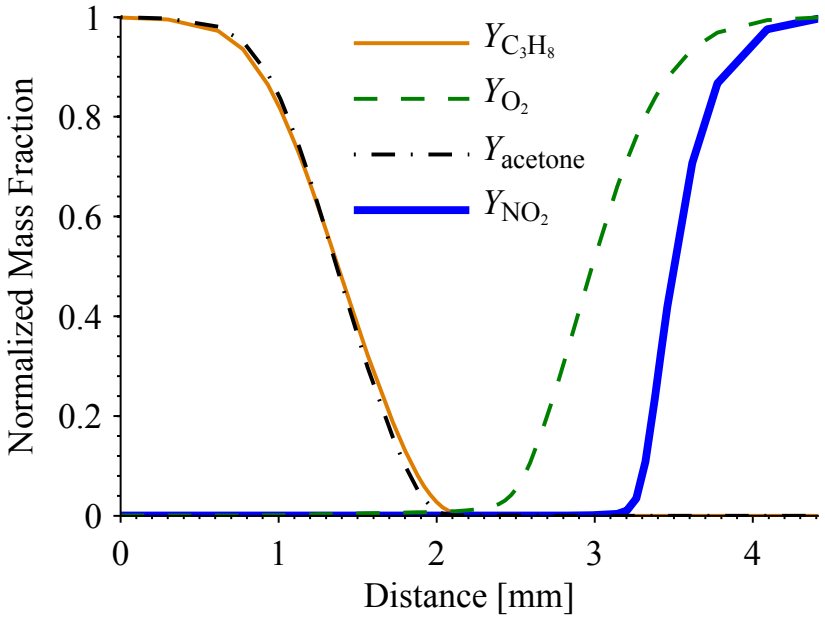

(b) High strain rate ($e = 455\,s^{-1}$) C_3H_8/acetone/air flame.

Figure 3.7: Computed fuel and oxidizer, NO_2 and acetone tracer normalized mass fractions showing that NO_2 and acetone are acceptable tracers for O_2 and C_3H_8. Determined using CHEMKIN, for opposed-flow non-premixed C_3H_8/acetone/air flames with NO_2 seeded at 5000 ppm by volume and acetone seeded at 20 % by volume. Shown at (a) a low strain rate of $e = 185\,s^{-1}$ and (b) a high strain rate of $e = 455\,s^{-1}$.

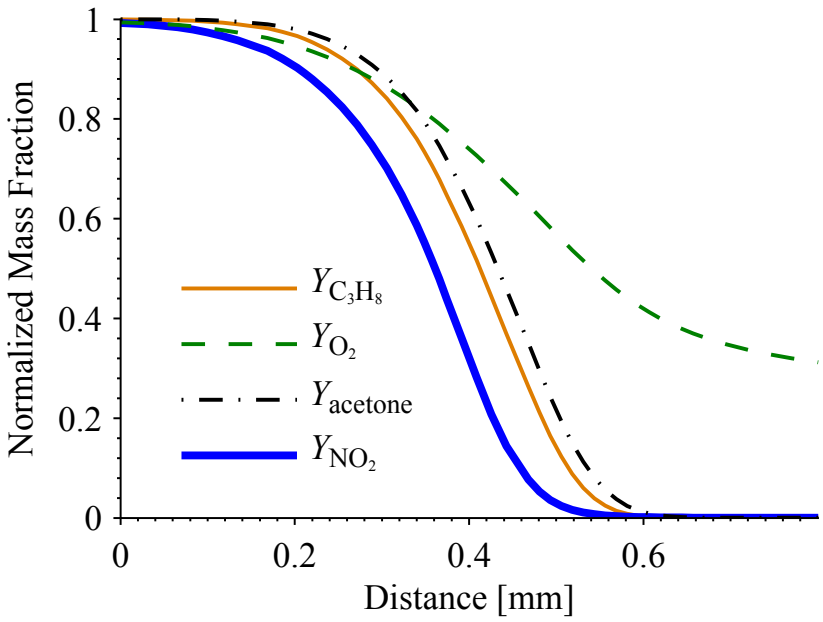

(a) Fuel-lean ($\phi = 0.75$) premixed C_3H_8/acetone/air flame.

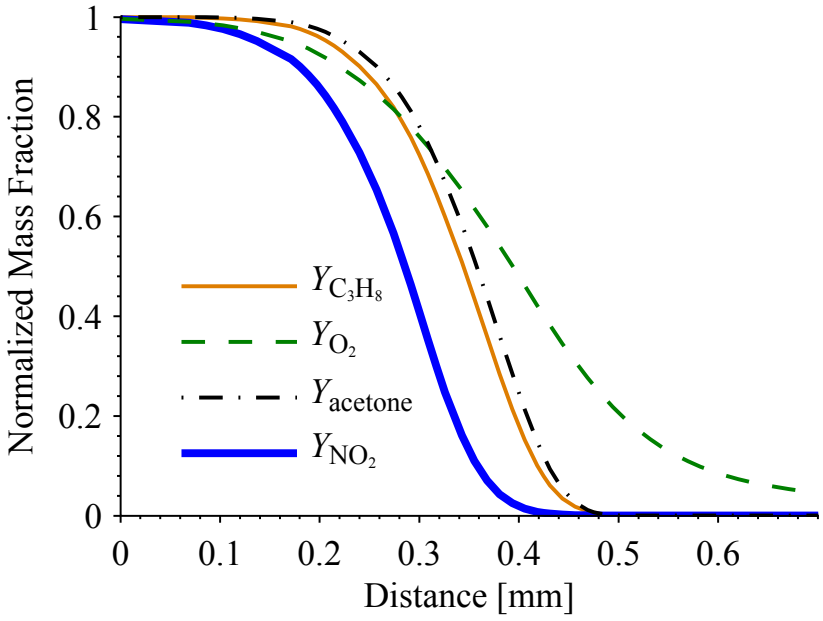

(b) Fuel-rich ($\phi = 1.20$) premixed C_3H_8/acetone/air flame.

Figure 3.8: Computed fuel and oxidizer, NO_2 and acetone tracer normalized mass fractions showing that NO_2 and acetone are acceptable tracers for O_2 and C_3H_8. Determined using CHEMKIN, for premixed C_3H_8/acetone/air flames with NO_2 seeded at 5000 ppm by volume and acetone seeded at 20 % by volume, at (a) lean ($\phi = 0.75$) and (b) rich ($\phi = 1.20$) equivalence ratios.

75 % CO, by volume. Syngas is a strange case, however. Both H_2 and CO are created in the flame, but overall their trend is a negative gradient, as is the acetone gradient, so it is valid. Quantitative measurements of H_2 or CO concentrations would be difficult, however. A syngas mixture consisting of 20 % H_2 and 80 % CO, by volume, was also studied, and yielded similar results to the 25 % H_2 and 75 % CO case. These are shown in Appendix A.

One very important finding from the flamelet modeling was that the locations of maximum acetone gradient and maximum NO_2 gradient do not overlap in the non-premixed cases, and sit close but do not always overlap in the premixed cases, as shown in Table 3.1. The results for the syngas mixture consisting of 20 % H_2 and 80 % CO, by volume, were found to be similar to that of the syngas mixture consisting of 25 % H_2 and 75 % CO, by volume, and are shown in Appendix A.

3.2 Tracer Fluorescence Properties

To determine the optimal energy of the lasers, the linearity and possible saturation limits of both acetone and NO_2 were studied. The NO_2 calibration was performed using the same setup as the GTMC experiments (with the same optics and knife edges in place), while the acetone calibration was performed with the same setup used for the enclosed co-flow burner. In both cases only the CH_4/acetone mixture or the air/NO_2 mixture flowed through the test chamber, which was at a pressure of 1 atm and a temperature of 293 K. Each data point represents the average fluorescence intensity over 30 laser pulses. Laser energies were measured with a pyroelectric power meter. Laser energies are provided in both the energy, in mJ/pulse, observed at the burner, and in the normalized spectral irradiance, in MW/(cm^2 cm^{-1}), as suggested by Partridge and Laurendeau [13].

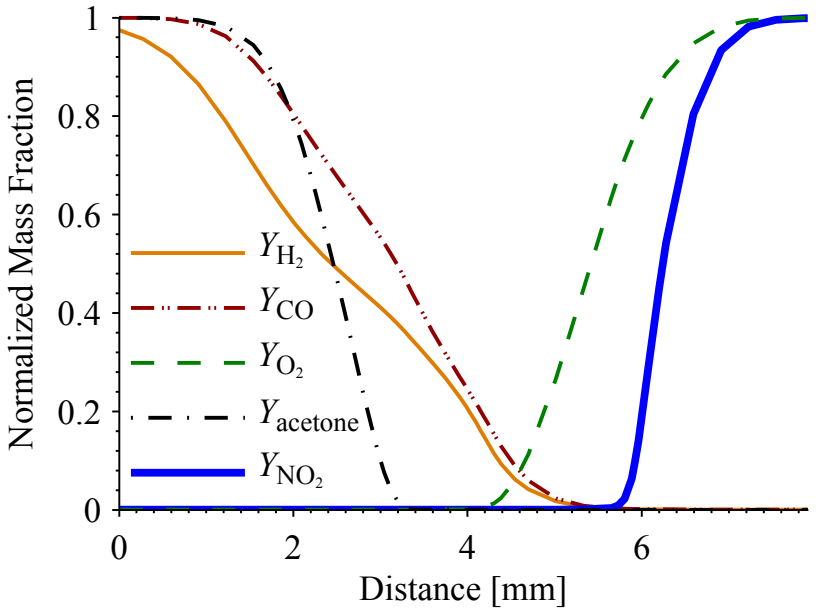

(a) Low strain rate ($e = 180\,s^{-1}$) syngas/acetone/air flame.

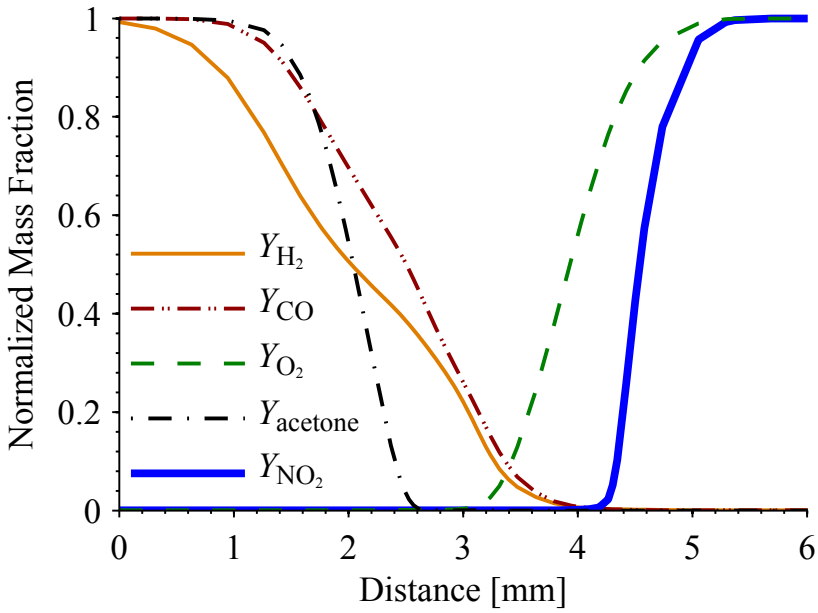

(b) High strain rate ($e = 440\,s^{-1}$) syngas/acetone/air flame.

Figure 3.9: Computed fuel and oxidizer, NO_2 and acetone tracer normalized mass fractions showing that NO_2 and acetone are acceptable tracers for O_2 and syngas. Determined using CHEMKIN, for opposed-flow non-premixed syngas/acetone/air flames with NO_2 seeded at 5000 ppm by volume and acetone seeded at 20 % by volume. Shown at (a) a low strain rate of $e = 180\,s^{-1}$ and (b) a high strain rate of $e = 440\,s^{-1}$. The syngas mixture was 25 % H_2 and 75 % CO, by volume.

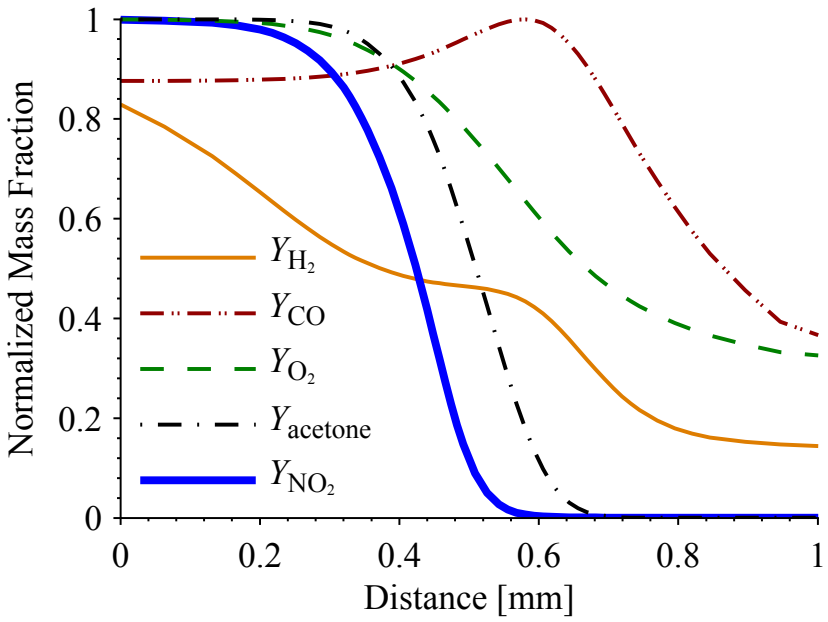

(a) Fuel-lean ($\phi = 0.75$) premixed syngas/acetone/air flame.

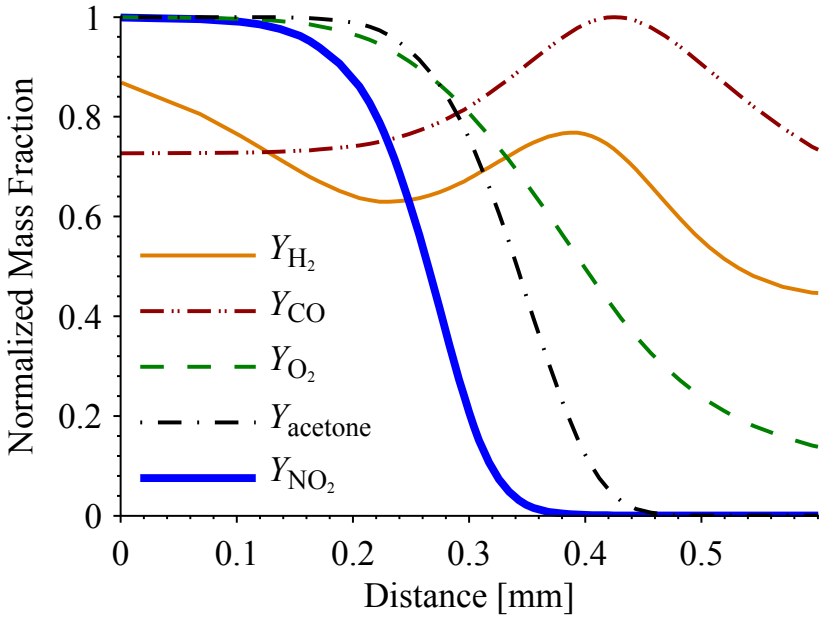

(b) Fuel-rich ($\phi = 1.20$) premixed syngas/acetone/air flame.

Figure 3.10: Computed fuel and oxidizer, NO_2 and acetone tracer normalized mass fractions showing that NO_2 and acetone are acceptable tracers for O_2 and syngas. Determined using CHEMKIN, for premixed syngas/acetone/air flames with NO_2 seeded at 5000 ppm by volume and acetone seeded at 20 % by volume, at (a) lean ($\phi = 0.75$) and (b) rich ($\phi = 1.20$) equivalence ratios. The syngas mixture was 25 % H_2 and 75 % CO, by volume.

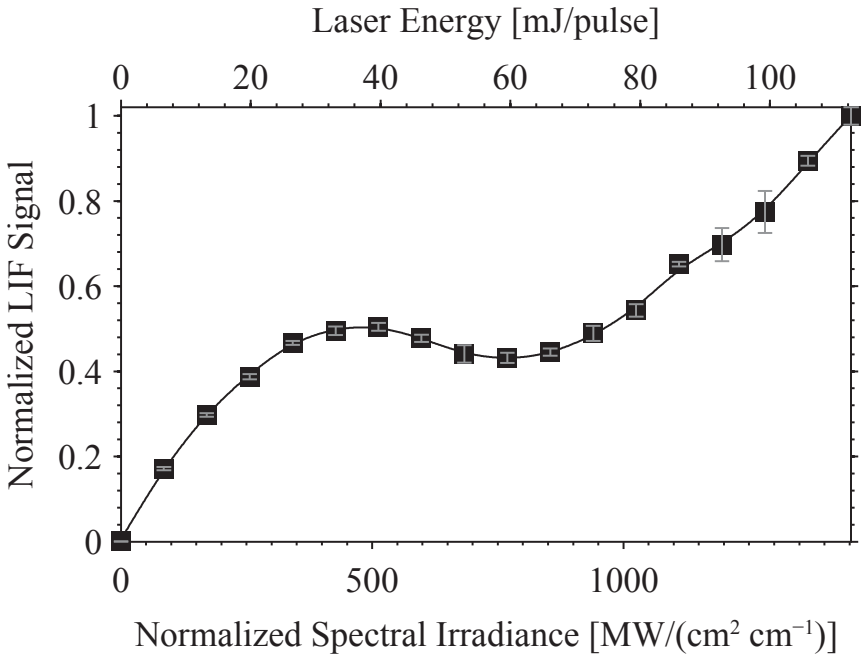

Figure 3.11: NO_2 calibration results with varying laser energy. NO_2 was at a volume fraction of 5000 ppm in air, at a pressure of 1 atm, and a temperature of 293 K.

3.2.1 Nitrogen Dioxide Fluorescence Linearity and Saturation Study

The NO_2 calibration results for varying laser energy, shown in Fig. 3.11, were obtained using a mixture of 5000 ppm NO_2 in air. The random uncertainty in the LIF signal, at a 95 % confidence level, is shown as well, which tended to be ±1–2 %, except for the data points at 1200 MW/(cm^2 cm^{-1}) and 1300 MW/(cm^2 cm^{-1}) which most likely have higher uncertainty from the jet of NO_2 and air moving around in the frame. Not shown, because it would have made aligning the upper and lower axes difficult, is the uncertainty in both the laser energy and normalized spectral irradiance. The laser energy, which was measured, had an uncertainty of ±3 % at all energy levels. The uncertainty in the normalized spectral irradiance (I_ν^0) was larger at ±13 % for all irradiance levels. The uncertainty in I_ν^0 is largely due to the uncertainty in the thickness of the laser sheet (±12 µm). So, while the uncertainties in I_ν^0 are large it is mostly a systematic uncertainty, meaning that the measurement is always off from the true value by the same amount. The random uncertainty in I_ν^0, which

comes from pulse to pulse variations in laser energy, is the smallest contributor at about 8 % of the total uncertainty in I_ν^0.

It can be seen that the NO_2 fluorescence signal is non-linear, which may mean that the NO_2 was partially saturated. The LIF signal is linear up to 250 MW/(cm^2 cm^{-1}) where it begins to saturate, and then starts increasing linearly again at about 850 MW/(cm^2 cm^{-1}). Between these two spectral irradiances, there is an unexpected dip in the LIF signal that has not been seen previously because earlier studies, such as that of Gulati and Warren [14], did not reach spectral irradiances as high as in the present study. The increase in the LIF signal at about 750 MW/(cm^2 cm^{-1}) may be additional fluorescence due to other electronic transitions caused by multiphoton excitation of NO_2. Another possible source is from the photodissociation of NO_2 and the subsequent fluorescence of the fragments. Photodissociation of NO_2 into vibrationally excited O and NO has been observed previously at a variety of laser wavelengths, including 532 nm [73, 74]. In fact, the vibrationally excited NO formed as a result of the photodissociation of NO_2 has been used as a tagging species in one form of the diagnostic technique known as molecular tagging velocimetry (MTV) [75–77].

Due to the unexpected dip around 750 MW/(cm^2 cm^{-1}) in Fig. 3.11, it is not recommended to operate above 500 MW/(cm^2 cm^{-1}) until the dip is explained, which will require further research. The uncertainty in the LIF signal is roughly constant across all laser energies at ±0.3.

The results of the NO_2 calibration for varying volume fraction in air are shown in Fig. 3.12. The random uncertainty in the LIF signal, to a 95 % confidence level, is shown here as well, which tended to be ±1 %. Also shown is the uncertainty in the NO_2 concentration. The NO_2 concentration was controlled by changing the flowrates of a gas cylinder with air and NO_2 at 5000 ppm and a gas cylinder with pure air. The flow rates were metered by choked-flow orifices. The experiment was run in such a way that two different orifices were used for the two different bottles for the first three concentrations, then the orifices were switched for the remaining three concentrations. The uncertainties in NO_2 concentra-

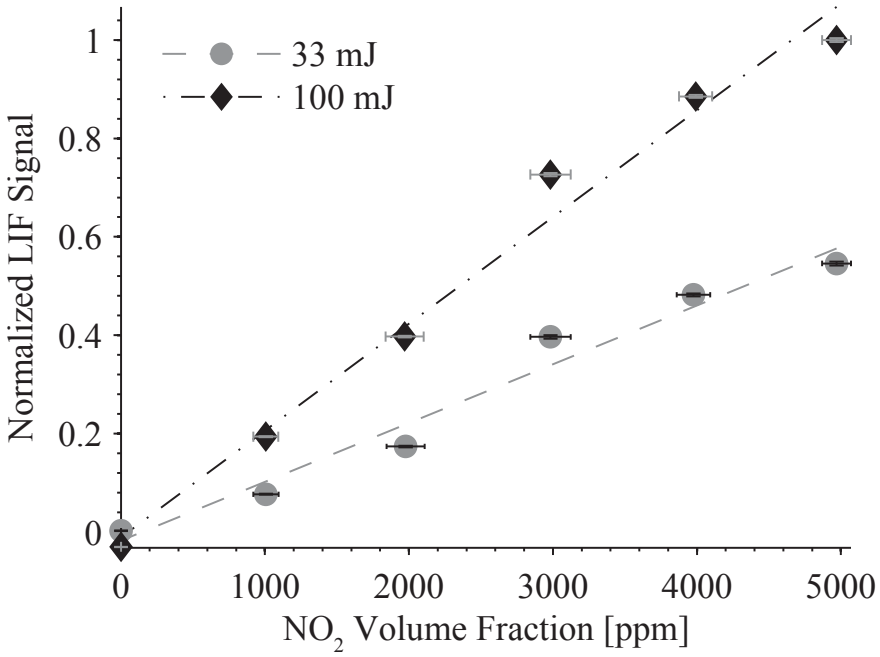

Figure 3.12: NO_2 calibration results for varying volume fraction at two laser energies. Laser energy was 33 mJ, 426 MW/(cm^2 cm^{-1}), and 100 mJ, 1300 MW/(cm^2 cm^{-1}). The air/NO_2 mixture was at a pressure of 1 atm, and a temperature of 293 K. Vertical uncertainty is due to noise in the LIF signal. Horizontal uncertainty is in the NO_2 volume fraction.

tion tended to be impacted mostly by which orifice had the higher flowrate. Specifically, the uncertainties were dominated by the uncertainty in the mass flowrate from whichever gas bottle was metered using the smaller of the two orifices. The uncertainty in the mass flow rate was then dominated by the uncertainty in the diameter of the orifice. The manufacturer of the orifices specifies that the accuracy of the orifice diameters is ±0.0005 in for all the orifices used in the experiments described in this dissertation (except for both CH_4 orifices used during case L-1). So, as orifices get smaller this uncertainty dominates. For the higher concentrations, when the flow through the smaller orifice was less, the uncertainty in the NO_2 concentration in the gas bottle (specified to be ±2 %) became as important as the uncertainty in the mass flowrates.

The study was performed at laser energies of 33 mJ and 100 mJ, or 426 MW/(cm^2 cm^{-1}) and 1300 MW/(cm^2 cm^{-1}). It can be seen that NO_2 fluorescence responds linearly to vari-

ations in the NO_2 volume fraction in air. Linearity was also observed by Gulati and Warren [14], who studied an NO_2/N_2 mixture, with the 488.0 nm line of an argon-ion laser, under similar conditions and at a similar range of NO_2 concentrations. The uncertainty in the NO_2 volume fraction was approximately 4 % for both cases. For the 33 mJ case the uncertainty in the LIF signal is 3.8 %, and for the 100 mJ case the uncertainty is 1.9 %. The uncertainty in the 100 mJ case is most likely lower due to the fluorescence being saturated with respect to the laser power.

3.2.1.1 Nitrogen Dioxide Signal-to-Noise Ratio

The Signal-to-Noise Ratios (SNRs) for the NO_2 fluorescence linearity and saturation study were determined to give an idea of the minimum laser energy and NO_2 concentration that could be detected. The SNR is the ratio between the mean signal in a uniform region of the LIF signal and the standard deviation of that signal. Figures 3.13 and 3.14 show the variation in SNR as the laser energy and NO_2 concentration are varied. As expected, the SNR ratio improves with larger bins.

For an intensified camera the shot noise depends on statistical fluctuations in the number of photoelectrons, and it may be described by Poisson statistics. The shot noise dominates over the read noise, which occurs during the process of converting the charge on a pixel to a voltage that can be read by an analog-to-digital converter [52]. The shot noise is proportional $\sqrt{S}$, and SNR is proportional to $\sqrt{S}$ as well. This trend is observed in Figs. 3.13 and 3.14. It can be seen that the SNR improves by a factor of approximately 1.6 in Fig. 3.13, and 1.3 for both cases in Fig. 3.14 as the binning is changed from 4×4 to 8×8. It would be expected that the SNR should increase by a factor of two because the signal increases by a factor of four, but this is not the case, possibly because of other sources of noise present in the room such as stray photons from other sources of light. It is also possible that the region selected for determining the SNR was not as uniform as would be ideal.

Shown in both Figs. 3.13 and 3.14 is the statistical uncertainty, to a 95 % confidence

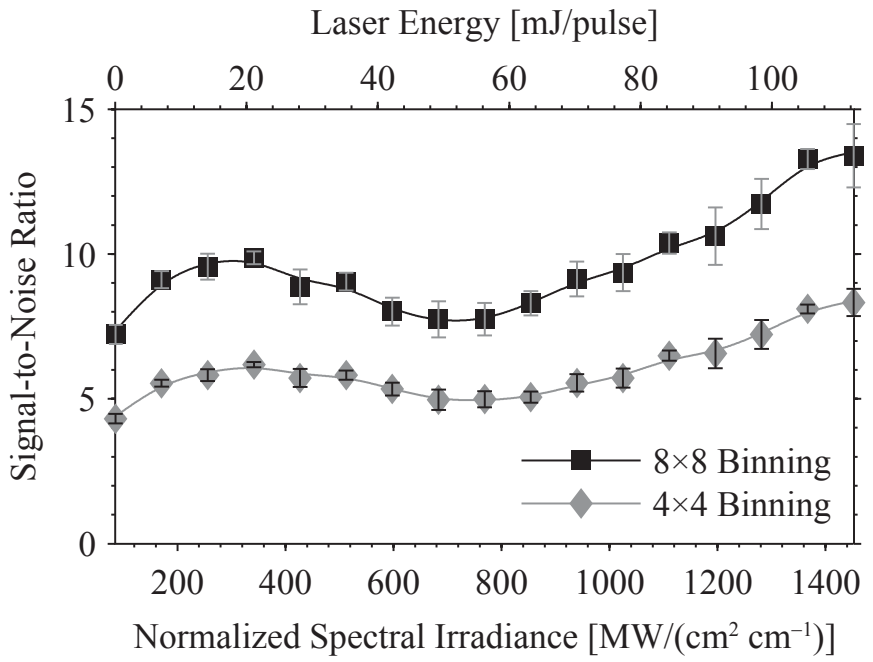

Figure 3.13: Signal-to-Noise Ratios of NO_2 LIF versus laser energy when LIF signal is processed by 4×4 and 8×8 binning. NO_2 at a volume fraction of 5000 ppm in air.

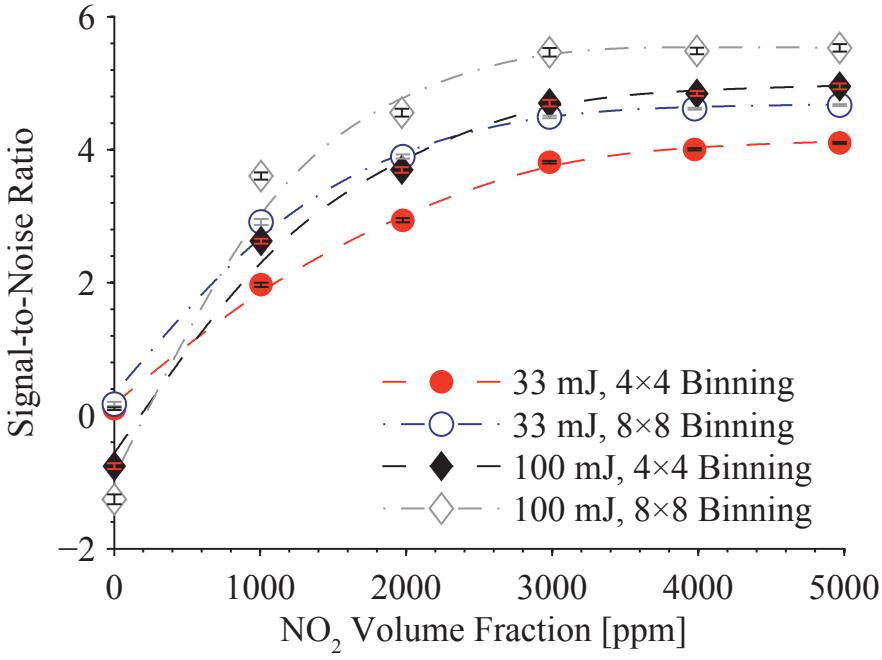

Figure 3.14: Signal-to-Noise Ratios of NO_2 LIF versus NO_2 volume fraction in air when LIF signal is processed by 4×4 and 8×8 binning. Laser energy at 33 mJ, 426 MW/(cm^2 cm^{-1}), and 100 mJ, 1300 MW/(cm^2 cm^{-1}).

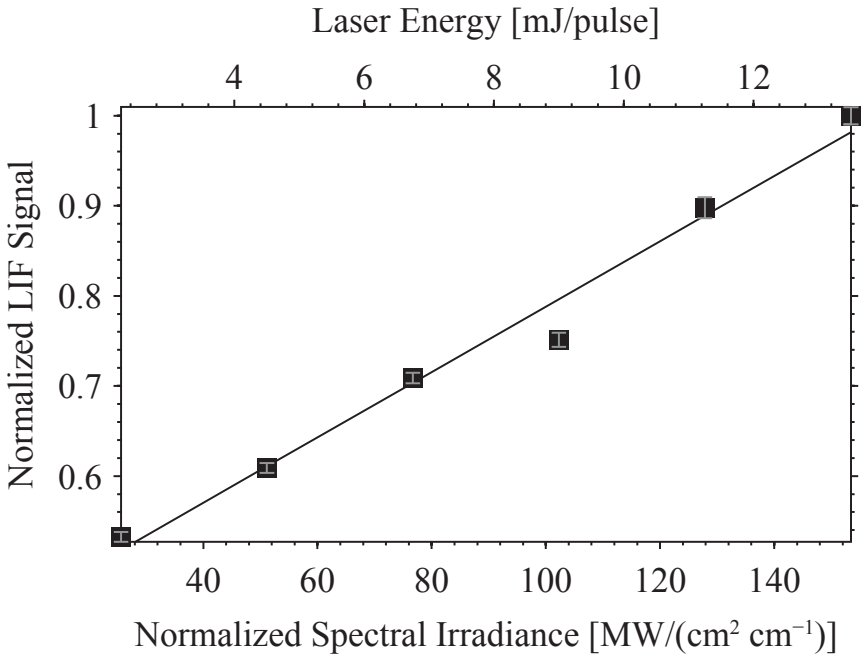

Figure 3.15: Acetone calibration with varying laser energy. Acetone was at a volume fraction of 13 % in CH_4, at a pressure of 1 atm, and a temperature of 293 K.

level, due to frame-to-frame variations in the SNR within a given run.

3.2.2 Acetone Fluorescence Linearity and Saturation Study

The acetone laser calibration results, shown in Fig. 3.15, were obtained for a mixture of 13 % acetone, by volume, in CH_4 over the range of possible energy outputs by the laser. As was observed by Lozano et al. [37], by Thurber and Hanson [36], and by Bryant et al. [38], the acetone fluorescence does not saturate in this regime. The statistical uncertainty in the LIF signal, at a 95 % confidence level, is roughly constant at ±0.2 for all energy levels. Like the uncertainty in I_ν^0 in Fig. 3.11, the uncertainty in Fig. 3.15 is about ±14 % at all irradiance levels. The slightly higher uncertainty is due to the slightly shorter laser pulse at 266 nm and larger pulse-to-pulse variations in the laser energy. The uncertainty in the laser energy is ±4 % at all energy levels. As with the NO_2 cases, the uncertainty in I_ν^0 is largely due to the uncertainty in the thickness of the 266 nm laser sheet (±14 µm).

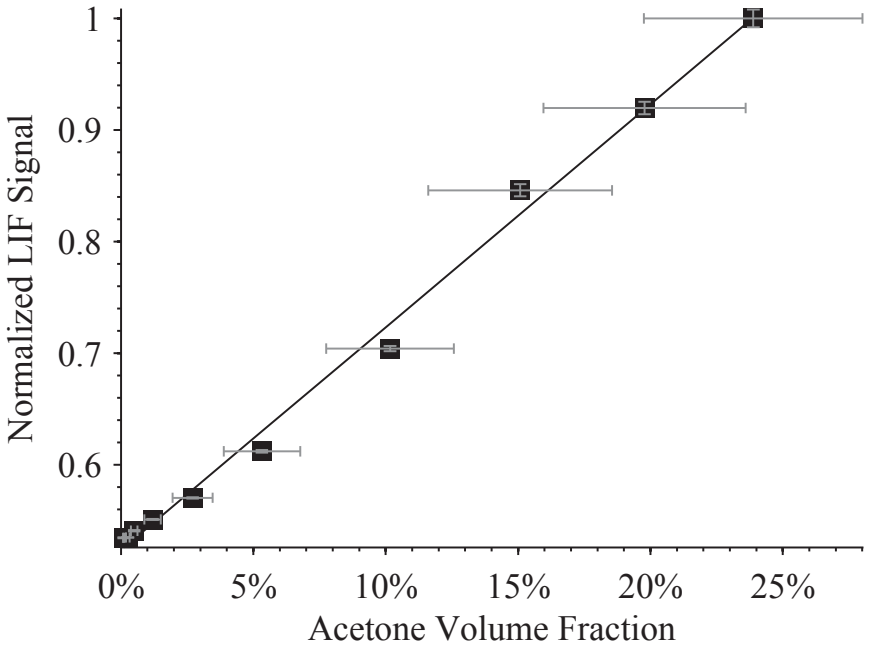

Figure 3.16: Acetone calibration results with varying volume fraction. Laser energy was 9 mJ, 100 MW/(cm^2 cm^{-1}). CH_4/acetone mixture was at a pressure of 1 atm, and a temperature of 293 K. Vertical uncertainty is due to noise in the LIF signal, horizontal uncertainty is in the acetone volume fraction.

The results of the acetone calibration for varying volume fraction in CH_4 are shown in Fig. 3.16. The study was performed at a laser energy of 9 mJ (100 MW/(cm^2 cm^{-1})). It can be seen that the acetone signal varies linearly with volume fraction and, in this regime, does not saturate. The same linearity was observed by Yuen et al. [39], by Thurber and Hanson [36], and by Bryant et al. [38]. The uncertainty in the LIF signal, about 5 %, is due to noise in the data. The uncertainty in the acetone concentration, about 25 % of the volume fraction, is largely due to the variance in the orifice diameters in the flow-metering orifices and the low flow rates used in some cases. The orifices used here are even smaller than the ones in the NO_2 concentration study, increasing the effect of their small diameters on the overall uncertainty. It should be noted that the uncertainty in acetone concentration is about 1 % during the GTMC test cases, where the flowrates are much higher, and the orifice diameters are much larger.

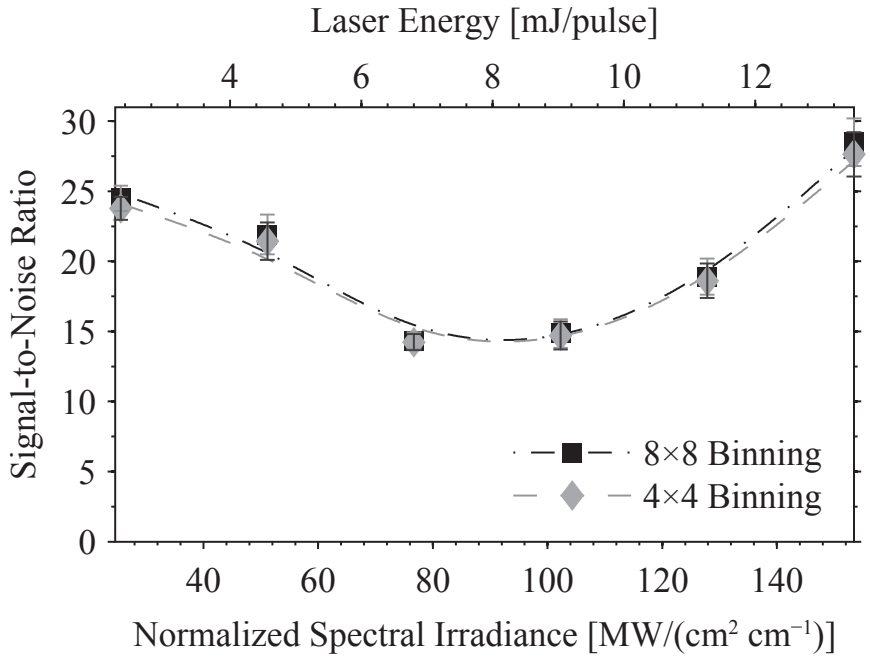

Figure 3.17: Signal-to-Noise Ratios of acetone LIF versus laser energy when LIF signal is processed by 4×4 and 8×8 binning. Acetone at a volume fraction of 13 % in CH_4.

3.2.2.1 Acetone Signal-to-Noise Ratio

The SNRs for the acetone fluorescence linearity studies are shown here in Figs. 3.17 and 3.18 for 4×4 and 8×8 binned fluorescence signals. In both cases, the statistical uncertainties between the 4×4 and 8×8 binned data were nearly the same. Like the NO_2 fluorescence linearity studies, the binning does provide some increase in SNR, a factor of 1.02 in Fig. 3.17 and 1.01 in Fig. 3.18, but it's much smaller, and not the predicted factor of 4. Additionally, the curves in the figures do not follow the predicted path of $\sqrt{S}$. Figure 3.17 is especially strange because for irradiances lower than 100 MW/(cm^2 cm^{-1}), the SNR decreases, despite the LIF signal increasing, as was shown in Fig. 3.15.

Unfortunately, the reason the SNRs in Figs. 3.17 and 3.18 do not behave as would be predicted is unknown. It's possible that there were other contributions to noise, like stray light in the room, or that cracks formed in the windows of the enclosed co-flow burner.

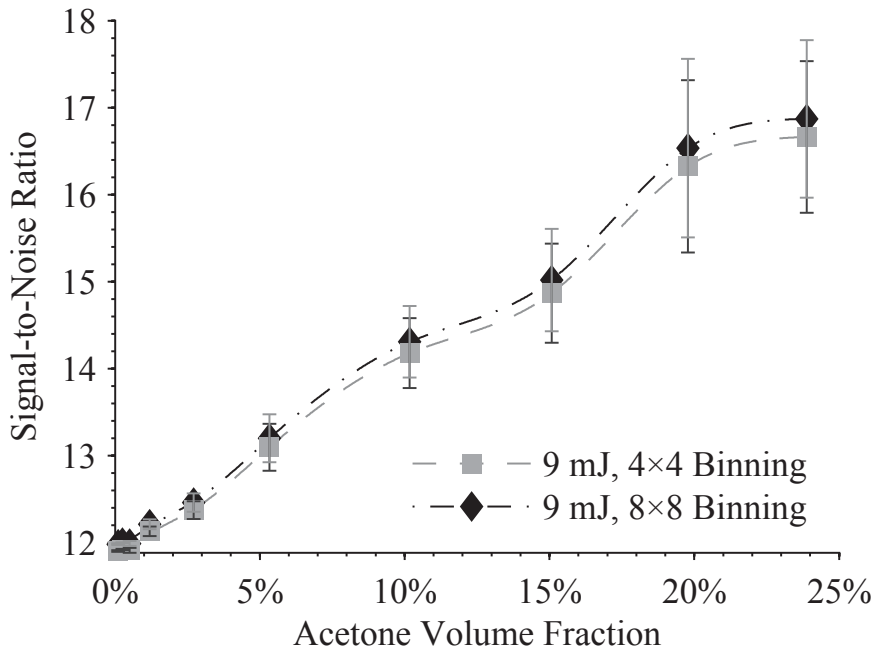

Figure 3.18: Signal-to-Noise Ratios of acetone LIF versus acetone volume fraction in CH_4 when LIF signal is processed by 4×4 and 8×8 binning. Laser energy at 9 mJ, 100 MW/(cm^2 cm^{-1}).

3.3 Reacting Flow Study

To demonstrate the viability of NO_2 as an O_2 tracer, the premixed (L-1) and non-premixed (L-2) laminar flame cases, described in Table 2.1, were studied using an enclosed co-flow burner.

The PLIF images were corrected[1] as suggested by Clemens [52], binned 8×8, and filtered using an NADF [60]. The NADF smooths the image within a given region, but resists smoothing the image across large gradients, so the edge of the LIF signal where the NO_2 breaks down is preserved and easily detectable. Figure 3.19 shows the results for flame L-1, based on the average of 222 image frames and 20 lines of 8×8 binned super-

[1]The acetone signal in case L-1 had only a background correction, no white-field or laser sheet uniformity correction. For an unknown reason, the white-field and laser sheet corrections made the acetone signal, in case L-1 only, almost entirely uniform so it was very difficult to make out the acetone LIF signal. It is possible this is a result of the background image being acquired with an on-camera binning of 2×2, which meant that both the raw PLIF image and the white-field correction had to be binned for the correction to be applied. It is also very likely that cracks in the windows contributed to un-correctable non-uniformities in the laser sheet.

pixels. Figure 3.20 shows the results for flame L-2, based on the average of 300 image frames and 23 lines of 8×8 binned super-pixels. Figures 3.19 and 3.20 show the average normalized NO_2 LIF signal for one half of the flame versus a dimensionless coordinate, r/r_{edge}. This coordinate represents the radial distance from the center of the flame, denoted by $r/r_{edge} = 0$, normalized by the r-value corresponding to the edge of the NO_2 signal, as determined by a Canny edge detector [64]. Through the flame, the NO_2 LIF signal follows a path similar to the breakdown of O_2 in the premixed and non-premixed flames shown in Figs. 3.3 and 3.4. The fact that the gradients in Figs. 3.19 and 3.20 are centered at $r/r_{edge} = 1$ and that the profiles are monotonically decreasing, in case L-1, or monotonically increasing, in case L-2, verifies that NO_2 will serve as an acceptable O_2 tracer.

The raw PLIF images had an average SNR of 7.5 for case L-1 and 6.7 for case L-2. After the 8×8 binning the SNR for case L-1 increased to 17.3 and 13.5 for case L-2. The SNR in this reacting flow study was better than that of the fluorescence linearity study, described in Section 3.2.1.1, most likely because the position of the ICCD was several centimeters farther from the fluorescence cell compared to the ICCD's position during the reacting flow study. Thus the collection solid angle was larger for the reacting flow study.

Similar to the breakdown of NO_2, the acetone follows a path similar to the breakdown of CH_4 in the premixed and non-premixed flames shown in Figs. 3.6 and 3.5. Like the NO_2 gradients, the fact that the acetone gradients in Figs. 3.21 and 3.22 are centered at $r/r_{edge} = 1$ and that the profiles are monotonically decreasing, in case L-1, or monotonically increasing, in case L-2, verifies that acetone will serve as an acceptable fuel tracer. The raw PLIF images had an average SNR of 84.4 for case L-1 and 21.6 for case L-2. After the 8×8 binning the SNR for case L-1 increased to 113.4 and 28.1 for case L-2.

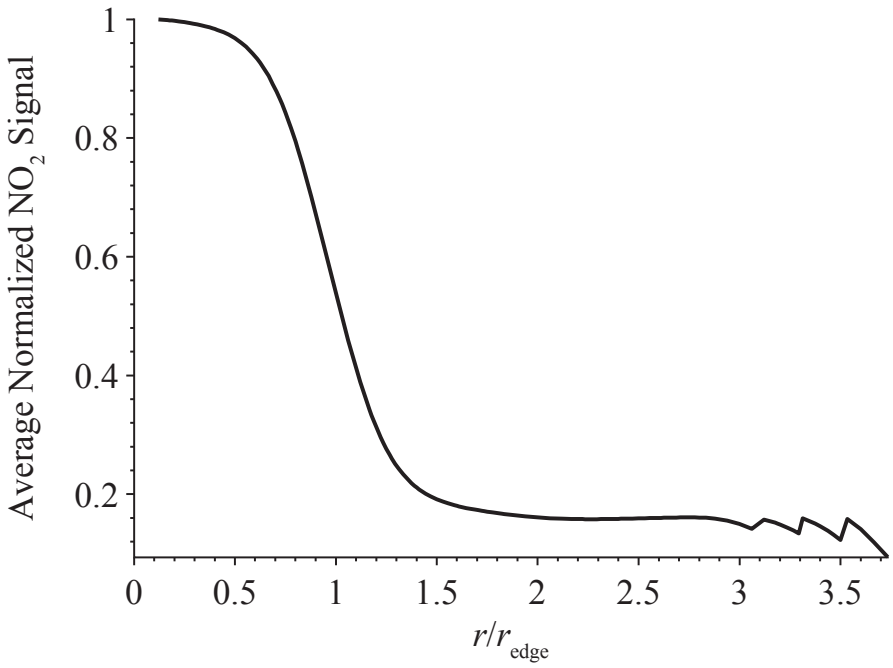

Figure 3.19: Normalized mean NO_2 LIF signal for case L-1, a premixed CH_4/acetone/air flame ($\phi = 1.2$) with NO_2 seeded at 2100 ppm by volume.

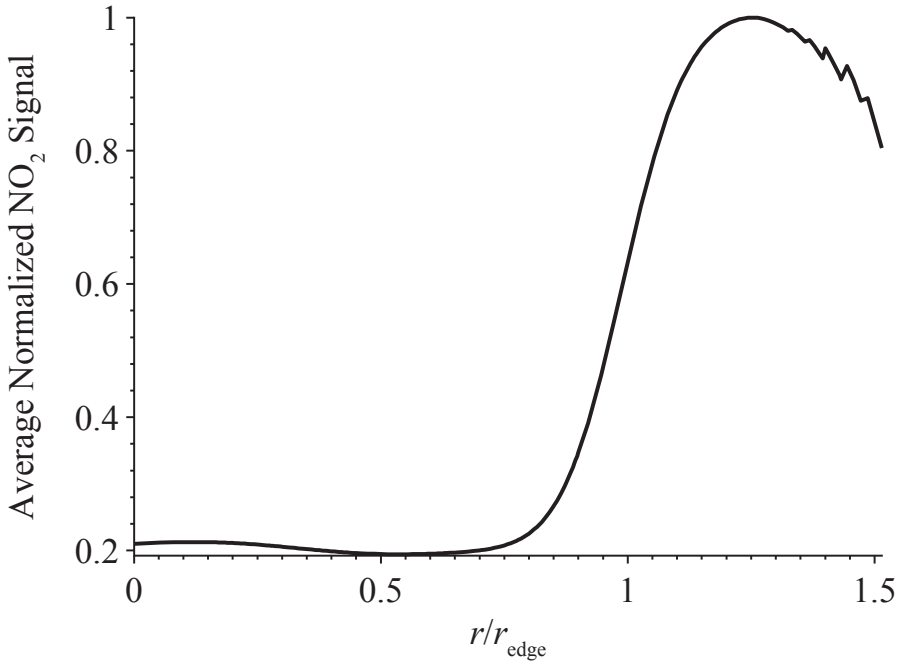

Figure 3.20: Normalized mean NO_2 LIF signal for case L-2, a non-premixed CH_4/acetone/air flame with NO_2 seeded at 5000 ppm by volume.

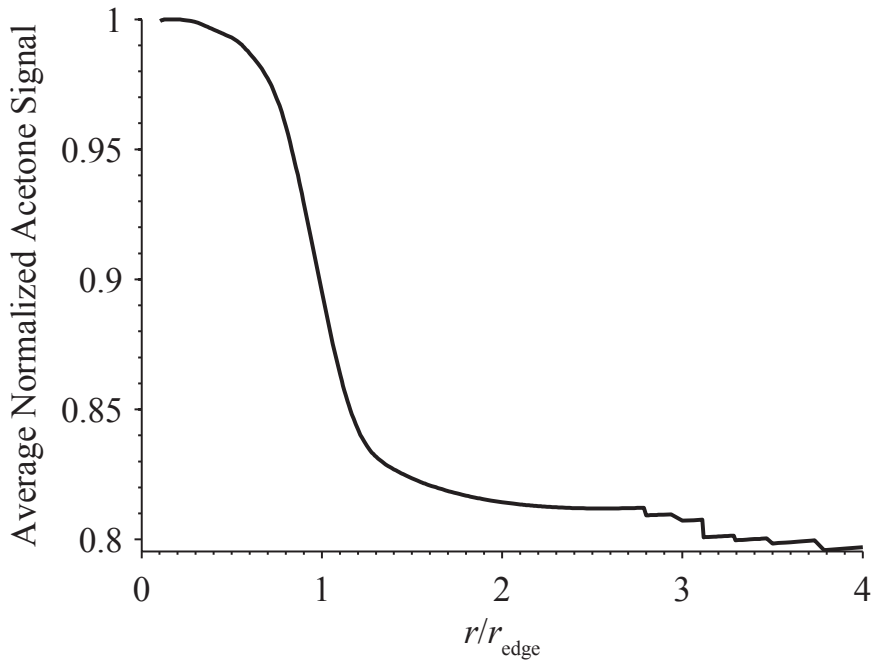

Figure 3.21: Normalized mean acetone LIF signal for case L-1, a premixed CH_4/acetone/air flame (ϕ = 1.2) with acetone seeded at 18 % by volume.

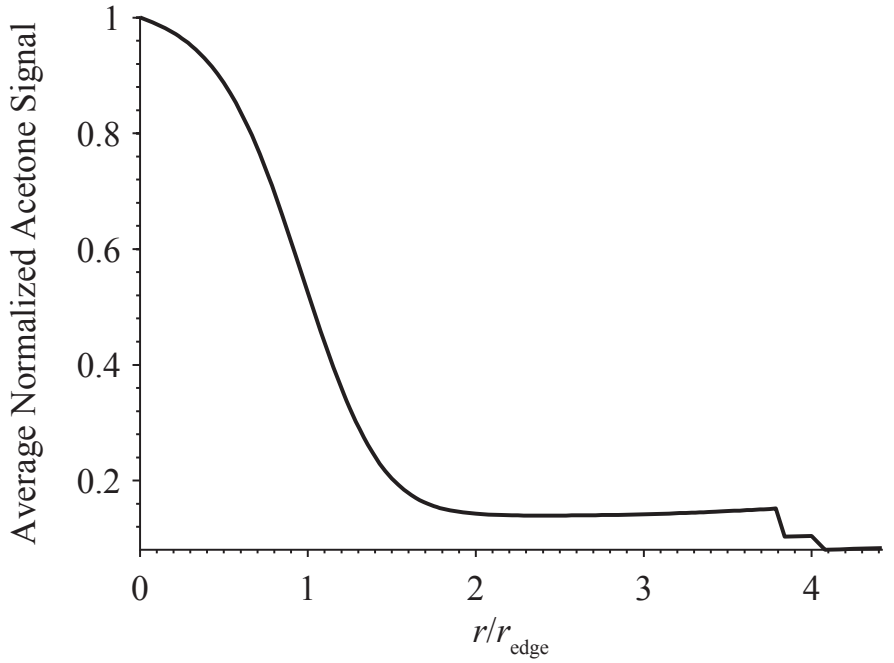

Figure 3.22: Normalized mean acetone LIF signal for case L-2, a non-premixed CH_4/acetone/air flame with acetone seeded at 18 % by volume.

CHAPTER 4

Flame Index Measurement Method

The development of the Flame Index Measurement Method (FIMM) began with the laminar premixed case L-1 and the laminar non-premixed case L-2 on the enclosed co-flow burner, and then continued with the turbulent GTMC flames. This chapter will discuss the final version of the FIMM, after the GTMC cases had been evaluated. The example images shown will all be from case P-1, because it was found, as was discussed in Section 3.1.2, that acetone was a better tracer for propane than it was for either CH_4 or syngas. A description of the FIMM as it was after studying cases L-1 and L-2, but before any turbulent flames had been evaluated, is in Appendix B.

As was mentioned in Section 3.1.2, it was found that $\left(\nabla S_{\text{acetone}}\right)_{\max}$ and $\left(\nabla S_{NO_2}\right)_{\max}$ do not overlap in non-premixed flamelets, and they sit close but do not always overlap in the premixed cases. This meant that some sort of searching method would need to be used, where given a location of $\left(\nabla S_{\text{acetone}}\right)_{\max}$, a corresponding $\left(\nabla S_{NO_2}\right)_{\max}$ would need to be located. The implementation of this searching method is largely why ξ was defined based on the *maximum* gradients of the LIF, rather than being defined from the entire field of signal gradients.

An appropriate magnitude for the acetone and NO_2 signal gradients near a flamelet was unknown, and the magnitude of the gradients of the noise in the PLIF images were frequently larger than the magnitude of the LIF signal gradients. For these reasons, it was decided that the locations of $\left(\nabla S_{\text{acetone}}\right)_{\max}$ and $\left(\nabla S_{NO_2}\right)_{\max}$ would most easily be

determined through the use of an edge detector. Thus the FIMM would involve three major components:

1. Image corrections to account for background signal, white-field response, and non-uniformity of the laser sheets.

2. The improvement of the Signal-to-Noise Ratio (SNR) in the PLIF images to provide accurate edge detection.

3. The searching method where given a location of $\left(\nabla S_{\text{acetone}}\right)_{\max}$, a corresponding $\left(\nabla S_{\text{NO}_2}\right)_{\max}$ would found.

4.1 Data Preparation

After the acquisition of the simultaneous acetone and NO_2 PLIF, the first concern of the FIMM was improving the SNR of the PLIF images. To demonstrate the need to improve the SNR, for case P-1 a raw unprocessed acetone PLIF image had an SNR of 14, while a raw NO_2 PLIF image had an SNR of 5. (After processing, the SNR of the acetone image was 24, and the SNR of the NO_2 image was 13.) This meant that if an edge detector were applied to either the unprocessed PLIF images, or the images after the corrections described in Section 2.5 had been applied, many of the edges detected would be due to noise rather than actual consumption of acetone or NO_2.

The NO_2 images in particular had a low SNR. To illustrate the low SNR of the NO_2 PLIF images, raw simultaneous images of both NO_2 and acetone are shown in Fig. 4.1. In the images shown, the NO_2 PLIF image has not yet been registered to the acetone PLIF image, so the *r*-axis is flipped. A schematic of the GTMC has been overlaid on top of the image. The fuel injector, inner air swirler, and outer air swirler locations are shown in the diagrams, as well as the fuel and air paths. At the location of $r = 8$ mm is the fuel injector. The location 0 mm on the *r*-axis corresponds to the centerline of the burner, and

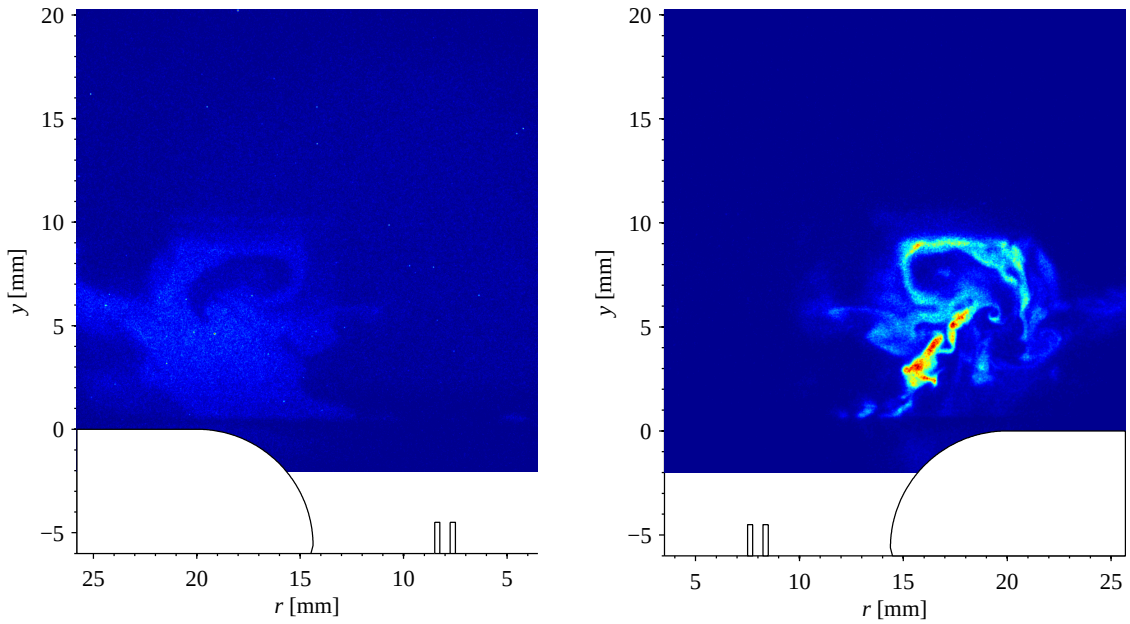

(a) Raw NO_2 PLIF image.

(b) Raw acetone PLIF image.

Figure 4.1: Simultaneous raw (a) NO_2 and (b) acetone PLIF images from case P-1. Images are of the same field of view, however the NO_2 PLIF image has not been registered to the acetone PLIF image.

the location 0 mm on the y-axis corresponds to the top of the injector face. The top of the fuel injector is located at −4.5 mm on the y-axis. For case P-1, the 266 nm laser sheet was 8.42 mm tall and sat 770 µm above the injector face. The 532 nm laser sheet was 8.29 mm tall and sat 640 µm above the injector face. These numbers are typical for all GTMC flame cases.

The poor NO_2 SNR can be clearly seen in Fig. 4.1(a). The range of intensities in the NO_2 image appears to be much smaller than that of the acetone image. In reality, they are very similar, but in the NO_2 PLIF image has stray pixels of very high intensity that skew the contrast. The stray pixels are likely from laser light scattered off of particles in the flow. The optical filters on the acetone-sensing camera did a very good job of filtering out the 266 nm light, while the optical filters on the NO_2-sensing camera still allowed some 532 nm light to pass, despite three separate filters being used. Figure 4.2 is the same image as in Fig. 4.1(a), but the image has been edited to exclude the top 0.005 % of pixel values

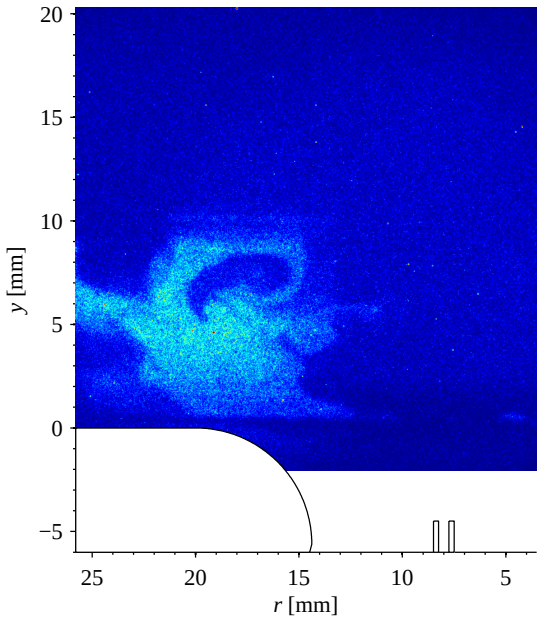

Figure 4.2: Raw NO_2 PLIF where contrast has been edited to exclude the top 0.005 % of pixel values from the color range, to illustrate the low SNR.

from the color range (this is never done in the processing of the data, it is only done here for illustrative purposes). The fact that there are gradients within the NO_2 signal now becomes apparent, however it is clear that they are not as drastic as those in the acetone signal.

The first step in the processing of the PLIF images was to apply the corrections described in Section 2.5, and then the NO_2 image was flipped, rotated, and stretched or shrunken to register it to the acetone image. The corrected and registered example frames can be seen in Fig. 4.3. Again, it is difficult to make out the structures in the NO_2 image, so a version that has been edited to exclude the top 0.005 % of pixel values from the color range is shown in Fig. 4.4. It should be noted that while the images shown here are cropped to the size of the laser sheet, this was not done in the data processing. The cropping of the image to the size of the laser sheet was done just before gradients were determined to avoid complications with the filtering of the images, which is described later in this section. It should be noted that for the image corrections, the elements in the three-dimensional matrix of images are not forced to have integer values, the elements are allowed to vary continu-

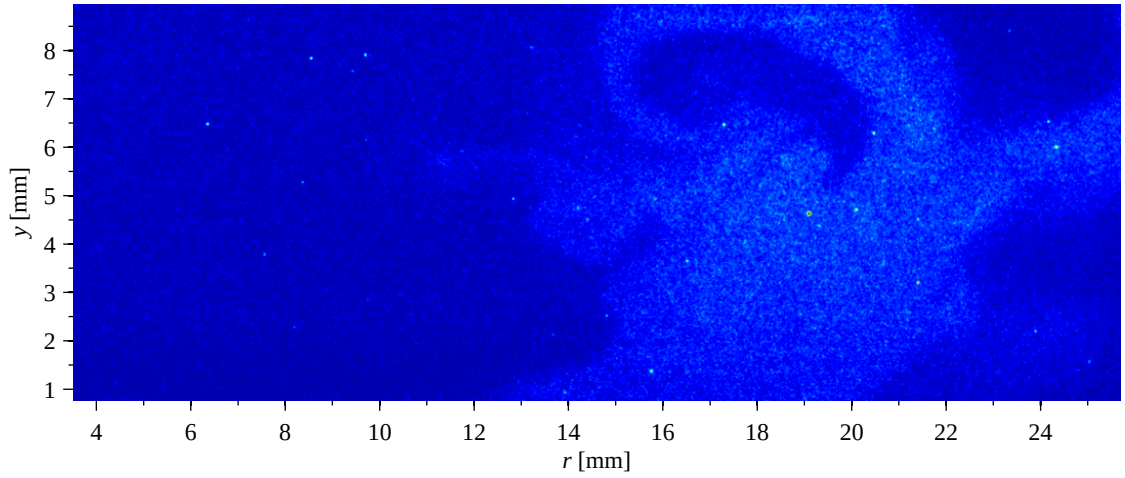

(a) Corrected and registered NO_2 PLIF image.

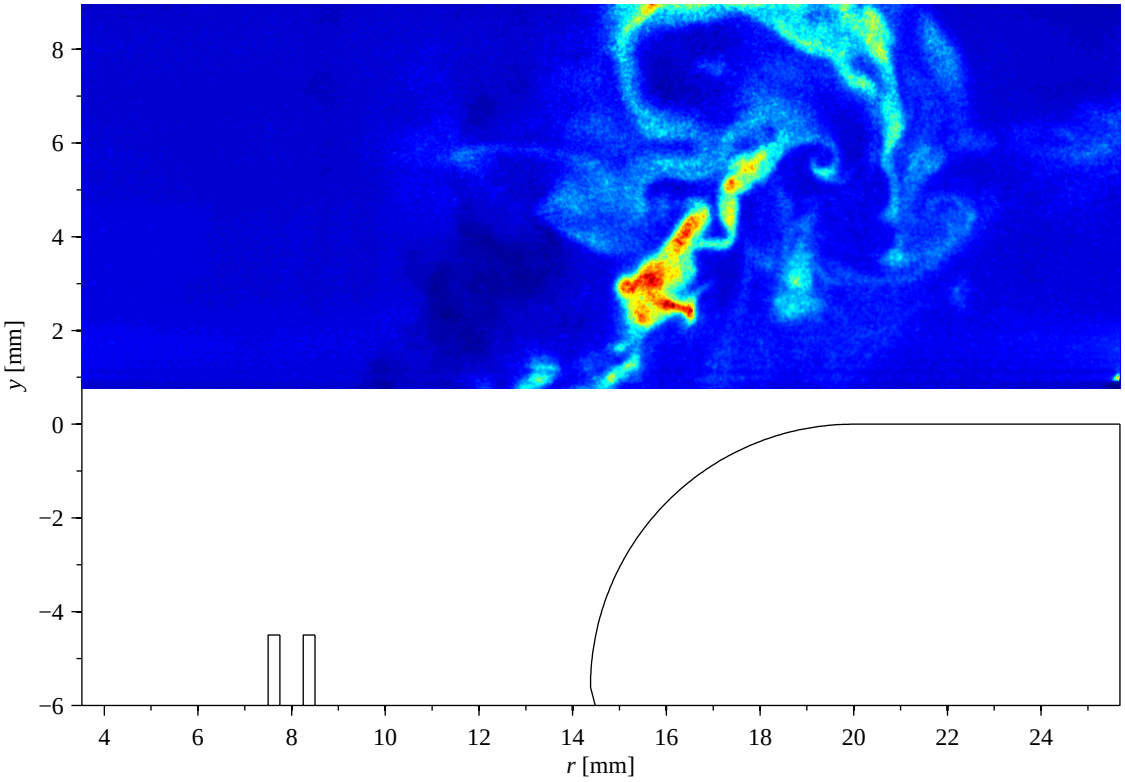

(b) Corrected and registered acetone PLIF image.

Figure 4.3: Simultaneous corrected and registered (a) NO_2 and (b) acetone PLIF images from case P-1.

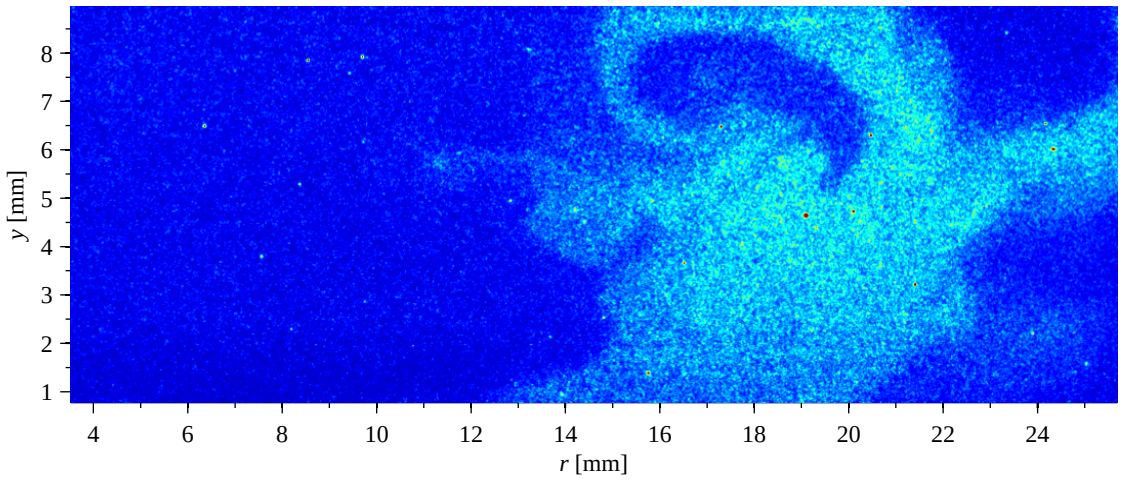

Figure 4.4: Corrected and registered NO_2 PLIF where contrast has been edited to exclude the top 0.005 % of pixel values from the color range, to illustrate the low SNR.

ously with double precision throughout their use in the FIMM.

If at this point the processing of the images was considered to be complete, and an edge detection was performed, the results can be seen in Fig. 4.5. Both the corrected and registered NO_2 and acetone example images with the edge detection overlapped are shown. The edge detection on the acetone image isn't great, but some structures are clearly outlined, like the structure existing from $r = 15$ mm to 17 mm and $y = 2$ mm to 5 mm. The interior of the structure has several detected edges as well, but nothing on the level of the NO_2 image. The overlapped NO_2 PLIF image and edge detection is nearly incomprehensible. Far too many edges were detected, and they appear to be related to small structures in the LIF signal (noise) rather than the larger structures that need to be detected. The only thing working correctly here is that there are clearly fewer detected edges in the NO_2 image in areas with less signal, such as the region from $r = 4$ mm to 12 mm, for the full height of the image.

The next phase of the image processing was focused on improving the SNR of the images. This was first accomplished by binning both the NO_2 and acetone images 4×4. This level of binning appeared to provide the best balance between improving the SNR and

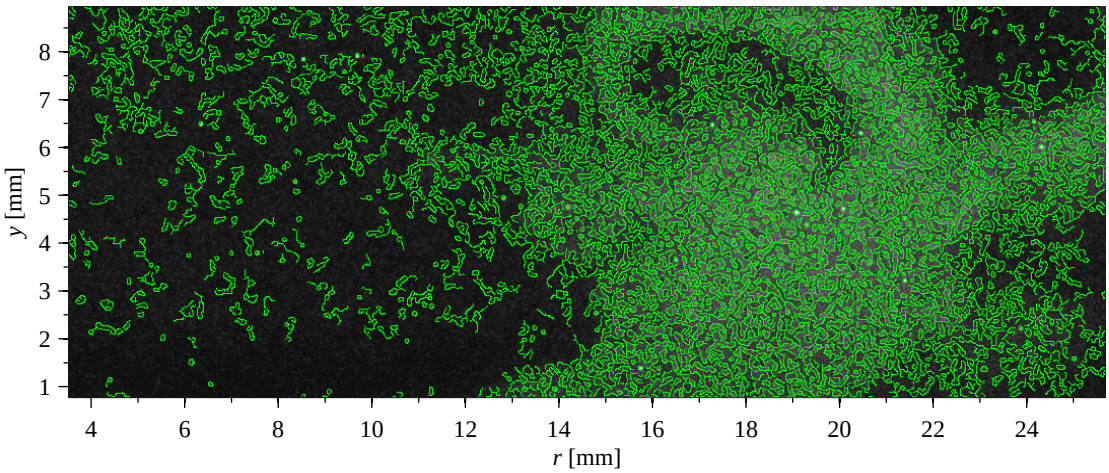

(a) Corrected and registered NO_2 PLIF image with overlapped edge detection.

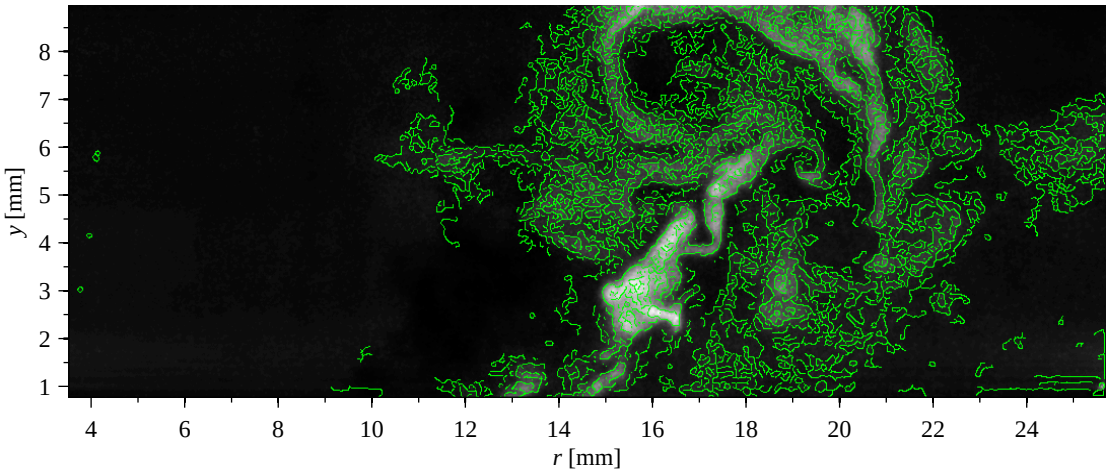

(b) Corrected and registered acetone PLIF image with overlapped edge detection.

Figure 4.5: Simultaneous corrected and registered (a) NO_2 and (b) acetone PLIF images with overlapped edge detection from case P-1.

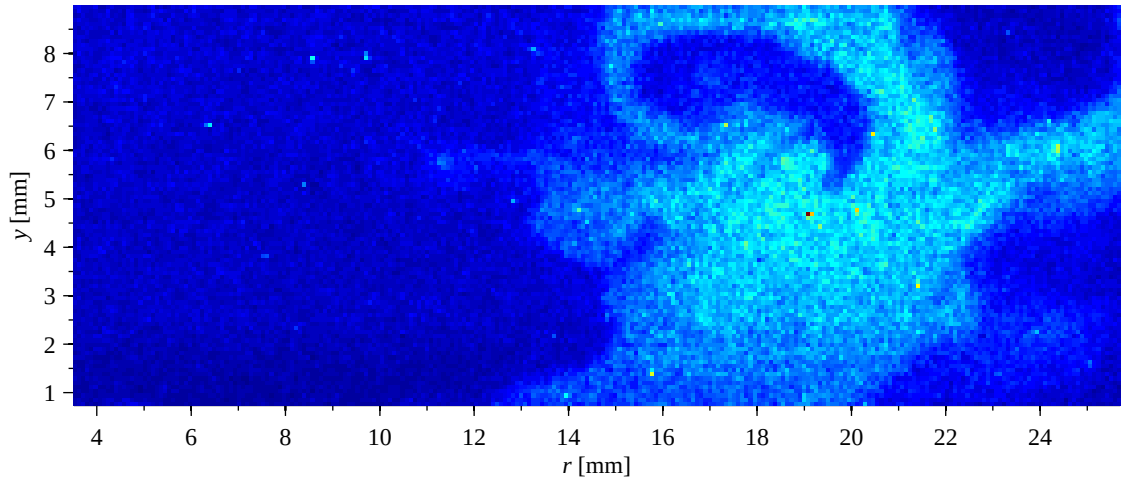

(a) 4×4 binned NO_2 PLIF image.

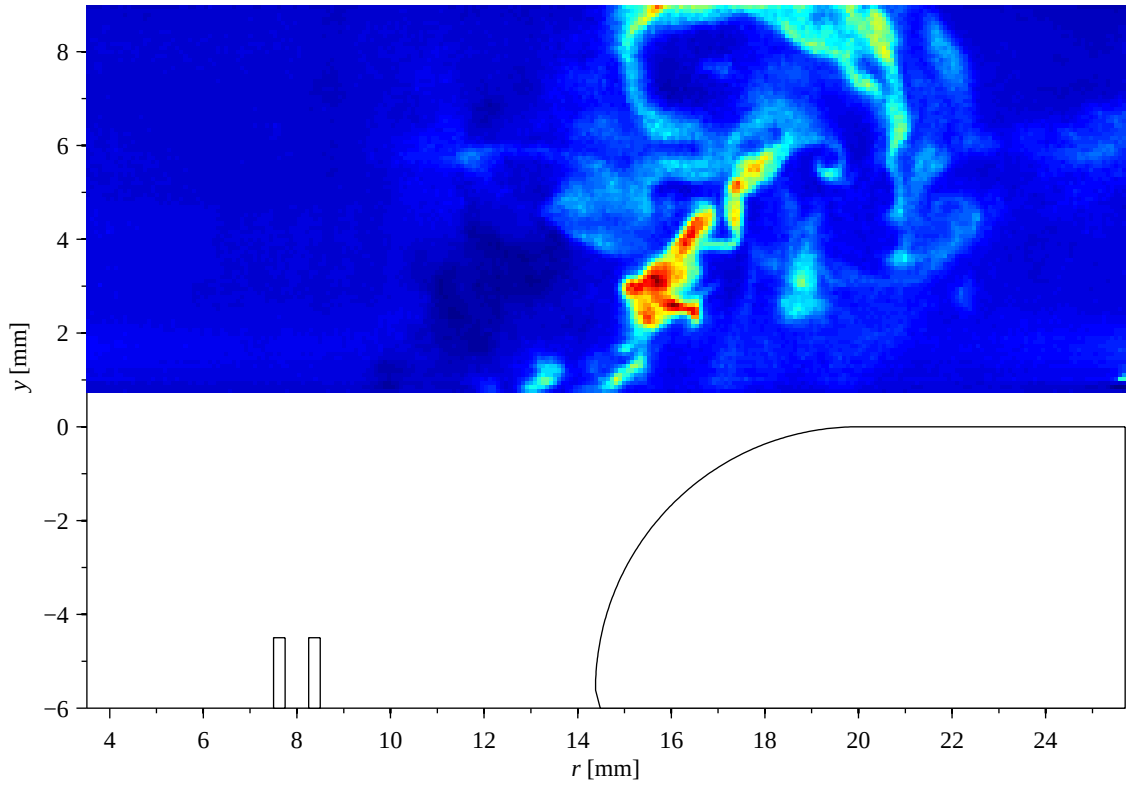

(b) 4×4 binned acetone PLIF image.

Figure 4.6: Simultaneous 4×4 binned (a) NO_2 and (b) acetone PLIF images from case P-1.

reducing the resolution of the images. The binned PLIF images can be seen in Fig. 4.6. After binning, the images had a resolution of 86.8 ± 6.7 μm/pixel. The binning process was described in Section 2.6.1. While the NO_2 PLIF image looks similar to the previous ones, there is a major difference. The NO_2 PLIF images shown in Figs. 4.2 and 4.4 were edited, for the purposes of this document, to give a contrast ratio that would exaggerate the structures in the LIF signal. In Fig. 4.6(a), no editing was performed. The native contrast ratio of the image makes the structures in the LIF signal visible.

An edge detection overlapped with the binned PLIF images can be seen in Fig. 4.7. The edge detection on the acetone image is fairly good, and the structures present in the image are clearly outlines. The edge detection on the NO_2 image is much better than before. The external structure of the fluorescence as well as some internal structures are outlined. However, there is still a lot of noise, and a still lot of edges based off that noise rather than real structures.

The final processing step for the PLIF images was to apply a Non-linear Anisotropic Diffusion Filter (NADF) to the images, which was described in Section 2.6.2. The NADF used was developed by Perona and Malik [60] and is intended to smooth an image within a given region, but resist smoothing the image across large gradients, so that edges are maintained. The NADF is excellent at preserving the edges in the image, while it helps the edge detection algorithm to avoid detecting false edges in the uniform regions. After processing, the SNR of the acetone image was 24, and the SNR of the NO_2 image was 13.

After filtering was complete, the images were cropped to the region in which the two laser sheets overlapped to produce a pair of images each 95 pixels tall by 256 pixels wide (the cropped image sizes for other cases were of similar sizes). The cropping of the PLIF images was held off until this point because the NADF tended to lead to detected edges at the sides of the frame. So the cropping was held off until after the filtering so that the rows and columns of pixels that would have been marked as edges could be trimmed away. These final, fully processed NO_2 and acetone PLIF images are shown in Fig. 4.8. It can be

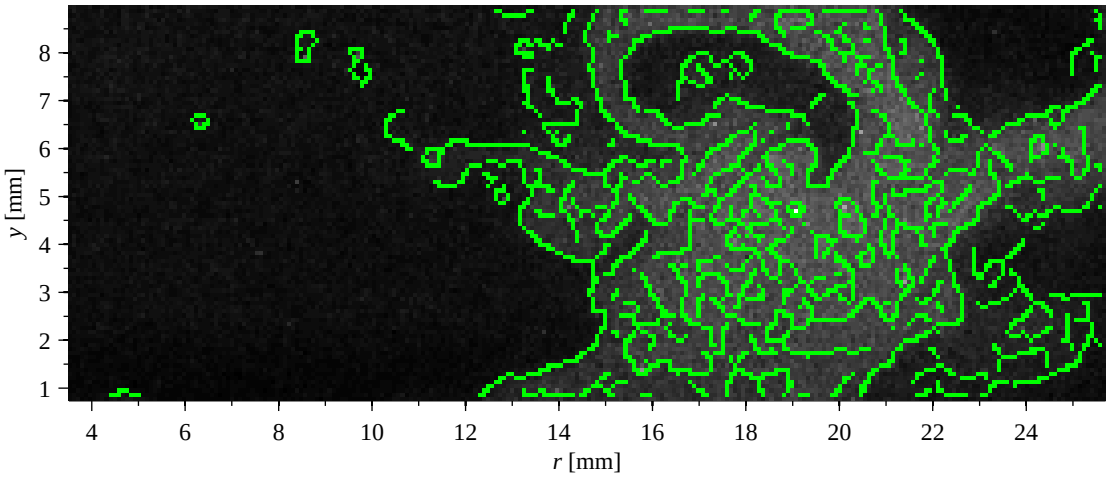

(a) 4×4 binned NO_2 PLIF image with overlapped edge detection.

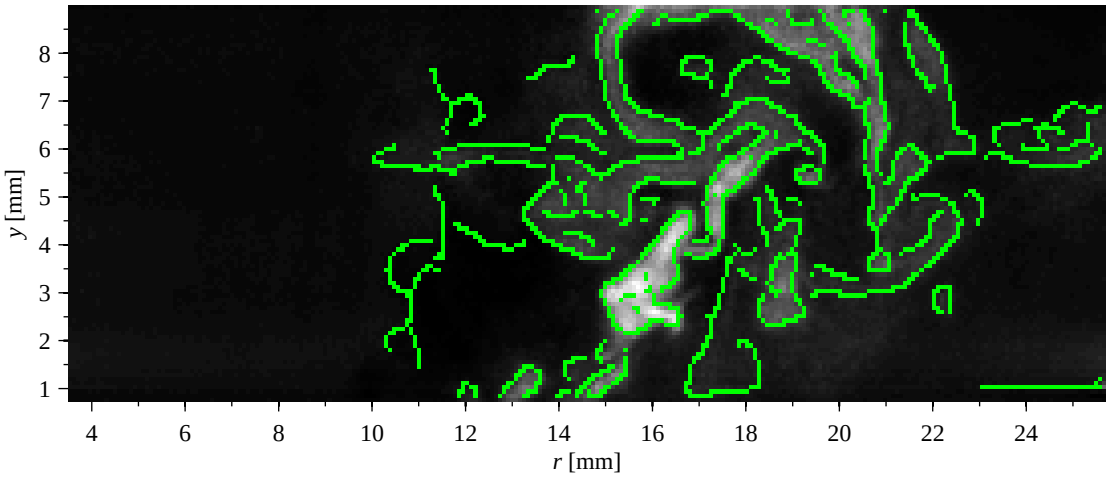

(b) 4×4 binned acetone PLIF image with overlapped edge detection.

Figure 4.7: Simultaneous 4×4 binned (a) NO_2 and (b) acetone PLIF images with overlapped edge detection from case P-1.

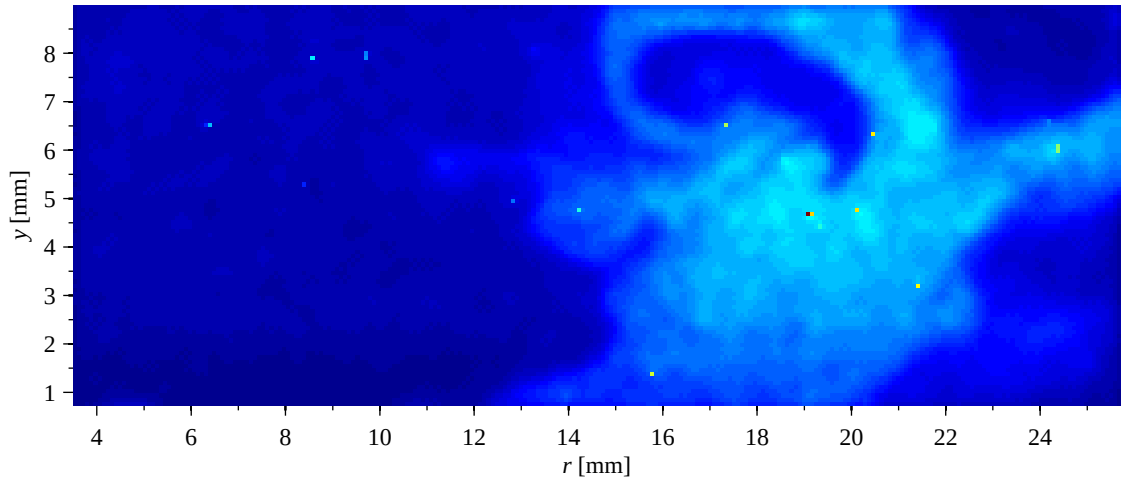

(a) Fully processed NO_2 PLIF image.

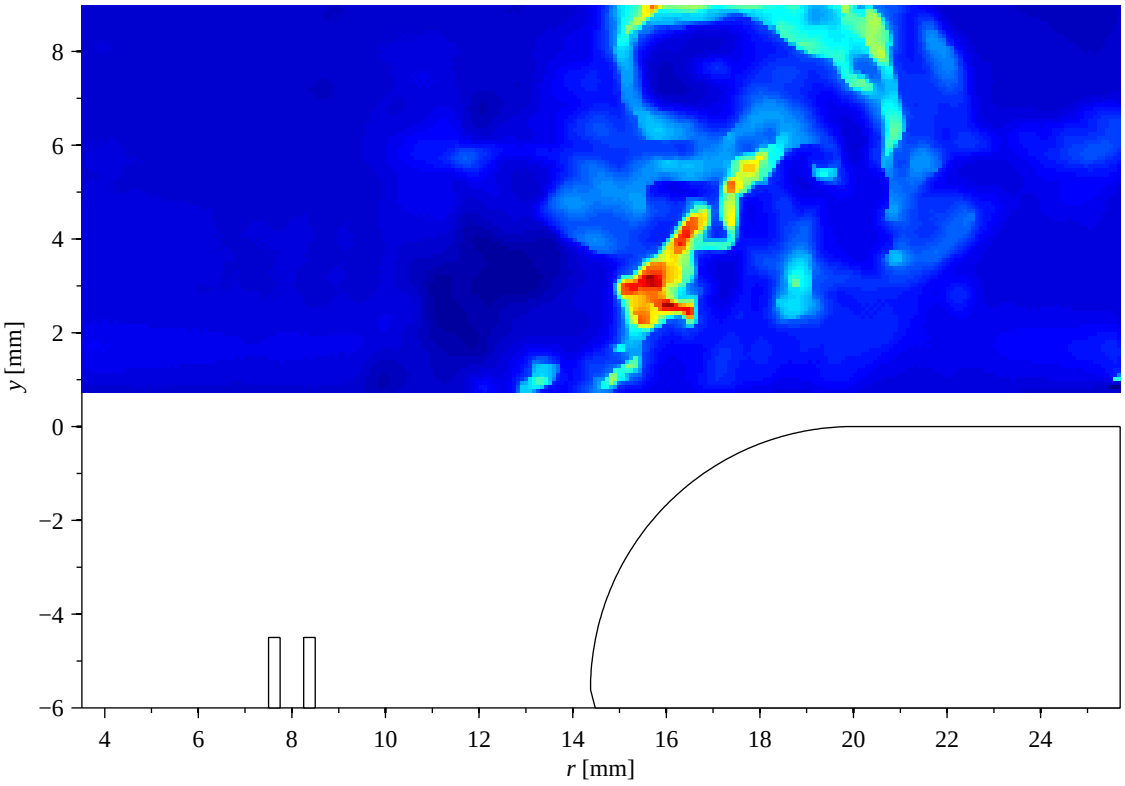

(b) Fully processed acetone PLIF image.

Figure 4.8: Simultaneous fully processed (a) NO_2 and (b) acetone PLIF images from case P-1.

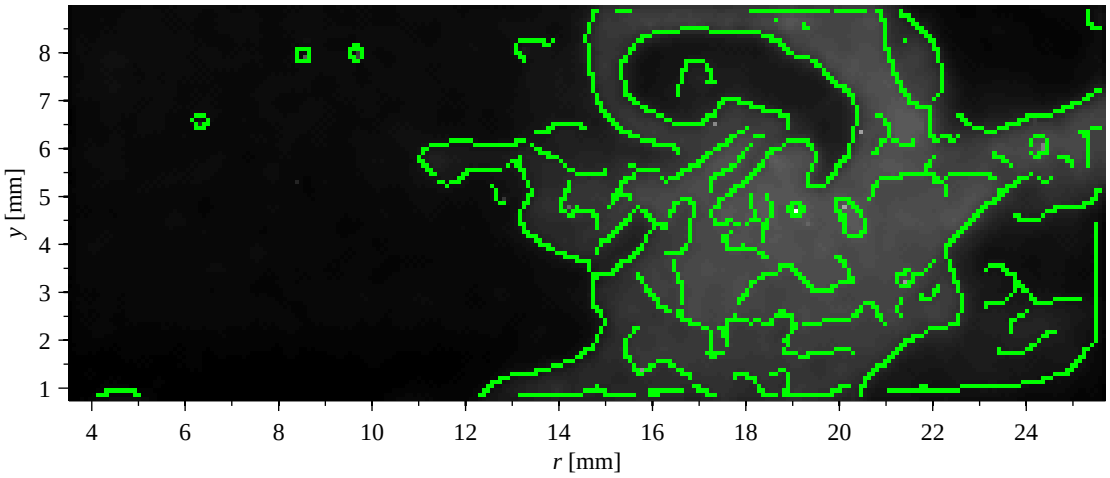

(a) Fully processed NO_2 PLIF image with overlapped edge detection.

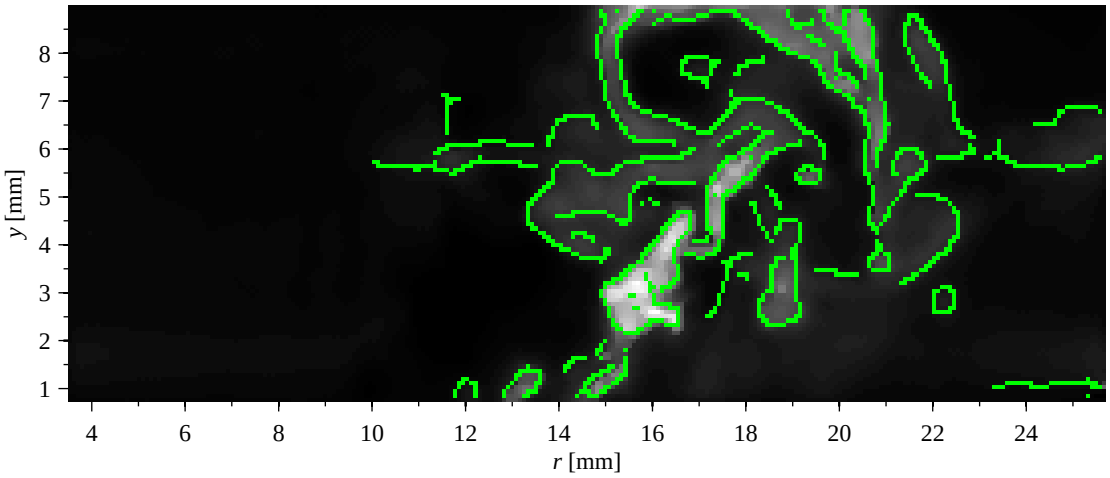

(b) Fully processed acetone PLIF image with overlapped edge detection.

Figure 4.9: Simultaneous fully processed (a) NO_2 and (b) acetone PLIF images with overlapped edge detection from case P-1.

seen that for both the NO_2 and acetone PLIF images that both the internal structures, and the boundaries of the structures as a whole are better defined, and will be easier to detect through an edge detection algorithm.

A Canny edge detection algorithm [64] was utilized, and was selected because it gave the most continuous edges, and provided the best balance between too many falsely detected edges or too few detected edges. The algorithm was described in further detail in Section 2.6.3. The algorithm was applied to the fully processed images, which are shown in Fig. 4.8, and the result can be seen overlaid on the fully processed PLIF images in Fig. 4.9. The edge detection on the acetone image is excellent with very few falsely detected edges. The NO_2 edge detection is vastly improved over the original one, shown in Fig. 4.5(a), and while it appears that there are still some false edges detected, the FIMM, which is described in greater detail in Section 4.2, requires that an acetone edge be located near an NO_2 edge. This means that a stray detected edge, like the ones from $r = 6$ mm to 10 mm and $y = 6$ mm to 8 mm would only lead to a value of ξ if there were a detected acetone edge nearby with the correct gradient. The ring-like structure existing from $r = 15$ mm to 22 mm and from $y = 6$ mm to 9 mm in both the NO_2 and acetone edge detection images is very well detected.

4.2 Flamelet Searching Method

The relation between the acetone and NO_2 fluorescence signals, S_{acetone} and S_{NO_2}, described in Eq. (1.5), depends on the locations of the maxima of the signal gradients, $\left(\nabla S_{\text{acetone}}\right)_{\max}$ and $\left(\nabla S_{NO_2}\right)_{\max}$. Up until this point the processing of the PLIF images, described in Section 4.1 was concerned with making the identification of these maxima easier and more accurate.

After the data preparation was complete, the edge detector described in Section 2.6.3 was applied to the images, and the locations of edges was noted. Then the gradients in both the r- and y-directions were determined through a central differencing method. Then, only

the gradient vectors at locations marked as edges were retained. The matrices storing the gradients were four-dimensional matrices, where the first two dimensions were the rows and columns of pixels making up an image and the fourth dimension carried each separate frame. So each individual frame was stored as a three-dimensional matrix, where the third dimension consisted of three pages. The first page stored the *r*-component of the gradient for a given pixel, the second page stored the *y*-component of the gradient for a given pixel, and the third page stored the magnitude of the gradient. The matrices were initialized with all elements having a value of 0. For a given frame, any pixel that was not on an edge was assigned a value of Not-a-Number (`NaN`) on the third page, where the magnitude of the vector would have been stored. This was to distinguish between pixels where one vector component had the value 0 and pixels where no edge was detected. This vector field for the example image pair from case P-1 is shown in Fig. 4.10. For the purposes of this figure, the vectors have been normalized so they are all visible.

As was shown in Section 3.1.2, the locations of $\left(\nabla S_{\text{acetone}}\right)_{\text{max}}$ and $\left(\nabla S_{\text{NO}_2}\right)_{\text{max}}$ do not overlap in non-premixed flamelets, and sit close but do not always overlap in premixed flamelets. This means that the gradients of the acetone and NO_2 signals could not simply be multiplied at each spatial location. To solve this problem, it was necessary to develop a method where given a location of $\left(\nabla S_{\text{acetone}}\right)_{\text{max}}$, the corresponding $\left(\nabla S_{\text{NO}_2}\right)_{\text{max}}$ would be found. This method has been termed the Flamelet Searching Method (as opposed to the Flamelet Shifting Method, described in Appendix B, which was the original method developed on the enclosed co-flow burner).

The matrix of ξ values, which will be referred to as $\boldsymbol{\xi}$ while an individual element of the matrix will be referred to as $\xi_{i,j}$ for the i^{th} row and j^{th} column, was initialized to be of the appropriate size—the same number of rows and columns as the PLIF images, and as many pages as there were frames—with all elements being equal to 0. The Flamelet Searching Method worked in such a way where it moves pixel-by-pixel through all the frames—moving left to right, horizontally in each row of pixels, before moving down to

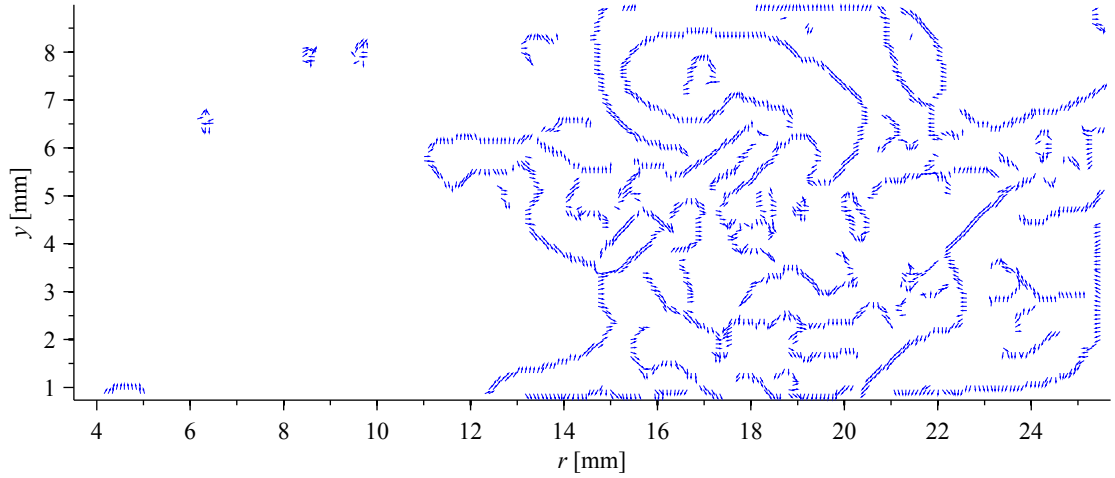

(a) Normalized NO_2 gradients at detected edges.

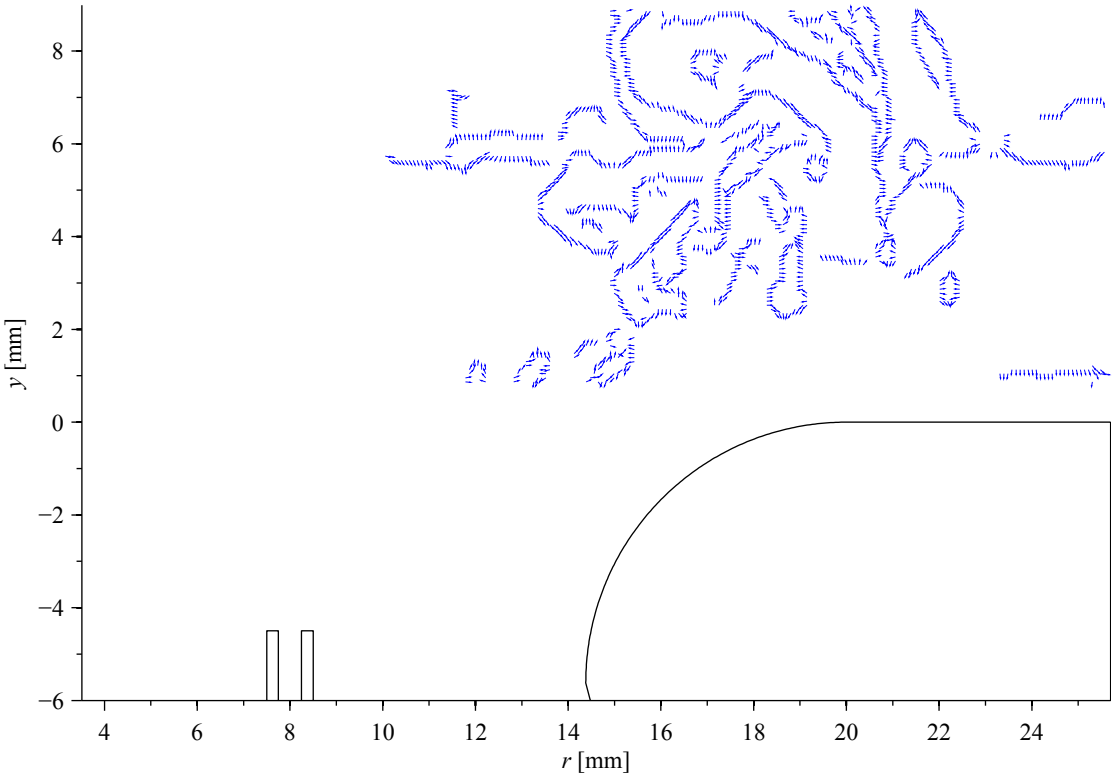

(b) Normalized acetone gradients at detected edges.

Figure 4.10: Simultaneous normalized (a) NO_2 and (b) acetone gradients at detected edges, from case P-1.

the next row. This was done sequentially while several frames were processed in parallel.

The method worked in two stages. During the first stage, each pixel in the acetone image was compared one-to-one with its corresponding pixel in the NO_2 image. The gradients at both pixels (say the pixel in the i^{th} row and j^{th} column in both images) were evaluated with the equation:

$$\frac{\left(\nabla S_{\text{acetone}}\right)_{i,j} \cdot \left(\nabla S_{\text{NO}_2}\right)_{i,j}}{\left|\left(\nabla S_{\text{acetone}}\right)_{i,j} \cdot \left(\nabla S_{\text{NO}_2}\right)_{i,j}\right|}, \tag{4.1}$$

to check if the output would be equal to $+1$ (premixed flamelet) or -1 (non-premixed flamelet). If it was, then $\xi_{i,j}$ was assigned the value $+1$ or -1, depending on which check was passed, and then the code moved onto the next pixel. The subscript max that was present in Eq. (1.5) is omitted here because this check was performed on every pixel, whether or not an edge was detected. Locations where an edge was not detected would return a non-number value. This was a holdover from an early version of the method where ξ was evaluated at every pixel rather than only at the locations of maximum signal gradient. As a note, the pixels were checked for $\xi_{i,j} = +1$ first and next for $\xi_{i,j} = -1$.

If both the $\xi_{i,j} = +1$ and $\xi_{i,j} = -1$ checks failed, $(\nabla S_{\text{acetone}})_{i,j}$ was next checked for a `NaN` value, specifically the third page of the acetone gradient matrix for that pixel and frame was checked for a `NaN` value. If the pixel was not `NaN`, the method proceeded to step 2. If the pixel was `NaN`, that $\xi_{i,j}$ would remain its initialized value of 0, and the method would move to the next pixel. A pixel with a value of $\xi_{i,j} = 0$ means that no flamelet was present. It does not mean that no combustion was occurring. FIMM is incapable of detecting all kinds of combustion, only flamelets. It is possible that flameless combustion was occurring in those regions. A pixel with a value of $\xi_{i,j} = 0$ means that it is unknown what is occurring there, but it is not flamelet combustion.

It is step 2 of the method that the Flamelet Searching Method takes its name "Searching" from. During this step, the method searched parallel to the vector existing at the acetone pixel being investigated both in the direction the vector pointed and in the opposite

direction. A new unit vector was created that pointed in the same direction as the original vector for that pixel, but had a length of 1. The code was designed to then iterate over multiples of that unit vector (so first 1 unit-vector–length away, then 2 unit-vector-lengths away, then 3 unit-vector–lengths away, etc.), checking NO_2 pixels for a value that when evaluated with the equation:

$$\frac{\left(\nabla S_{\text{acetone}}\right)_{\max_{i,j}} \cdot \left(\nabla S_{NO_2}\right)_{\max_{i',j'}}}{\left|\left(\nabla S_{\text{acetone}}\right)_{\max_{i,j}} \cdot \left(\nabla S_{NO_2}\right)_{\max_{i',j'}}\right|}, \tag{4.2}$$

where i' and j' are the indices of the NO_2 image pixel being evaluated, give either $+1$ or -1. The way the method was designed, either the acetone or the NO_2 image would have to be the base from which to search for the other. Acetone was selected as the base because it tended to contain the fewest false edges. This means that the acetone pixel with indices (i, j) was evaluated along with the NO_2 pixel selected for that round, with indices (i', j').

The order in which this evaluation took place was first an NO_2 pixel in the *opposite* direction that $(\nabla S_{\text{acetone}})_{\max_{i,j}}$ pointed, one unit-vector–length away, was evaluated for a value that would give $\xi_{i^*,j^*} = -1$ (non-premixed flamelet). (The issue of which pixel to mark required some thought and will be discussed shortly. However, that pixel will be denoted by indices (i^*, j^*). There are three sets of indices: (i, j) are indices for the acetone pixel and are constant for this while loop; (i', j') are the indices for the NO_2 pixel and change every iteration of this loop, assuming the integer multiple of the unit-vector–length rounds to index values higher than the previous loop iteration; and (i^*, j^*) are the indices for the pixel in the $\boldsymbol{\xi}$ matrix that will be marked.) Then the same NO_2 pixel was evaluated for a value that would give $\xi_{i^*,j^*} = +1$ (premixed flamelet). Next an NO_2 pixel that is one unit-vector–length away in the *same* direction that $(\nabla S_{\text{acetone}})_{\max_{i,j}}$ pointed was evaluated for a value that would give $\xi_{i^*,j^*} = +1$. Finally, the same NO_2 pixel, located in the same direction $(\nabla S_{\text{acetone}})_{\max_{i,j}}$ pointed, would be evaluated for a value that would give $\xi_{i^*,j^*} = -1$. If one of these four evaluations led to a value of $+1$ or -1, the while loop would stop, ξ_{i^*,j^*} would

have its value assigned, and the next acetone pixel would be evaluated. If none of these four checks succeeded, the loop would continue to check the NO_2 pixel two unit-vector–lengths away, then three unit-vector–lengths away, and so on.

Limits were placed on the loop, however. In the direction that the flamelet modeling suggested searching—the opposite direction of $(\nabla S_{\text{acetone}})_{\max_{i,j}}$ for a non-premixed flamelet and the same direction $(\nabla S_{\text{acetone}})_{\max_{i,j}}$ pointed for a premixed flamelet—the search distance, Δs, would be limited to 1.0 mm. In the direction opposite to what the modeling suggested—the opposite direction of $(\nabla S_{\text{acetone}})_{\max_{i,j}}$ for a premixed flamelet and the same direction $(\nabla S_{\text{acetone}})_{\max_{i,j}}$ pointed for a non-premixed flamelet—Δs would be limited to 0.5 mm. Searching in the opposite direction to what the flamelet modeling suggested allowed for errors in the registration of the acetone and NO_2 PLIF images. These distances were selected based on a combination of what the flamelet modeling suggested, the distances observed in cases L-1 and L-2, and what would provide the most continuous flame index contours.

When shorter searching distances were used, some flamelets or portions of flamelets went undetected, as indicated by breaks in what had previously been continuous contours. When longer searching distances were used, many more solitary-pixel flamelets were detected, which did not resolve into continuous contours when the distances were increased. This indicated that these solitary-pixel flamelets were falsely detected flamelets. The limits of 1.0 mm and 0.5 mm gave the best balance between too many solitary-pixel flamelets and too many flamelets or portions of flamelets going undetected.

When the evaluation from step 1 succeeded, the pixel marked in $\boldsymbol{\xi}$ was the one shared by both the acetone and NO_2 images. For this case $(i, j) = (i', j') = (i^*, j^*)$. When an evaluation from step 1 failed and the evaluation from step 2 succeeded, the selection of a pixel in $\boldsymbol{\xi}$ to mark was not straightforward. For this case (i, j) and (i', j') were not equal, so the values for (i^*, j^*) were not straightforward. The options considered were: that the acetone pixel location, (i, j), could be marked; the NO_2 pixel location, (i', j'), could be marked; or a pixel

somewhere in between could be marked. In the end, this third option was selected and it was decided to mark the pixel half-way between (i, j) and (i', j'), as this option provided the most continuous ξ contour lines.

4.2.1 Flamelet Searching Method Results

The results of the Flamelet Searching Method can be seen for this chapter's example frame and two other frames from case P-1 in Fig. 4.11. Recognizable structures are clearly visible in these images. Figure 4.11(a), this chapter's example figure, clearly shows the ring-like structure, discussed previously, which exists from $r = 15$ mm to 22 mm and from $y = 6$ mm to 9 mm. Figure 4.11(b) shows a time when non-premixed flamelets dominated from $r = 5$ mm to 15 mm and premixed flamelets dominated at $r > 15$ mm. Figure 4.11(c) shows a time when predominantly non-premixed flamelets occurred near the injector face from $r = 10$ mm to 16 mm, predominantly premixed flamelets occurred at $r > 16$ mm near the injector face, and predominantly premixed flamelets occurred away from the injector face.

The same $\boldsymbol{\xi}$ matrices can be seen overlapped on top of their respective NO_2 and acetone PLIF images to give an idea of where the method marks the flame index. The $\boldsymbol{\xi}$ from Fig. 4.11(a), this chapter's example image, can be seen overlapped on top of its NO_2 and acetone signals in Fig. 4.12, where it can be seen that the ring-like structure is very well defined as a premixed flamelet. The $\boldsymbol{\xi}$ from Fig. 4.11(b) can be seen overlapped on top of its NO_2 and acetone signals in Fig. 4.13, and the $\boldsymbol{\xi}$ from Fig. 4.11(c) can be seen overlapped on top of its NO_2 and acetone signals in Fig. 4.14.

4.2.2 Flamelet Searching Method Post-Processing

As was mentioned previously, for each of the GTMC data sets, 450 image pairs were acquired. With the ensemble of 450 separate frames with flame index measurements, some statistical analysis was performed. To perform this analysis, the field of view was divided

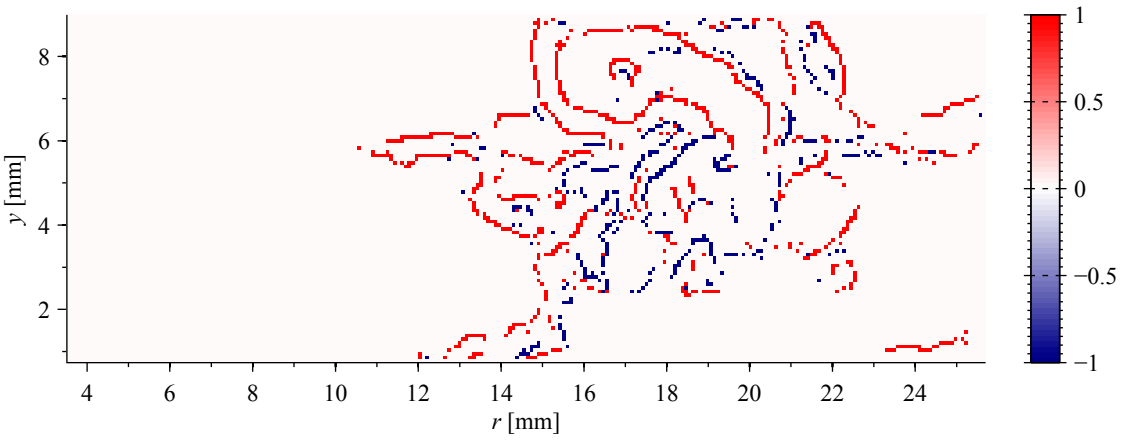

(a) The example frame for this chapter. Predominantly premixed flamelets occur.

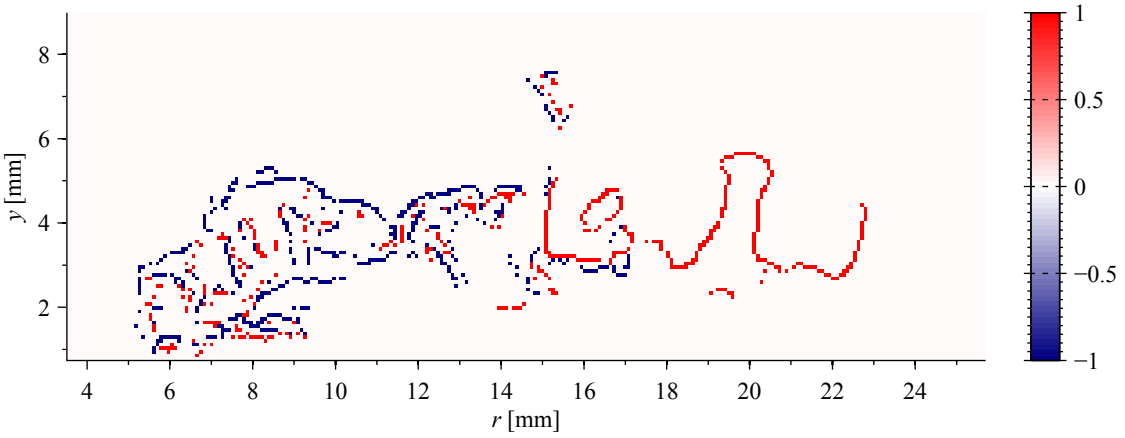

(b) Time when non-premixed flamelets occurred from $r = 5$ mm to 15 mm and premixed flamelets dominated at $r > 15$ mm.

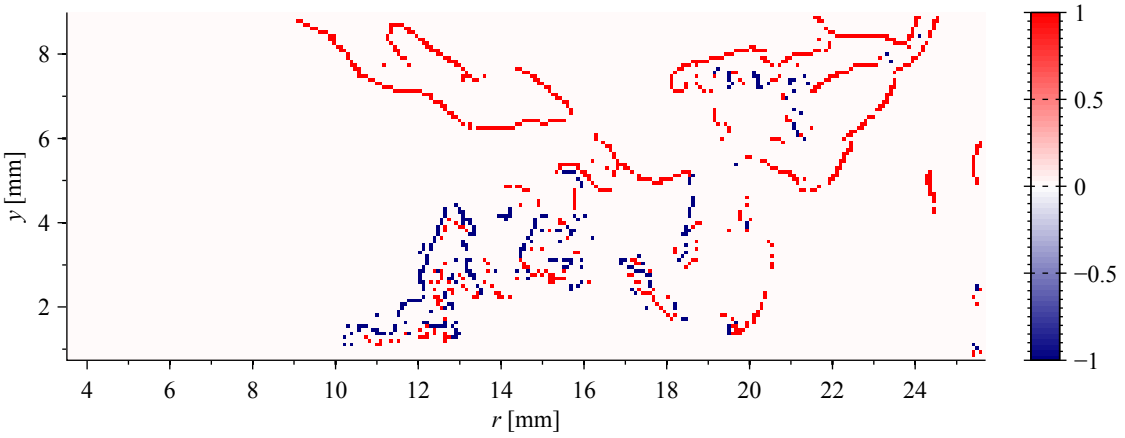

(c) Time when predominantly non-premixed flamelets occurred near the injector face from $r = 10$ mm to 16 mm, predominantly premixed flamelets occurred at $r > 16$ mm near the injector face, and predominantly premixed flamelets occurred away from the injector face.

Figure 4.11: Three instantaneous images of flame index, ξ, from case P-1. A value of -1 marks a non-premixed flamelet in dark navy blue, and a value of $+1$ marks a premixed flamelet in red.

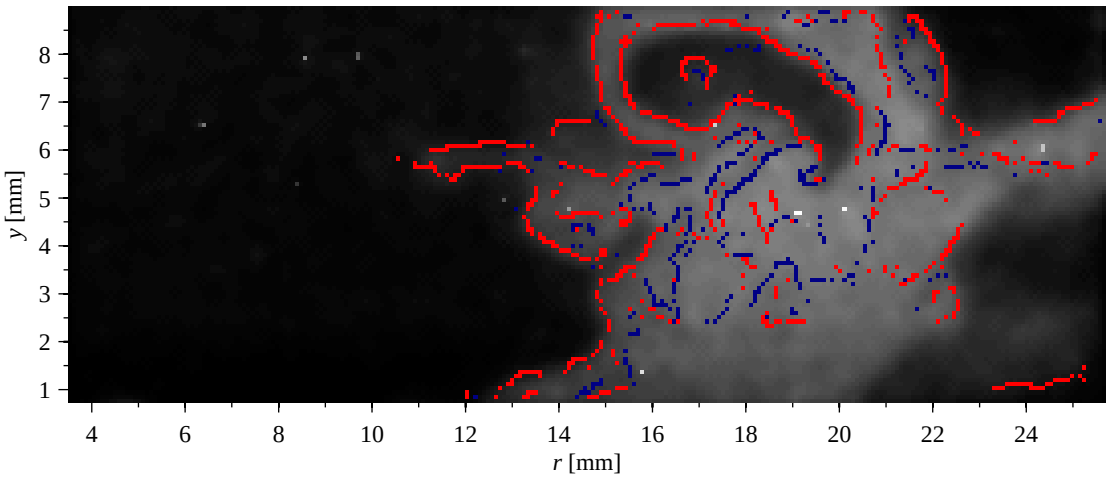

(a) Fully processed NO_2 PLIF image overlapped with ξ.

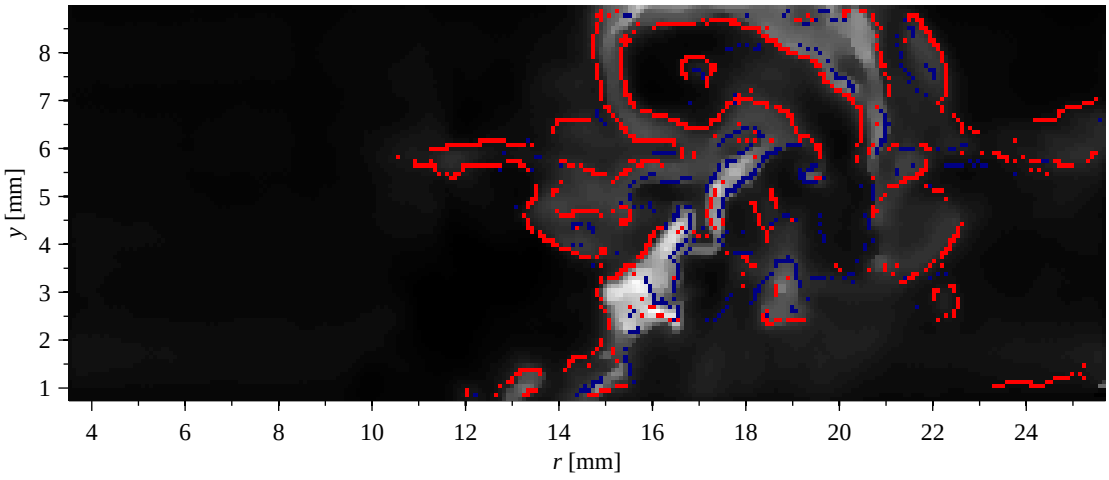

(b) Fully processed acetone PLIF image overlapped with ξ

Figure 4.12: Simultaneous fully processed (a) NO_2 and (b) acetone PLIF images with overlapped instantaneous ξ, previously shown in Fig. 4.11(a), from case P-1. A value of -1 marks a non-premixed flamelet in dark navy blue, and a value of $+1$ marks a premixed flamelet in red.

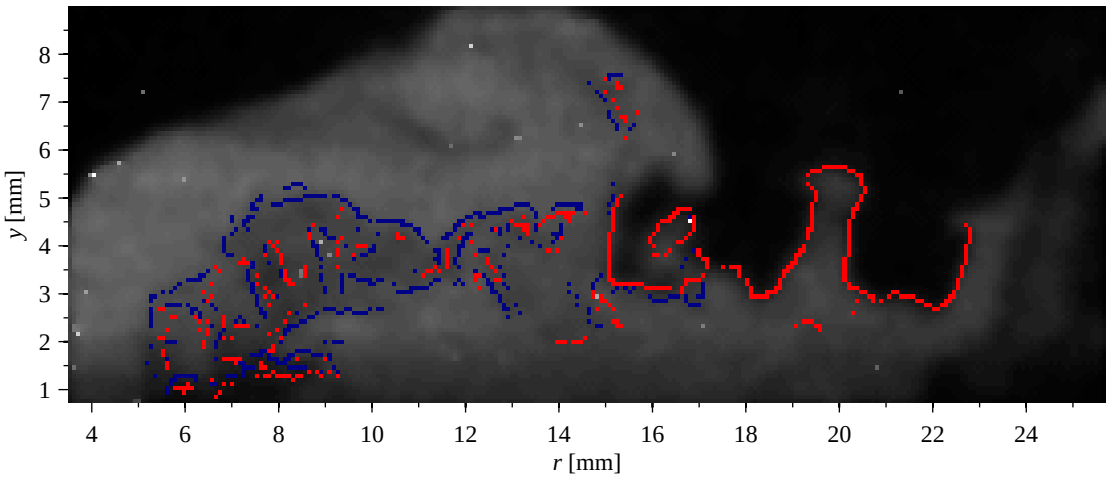

(a) Fully processed NO_2 PLIF image overlapped with ξ.

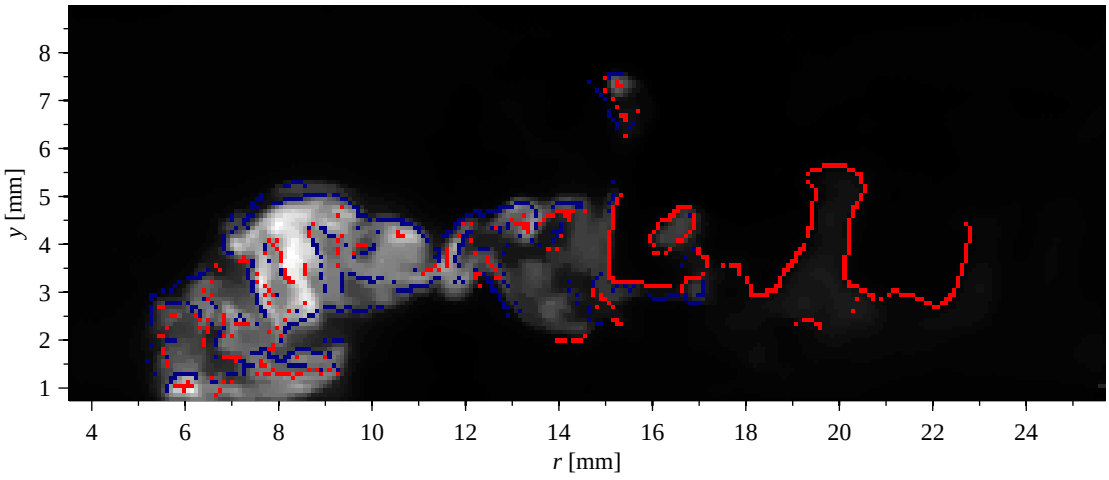

(b) Fully processed acetone PLIF image overlapped with ξ

Figure 4.13: Simultaneous fully processed (a) NO_2 and (b) acetone PLIF images with overlapped instantaneous ξ, previously shown in Fig. 4.11(b), from case P-1. A value of -1 marks a non-premixed flamelet in dark navy blue, and a value of $+1$ marks a premixed flamelet in red.

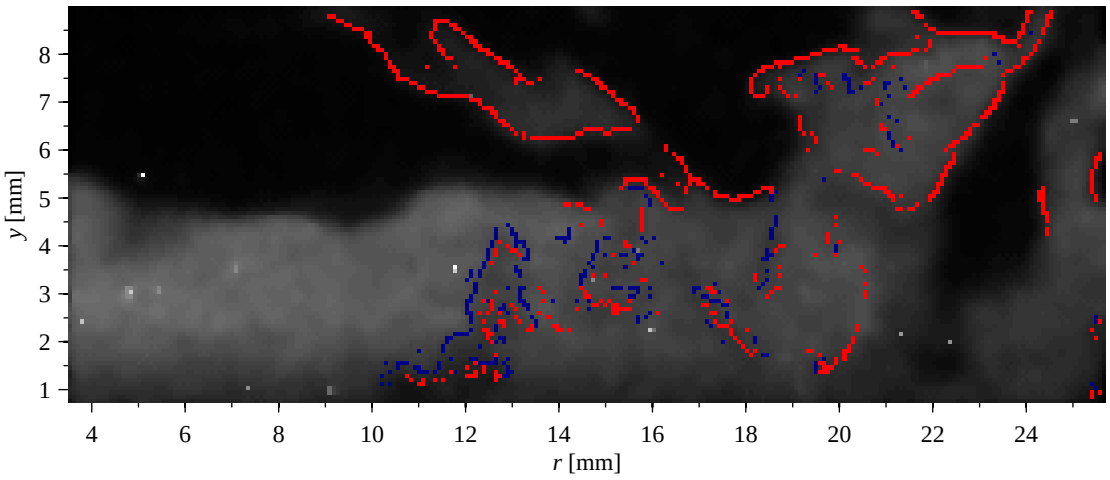

(a) Fully processed NO_2 PLIF image overlapped with ξ.

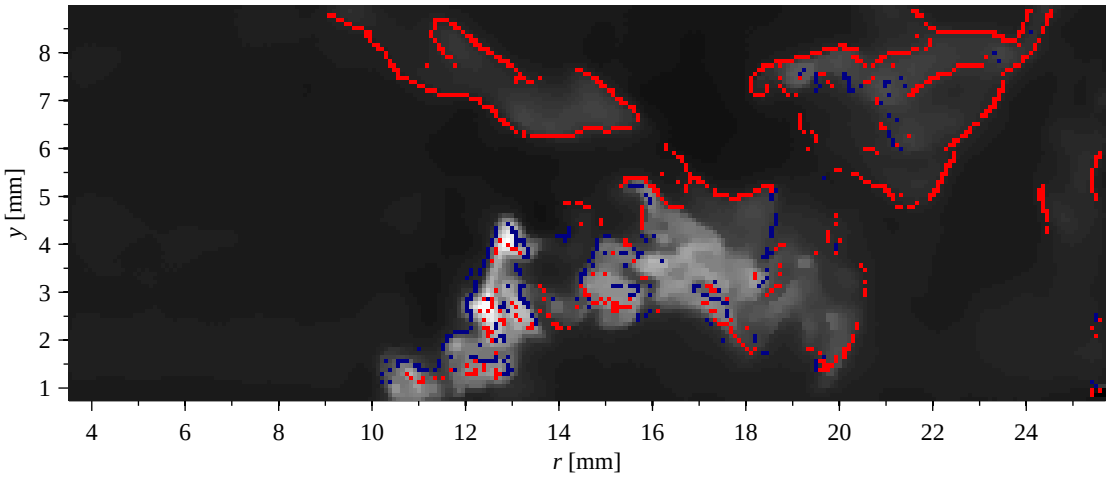

(b) Fully processed acetone PLIF image overlapped with ξ

Figure 4.14: Simultaneous fully processed (a) NO_2 and (b) acetone PLIF images with overlapped instantaneous ξ, previously shown in Fig. 4.11(c), from case P-1. A value of -1 marks a non-premixed flamelet in dark navy blue, and a value of $+1$ marks a premixed flamelet in red.

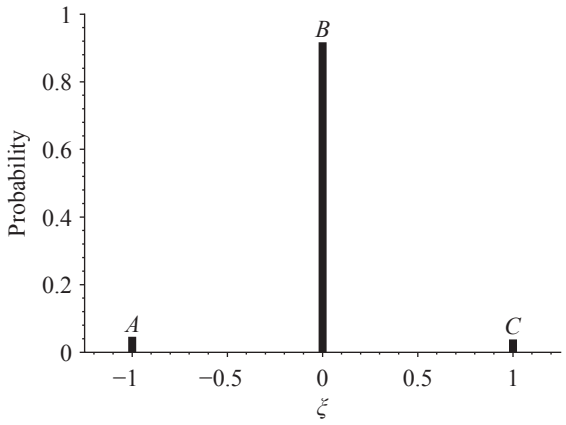

Figure 4.15: Probability mass function of ξ for a single super-pixel. A is the probability that $\xi = -1$, B is the probability that $\xi = 0$, and C is the probability that $\xi = +1$. From case P-1.

into super-pixels in an attempt to give a grid of as close to 10×20 super-pixels as possible, without losing any sub-pixels in the process. For case P-1, each super-pixel was composed of a grid of $9 \times 16 \times 450$ sub-pixels for a horizontal resolution of 1254.4 ± 14.3 μm/pixel and a vertical resolution of 765.7 ± 9.0 μm/pixel (the super-pixels were not square). The $\boldsymbol{\xi}$ matrix in case P-1 was reduced from a size of 95×256 pixels down to 10×16 pixels, with 4 rows and 1 column of pixels lost. This binning, like the summation one used to improve the image's SNR, was constructed so that the lost sub-pixels would be the left-most columns and top-most rows of sub-pixels.

The decision to bin $\boldsymbol{\xi}$ was a graphic one. Each pixel could vary enough from its neighbors that the statistical quantities were incomprehensible when the figure was left unbinned. So while the newly defined quantities $\overline{\beta_p}$ and ϵ_{pp}—which will be discussed at the end of this section—were determined from the full, unbinned $\boldsymbol{\xi}$ and all the statistical analysis was first performed on the unbinned $\boldsymbol{\xi}$, to portray that information graphically, $\boldsymbol{\xi}$ had to be binned and the analysis performed on each super-pixel.

For each super-pixel, a Probability Mass Function (PMF) of ξ was determined for the three possible values -1, 0, and $+1$. This is represented by a Probability Mass Function rather than a Probability Density Function (PDF) because the variable ξ does not vary

continuously, it is a discrete variable. ξ is only allowed to have one of three values: -1, 0, or $+1$. An example PMF for a single super-pixel is shown in Fig. 4.15, where A is the probability that $\xi = -1$ (non-premixed flamelet):

$$A \equiv \Pr(\xi = -1), \tag{4.3}$$

B is the probability that $\xi = 0$ (no flamelet):

$$B \equiv \Pr(\xi = 0), \tag{4.4}$$

and C is the probability that $\xi = +1$ (premixed flamelet):

$$C \equiv \Pr(\xi = -1). \tag{4.5}$$

While the lines in the figure appear to have some thickness, in reality they are delta functions so probabilities A, B, and C are located only at -1, 0, and $+1$, respectively, and are thus infinitely thin. The sum of the areas under all three curves, $A + B + C = 1$. Contours of the PMF for the full data set are shown in Fig. 4.16 for case P-1.

The meaning of A and C in Fig. 4.16, the probabilities for a non-premixed and for a premixed flamelet, are fairly straightforward. They tell us which regions of the flame have more or less of premixed or non-premixed flamelets. The meaning of B, the probability for no flamelet, is less straightforward. If only the value of B is observed, it gives exactly that, the probability of no flamelet. However, the inverse of B, $(1 - B)$, provides another useful insight to the properties of the flame being studied. The inverse of B gives the probability of a flamelet existing, with no differentiation between premixed and non-premixed flamelets. For this reason, the colormap of the contour plots of B, as shown in Fig. 4.16(a), is the reverse of those used for the A and C contours, in that the darker regions are where B has the smallest value, while the darker regions in the plots of A and C are where their

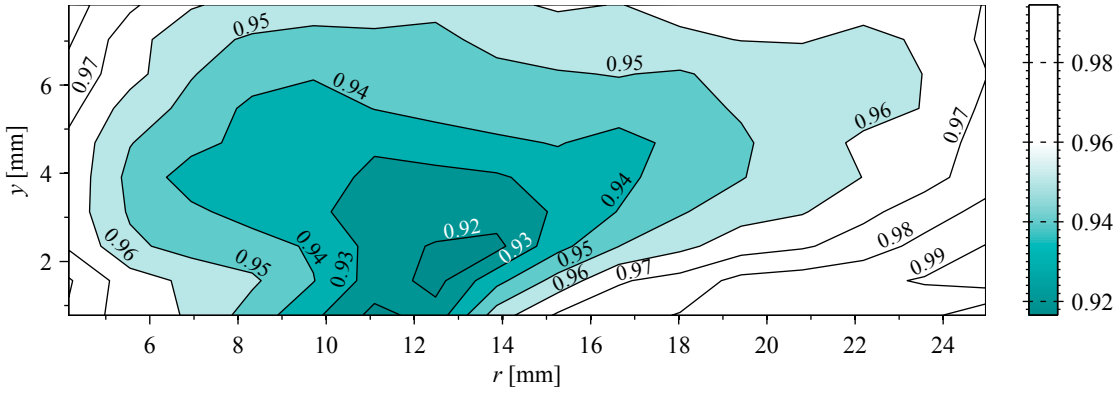

(a) Probability that $\xi = 0$ (B) in case P-1.

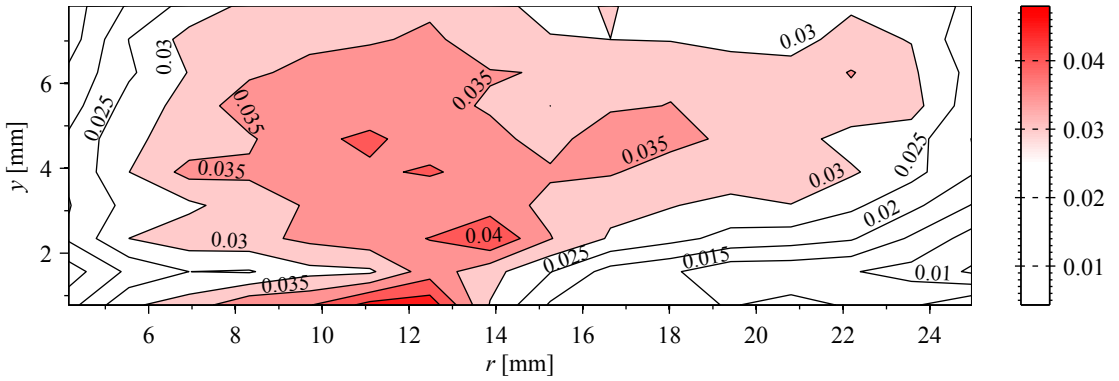

(b) Probability that $\xi = +1$ (C) in case P-1.

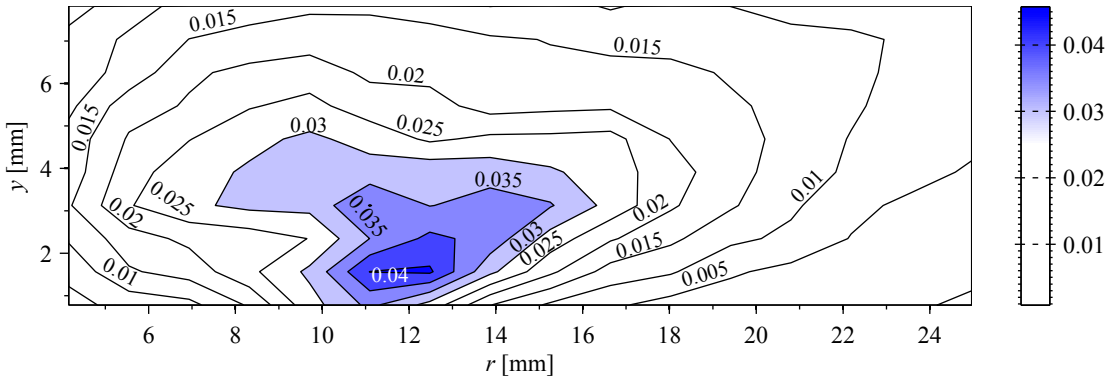

(c) Probability that $\xi = -1$ (A) in case P-1.

Figure 4.16: The probability mass function for ξ in case P-1.

respective flamelet-types are more likely to appear. This reversal of the colormap was done so that an observer of Fig. 4.16(a) would get a sense for where flamelets of all types are more likely to appear. It should be stated again, however, that regions with higher values of B do not mean that combustion is less likely, only that flamelets are less likely. This method says nothing about forms of combustion that do not involve flamelets, like flameless combustion. To emphasize the regions with higher probabilities (or lower, in the case of B) for their particular type of flamelet, the contours in Fig. 4.16 have been shaded at only the regions with the highest probabilities.

Using the PMF, the average value of the flame index for each super-pixel is:

$$\langle \xi \rangle = \frac{(-1)A + (0)B + (1)C}{A + B + C}, \tag{4.6}$$

where $\langle \xi \rangle$ is the average flame index for that super-pixel. Because B is centered at $\xi = 0$ and $A + B + C = 1$, Eq. (4.6) can be simplified to be:

$$\langle \xi \rangle = C - A. \tag{4.7}$$

This ensemble average flame index, while useful, is not the best indicator of where pre-mixed and non-premixed flamelets occur. A better indicator is the following conditioned average:

$$\langle \xi \mid \xi \neq 0 \rangle = \frac{(-1)A + (1)C}{A + C}, \tag{4.8}$$

where $\langle \xi \mid \xi \neq 0 \rangle$ is the average of ξ, conditioned on the condition that ξ is nonzero, meaning that a flamelet was present. Equation (4.8) can be simplified to be:

$$\langle \xi \mid \xi \neq 0 \rangle = \frac{C - A}{A + C}. \tag{4.9}$$

Both the average flame index and the conditionally averaged flame index are shown in Fig. 4.17 for case P-1. In the conditionally averaged contour, Fig. 4.17(b), regions that are,

on average, more non-premixed are marked with shades of blue and a hatching of diagonal lines while regions that are, on average, highly premixed are marked with shades of red and a hatching of crosses. This is done to emphasize the non-premixed and highly premixed regions.

The conditional average, $\langle \xi \mid \xi \neq 0 \rangle$ is far more useful than the average, $\langle \xi \rangle$, because it differentiates between super-pixels where the average is 0 and super-pixels where there is never a flamelet ($\xi = 0$ in all frames). For case P-1, every super-pixel contains a flamelet at some point, so the fact that $\langle \xi \mid \xi \neq 0 \rangle$ differentiates between the two is not immediately apparent, although the values of the averages do change, so the contour plots look different. The use of locations where there is never a pixel can only be seen in cases P-3 and S-1, where the flames were smaller and filled less of the frame. The full data sets, including their contour plots of $\langle \xi \mid \xi \neq 0 \rangle$ can be seen in Appendix C. In cases P-3 and S-1, the regions that never have a flamelet, meaning that $\langle \xi \mid \xi \neq 0 \rangle$ is undefined, are marked with dark cyan and a hatching of short horizontal lines.

In addition to the average flame indices, the standard deviation of the flame index, σ_ξ, for a given super-pixel was calculated to be:

$$\sigma_\xi = \sqrt{A\left[(-1) - \langle \xi \rangle\right]^2 + B\left[(0) - \langle \xi \rangle\right]^2 + C\left[(+1) - \langle \xi \rangle\right]^2}. \tag{4.10}$$

The standard deviation can also be defined based off of the conditionally averaged flame index, $\langle \xi \mid \xi \neq 0 \rangle$, to be:

$$\sigma_{\langle \xi | \xi \neq 0 \rangle} = \sqrt{A\left[(-1) - \langle \xi \mid \xi \neq 0 \rangle\right]^2 + C\left[(+1) - \langle \xi \mid \xi \neq 0 \rangle\right]^2}. \tag{4.11}$$

Values for both standard deviations can be seen in Fig. 4.18 for case P-1.

The two quantities $\overline{\beta_p}$ and ϵ_{pp} were newly defined. The quantity $\overline{\beta_p}$ is the average probability, for an entire data set, that a flamelet is premixed ($\xi = +1$) if a flamelet is present. So, $\overline{\beta_p} = +1$ if all flamelets are premixed, 0.5 if all flamelets are fully partially-premixed

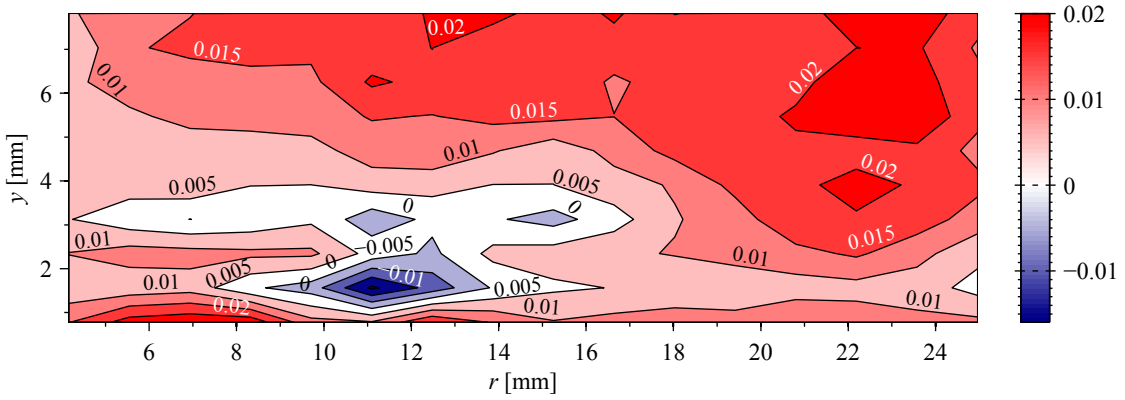

(a) Averaged flame index, $\langle \xi \rangle$, in case P-1.

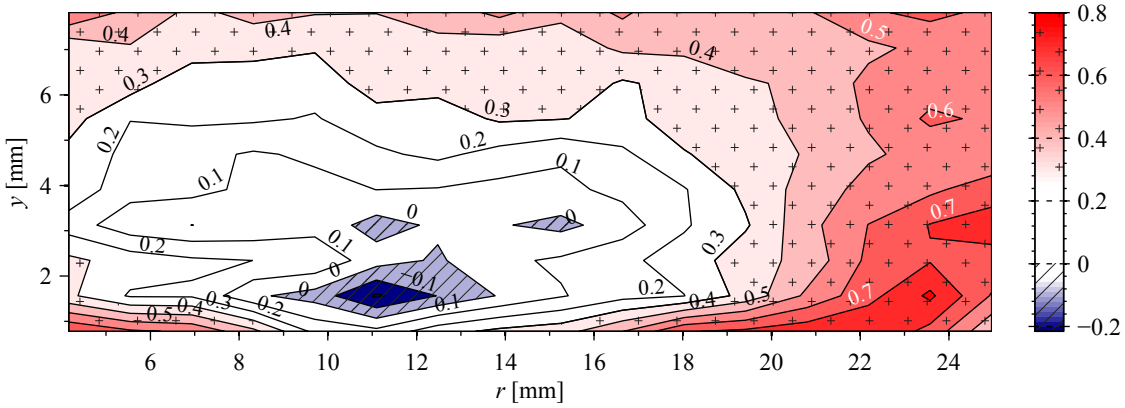

(b) Conditionally averaged flame index, ignoring locations with no flamelets, $\langle \xi \mid \xi \neq 0 \rangle$, in case P-1. Regions that are, on average, more non-premixed are marked with shades of blue and a hatching of diagonal lines while regions that are, on average, highly premixed are marked with shades of red and a hatching of crosses.

Figure 4.17: For case P-1, (a) the average flame index $\langle \xi \rangle$ and (b) the conditionally averaged flame index $\langle \xi \mid \xi \neq 0 \rangle$, where locations without flamelets were ignored.

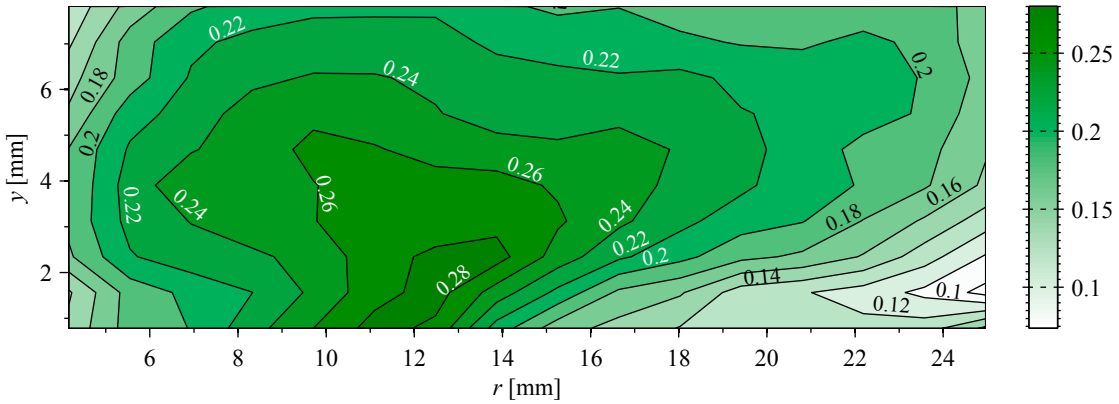

(a) Standard deviation of ξ, σ_ξ, in case P-1.

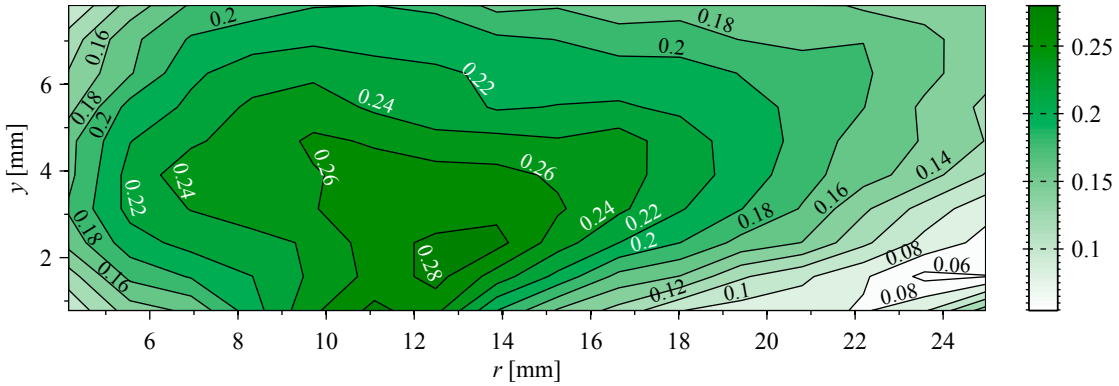

(b) Conditional standard deviation of ξ, $\sigma_{\langle\xi|\xi\neq 0\rangle}$, in case P-1.

Figure 4.18: For case P-1, the standard deviation derived from (a) the average of ξ, σ_ξ, and (b) the conditional average of ξ, $\sigma_{\langle\xi|\xi\neq 0\rangle}$, where all locations without flamelets were ignored.

(meaning they are premixed just as often as they are non-premixed), and 0 if all flamelets are non-premixed. The degree of partial-premixing, ϵ_{pp}, is a re-normalization of $\overline{\beta_p}$ to simplify it somewhat. The quantity ϵ_{pp} is defined such that it only indicates if all flamelets are fully partially-premixed ($\epsilon_{pp} = 1$) or are entirely premixed or non-premixed ($\epsilon_{pp} = 0$), but doesn't say whether the flame is leaning more toward premixed or non-premixed flamelets.

While both $\overline{\beta_p}$ and ϵ_{pp} can be measured from both the binned and unbinned $\boldsymbol{\xi}$ matrix, the uncertianty increases by roughly an order of magnitude when determining $\overline{\beta_p}$ and ϵ_{pp} from the binned $\boldsymbol{\xi}$ matrix. So $\overline{\beta_p}$ and ϵ_{pp} were determined from the unbinned $\boldsymbol{\xi}$ matrix.

It now becomes useful to quantify how premixed or non-premixed the flame is. For each pixel (or super-pixel) the probability that a flamelet is premixed ($\xi = +1$) if a flamelet is present, β_p, is defined as:

$$\beta_p = \Pr(\xi = +1 \mid \xi \neq 0) = \frac{C}{A + C}. \tag{4.12}$$

Then $\overline{\beta_p}$ can be defined to be equal to the spatial average of β_p for the entire flame. This quantity, $\overline{\beta_p}$, can have any value from 0 to 1. The notable values of $\overline{\beta_p}$ are explained as:

$$\overline{\beta_p} = \begin{cases} 1 & \text{if all flamelets are premixed} \\ 0.5 & \text{if all flamelets are fully partially-premixed} \\ 0 & \text{if all flamelets are non-premixed} \end{cases}. \tag{4.13}$$

As a note, the inverse of $\overline{\beta_p}$, the probability for a non-premixed flamelet if a flamelet exists, $\overline{\beta_{np}}$, was not used introduced and will not be discussed in this thesis because the two probabilities must sum to 1. So, $\overline{\beta_{np}}$ would simply be defined as $\overline{\beta_{np}} = 1 - \overline{\beta_p}$.

The degree of partial-premixing in the flame, ϵ_{pp}, can now be defined as:

$$\epsilon_{pp} = \frac{\overline{\beta_p}\left(1 - \overline{\beta_p}\right)}{0.25}. \tag{4.14}$$

As with $\overline{\beta_p}$, ϵ_{pp} can have any value from 0 to 1. It is obvious from Eq. (4.14) that the notable values of ϵ_{pp} can be explained as:

$$\epsilon_{pp} = \begin{cases} 1 & \text{if all flamelets are fully partially-premixed} \\ 0 & \text{if all flamelets are either premixed or non-premixed} \end{cases} . \qquad (4.15)$$

For case P-1, $\overline{\beta_p} = 0.668$ and $\epsilon_{pp} = 0.887$.

CHAPTER 5

Results & Discussion

5.1 Turbulent Flame Results

The results for the Flame Index Measurement Method on all GTMC cases, in terms of the probability of a premixed flamelet, $\overline{\beta_p}$, and the degree of partial-premixing, ϵ_{pp}, are presented in Table 5.1.

A comparison of the probability for no flamelet, B, for all GTMC cases can be seen in Fig. 5.1. As with the contour map of B for case P-1, described in Section 4.2.2, the contours have been colored with a reverse colormap so that they are darkest where flamelets are more likely to occur. A comparison of the probability for a premixed flamelet, C, for all GTMC cases is shown in Fig. 5.2, and a comparison of the probability for a non-premixed flamelet, A, for all GTMC cases is shown in Fig. 5.3. To emphasize the regions with higher probabilities (or lower, in the case of B) for their particular type of flamelet, the contours in

Table 5.1: Probability of a premixed flamelet if only flamelets are considered, $\overline{\beta_p}$, and degree of partial-premixing, ϵ_{pp}, for all flame conditions studied in the GTMC.

Case	$\overline{\beta_p}$	ϵ_{pp}
M-1	0.663	0.894
P-1	0.668	0.887
P-2	0.694	0.850
P-3	0.733	0.782
S-1	0.663	0.893

Figs. 5.1, 5.2, and 5.3 have been shaded at only the regions with the highest probabilities.

A comparison of the average flame index value, $\langle \xi \rangle$, is shown in Fig. 5.4, while the standard deviation of the PMF with respect to the mean, σ_ξ, is shown in Fig. 5.5. A comparison of the conditional mean flame index, $\langle \xi \mid \xi \neq 0 \rangle$, which ignores times when $\xi = 0$, is shown in Fig. 5.6. As with the contour for case P-1, regions that are, on average, more non-premixed are marked with shades of blue and a hatching of diagonal lines while regions that are, on average, highly premixed are marked with shades of red and a hatching of crosses. Regions that never have a flamelet, which occurs only in cases P-3 and S-1, are marked with dark cyan and a hatching of short horizontal lines. This is done to emphasize the non-premixed and highly premixed regions. Finally, the standard deviation of the probabilities A and C with respect to the conditional mean, $\sigma_{\langle \xi | \xi \neq 0 \rangle}$, is shown in Fig. 5.7. As a note, a contour plot of β_p is not provided because it is identical, in terms of shape, to that of $\langle \xi \mid \xi \neq 0 \rangle$.

From Table 5.1, it appears that both $\overline{\beta_p}$ and ϵ_{pp} do not vary with various fuels. At an air flowrate of $\dot{m}_\mathrm{a} = 300\,\mathrm{g/s}$ and an equivalence ratio of $\phi = 0.75$ (cases M-1, P-1, and S-1), $\overline{\beta_p}$ was 0.66 and ϵ_{pp} was 0.89. Both $\overline{\beta_p}$ and ϵ_{pp} are impacted more by the fuel-air equivalence ratio and possibly the mass flowrate. Higher equivalence ratios and larger mass flowrates appear to result in a shift toward more premixed flamelets. The higher probability of premixed flamelets in case P-3, which had about 60 % of the air mass flowrate of the other cases, appears to suggest that lower flowrates give more premixed flamelets, but the outer air swirler was blocked as well. This means there were two factors changed, and the independent impact of each of them is unknown. More research would need to be conducted to evaluate and quantify the impact of these factors.

It can be seen from Table 5.1 that case P-3 is the most premixed, with 73 % of flamelets being premixed, and therefore least partially-premixed of all the cases with an ϵ_{pp} of 0.78. The attempt to reduce mixing with case P-3 failed, but a result different than the other propane cases was produced anyway. As for why this case is more premixed than the

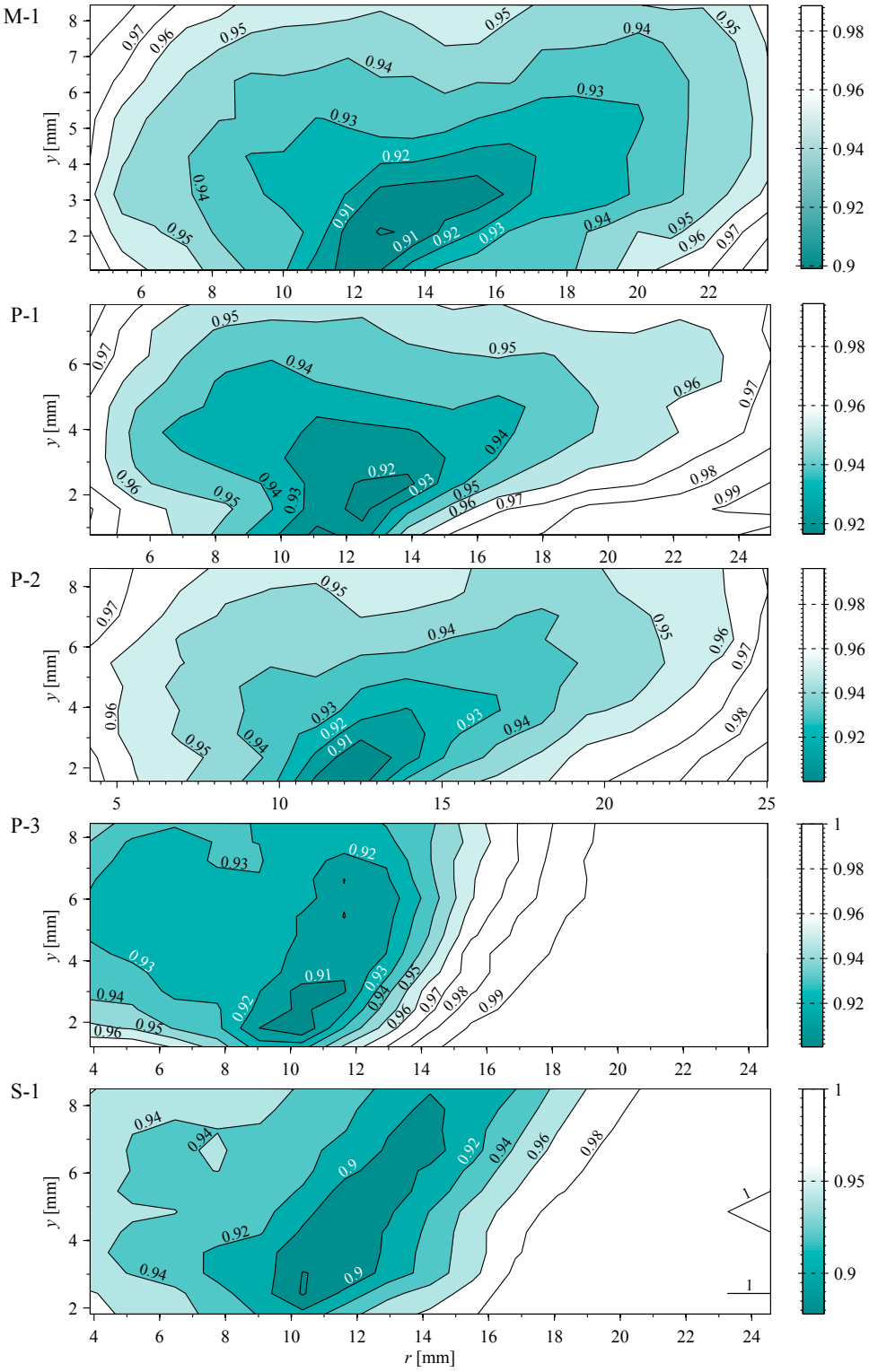

Figure 5.1: Probability that $\xi = 0$ (B) for all GTMC cases.

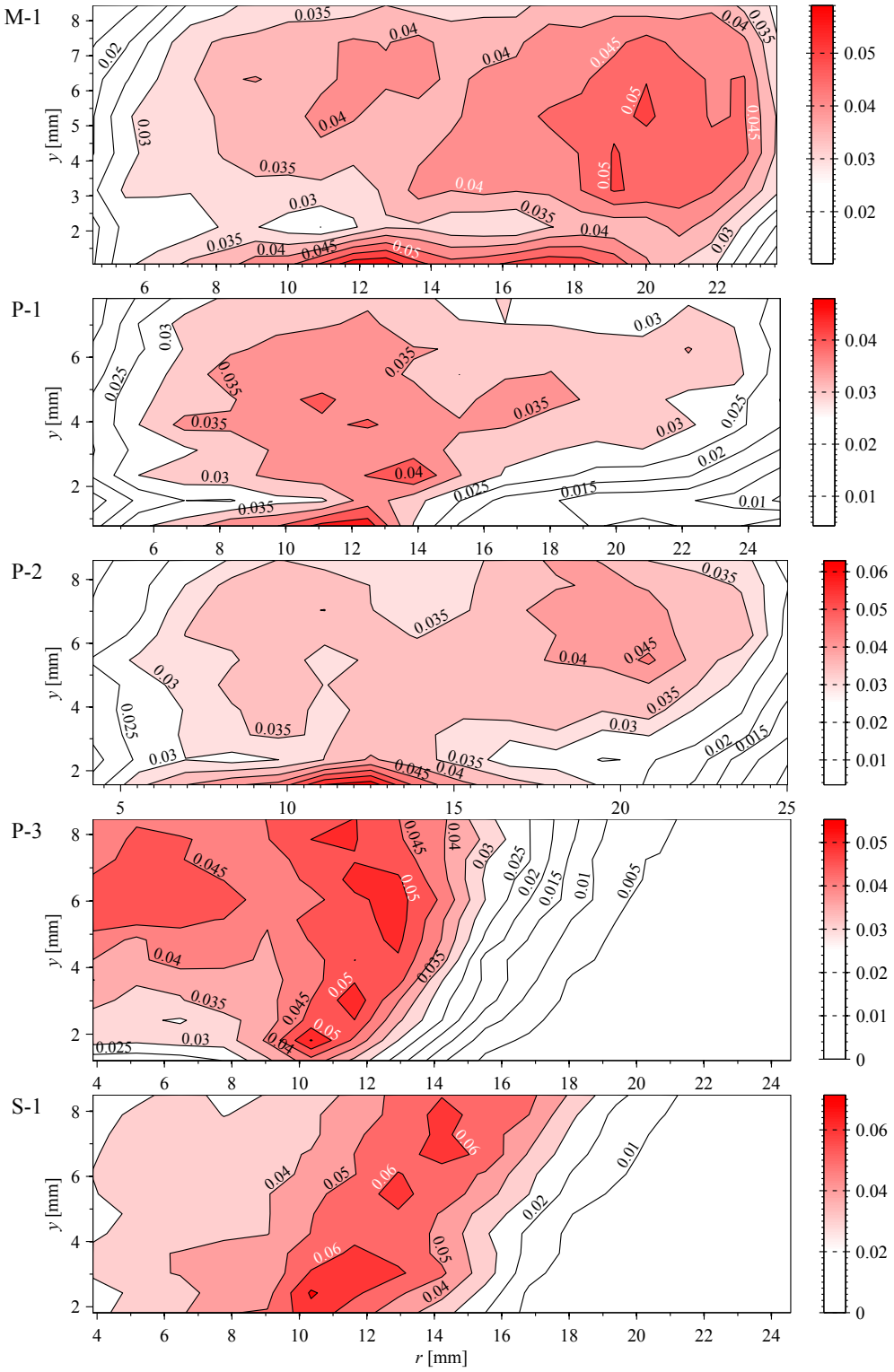

Figure 5.2: Probability that $\xi = +1$ (C) for all GTMC cases.

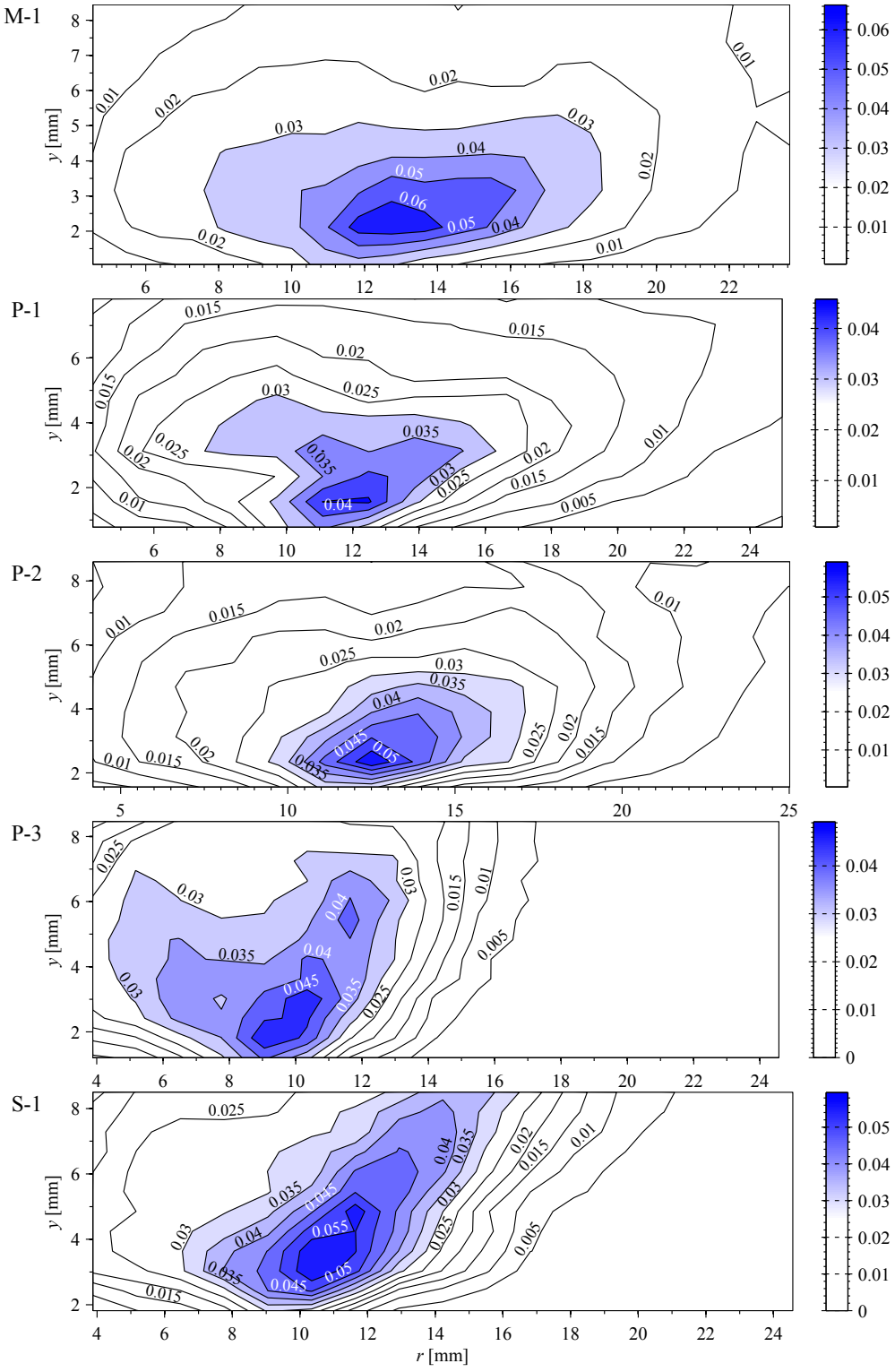

Figure 5.3: Probability that $\xi = -1$ (A) for all GTMC cases.

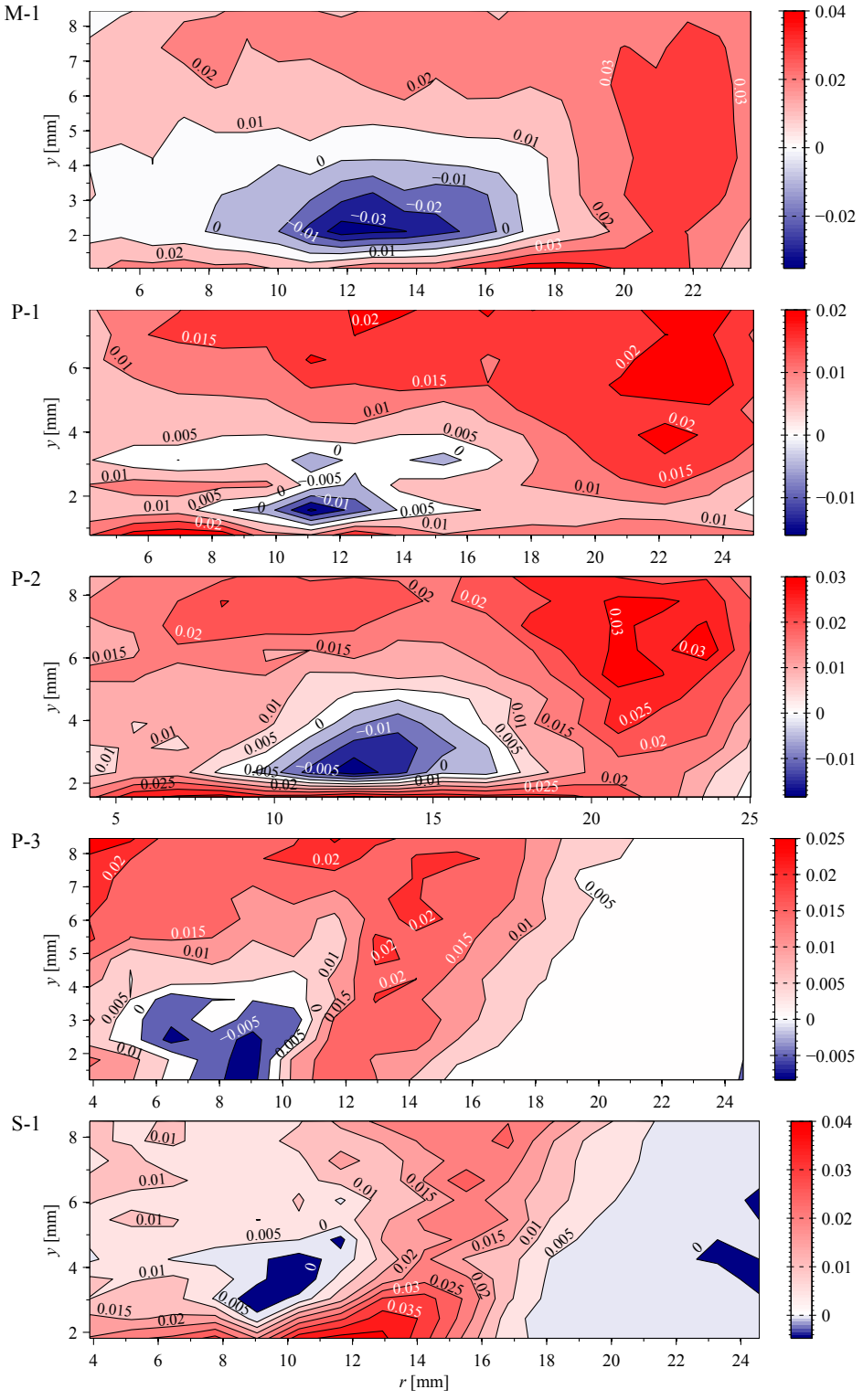

Figure 5.4: Average flame index, $\langle \xi \rangle$, for all GTMC cases.

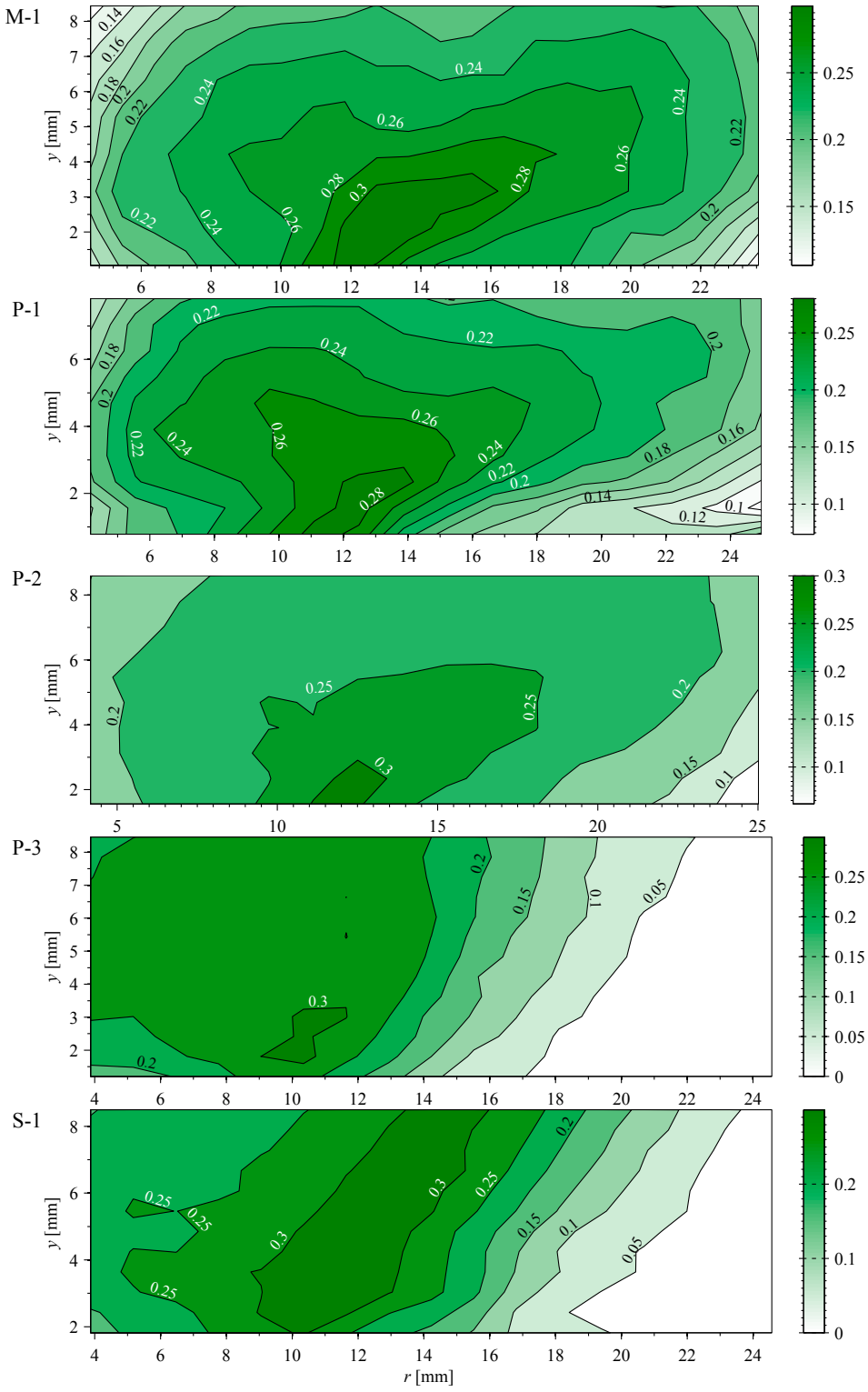

Figure 5.5: Standard deviation, σ_ξ, contours for all GTMC cases.

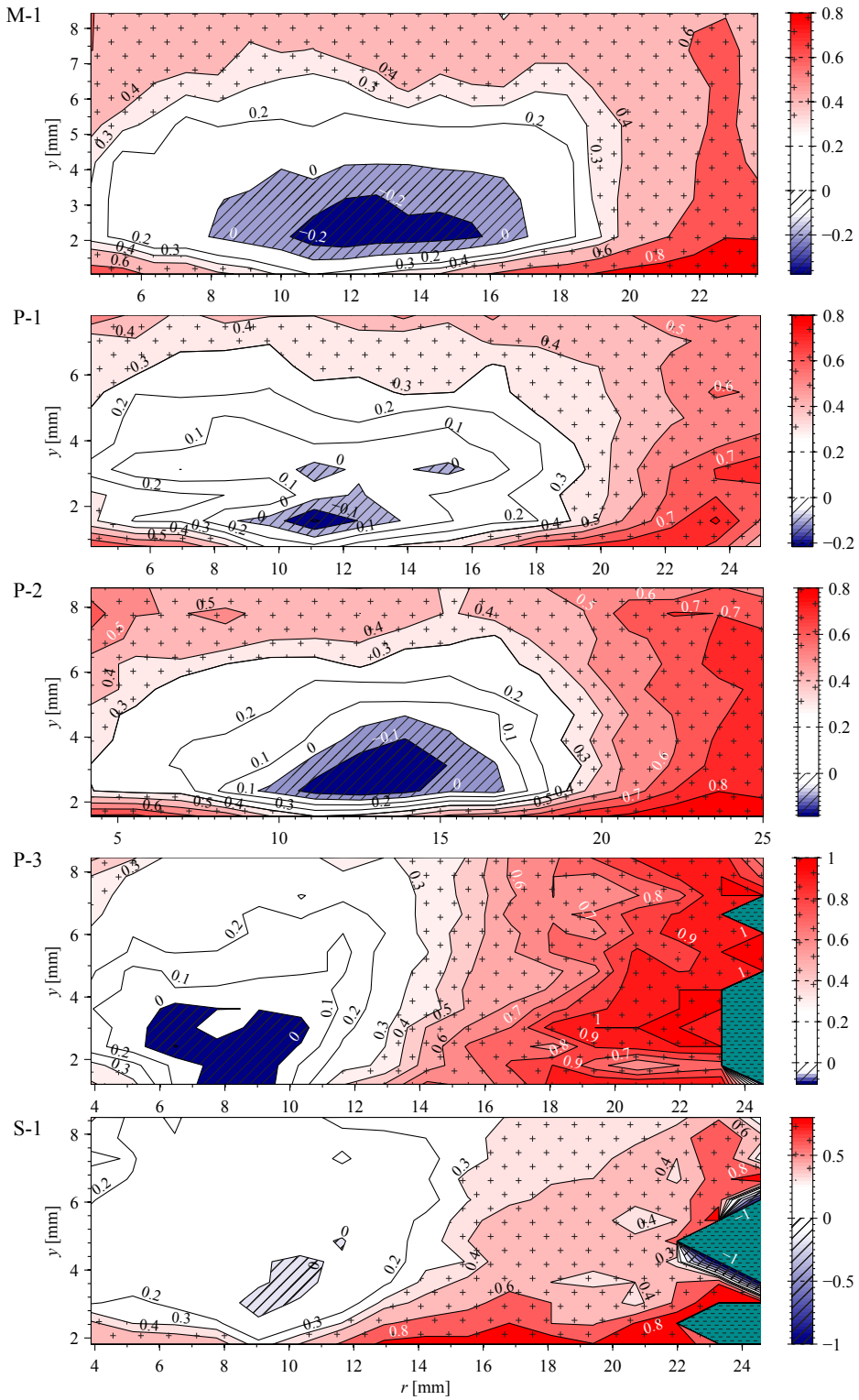

Figure 5.6: Conditionally averaged flame index, $\langle \xi \,|\, \xi \neq 0 \rangle$, where locations with no flamelets are ignored, for all GTMC cases. Non-premixed regions are marked with shades of blue and a hatching of diagonal lines while highly premixed regions are marked with shades of red and a hatching of crosses. Regions that never have a flamelet are marked with dark cyan and a hatching of short horizontal lines.

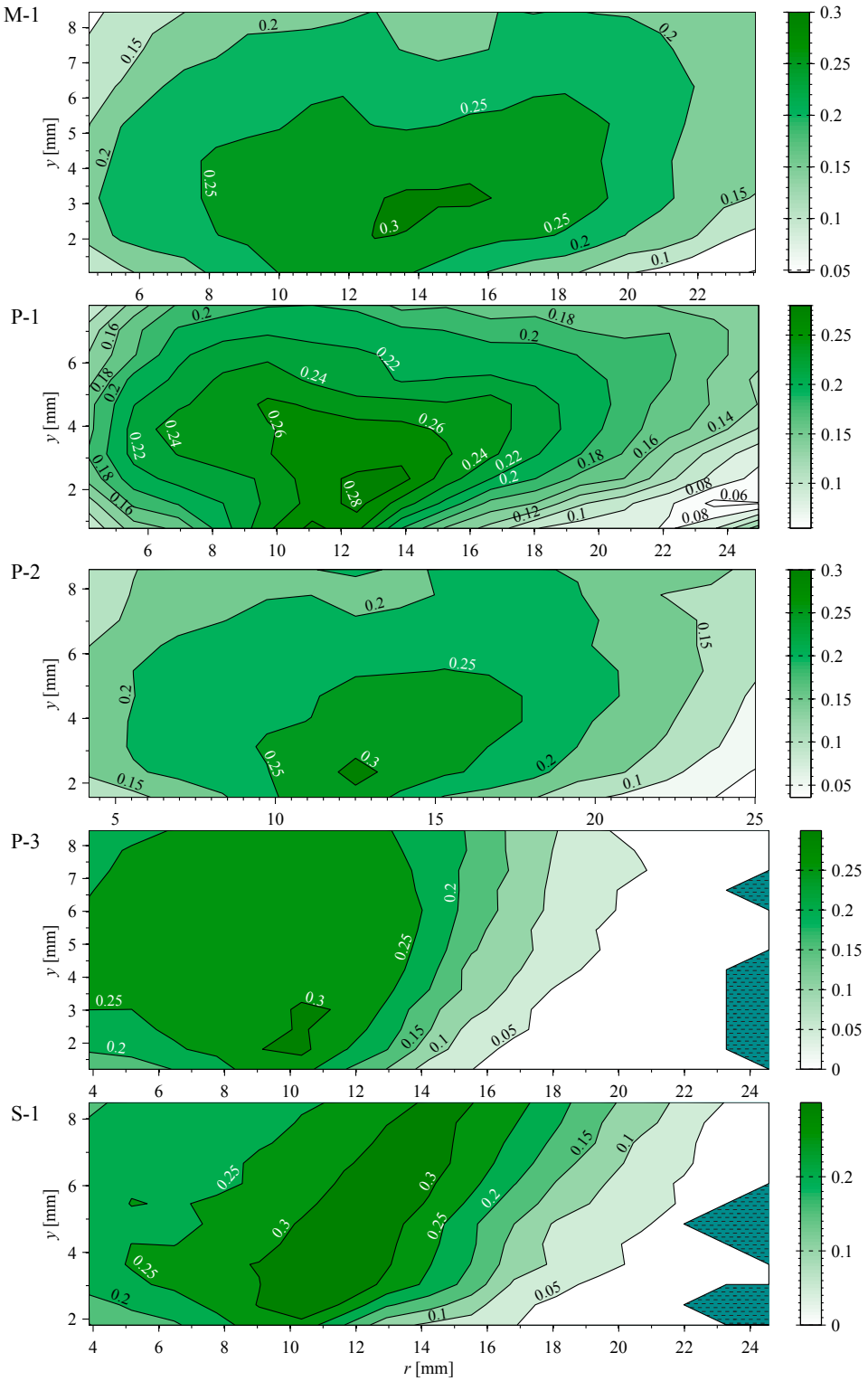

Figure 5.7: Conditional standard deviation, $\sigma_{\langle\xi|\xi\neq 0\rangle}$, contours for all GTMC cases. Regions that never have a flamelet are marked with dark cyan and a hatching of short horizontal lines.

others, there are several possible explanations. Looking at the probability of B in Fig. 5.1 it can be seen that the likelihood of a flamelet decreases (B increases) as one looks further away from the center of the GTMC, which is located at $r = 0\,\text{mm}$. This occurs for all cases, but it occurs most quickly for case P-3. In the binned PMF, most cases have a maximum B of nearly 1, but don't actually get there. Only in cases P-3 and S-1 are there super-pixels that never contain a flamelet. (In the unbinned PMFs, all of the cases have pixels that never contain a flamelet, typically near the edges of the frame.) The smaller, V-shaped flame in case P-3 may be caused by the same phenomena that drive an increase in the proportion of premixed flamelets. However, this is unlikely because while the flame in case S-1 is only slightly larger than that of case P-3, case S-1 does not have a slightly higher proportion of premixed flamelets. In fact, case S-1 isn't even the next most premixed case, it is tied with case M-1 for the lowest proportion of premixed flamelets.

The smaller size of the flames in cases P-3 and S-1 can also been seen by comparing the average flame index, shown in Fig. 5.4, with the conditionally averaged flame index, shown in Fig. 5.6. The region from $r = 15\,\text{mm}$ for case P-3, and $r = 17.5\,\text{mm}$ for case S-1, to distances farther from the center of the GTMC has a $\langle\xi\rangle$ of nearly zero, but the same regions have other values for $\langle\xi \mid \xi \neq 0\rangle$. In addition, the standard deviation of the average flame index, σ_ξ in Fig. 5.5 is smallest in these regions. All of this suggests that these regions very rarely contained flamelets, and averaged to zero in Fig. 5.4 not because there were equal instances of premixed and non-premixed flamelets, but because the instances of no flamelets overpowered the average. The low σ_ξ further suggests that ξ didn't vary much in this region, so it must have been predominantly $\xi = 0$. In addition, the scalloping of the contour lines in the conditional average, Fig. 5.6, in this region for case P-3 especially suggests that $\langle\xi \mid \xi \neq 0\rangle$ changes value rapidly because it is based on very little data, meaning flamelets were rare in this region.

A comparison of the conditionally averaged contours, $\langle\xi \mid \xi \neq 0\rangle$, can be seen in Fig. 5.6. It can be seen that in most cases, a *bubble* of higher likelihood for non-premixed flamelets

exists lifted off of the injector face from $r = 8$ mm to 17 mm and from $y = 1.5$ mm to 4.5 mm, with some variations from one case to the other, except for case P-3. This bubble tends to be surrounded by a ring where the probabilities of premixed and non-premixed flamelets are equal, and outside this ring flamelets are more likely to be premixed. The GTMC is known to have combustion instabilities that resonate from 250 Hz to 480 Hz, depending on the air mass flowrate, the equivalence ratio, and the fuel being used. In addition, the GTMC being a swirl-stabilized burner means that it exhibits a Precessing Vortex Core (PVC) [78]. The flow in the GTMC is known to resonate axially at 515 Hz [79]. Coupled with the instabilities are large-scale fluctuations in the flame shape and liftoff height. The liftoff height can vary such that the base of the flame lies below or up to 8 mm above the injector face. As the liftoff height oscillates, the fuel-air residence time between the injector nozzle and flame-base also varies. This fluctuation in residence time may result in various degrees of premixedness. In addition to changes in flame location, velocity fluctuations near the injector nozzle can alter the mixing mechanics of the combustor such that the flame index can drastically shift in time around this region.

Unlike the other cases, case P-3 does not exhibit this non-premixed bubble. Allison et al. [50] showed that at low flowrates, like the flowrate used in case P-3, the amplitude of the instability is about 100 times smaller than that of the other cases. That case P-3 is non-resonating is confirmed by the average and conditionally averaged flame indices, Figs. 5.4 and 5.6, which show a non-premixed region sitting from the bottom of the camera's field of view up to $y = 4$ mm. This non-premixed region appears to be attached to the injector face, or sits much closer to it than in the other cases. This could be another reason case P-3 is the most premixed of the cases, there may be more non-premixed flamelets below the camera's field of view that could not be captured as the outer air nozzle on the GTMC obscures the fuel injector nozzle.

Some cases, like case S-1, do not exhibit strong regions of non-premixed flamelets, except for the region from $r = 22$ mm to 25 mm, but this is most likely due to the flame

being smaller, so very few flamelets were observed in that region. Thus when a few non-premixed flamelets occurred, they dominated the average.

5.2 Uncertainty

Two kinds of uncertainties are present in this, and any experiments. Random, or statistical, uncertainty is the sort of variation that gives a scatter to repeated measurements. The more measurements taken, the lower the random uncertainty will be. Systematic, or bias, uncertainty is the offset between a measured value and the true value, due to imperfect measurement instruments. Systematic uncertainty is independent of the number of measurements, and can only be reduced by better calibration of the instruments. These uncertainties then are important in two kinds of measurements in this dissertation. The first kind is quantifiable measurements, like flowrates, and the second kind is qualitative measurements, like $\overline{\beta_p}$. The uncertainty in quantifiable measurements here typically involved the propagation of uncertainties, where the uncertainty in one measurement is carried over into another, like the uncertainty in $\dot{m}_\mathrm{a}$ and $\dot{m}_\mathrm{f}$, and their impact on the uncertainty in ϕ_global. The evaluation of this propagation of uncertainty was performed as had been described by Wheeler and Ganji [80]. When possible, uncertainties were given to a confidence level of 95 %, and manufacturer-supplied uncertainties were assumed to be at the same level.

5.2.1 Flowrates

A table of the uncertainties involved in the flow conditions of the experiments is presented in Table 5.2. These conditions were all based off of single measurements, so the only statistical uncertainties were involved in the manufacturer's specified uncertainties.

The uncertainty determination began with the equation for the mass flowrate through a

Table 5.2: Flame conditions with uncertainties. NO_2 and acetone mass fractions are given for the pure fuel and pure air streams. The syngas mixture had an H_2 mole fraction of $\chi_{H_2} = 0.250 \pm 0.074$ and a CO mole fraction of $\chi_{CO} = 0.750 \pm 0.005$.

Case	$\dot{m}_a$, g/min	$\dot{m}_f$, g/min	ϕ_{global}	$Y_{NO_2} \times 10^{-3}$	$Y_{acetone}$
L-1	3.23 ± 0.30	0.28 ± 0.45	1.17 ± 2.39	3.335 ± 0.067	0.441 ± 0.830
L-2	7.71 ± 0.41	1.38 ± 0.65	2.42 ± 2.25	8.003 ± 0.161	0.443 ± 0.378
M-1	303.89 ± 2.73	17.44 ± 2.35	0.76 ± 0.12	7.791 ± 0.090	0.488 ± 0.068
P-1	299.61 ± 2.34	16.91 ± 1.91	0.77 ± 0.10	8.091 ± 0.081	0.269 ± 0.046
P-2	301.78 ± 2.35	26.57 ± 2.22	1.21 ± 0.11	8.116 ± 0.082	0.263 ± 0.031
P-3	172.53 ± 1.53	14.99 ± 2.43	1.20 ± 0.21	8.078 ± 0.081	0.252 ± 0.059
S-1	304.02 ± 2.37	36.71 ± 1.01	0.65 ± 0.02	8.078 ± 0.081	0.349 ± 0.011

choked-flow orifice:

$$\dot{m} = C_d A p \sqrt{\frac{\gamma}{\frac{R_u}{M_i} T} \left(\frac{\gamma}{\gamma + 1} \right)^{\frac{\gamma+1}{\gamma-1}}}, \tag{5.1}$$

where C_d is the orifice discharge coefficient, determined through manufacturer-supplied flowrates; A is the area of the orifice and is dependent on the orifice diameter d; p is the upstream pressure; γ is the ratio of specific heats, and was assumed to be γ_{air}, 1.4, for all cases; R_u is the universal gas constant; M_i is the species molecular weight; and T is the upstream temperature. From this, the uncertainty in $\dot{m}$ is determined by:

$$w_{\dot{m}} = \sqrt{\left(\frac{\partial \dot{m}}{\partial C_d} w_{C_d} \right)^2 + \left(\frac{\partial \dot{m}}{\partial d} w_d \right)^2 + \left(\frac{\partial \dot{m}}{\partial p} w_p \right)^2}, \tag{5.2}$$

where w_i is the uncertainty in quantity i. The partial derivatives are called the sensitivity coefficients. In the case of the air flowrate, the uncertainty in the molecular weight of the air/NO_2 mixture was considered as well, because this varied with the NO_2 concentration.[1] The temperature of the gas upstream of the orifice was not measured, and was assumed to be 300 K. If the uncertainty in this temperature is considered to be ±2.5 K, then the uncertainty in temperature accounts for only 1 % of the overall mass flowrate uncertainty.

[1] The manufacturer-reported NO_2 concentration in the gas bottles ranged from 4900 ppm to 5100 ppm, with an uncertainty of ±2 %.

So the uncertainty in temperature was not considered. The uncertainties in $\dot{m}$ would then be carried over into the various other calculations to determine the conditions of the flow. The only other measurement uncertainty considered was the temperature of the acetone bubbler (± 0.05 K).

The largest contributor to the uncertainties in the flowrate, acetone concentration, and ϕ, was the uncertainty in the diameter of the flow-controlling orifices. The manufacturer specified the uncertainty as ± 0.0005 in, which was not a big problem for the GTMC cases, but the fuel orifices in case L-2 had diameters of 0.0039 in, and in case L-1 the fuel orifices had diameters of 0.002 in, making $w_{\dot{m}}$ very large compared to $\dot{m}$. The significance of $\left(\frac{\partial \dot{m}}{\partial d} w_d\right)$ could vary widely with the flowrate and size of the orifice, but frequently accounted for at least 75 % of the total uncertainty in the flowrate, and could account for over 99 % of the uncertainty in some cases, like in the CH_4 flowrates in case M-1. The need to split the fuel line into two lines—one going through the acetone bubbler, and one as a dilution bypass—likely contributed to higher uncertainties. The uncertainties in cases L-1 and L-2 are high largely because of manufacturer-specified uncertainties in the orifice size. This uncertainty is a bias uncertainty, so while the exact flowrates are not known, the conditions are repeatable, with the same equipment.

5.2.2 Flame Index

There are several possible sources for uncertainty in the flame index measurement. The quantifiable uncertainty was the random uncertainty, which is presented for $\overline{\beta_p}$ and ϵ_{pp} in Table 5.3. As before, these uncertainties are determined for the unbinned ξ data. The uncertainties for the PMF of ξ with respect to the average flame index, $\langle \xi \rangle$, and conditionally averaged flame index, $\langle \xi \mid \xi \neq 0 \rangle$, are shown in Figs. 5.8 and 5.9. These uncertainties were determined to a 95 % confidence level through the equation:

$$P_{\bar{x}} = t \frac{\sigma_x}{\sqrt{N}}, \tag{5.3}$$

Table 5.3: Probability of a premixed flamelet if only flamelets are considered, $\overline{\beta_p}$, and degree of partial-premixing, ϵ_{pp}, for all flame conditions studied in the GTMC, along with uncertainties to a 95 % confidence level.

Case	$\overline{\beta_p}$	ϵ_{pp}
M-1	0.6628 ± 0.0023	0.8940 ± 0.0030
P-1	0.6683 ± 0.0020	0.8866 ± 0.0027
P-2	0.6935 ± 0.0022	0.8502 ± 0.0033
P-3	0.7332 ± 0.0027	0.7824 ± 0.0050
S-1	0.6632 ± 0.0027	0.8935 ± 0.0035

where $\overline{x}$ is the mean of random variable x which has been sampled several times, $P_{\overline{x}}$ is the random uncertainty of that mean, σ_x is the standard deviation of the values of x, N is the number of data sets, and t is the Student's t-value. The t-value is determined from a lookup table based on the confidence level ($\alpha = (1 - 0.95)$ for a 95 % confidence level), and degrees of freedom ($\nu = N - 1$). For values of ν that are 30 or less, t is determined from a lookup table to be 2.042, or more for smaller values of ν. If ν is greater than 30, it is essentially infinite and $t = 1.960$. For all cases where ξ was measured, ν was more than 30. For many of the data sets other than ξ—like the fluorescence linearity and saturation studies—x was actually a mean value determined for each image frame from a data set, and $\overline{x}$ was the mean of that mean. This means that σ_x was not the standard deviation of all pixels in the entire data set, but the standard deviation of the mean fluorescence signal for each frame.

It can be seen, in Table 5.3, that the uncertainty in both $\overline{\beta_p}$ and ϵ_{pp} is fairly low at ±0.4 % or less for $\overline{\beta_p}$, and ±0.6 % or less for ϵ_{pp}. The uncertainties are so low most likely as a result of the large number of images taken for each data set (450 frames). As a conservative estimate, each super-pixel may contain 100 pixels for each frame (it was usually higher, as high as 150 pixels), and there were 450 frames. This gives 45 000 pixels in a conservatively estimated super-pixel. If a conservative estimate is made that 4 % of those pixels contain a flamelet, that gives 1800 pixels from which to determine β_p. If the matrix of β_p values is 10×15, then $\overline{\beta_p}$ is determined from 270 000 pixels. This is a fairly large sample size.

Of course, the values for $\overline{\beta_p}$ reported in this dissertation were based off of the unbinned $\boldsymbol{\xi}$ matrix, so while each β_p was based off of fewer data points (450), there were many more samples of β_p that were used to calculate $\overline{\beta_p}$. For example, in case P-1, the $\boldsymbol{\xi}$ matrix was 95×256 pixels and 450 frames, if the same estimate of 4 % of those pixels contain a flamelet is made, this gives just under 438 000 pixels from which to determine $\overline{\beta_p}$. Again, a very large sample size.

It is the normalization of σ_x by $\sqrt{N}$ that gives uncertainties in the average and conditionally averaged ξ that look different from the standard deviation contours shown in Figs. 5.5 and 5.7. N is constant for all super pixels in a given data set for $\langle \xi \rangle$, but the number of instances of no flamelet varies from super-pixel to super-pixel, so N varies for $\langle \xi \,|\, \xi \neq 0 \rangle$. Like with $\overline{\beta_p}$ and ϵ_{pp}, the uncertainties in $\langle \xi \rangle$ and $\langle \xi \,|\, \xi \neq 0 \rangle$ are so low primarily due to the large number of image pairs.

5.2.2.1 Sources of Uncertainty

The Flame Index Measurement Method has several sources of uncertainty. The quantifiable uncertainty, which has been described above, is relatively insignificant. The more significant, and more difficult to quantify, uncertainties are those that are associated with how well the NO_2 and acetone track the fuel and O_2. This uncertainty could be quantified, and it would depend on the strain rate and equivalence ratio of a particular flamelet, but these quantities vary from flamelet to flamelet so the accuracy cannot be higher than what was presented in Table 3.1. The other significant uncertainty is a result of the flamelet search, described in Section 4.2, that is impacted largely by factors which may do one of two things: make the edge detection more difficult, or change the gradients in the PLIF images. The SNR for both PLIF images would be the major factor in both of these, although the intent of the binning and filtering was to reduce the impact. Poor SNR could lead to either falsely detected edges (which may lead to non-zero values of ξ where it should be zero), or edges that are not detected even though a flamelet exists nearby. It is possible

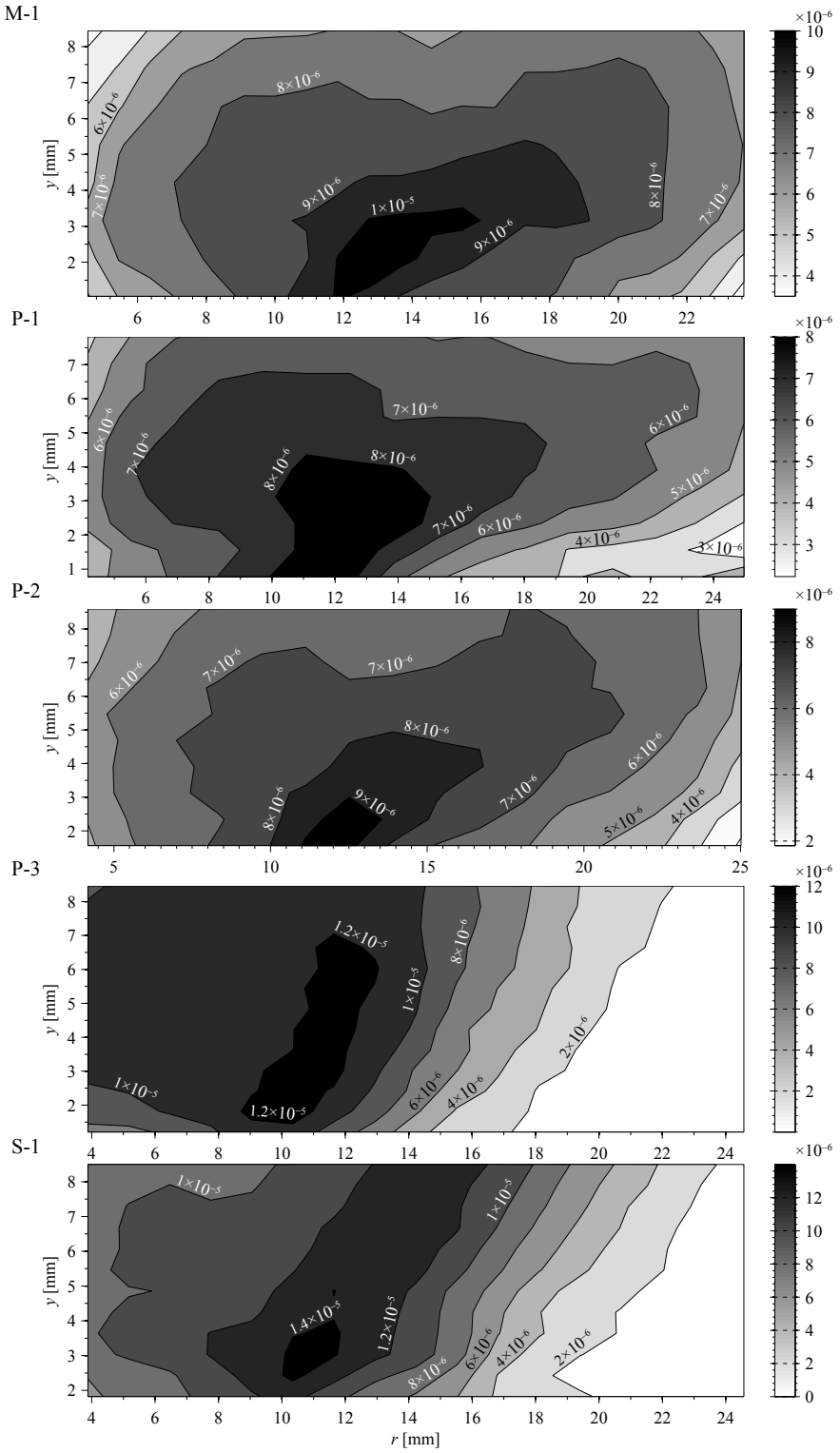

Figure 5.8: Statistical uncertainty of the average flame index, $\langle \xi \rangle$ for all GTMC cases, to a 95 % confidence level.

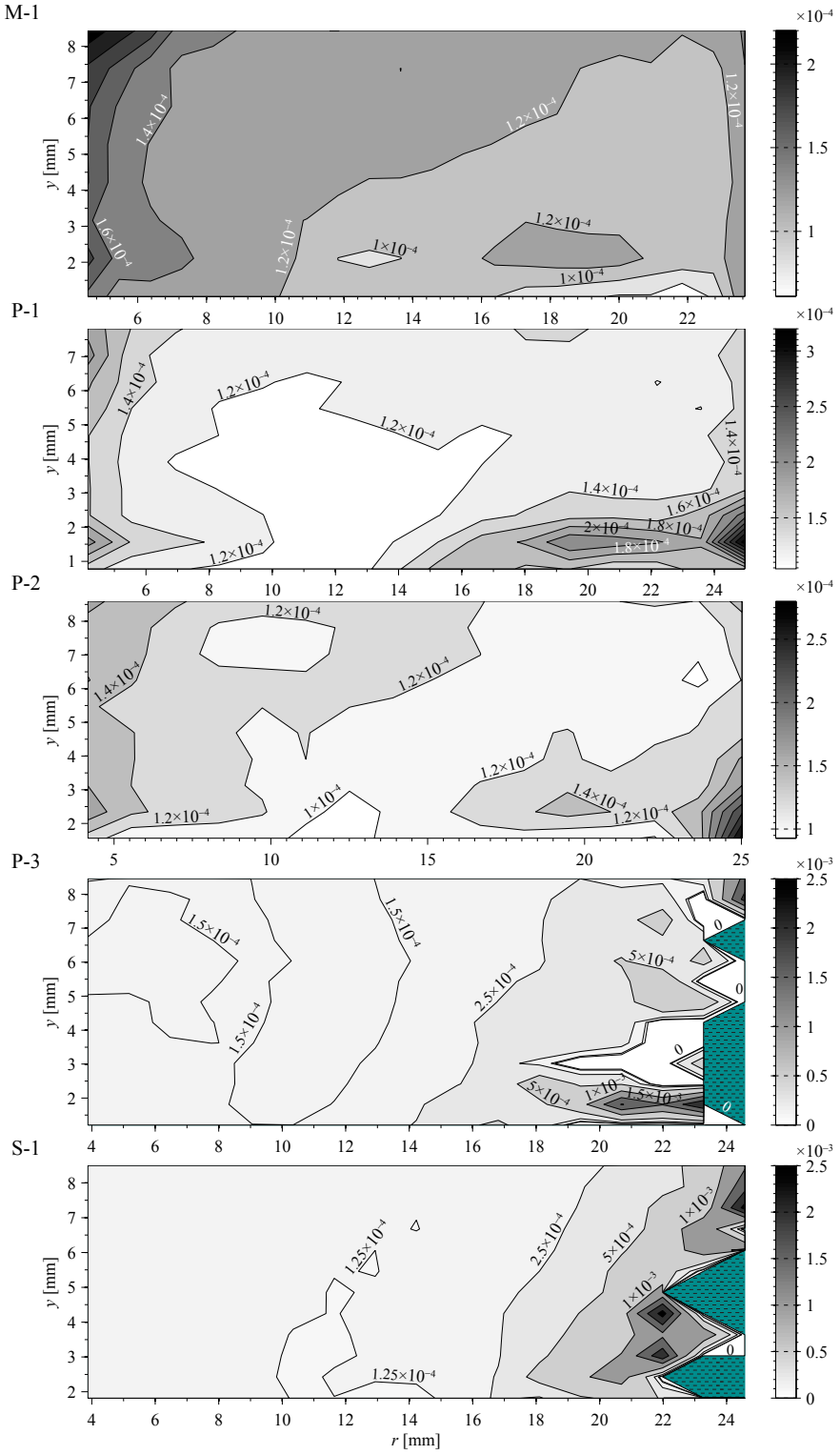

Figure 5.9: Statistical uncertainty of the conditionally averaged flame index, $\langle \xi \,|\, \xi \neq 0 \rangle$, which ignores locations with no flamelets for all GTMC cases, to a 95 % confidence level. Regions that never have a flamelet are marked with dark cyan and a hatching of short horizontal lines.

that the binning and filtering resulted in some edges that were not detected, although this was likely rare due to the low binning and filtering amounts. In addition, the NADF was designed specifically to prevent the loss of edges in the filtered image. These uncertainties are expressed as the uncertainty in the validity of Eq. (1.5), which relates the LIF-based flame index to the true flame index.

Many of the uncertainties in the FIMM could be evaluated through a careful analysis of the laminar cases L-1 and L-2. The frequency with which the FIMM either detects a flamelet where none exist or doesn't detect a flamelet where one does exist would provide some insight into the uncertainties of the FIMM. An even better uncertainty determination method would be to compare the results of the GTMC cases to a Direct Numerical Simulation (DNS) model of the GTMC. Using the DNS data, the accuracy of the FIMM could be determined both with respect to flamelets being detected when they do not exist and flamelets going undetected when they do exist, but also with respect to how well the acetone and NO_2 track the fuel and O_2. Unfortunately, no DNS model of the GTMC currently exists. There is, however, a high likelihood that a DNS model of the GTMC will exist in the future. Another possibility would be to use the FIMM on a burner and flame conditions that have been modeled through DNS, such as a jet in cross-flow [81].

Several other uncertainty sources exist as well. The first is the statistical uncertainties described above, which are negligible. This uncertainty depends largely on the number of frames acquired, and enough had been acquired to reduce the statistical uncertainty to a negligible amount. There is also the possibility that flamelets smaller than the resolution of the cameras (about 85 µm/pixel) existed and were not detected. However, this is unlikely because, as was discussed in Section 2.3.2, the premixed flamelets should have been between 350 µm and 600 µm thick, which gives between 4 and 7 pixels across a flamelet. This is further evidence that the binning of the images did not cause some flamelets, which would have otherwise been detected, to go undetected.

There was also some uncertainty in the raw PLIF images that was corrected for with

the background subtraction, laser sheet corrections, and white-field correction. When no corrections to the PLIF images were performed, the quality of the edge detection on the fully processed PLIF images was similar to that of the binned, unfiltered PLIF images—if the uncorrected images were binned and filtered by the same amounts as the corrected PLIF images. This led to contours in the instantaneous $\boldsymbol{\xi}$ images which were speckled with both premixed and non-premixed pixels, as well as random, solitary pixels. The uncorrected instantaneous $\boldsymbol{\xi}$ frame for the example frame from case P-1, used in Chapter 4, is shown in Fig. 5.10 along with the $\boldsymbol{\xi}$ frame originally shown in Fig. 4.11(a), which had image corrections applied. The randomness in the ξ values is primarily a result of the poor edge detection, which itself is a result of the filtering not improving the SNR by as much as it does when image corrections are applied to the PLIF images. The PMFs and both averaged and conditionally averaged ξ contours looked different from that of the versions based off of the corrected PLIF images, but were still sensible.

Finally, there was the uncertainty of what was happening in the regions where $\xi = 0$. It is certain that there are no flamelets in these regions, but there remains the possibility of distributed reactions.

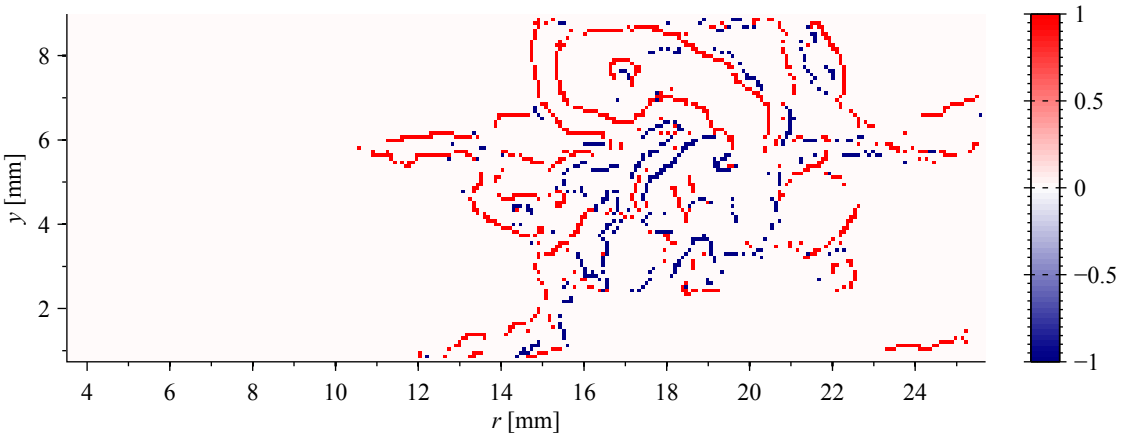

(a) ξ with image corrections applied.

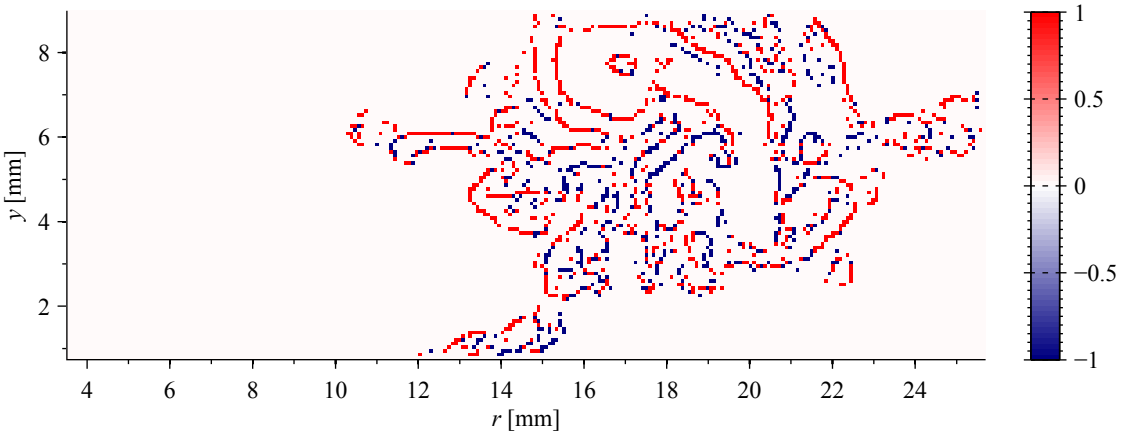

(b) ξ without image corrections applied.

Figure 5.10: Instantaneous images of flame index, ξ, from case P-1 showing the results (a) with and (b) without the application of image corrections. The poor quality of the flame index measurement method with no image corrections is shown and is largely due to the detection of too many false edges. A value of -1 marks a non-premixed flamelet in dark navy blue, and a value of $+1$ marks a premixed flamelet in red.

CHAPTER 6

Summary and Conclusions

6.1 Summary

An effective method by which to measure the flame index (ξ) in partially-premixed, turbulent flames has been described. The development of this method required the use of fuel and O_2 tracers. Acetone was selected as a fuel tracer, and had been used as such by researchers in the past. NO_2 was selected as an O_2 tracer, something NO_2 has not been used for previously. In particular, NO_2 and acetone were used as markers of the O_2 and fuel gradient sign and locations. The performance of both NO_2 and acetone as fluorescence tracers was evaluated through computational models of laminar premixed and non-premixed flames, as well as the application of the Flame Index Measurement Method (FIMM) to laminar premixed and non-premixed flames in a laboratory.

The fluorescence linearity and saturation of NO_2 and acetone were studied with respect to varying laser power and concentration in air, for NO_2, and in CH_4, for acetone. These had been studied previously for NO_2, but not with an the second harmonic of an Nd:YAG laser (532 nm), and not with laser energies as high as was used in this dissertation. The fluorescence linearity and saturation of acetone has been studied previously, and previous results were confirmed.

The experimental setup necessary for the FIMM was described. Of particular importance was the need for a red-sensitive third generation ICCD to capture the NO_2 fluores-

cence signal. An extensive process by which to account for the non-uniformity of the laser sheets, as well as the background signal due to flame luminosity, scattered laser light, and fluorescence from the other tracer gas (i.e., acetone fluorescence observed by the NO_2-sensing camera) was described.

The process by which the acetone and NO_2 PLIF images were processed to improve their Signal-to-Noise Ratio (SNR) was described. This process involved the binning of the images, and the application of a Non-linear Anisotropic Diffusion Filter (NADF). An edge detection algorithm was applied to the PLIF images to determine the locations of the maximum acetone and NO_2 LIF signal gradients.

The flamelet searching method, by which the flame index is determined, and the locations that will be marked with the appropriate values of flame index, was described. The method was necessary because the locations of maximum acetone and NO_2 gradient do not typically overlap. Essentially, the method searches parallel to the acetone signal's gradient vector at detected edges for NO_2 gradient vectors that will indicate the presence of premixed or non-premixed flamelets. The reasoning behind the decision to mark the location half-way between the acetone and NO_2 signal vectors was described as well.

The post-processing of the ξ measurements was described. The creation of Probability Mass Functions (PMFs) for the likelihood of a premixed flamelet, a non-premixed flamelet, and no flamelet were described. A conditional average flame index, $\langle \xi \,|\, \xi \neq 0 \rangle$, was introduced, where locations without flamelets were ignored, in order to provide statistics for when a flamelet exists. Two new quantities were introduced based on this condition. The quantity $\overline{\beta_p}$ is the average probability, for an entire data set, that a flamelet is premixed if a flamelet is present. So, $\overline{\beta_p} = +1$ if all flamelets are premixed, 0.5 if all flamelets are fully partially-premixed (meaning they are premixed just as often as they are non-premixed), and 0 if all flamelets are non-premixed. The degree of partial-premixing, ϵ_{pp}, is a re-normalization of $\overline{\beta_p}$ to simplify it somewhat. The quantity ϵ_{pp} is defined such that it only indicates if all flamelets are fully partially-premixed ($\epsilon_{pp} = 1$) or are entirely premixed or

non-premixed ($\epsilon_{pp} = 0$), but doesn't say whether the flame is leaning more toward premixed or non-premixed flamelets.

Finally, the Flame Index Measurement Method was demonstrated on a co-annular dual-swirl burner, the GTMC. The results were presented for five separate cases with various fuel, flow rates, and fuel-air equivalence ratios. The uncertainties in the method were discussed as well.

6.2 Conclusions

It has been shown that for both laminar and turbulent combustion, NO_2 is an acceptable tracer of O_2, and reliably indicates the location and direction of O_2 gradients in the flame. Three criteria for an acceptable tracer of O_2 gradients were defined: that the spatial gradients of the tracer and O_2 mass fractions are of the same sign, that the tracer is not created in the flame, and that the separation distance between the locations of maximum gradients in the tracer and O_2 mass fractions, δ_{NO_2,O_2}, is no greater than 1.0 mm. The NO_2 tracer meets all three criteria.

When excited by a 532 nm laser beam, NO_2 fluoresces from 550 nm to wavelengths longer than 800 nm. Most ICCDs have a low quantum efficiency in this regime, so a third-generation red-sensitive ICCD was needed to observe the fluorescence.

The linearity and possible saturation of NO_2 fluorescence were studied for laser spectral irradiance values that are several times that of previous studies. NO_2 fluorescence was found to be linear with respect to variations in concentration from 0 ppm to 5000 ppm in air. NO_2 fluorescence was found to be a linear function of spectral irradiance up to 250 MW/(cm^2 cm^{-1}) where it started to saturate, and then began to increase linearly again at 850 MW/(cm^2 cm^{-1}). In between there was an unexpected dip in the LIF signal at around 750 MW/(cm^2 cm^{-1}), which has not been observed before because spectral irradiances this high have not been used in the past. The increase in the LIF signal around

850 MW/(cm^2 cm^{-1}) may be due to multiphoton excitation of NO_2 or photodissociation of NO_2 into vibrationally excited O and NO, and the subsequent fluorescence of the fragments. Due to the unexpected dip around 750 MW/(cm^2 cm^{-1}), it is not recommended to operate above 450 MW/(cm^2 cm^{-1}) until the dip is explained, which will require further research. NO_2 was, however, found to respond linearly to variations in the NO_2 concentration in air, as previous studies had shown with different excitation wavelengths (532 nm in this dissertation, 488 nm in the previous study). Acetone fluorescence was studied as well, and was found to respond linearly with respect to both laser energy and concentration, as previous studies have shown.

A method has been developed for measuring the flame index in turbulent, partially-premixed flames, and was demonstrated on a turbulent flame. The method utilized acetone and NO_2 PLIF to indicate the sign and locations of fuel and O_2 gradients.

When defining the method, it was found that a Non-linear Anisotropic Diffusion Filter was ideal to maintain the locations of maximum signal gradients, for better detection by an edge detection algorithm. After processing the images through binning and filtering to ensure accuracy of the Flame Index Measurement Method, a good SNR of 24 was achieved for the acetone PLIF images, and an SNR of 13 was achieved for the NO_2 PLIF images.

It was also found during the flamelet modeling that the locations of the maximum acetone and NO_2 mass fraction gradients would never overlap for non-premixed flamelets, and would occasionally overlap for premixed flamelets. A flamelet searching method was developed as a result of this, and it was found that for the most continuous flame index contours, the search from a maximum acetone signal gradient location for the location of a maximum NO_2 signal gradient, Δs, should be limited to 1.0 mm in the direction suggested by the flamelet modeling, and to 0.5 mm in the opposite direction suggested by the modeling. It was also found that marking the pixel half-way between the acetone and NO_2 locations would lead to the most continuous flame index contour lines.

Useful quantities, based on the flame index, have been identified, such as the prob-

abilities for premixed and non-premixed flamelets. A conditional average flame index, $\langle \xi \mid \xi \neq 0 \rangle$, has been defined, which only includes instances where a flamelet exists. Two new quantities—$\overline{\beta_p}$, the probability for a premixed flamelet is a flamelet exists, and ϵ_{pp}, the degree of partial premixing—have been defined as well.

It was found that the particular burner studied, the Gas Turbine Model Combustor (GTMC), was predominantly premixed, with an average $\overline{\beta_p}$ of 0.68, and an average ϵ_{pp} of 0.86. Both $\overline{\beta_p}$ and ϵ_{pp} did not vary between different fuels, at the same flowrate and fuel-air equivalence ratio. At an air flowrate of $\dot{m}_\mathrm{a} = 300\,\mathrm{g/s}$ and an equivalence ratio of $\phi = 0.75$ (cases M-1, P-1, and S-1), $\overline{\beta_p}$ was 0.66 and ϵ_{pp} was 0.89. Higher equivalence ratios and lower mass flowrates appear to result in an increase in the number of premixed flamelets. Although, not much can be said about the impact of the flowrates, because case P-3, which had about 60 % of the flowrate of the other cases, had the outer air nozzle blocked, reducing the swirl in the GTMC, in addition to the lower flowrate.

It was found for all GTMC cases, except case P-3, that the region with a higher probability for non-premixed flamelets existed as a bubble lifted off of the injector face from $r = 8\,\mathrm{mm}$ to $17\,\mathrm{mm}$ and from $y = 1.5\,\mathrm{mm}$ to $4.5\,\mathrm{mm}$, with some variations from one case to the other. This bubble tended to be surrounded by a ring where the probabilities of premixed and non-premixed flamelets were equal, and outside this ring flamelets were more likely to be premixed. The GTMC is known to exhibit combustion instabilities that cause large-scale fluctuations in the flame shape and liftoff height. So, it is likely that this bubble exists in the data because only averaged flame indices were computed. If the flame index measurements were phase-resolved to either the combustion instability or the oscillations due to the PVC, it may be observed that the non-premixed region oscillates both vertically and horizontally.

It was found that the flames in cases P-3 and S-1 were smaller than the other flames, and contained more locations where a flamelet never existed.

6.3 Future Work

While the Flame Index Measurement Method is largely complete, it has not been compared to computationally modeled flame index. Doing so for the GTMC would provide some greater insight into both the combustion properties GTMC and into the uncertainties of the FIMM. Alternatively, the FIMM may be applied to turbulent flames that are easier to model, like a jet-in-crossflow configuration.

Pressure oscillations in the plenum of the GTMC were measured during cases P-1, P-2, and S-1. The intent of this data was to phase-average the flame index to the pressure, and see if there is any relation. Unfortunately the pressure data was extremely noisy, having something to do with the lasers (when the lasers were shut off, the noise stopped). One or more of the cases may be salvageable, so if enough frames were captured in each phase-angle bin, a phase-resolved flame index may explain the mechanisms behind the non-premixed bubble, and provide insight into how the flame index changes with the GTMC's instabilities.

Determining what is happening in the regions where $\xi = 0$ would be interesting. The first step in evaluating this may be the simultaneous measurement of the flame index and the temperature.

APPENDIX A

More Flamelet Modeling Results

For non-premixed and premixed syngas/acetone/air flames, the flamelet modeling results are shown in Figs. A.1 and A.2. The syngas mixture was 20 % H_2 and 80 % CO, by volume. The results are similar to that of the 25 % H_2, 75 % CO syngas mixture, shown in Figs. 3.9 and 3.10. While this syngas mixture was studied computationally, it was never studied experimentally.

Separation distances between the fluorescence tracers and O_2 or the syngas components—$\left(\nabla Y_{NO_2}\right)_{max}$ and $\left(\nabla Y_{O_2}\right)_{max}$, $\left(\nabla Y_{acetone}\right)_{max}$ and $\left(\nabla Y_{CO}\right)_{max}$, and $\left(\nabla Y_{acetone}\right)_{max}$ and $\left(\nabla Y_{H_2}\right)_{max}$—are shown in Table A.1. Again, the results are similar to that of the 25 % H_2, 75 % CO syngas mixture, shown in Table 3.1.

Table A.1: Computed separation distances between the locations of the fluorescence tracers' maximum mass fraction gradients and that of the tracer and fuel or O_2. Determined using CHEMKIN. Premixed flames have the equivalence ratio (ϕ) provided, while non-premixed flames have the strain rate (e) provided provided. Uncertainties are based on the grid size. The syngas mixture was 20 % H_2 and 80 % CO, by volume.

ϕ	e, s^{-1}	δ_{ace,NO_2}, µm	δ_{NO_2,O_2}, µm	$\delta_{ace,f}$, µm	δ_{ace,H_2}, µm
0.75	—	77 ± 19	120 ± 15	194 ± 21	143 ± 21
1.20	—	75 ± 11	113 ± 11	158 ± 14	120 ± 14
—	182	3276 ± 197	750 ± 337	632 ± 198	1421 ± 177
—	435	2290 ± 177	711 ± 112	474 ± 169	987 ± 163

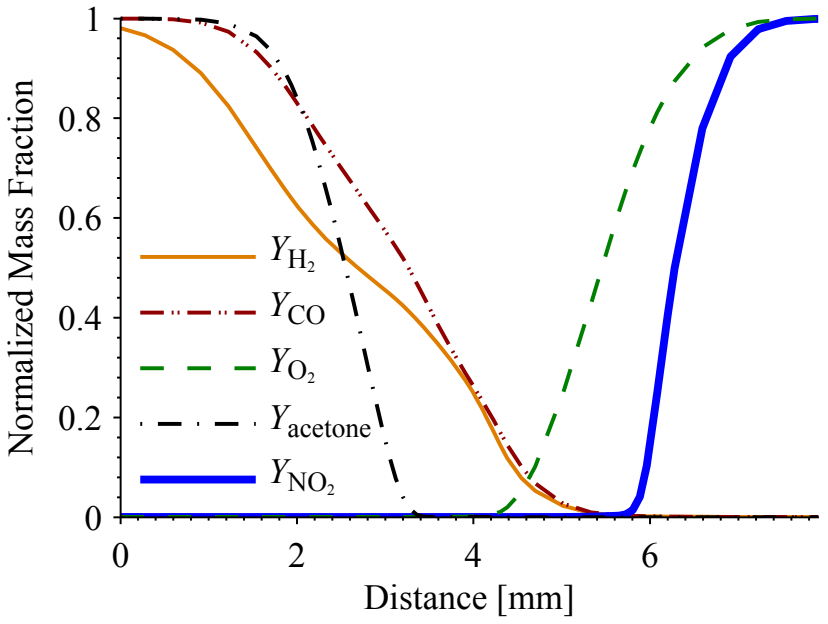

(a) Low strain rate ($e = 180\,s^{-1}$) syngas/acetone/air flame.

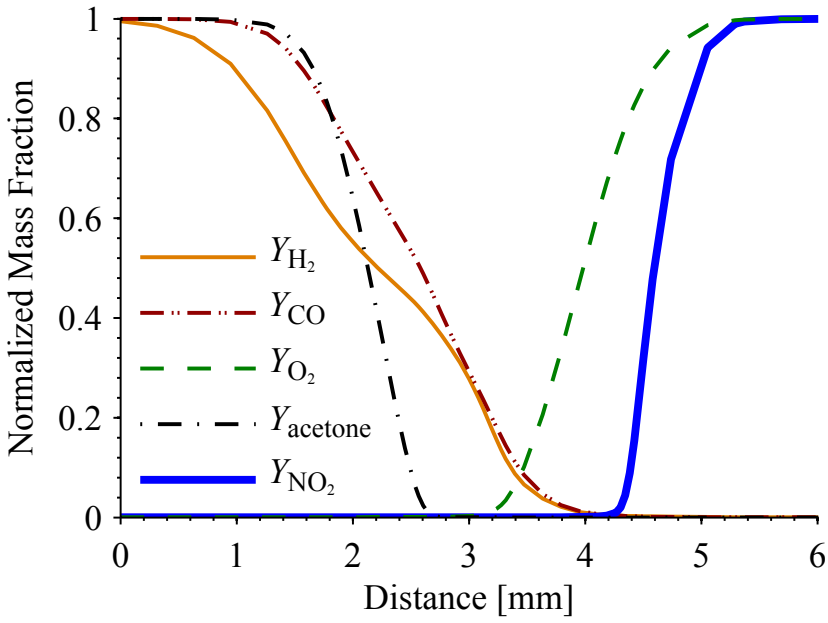

(b) High strain rate ($e = 435\,s^{-1}$) syngas/acetone/air flame.

Figure A.1: Computed fuel and oxidizer, NO_2 and acetone tracer normalized mass fractions showing that NO_2 and acetone are acceptable tracers for O_2 and syngas. Determined using CHEMKIN, for opposed-flow non-premixed syngas/acetone/air flames with NO_2 seeded at 5000 ppm by volume and acetone seeded at 20 % by volume. Shown at (a) a low strain rate of $e = 180\,s^{-1}$ and (b) a high strain rate of $e = 435\,s^{-1}$. The syngas mixture was 20 % H_2 and 80 % CO, by volume.

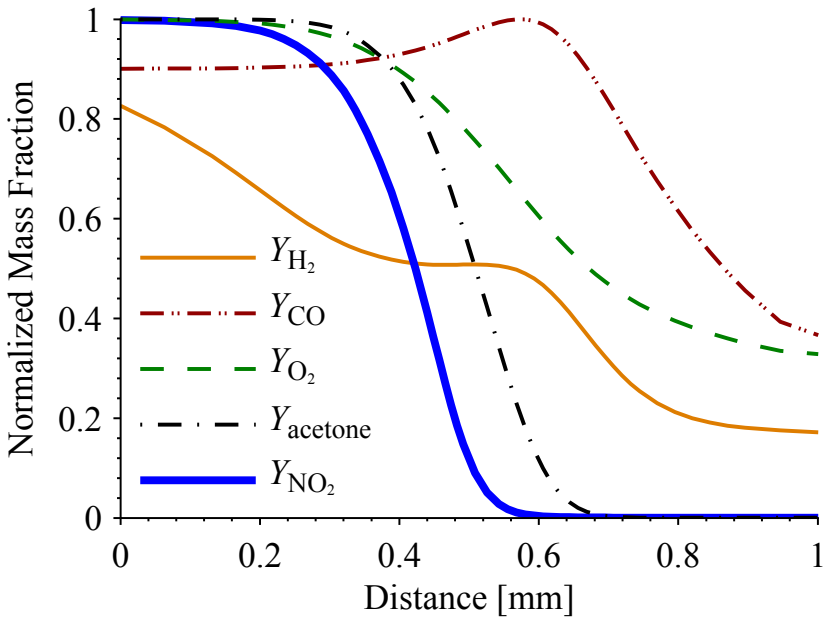

(a) Fuel-lean ($\phi = 0.75$) premixed syngas/acetone/air flame.

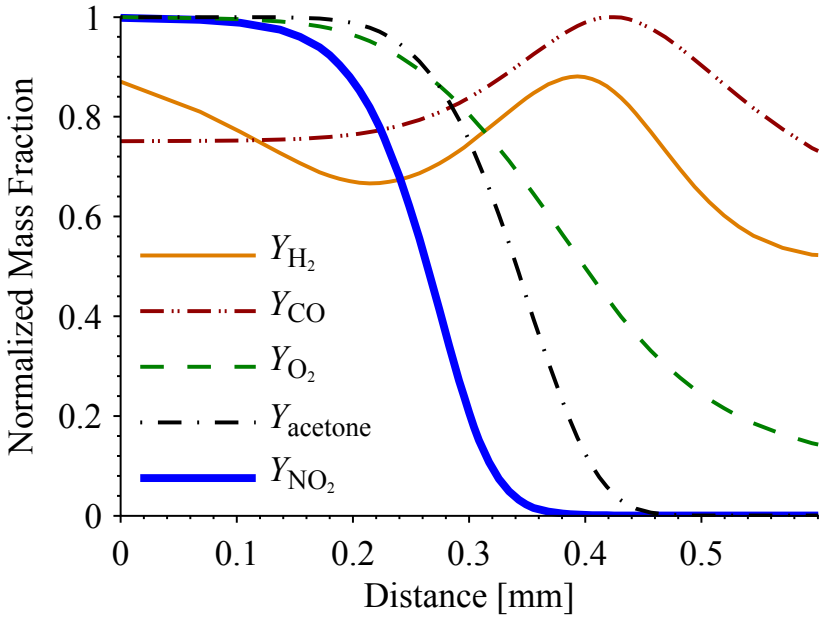

(b) Fuel-rich ($\phi = 1.20$) premixed syngas/acetone/air flame.

Figure A.2: Computed fuel and oxidizer, NO_2 and acetone tracer normalized mass fractions showing that NO_2 and acetone are acceptable tracers for O_2 and syngas. Determined using CHEMKIN, for premixed syngas/acetone/air flames with NO_2 seeded at 5000 ppm by volume and acetone seeded at 20 % by volume, at (a) lean ($\phi = 0.75$) and (b) rich ($\phi = 1.20$) equivalence ratios. The syngas mixture was 20 % H_2 and 80 % CO, by volume.

APPENDIX B

Flamelet Shifting Method

The Flamelet Shifting Method is the failed method that was developed on the enclosed co-flow burner. However, to say that it was a failed method does not provide proper credit to the method. The method provided insight into how to develop the Flame Index Searching Method, described in Section 4.2. The following is an excerpt from a conference paper, written by the author, on the method [82]. The experimental setup and processing of the images (background subtraction only and 8×8 binning) was described previously in Chapter 2. It should be noted that some estimates for values such as laser sheet height, laser energy, or camera resolution have been re-evaluated since this paper was written. The re-evaluated numbers are presented elsewhere in this dissertation.

The paper begins by defining the normalized flame index, Eq. (1.2) in this dissertation, as:

$$\xi = \frac{\nabla Y_{\mathrm{F}} \cdot \nabla Y_{\mathrm{O}}}{|\nabla Y_{\mathrm{F}}|_{\max} \cdot |\nabla Y_{\mathrm{O}}|_{\max}}. \tag{B.1}$$

The following is the description of the image processing and Flamelet Shifting Method.

B.1 Results

B.1.1 Data and Process

The second step of the background removal process was to fit a curve to the remaining section where the signal was not zero at locations where the fluorescing species should not exist. The results of this background removal have

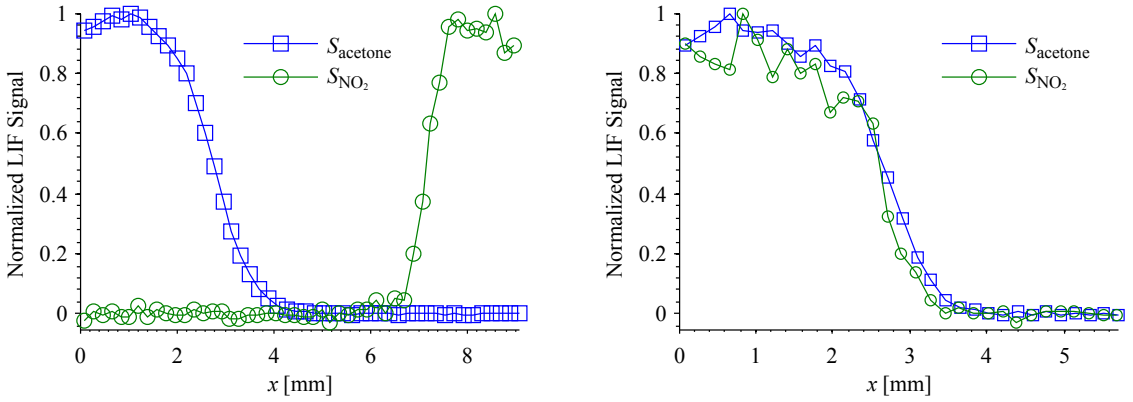

(a) Normalized acetone and NO_2 PLIF signals for a non-premixed flame.

(b) Normalized acetone and NO_2 PLIF signals for a premixed flame.

Figure B.1: Normalized acetone and NO_2 PLIF signals for (a) a non-premixed and (b) a premixed flame.

been normalized and are shown in Fig. B.1(a) for the non-premixed case, and in Fig. B.1(b) for the premixed case.

Gradients of the non-normalized versions of the acetone and NO_2 signals shown in Figs. B.1(a) and B.1(b) were determined with a central differencing method, shown in Figs. B.2(a) and B.2(b). At locations where the signal was less than 5 % of the maximum signal it is known that the tracer gas concentration is negligible, so the gradients in these regions are meaningless and were set to zero. The error bars shown are the errors bounds for a 95 % confidence level due to the uncertainty in the resolution of the images, showing that 8×8 binning is well within the bounds of what would begin to introduce significant error. However, an uncertainty of 5–10 % is acceptable in the present study because the goal is to measure the sign of the flame index, and its absolute value is of lesser importance. It can be observed that there is a significant amount of noise in the NO_2 gradient of the premixed case in the region located where the signal is at its highest. However, this noise has peaks smaller than the maximum peak of the gradient with 8×8 binning.

The next step was to fit a curve to the gradients so they could be shifted and multiplied to find the flame index. In all cases, points were selected that would give the best curve fit, and all curves were third-order polynomials.

In order to multiply the gradients and calculate the flame index, the curves needed to be shifted. The shifting amount was entirely based on whether the flame was premixed or non-premixed. It was decided to shift the gradient curve fits so that the maximum absolute values would overlap, normalize the gradient curve fits, and then multiply the gradient curve fits. With this rule for shifting, it can be seen that the premixed case requires little to no shifting, while the non-premixed case requires a significant amount of shifting. Because the pixel locations do not line up exactly between the acetone and NO_2 images,

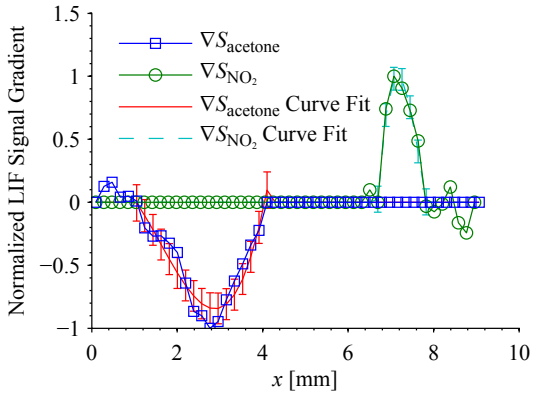

(a) Normalized acetone and NO_2 PLIF gradients for a non-premixed flame.

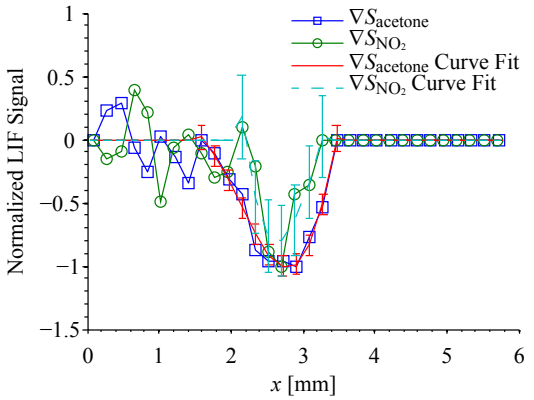

(b) Normalized acetone and NO_2 PLIF gradients for a premixed flame.

Figure B.2: Normalized acetone and NO_2 PLIF gradients for (a) a non-premixed and (b) a premixed flame. [The conference paper did not include the curve fits in this figure. They have been included here for completeness.]

the acetone gradient curve was selected to remain constant, while the NO_2 gradient curve was recalculated at the acetone pixel locations. Then, following Eq. (B.1), the flame index was measured, as shown in Figs. B.3(a) and B.3(b). We see that for the non-premixed case, a flame index of -1 was determined, and that for the premixed case, a flame index of $+1$ was measured. These were the expected values for premixed and non-premixed flames. The error bars shown in Figs. B.3(a) and B.3(b) are the error bounds for a 50 % confidence level due to the gradient curve fits.

B.1.2 Discussion

When the proposed method to measure flame index is applied to a turbulent flame, it should provide the same level of signal to noise (of between 48 and 71 for the fuel tracer and between 21 and 27 for the O_2 tracer) for the same spatial resolution of 190 mm that was achieved. Therefore it should be possible to measure the gradients in the fuel tracer and the O_2 tracer with the same accuracy as demonstrated here. However, the turbulent flame presents several additional challenges. There will be a maximum Reynolds number above which the gradients will be too large to measure unless improvements are made to the diagnostic method. This is true of all measurement methods, and this limit should be determined for each method. Better spatial resolution is possible, but only at the price of a reduced signal to noise unless improvements are made. The PLIF signal is proportional to the product of several quantities including: laser energy/pulse, the square of the diameter of the collection lens, the quantum efficiency of the camera intensifier, and the concentration of the tracer gas, as shown in Eq. (B.2). To apply the method to high Reynolds

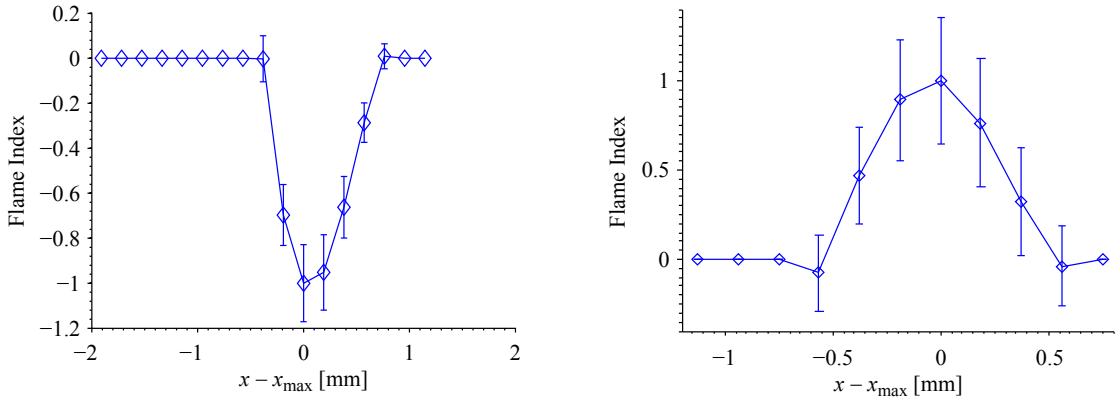

(a) Flame Index for a non-premixed flame.

(b) Flame Index for a premixed flame.

Figure B.3: Flame index for (a) a non-premixed and (b) a premixed flame.

number turbulent flows, ways to maximize each of these quantities needs to be investigated. For moderate Reynolds numbers associated with most of the current laboratory studies of turbulent flames, the spatial resolution and signal to noise demonstrated in the present work should be adequate.

The PLIF signal is proportional to the following equation.

$$S_i = C\frac{ED^2Q(\Delta x)^2\chi_i n}{HL_1^2} \tag{B.2}$$

where C is some constant value, S_i is the signal from species i, E is the laser energy/pulse, D is the collection lens diameter, Q is the quantum efficiency of the camera, Δx is the bin size, χ_i is the mole fraction of species i, n is the gas number density, H is the laser sheet height, and L_1 is the distance from the laser sheet to the collection lens. In this study, the laser energy/pulse, E, was set to 20 mJ for the 266 nm sheet, and 30 mJ for the 532 nm sheet. [The lens diameter, D, was 35 mm for both the NO_2- and acetone-sensing cameras.] The quantum efficiency, Q, of the acetone camera was 15 %, and for the NO_2 camera 30 %. For the acetone camera, Δx was 191 ± 16 µm/pixel for the non-premixed case, and 187 ± 16 µm/pixel for the premixed case. For the NO_2 camera, Δx was 189 ± 16 µm/pixel for the non-premixed case, and 187 ± 16 µm/pixel for the premixed case. All of these Δx values are after the images were binned. The acetone mole fraction, $\chi_{acetone}$, was 0.201 for both the premixed and non-premixed cases. The NO_2 mole fraction, χ_{NO_2}, was 0.0015 for the premixed case [this number was later found to be wrong, it was really 0.002] and 0.005 for the non-premixed case. The gas number density, n, [was] 2.0×10^{25} m^{-3} for the CH_4-acetone mixture in the diffusion flame, and 5.1×10^{24} m^{-3} for the air-NO_2 mixture in the diffusion flame. The laser sheet height, H, was 15 mm for the 266 nm laser sheet, and 4 mm for the 532 nm laser sheet. The distance from the laser sheet to the collection lens, L_1, was 14 cm for the acetone camera, and

18 cm for the NO_2 camera.

Another issue is how to properly shift the gradients to measure the flame index in a turbulent flame. As shown above, this is not necessary at locations where premixed combustion occurs, since the [gradients] in the fuel and the air overlap. At locations of non-premixed combustion, the fuel and air gradients do not overlap except in a very thin region where both the fuel and oxygen concentrations are too small to measure. A general data analysis method needs to be developed for the turbulent case, which should follow the following procedure.

1. Determine the spatial gradient of the acetone and NO_2 PLIF signals at each location in each instantaneous image.
2. Identify flamelets by removing all regions where the PLIF signal is sufficiently close to the maximum value, which indicates that the region is either pure fuel or pure air. Also remove regions where the signal is sufficiently close to zero since these regions cannot be high gradient regions where flamelets exist. All gradients should be set to zero in these removed regions.
3. Each resulting image should contain thin high gradient layers which correspond to flamelets.
4. Determine the direction that is normal to each high gradient layer.
5. Select the acetone gradient layers first. The code should march along the line that is normal to each layer. There are two possible directions to go along this line. The code should always select the direction that goes from right to left (i.e., the x-coordinate increases).
6. Along this path, the values of the gradient of NO_2 should be checked. If both the acetone and NO_2 gradients are of the same sign, then this is a region of premixed flame and the flame index for this region is computed.
7. If the gradient of NO_2 is zero or has a sign that is opposite to the acetone gradient, then non-premixed combustion occurs. The code must select the proper direction along the normal line to look to find the gradient in NO_2, since in a non-premixed flame the NO_2 and acetone gradients do not overlap but are near each other. The code should select the direction along the normal line that goes from large to small acetone signal. Marching should proceed until the gradient of NO_2 is such that the NO_2 signal increases to a maximum. Then the profile of the NO_2 signal along this line must be shifted so that the maximum gradient of NO_2 and acetone signals overlap. This guarantees that the flame index will be -1 at the maximum gradient location.

It should be pointed out that shifting the oxygen concentration profile when a non-premixed region is detected is simply a way to define the flame index so that it has a value of -1 where a non-premixed flame occurs. If no shifting were done, all non-premixed flames would have a flame index of nearly zero,

since fuel and air gradients do not overlap (except in very small regions). Forcing the maximum gradients to overlap is a somewhat arbitrary definition of the flame index, but once the flame index is defined in this way, it is not ambiguous; the exact same definition can be used when comparing DNS simulation to experiments.

The conclusions of the paper went on to define an equation for determining the flame index, upon which Eq. (1.4) is based:

$$\text{F.I.} = \frac{\nabla S_{\text{acetone}} \cdot \nabla S_{\text{NO}_2}}{\left|\nabla S_{\text{acetone}}\right|_{\text{max}} \cdot \left|\nabla S_{\text{NO}_2}\right|_{\text{max}}}. \tag{B.3}$$

The key difference between this equation and Eq. (1.4) is that Eq. (B.3) is not defined to have only values $+1$, 0, and -1. Instead Eq. (B.3) is allowed to vary continuously from -1 or $+1$. The flame index in Eq. (B.3) is also defined not only at the flamelets, but in the region around the flamelet.

The flamelet shifting method was applied to a single line of pixels, meaning it would be impractical for a turbulent flame, because it would make evaluating the flame index in a two-dimensional plane difficult. To determine the flame index in a two-dimensional flame, different regions of a given PLIF signal would be shifted in different directions by different amounts. However, the flamelet shifting method did help to outline some problems that would need to be overcome, like the fact that the acetone and NO_2 signals never overlap, the solution just wasn't very good.

APPENDIX C

Complete Data Set

It was not practical or necessary to give the complete results for all data sets in the body of this document. They will be presented here.

C.1 Case L-1: Laminar Premixed Flame

The data presented here for case L-1 is for the unbinned statistical analysis. Case L-1 had only a background correction applied, no white-field or laser sheet non-uniformity correction due to complications with correcting the acetone images. The detection of non-premixed flamelets is most likely related to non-uniformities in the laser sheet that were caused by cracks in the enclosed co-flow burner's windows.

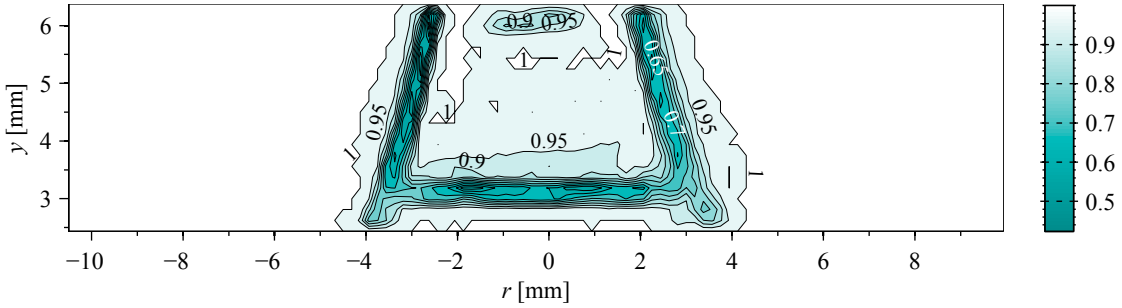

(a) Probability that $\xi = 0$ (B) in case L-1.

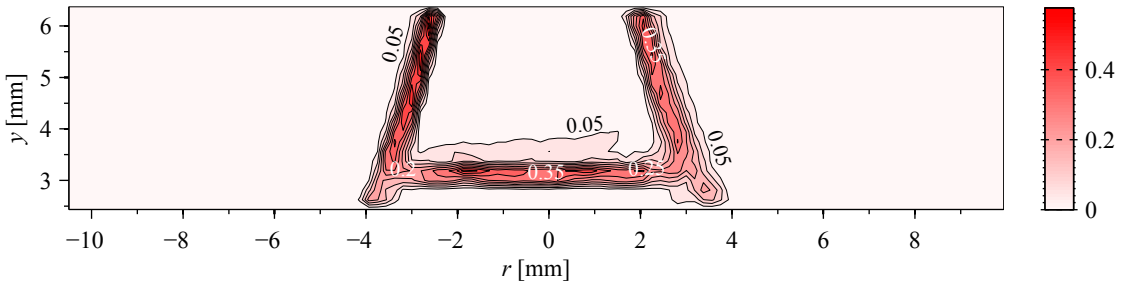

(b) Probability that $\xi = +1$ (C) in case L-1.

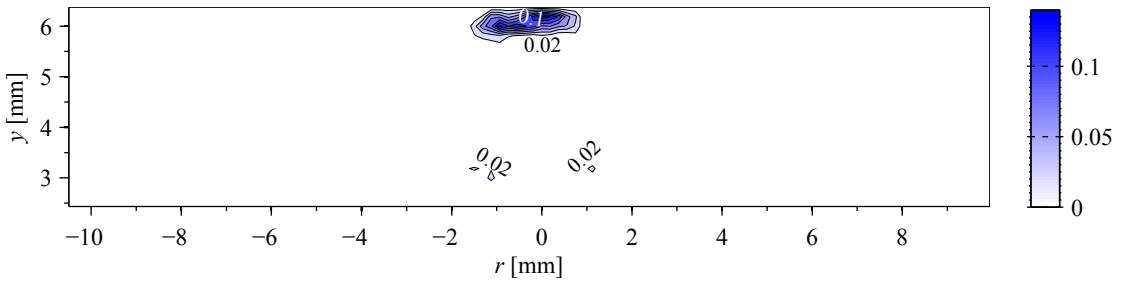

(c) Probability that $\xi = -1$ (A) in case L-1.

Figure C.1: The probability mass function for ξ in case L-1.

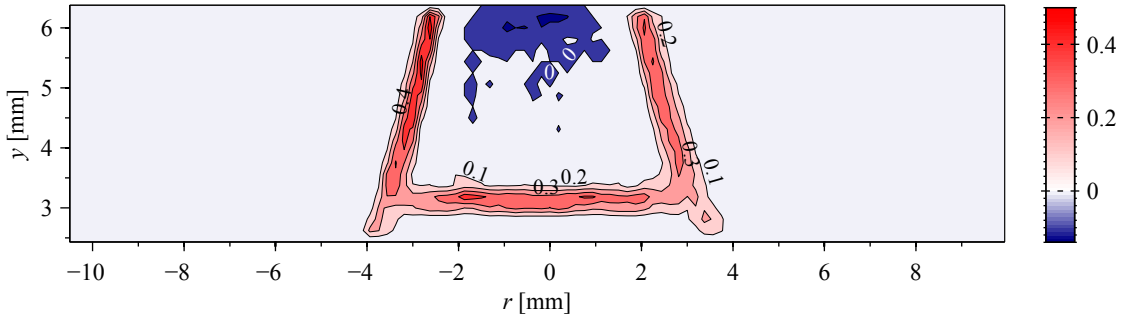

(a) Averaged flame index, $\langle \xi \rangle$ in case L-1.

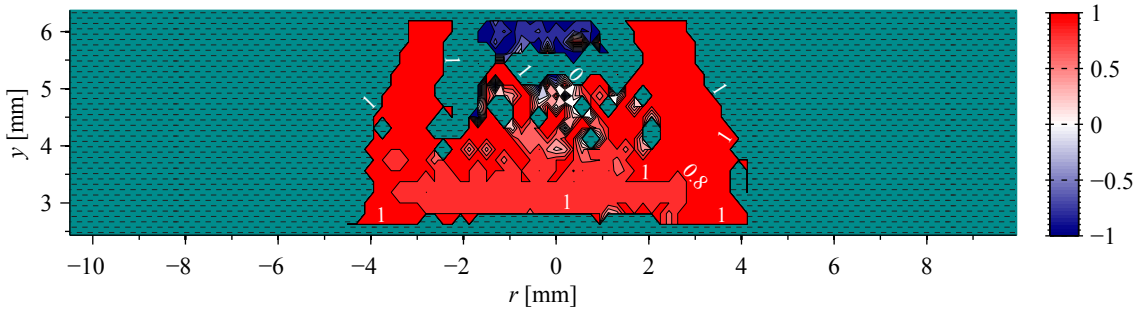

(b) Conditionally averaged flame index, ignoring locations with no flamelets, $\langle \xi \mid \xi \neq 0 \rangle$, in case L-1. Regions that are, on average, more non-premixed are marked with shades of blue and while regions that are, on average, highly premixed are marked with shades of red. Regions that never have a flamelet are marked with dark cyan and a hatching of short horizontal lines.

Figure C.2: For case L-1, (a) the average flame index $\langle \xi \rangle$ and (b) the conditionally averaged flame index $\langle \xi \mid \xi \neq 0 \rangle$, where locations without flamelets were ignored.

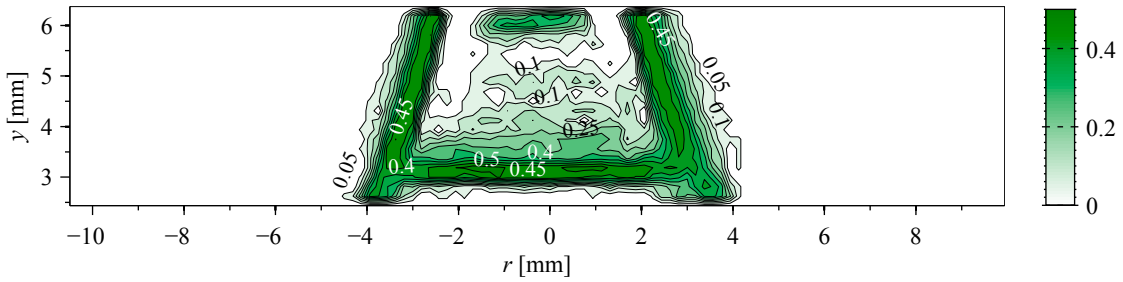

(a) Standard deviation of ξ, σ_ξ, in case L-1.

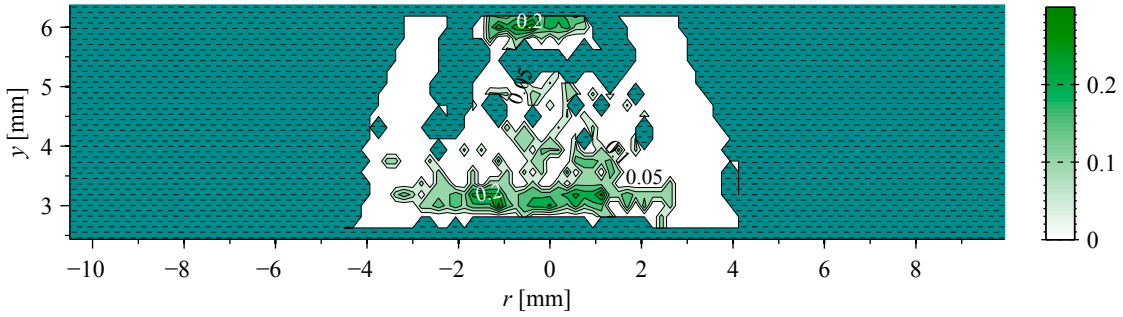

(b) Conditional standard deviation of ξ, $\sigma_{\langle\xi|\xi\neq 0\rangle}$, in case L-1. Regions that never have a flamelet are marked with dark cyan and a hatching of short horizontal lines.

Figure C.3: For case L-1, the standard deviation derived from (a) the average of ξ, σ_ξ, and (b) the conditional average of ξ, $\sigma_{\langle\xi|\xi\neq 0\rangle}$, where all locations without flamelets were ignored.

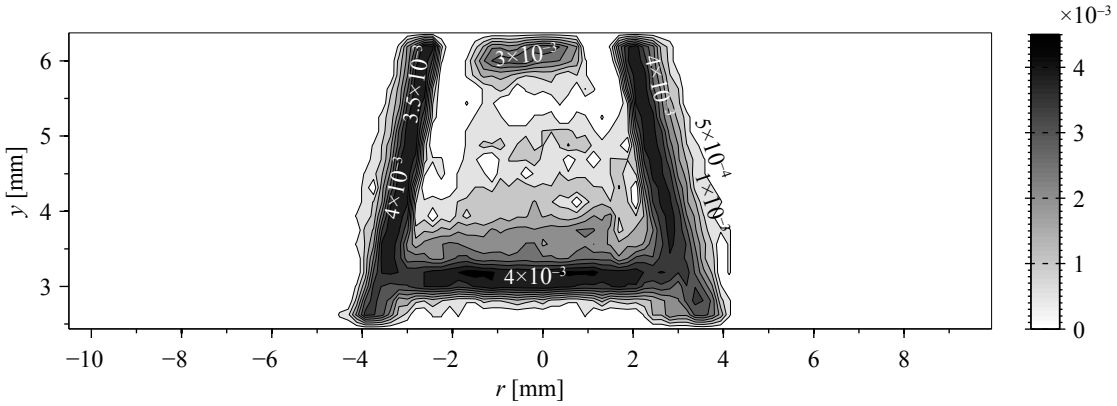

(a) Statistical uncertainty of the average flame index, $\langle \xi \rangle$, in case L-1.

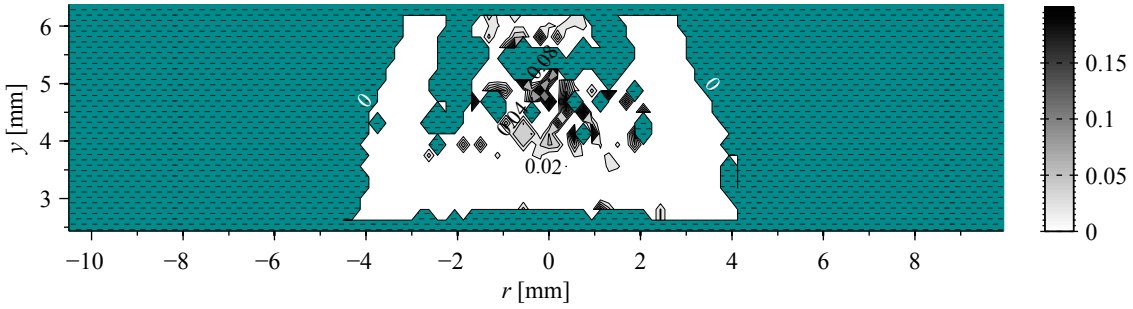

(b) Statistical uncertainty of the conditionally averaged flame index, $\langle \xi \mid \xi \neq 0 \rangle$, which ignores locations with no flamelets, in case L-1. Regions that never have a flamelet are marked with dark cyan and a hatching of short horizontal lines.

Figure C.4: For case L-1, (a) the uncertainty of the average flame index $\langle \xi \rangle$ and (b) the uncertainty of the conditionally averaged flame index, $\langle \xi \mid \xi \neq 0 \rangle$, where all locations without flamelets were ignored. Uncertainties are to a 95 % confidence level.

C.2 Case L-2: Laminar Non-premixed Flame

The data presented here for case L-2 is for the unbinned statistical analysis. Unlike case L-1, case L-2 was corrected for the white-field and the non-uniformities that existed in the laser sheets, upstream of the windows. The detection of premixed flamelets is most likely related to non-uniformities in the laser sheet that were caused by cracks in the enclosed co-flow burner's windows.

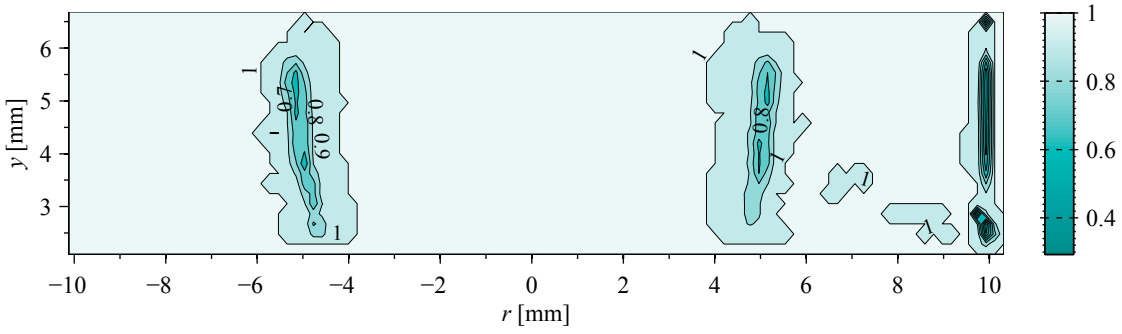

(a) Probability that $\xi = 0$ (B) in case L-2.

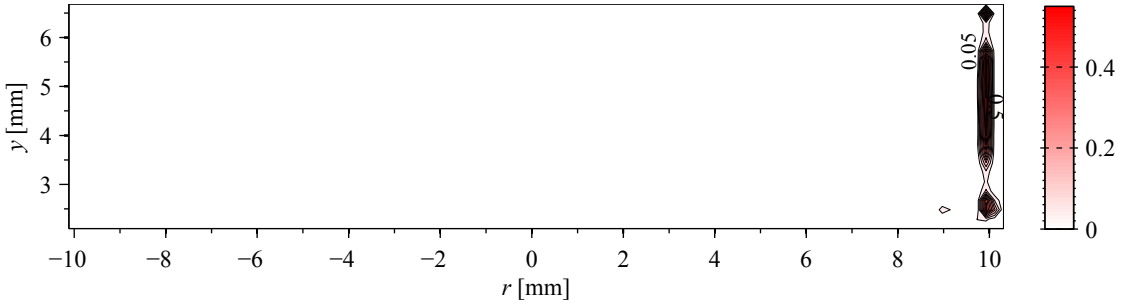

(b) Probability that $\xi = +1$ (C) in case L-2.

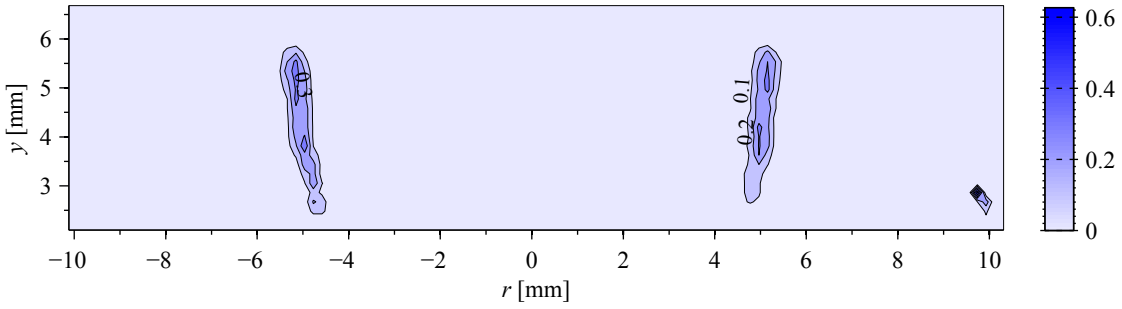

(c) Probability that $\xi = -1$ (A) in case L-2.

Figure C.5: The probability mass function for ξ in case L-2.

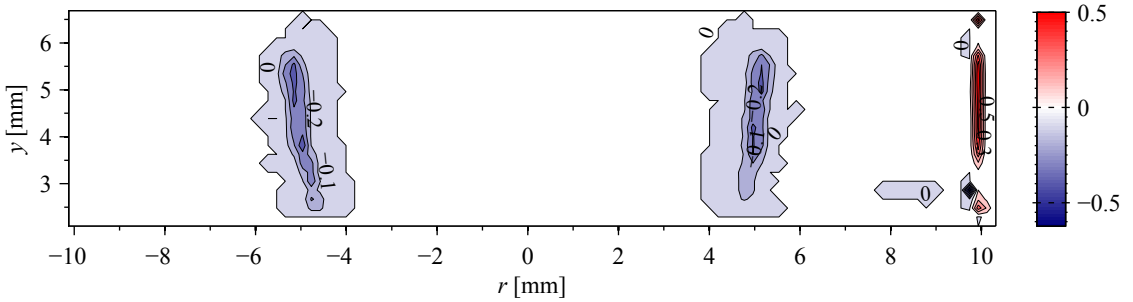

(a) Averaged flame index, $\langle \xi \rangle$ in case L-2.

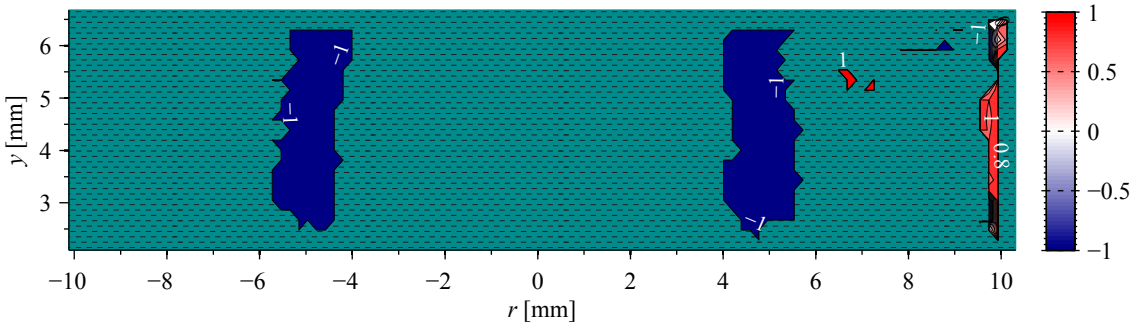

(b) Conditionally averaged flame index, ignoring locations with no flamelets, $\langle \xi \mid \xi \neq 0 \rangle$, in case L-2. Regions that are, on average, more non-premixed are marked with shades of blue and while regions that are, on average, highly premixed are marked with shades of red. Regions that never have a flamelet are marked with dark cyan and a hatching of short horizontal lines.

Figure C.6: For case L-2, (a) the average flame index $\langle \xi \rangle$ and (b) the conditionally averaged flame index $\langle \xi \mid \xi \neq 0 \rangle$, where locations without flamelets were ignored.

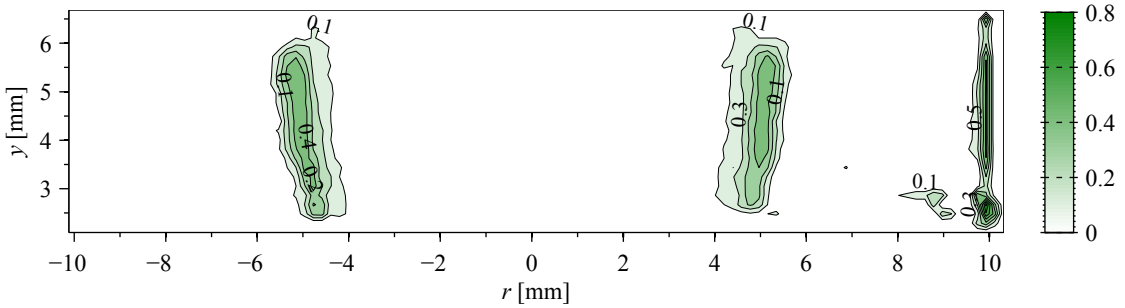

(a) Standard deviation of ξ, σ_ξ, in case L-2.

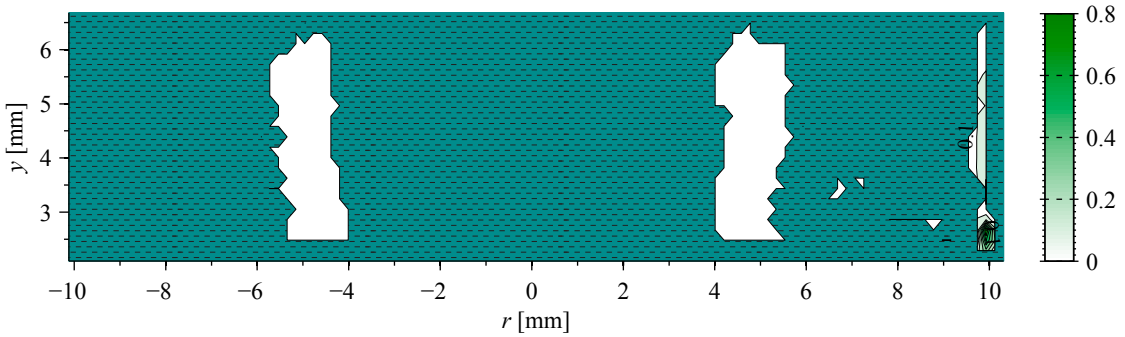

(b) Conditional standard deviation of ξ, $\sigma_{\langle\xi|\xi\neq 0\rangle}$, in case L-2. Regions that never have a flamelet are marked with dark cyan and a hatching of short horizontal lines.

Figure C.7: For case L-2, the standard deviation derived from (a) the average of ξ, σ_ξ, and (b) the conditional average of ξ, $\sigma_{\langle\xi|\xi\neq 0\rangle}$, where all locations without flamelets were ignored.

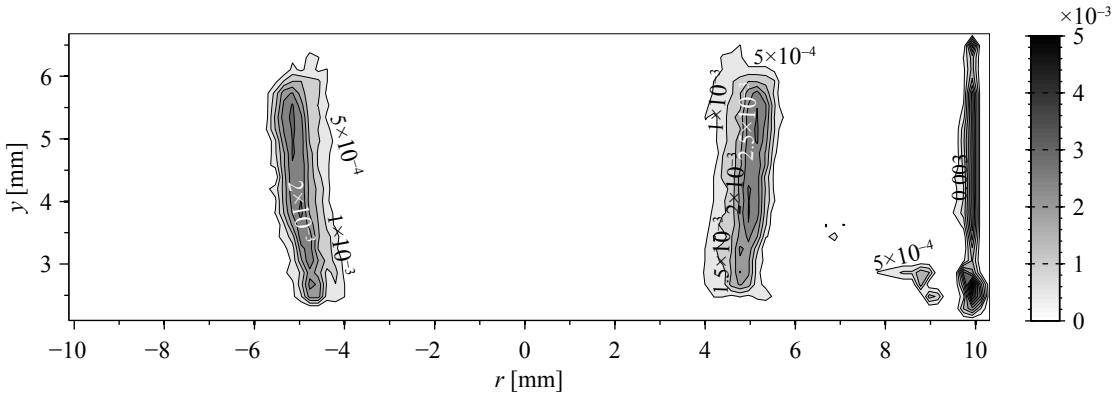

(a) Statistical uncertainty of the average flame index, $\langle \xi \rangle$, in case L-2.

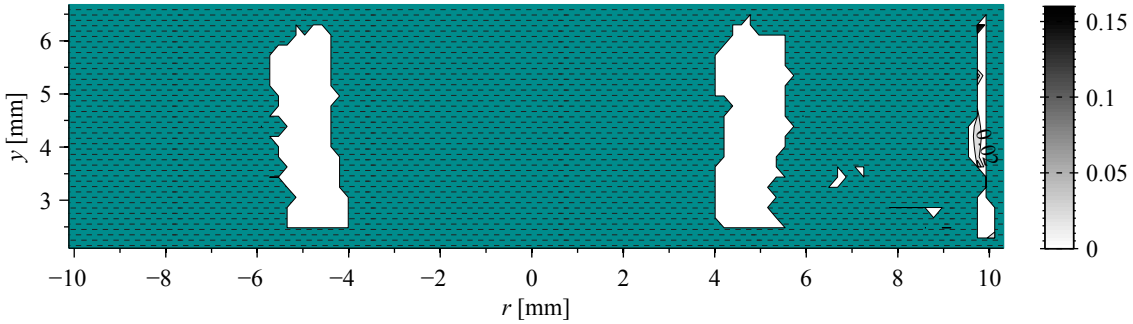

(b) Statistical uncertainty of the conditionally averaged flame index, $\langle \xi \mid \xi \neq 0 \rangle$, which ignores locations with no flamelets, in case L-2. Regions that never have a flamelet are marked with dark cyan and a hatching of short horizontal lines.

Figure C.8: For case L-2, (a) the uncertainty of the average flame index $\langle \xi \rangle$ and (b) the uncertainty of the conditionally averaged flame index, $\langle \xi \mid \xi \neq 0 \rangle$, where all locations without flamelets were ignored. Uncertainties are to a 95 % confidence level.

C.3 Case M-1: Methane Turbulent Flame

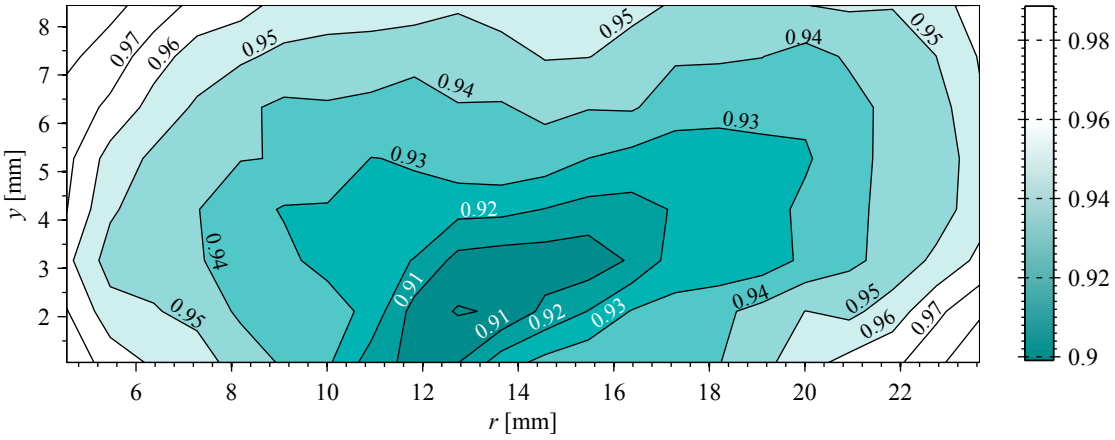

(a) Probability that $\xi = 0$ (B) in case M-1.

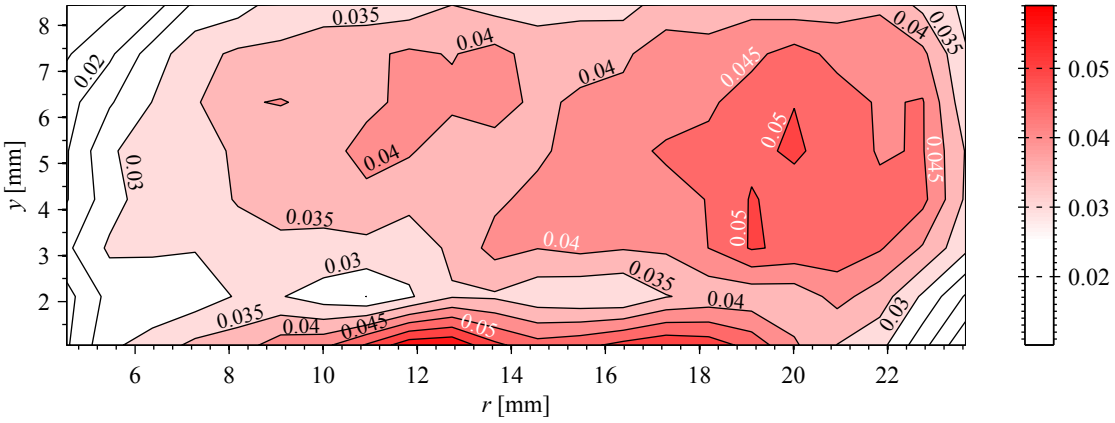

(b) Probability that $\xi = +1$ (C) in case M-1.

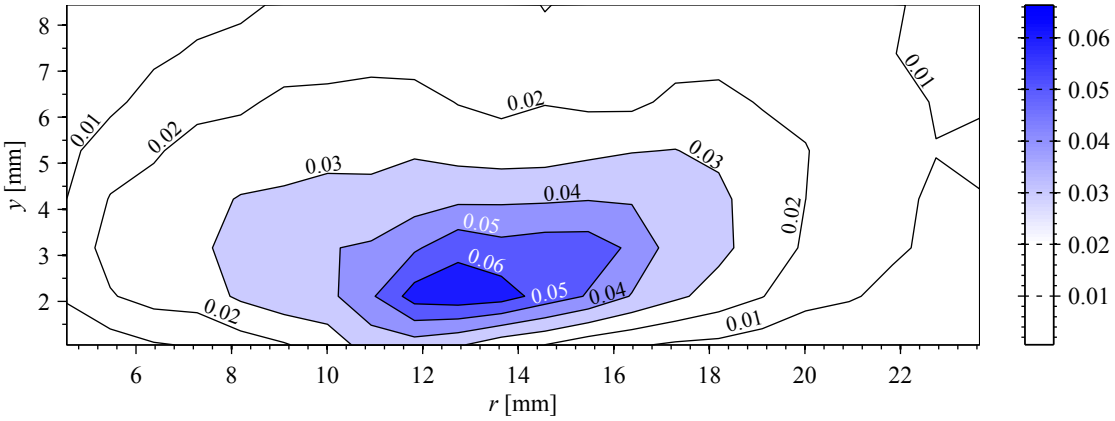

(c) Probability that $\xi = -1$ (A) in case M-1.

Figure C.9: The probability mass function for ξ in case M-1.

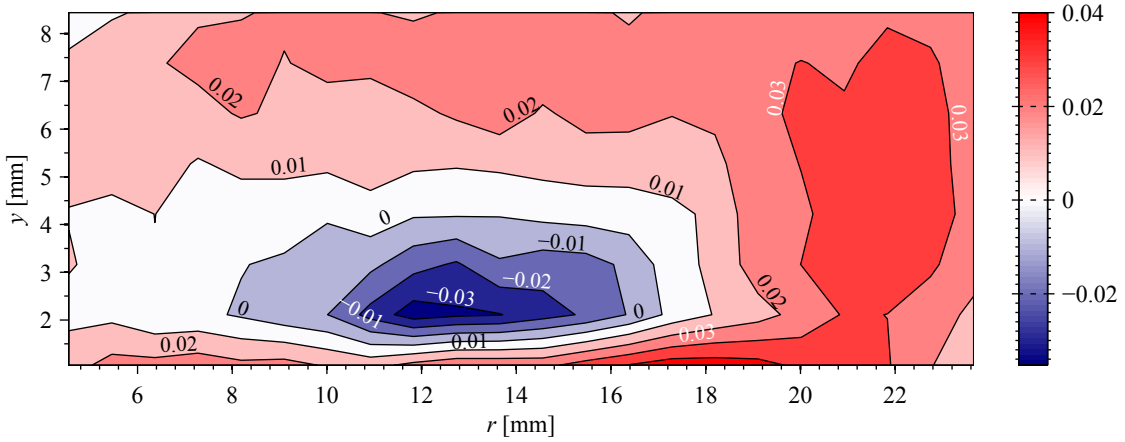

(a) Averaged flame index, $\langle \xi \rangle$ in case M-1.

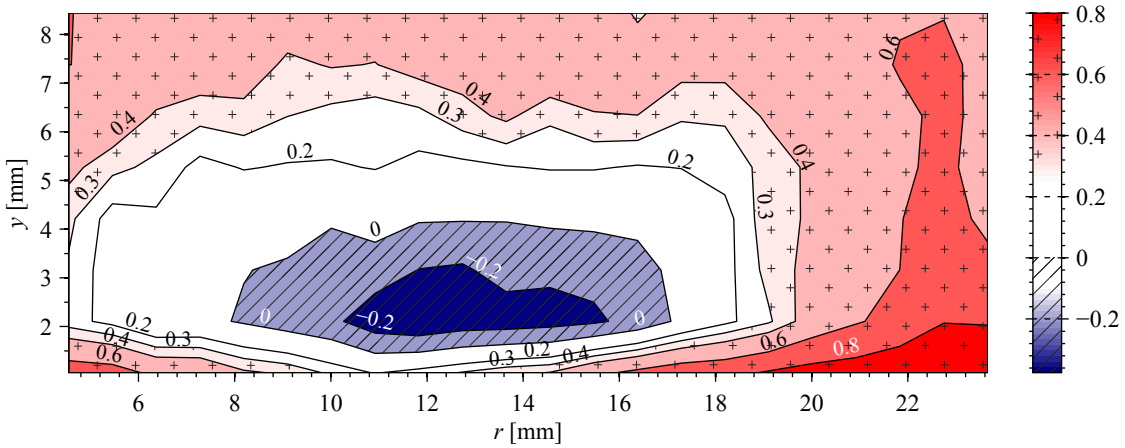

(b) Conditionally averaged flame index, ignoring locations with no flamelets, $\langle \xi \mid \xi \neq 0 \rangle$, in case M-1. Regions that are, on average, more non-premixed are marked with shades of blue and a hatching of diagonal lines while regions that are, on average, highly premixed are marked with shades of red and a hatching of crosses.

Figure C.10: For case M-1, (a) the average flame index $\langle \xi \rangle$ and (b) the conditionally averaged flame index $\langle \xi \mid \xi \neq 0 \rangle$, where locations without flamelets were ignored.

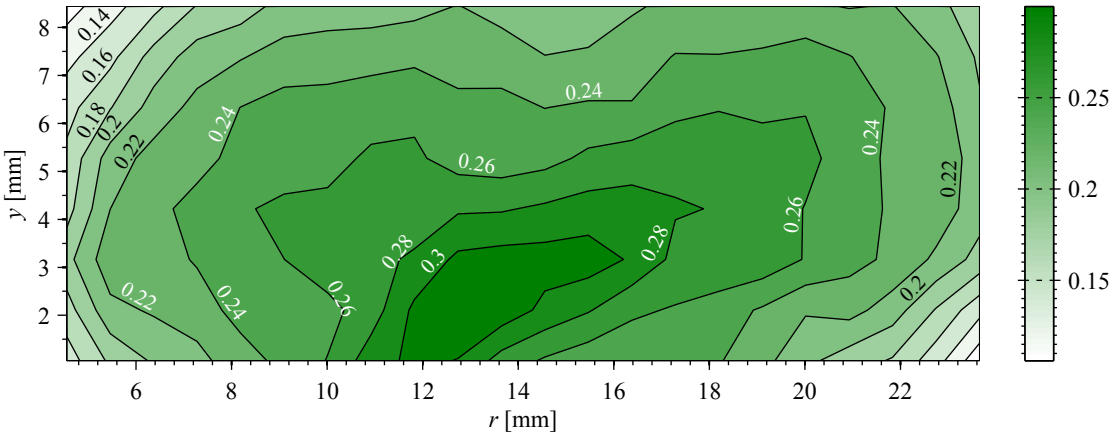

(a) Standard deviation of ξ, σ_ξ, in case M-1.

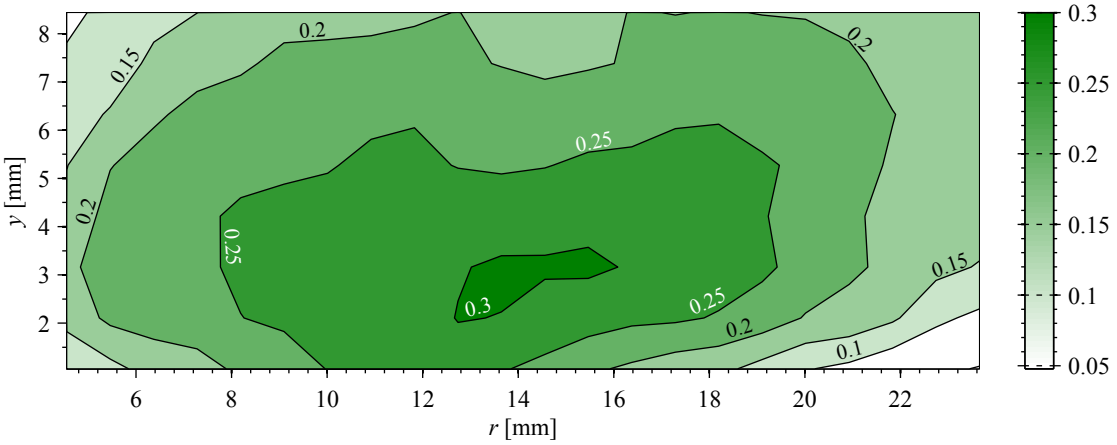

(b) Conditional standard deviation of ξ, $\sigma_{\langle\xi|\xi\neq 0\rangle}$, in case M-1.

Figure C.11: For case M-1, the standard deviation derived from (a) the average of ξ, σ_ξ, and (b) the conditional average of ξ, $\sigma_{\langle\xi|\xi\neq 0\rangle}$, where all locations without flamelets were ignored.

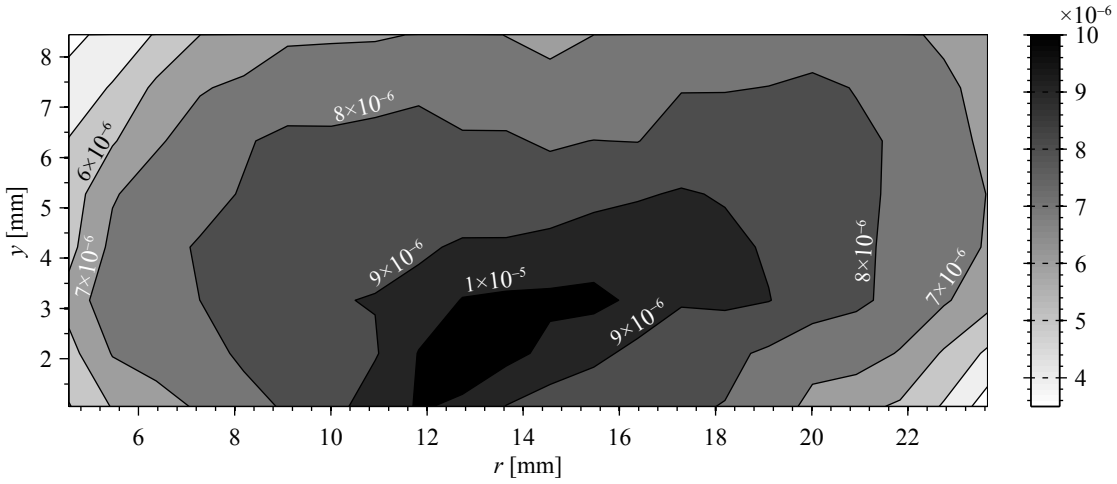

(a) Statistical uncertainty of the average flame index, $\langle \xi \rangle$, in case M-1.

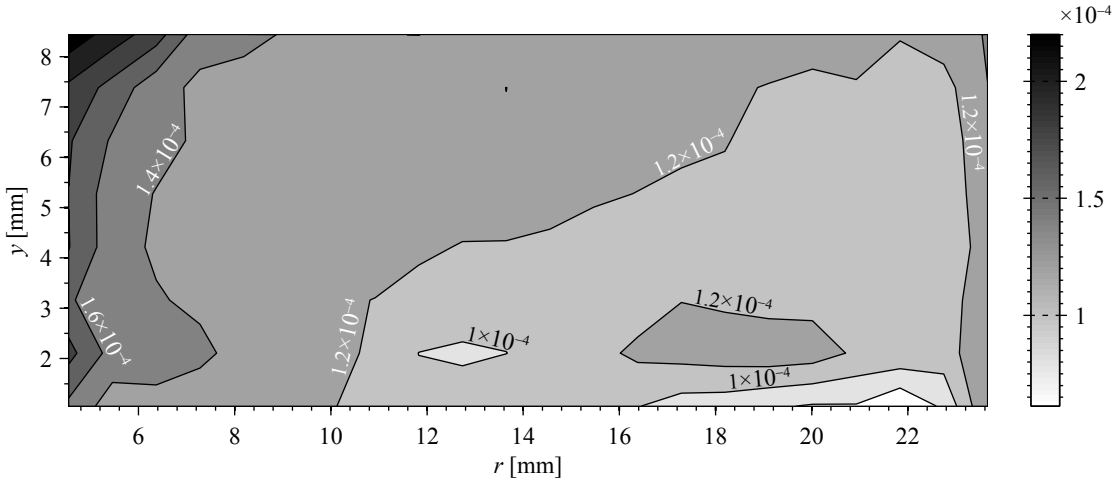

(b) Statistical uncertainty of the conditionally averaged flame index, $\langle \xi \,|\, \xi \neq 0 \rangle$, which ignores locations with no flamelets, in case M-1.

Figure C.12: For case M-1, (a) the uncertainty of the average flame index $\langle \xi \rangle$ and (b) the uncertainty of the conditionally averaged flame index, $\langle \xi \,|\, \xi \neq 0 \rangle$, where all locations without flamelets were ignored. Uncertainties are to a 95 % confidence level.

C.4 Case P-1: Fuel-Lean Propane Turbulent Flame

The majority of the P-1 data set was given in Chapter 4, but will be repeated here for the sake of completeness.

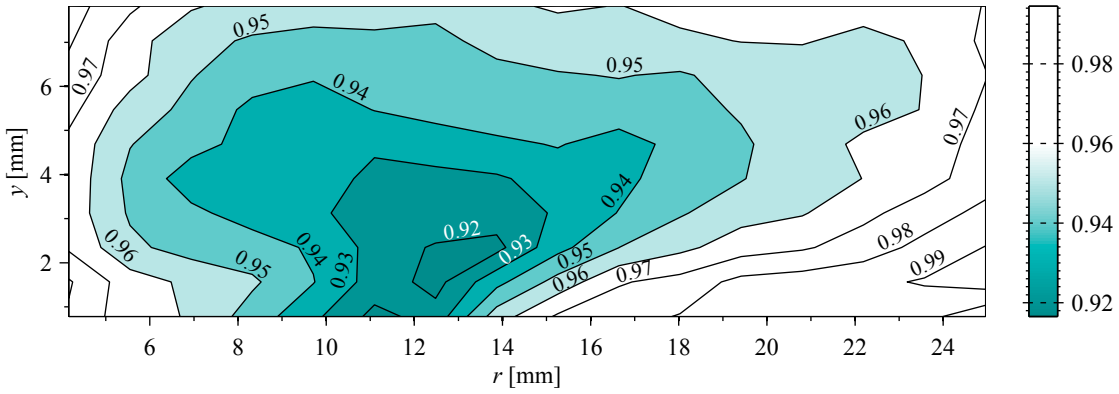

(a) Probability that $\xi = 0$ (B) in case P-1.

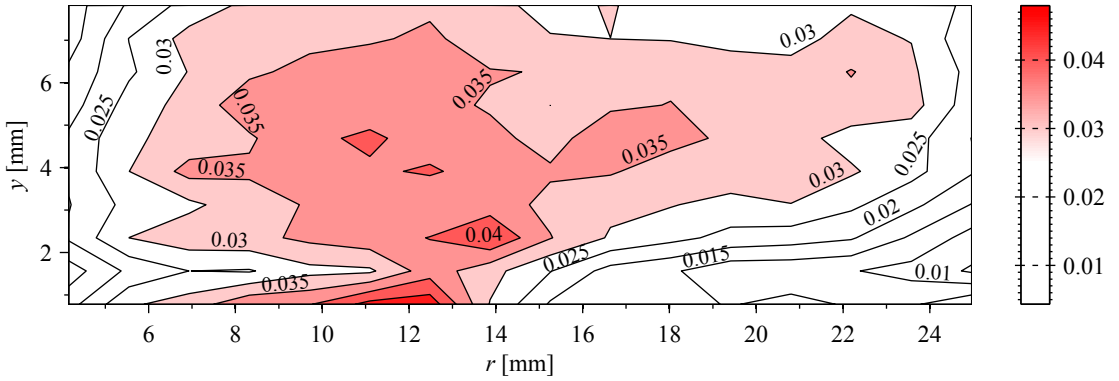

(b) Probability that $\xi = +1$ (C) in case P-1.

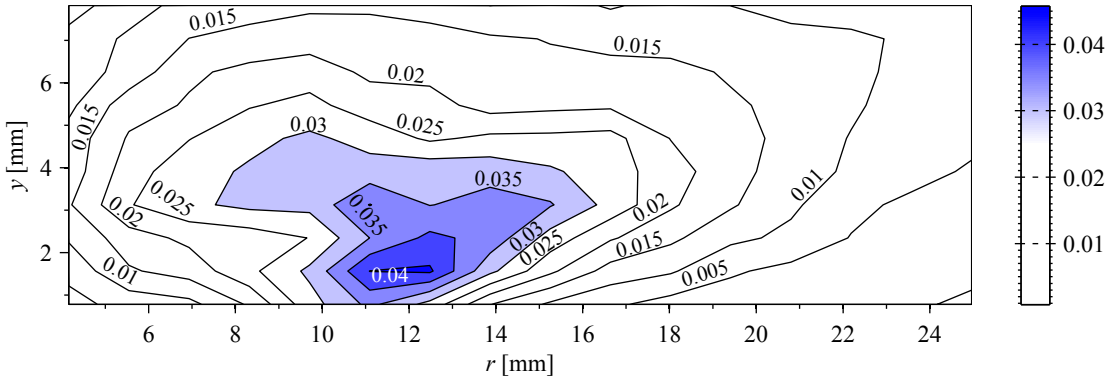

(c) Probability that $\xi = -1$ (A) in case P-1.

Figure C.13: The probability mass function for ξ in case P-1.

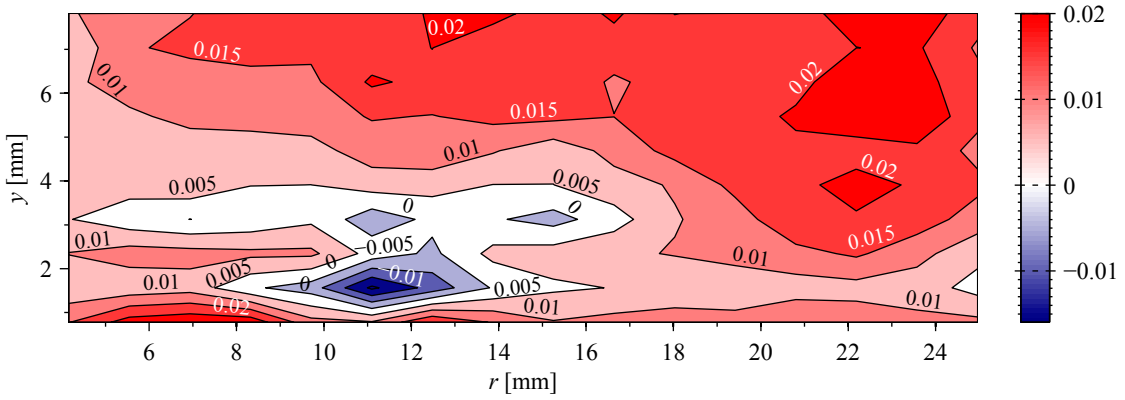

(a) Averaged flame index, $\langle \xi \rangle$ in case P-1.

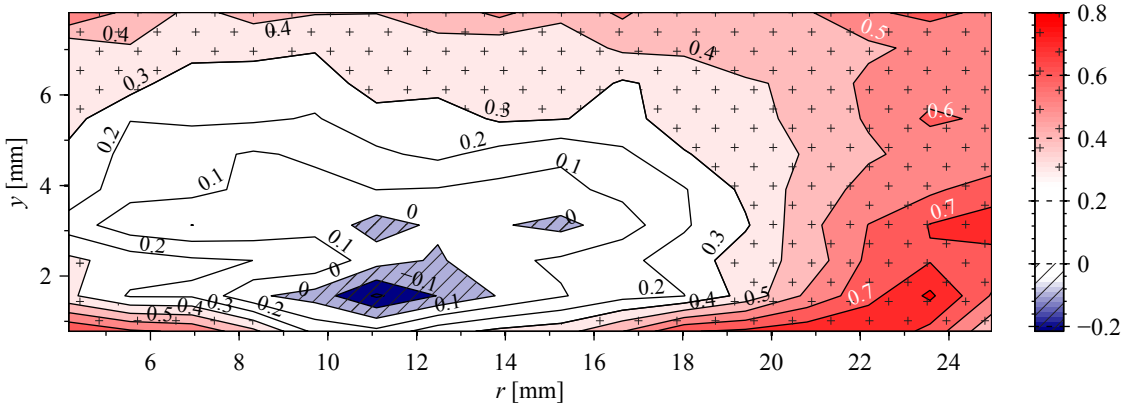

(b) Conditionally averaged flame index, ignoring locations with no flamelets, $\langle \xi \mid \xi \neq 0 \rangle$, in case P-1. Regions that are, on average, more non-premixed are marked with shades of blue and a hatching of diagonal lines while regions that are, on average, highly premixed are marked with shades of red and a hatching of crosses.

Figure C.14: For case P-1, (a) the average flame index $\langle \xi \rangle$ and (b) the conditionally averaged flame index $\langle \xi \mid \xi \neq 0 \rangle$, where locations without flamelets were ignored.

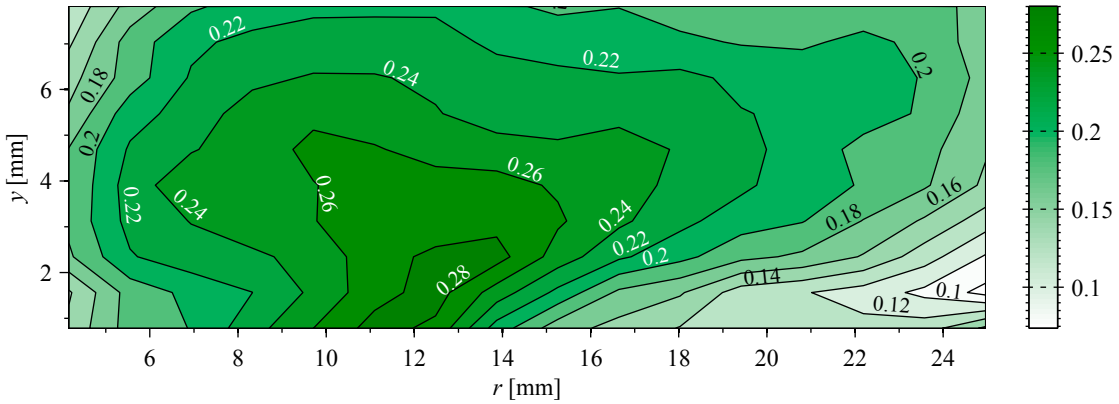

(a) Standard deviation of ξ, σ_ξ, in case P-1.

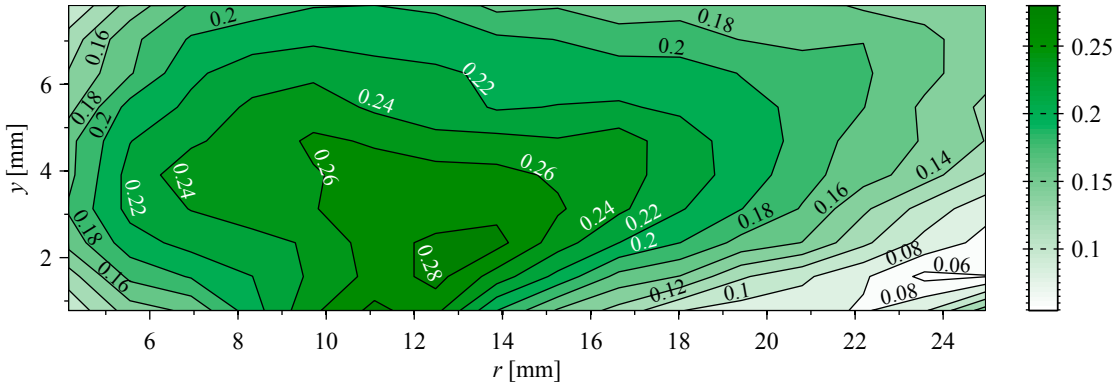

(b) Conditional standard deviation of ξ, $\sigma_{\langle\xi|\xi\neq 0\rangle}$, in case P-1.

Figure C.15: For case P-1, the standard deviation derived from (a) the average of ξ, σ_ξ, and (b) the conditional average of ξ, $\sigma_{\langle\xi|\xi\neq 0\rangle}$, where all locations without flamelets were ignored.

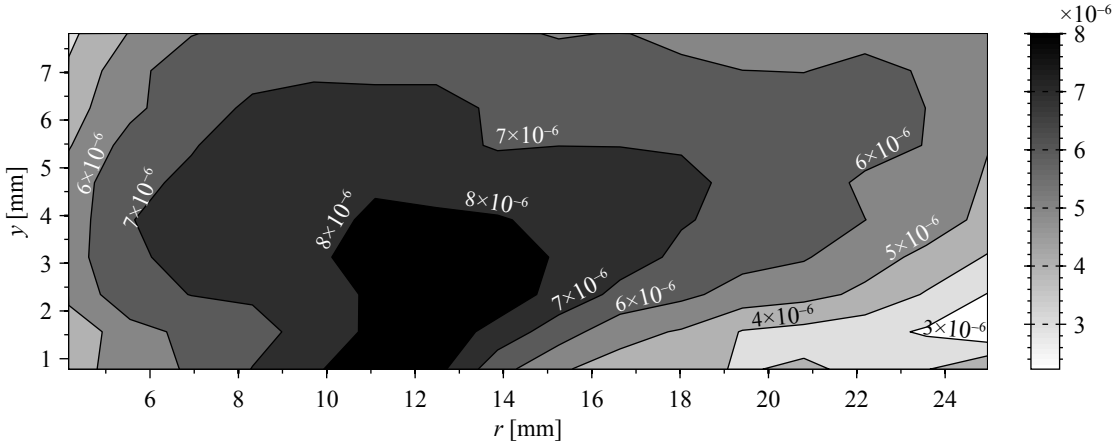

(a) Statistical uncertainty of the average flame index, $\langle \xi \rangle$, in case P-1.

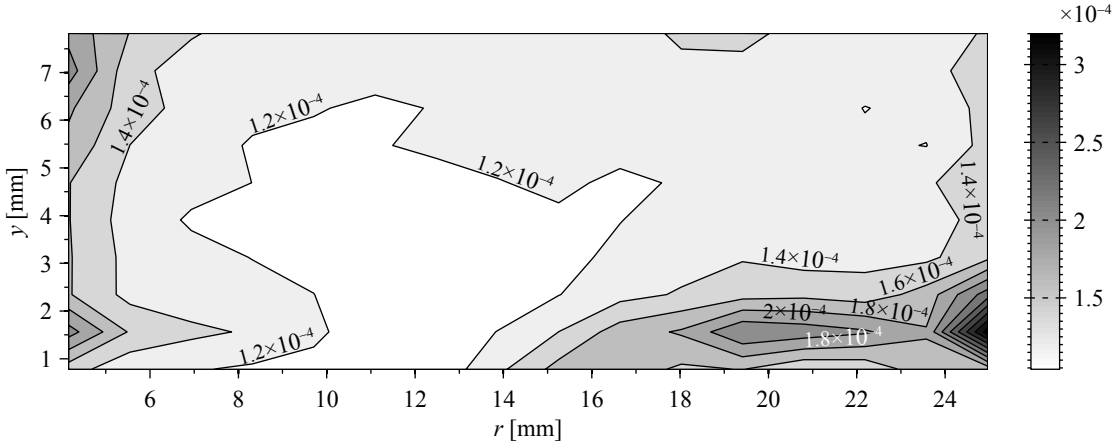

(b) Statistical uncertainty of the conditionally averaged flame index, $\langle \xi \mid \xi \neq 0 \rangle$, which ignores locations with no flamelets, in case P-1.

Figure C.16: For case P-1, (a) the uncertainty of the average flame index $\langle \xi \rangle$ and (b) the uncertainty of the conditionally averaged flame index, $\langle \xi \mid \xi \neq 0 \rangle$, where all locations without flamelets were ignored. Uncertainties are to a 95 % confidence level.

C.5 Case P-2: Fuel-Rich Propane Turbulent Flame

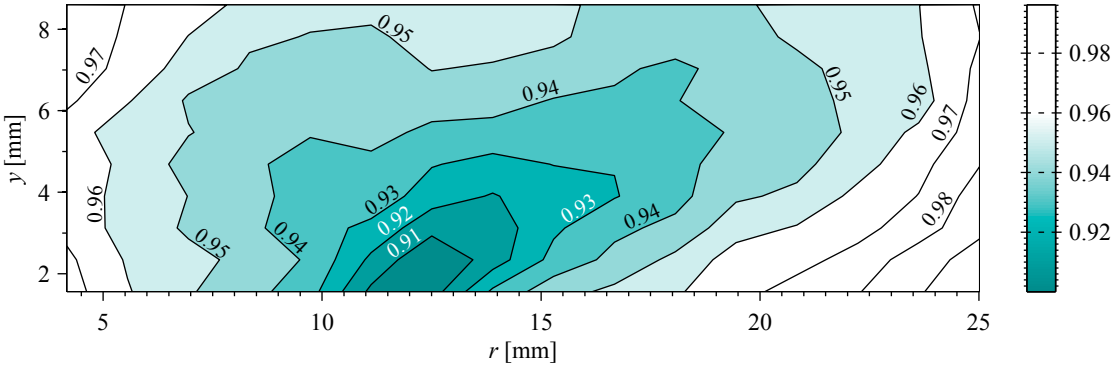

(a) Probability that $\xi = 0$ (B) in case P-2.

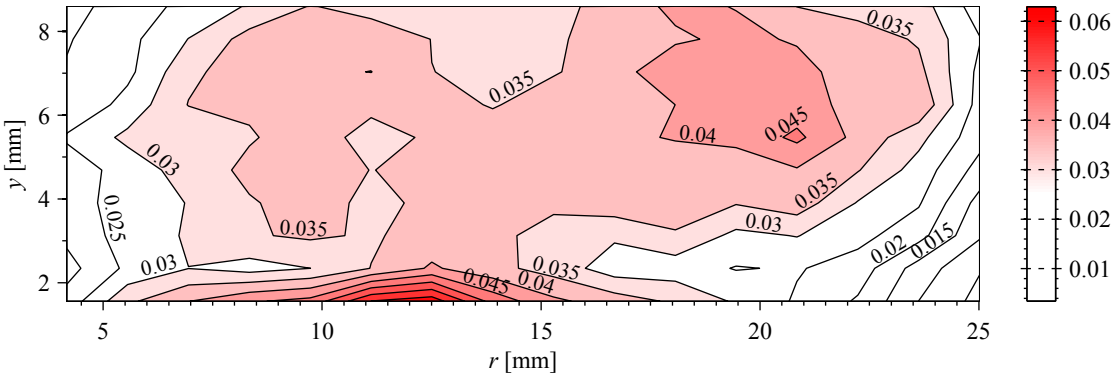

(b) Probability that $\xi = +1$ (C) in case P-2.

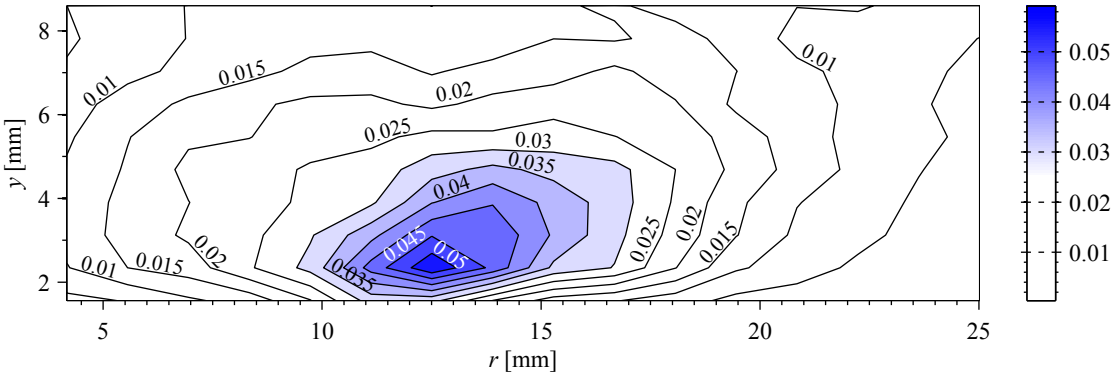

(c) Probability that $\xi = -1$ (A) in case P-2.

Figure C.17: The probability mass function for ξ in case P-2.

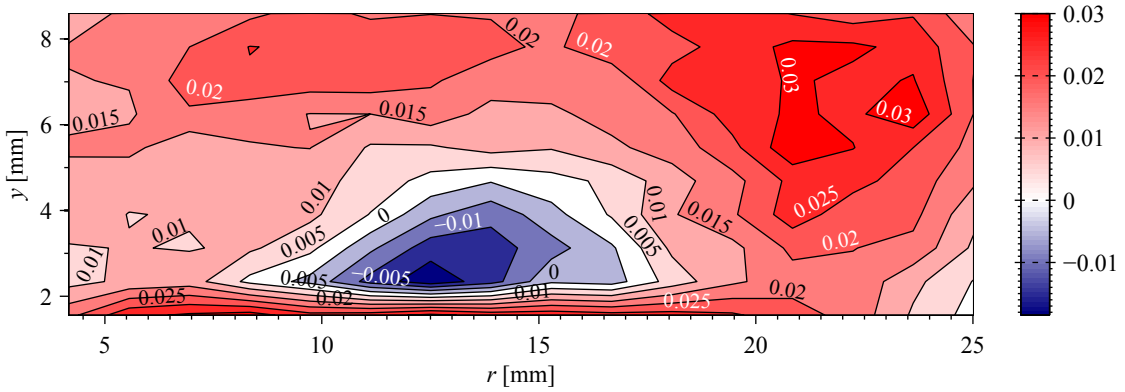

(a) Averaged flame index, $\langle \xi \rangle$ in case P-2.

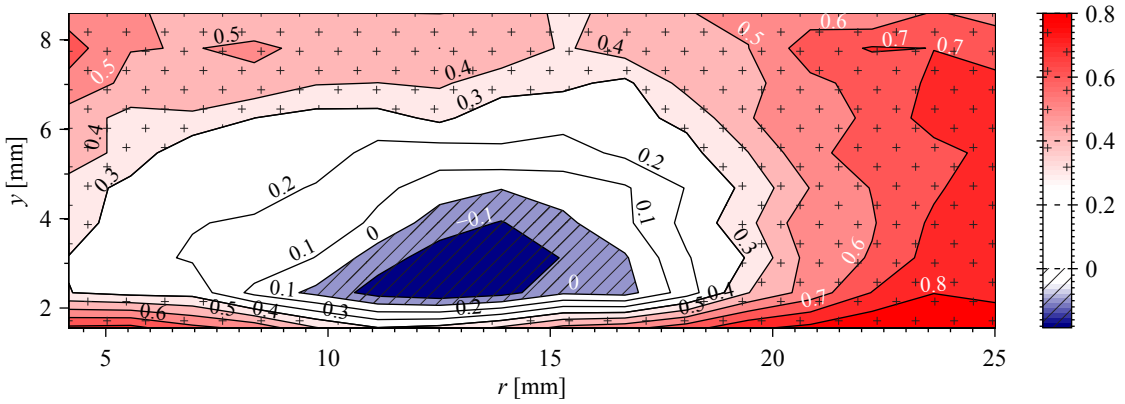

(b) Conditionally averaged flame index, ignoring locations with no flamelets, $\langle \xi \mid \xi \neq 0 \rangle$, in case P-2. Regions that are, on average, more non-premixed are marked with shades of blue and a hatching of diagonal lines while regions that are, on average, highly premixed are marked with shades of red and a hatching of crosses.

Figure C.18: For case P-2, (a) the average flame index $\langle \xi \rangle$ and (b) the conditionally averaged flame index $\langle \xi \mid \xi \neq 0 \rangle$, where locations without flamelets were ignored.

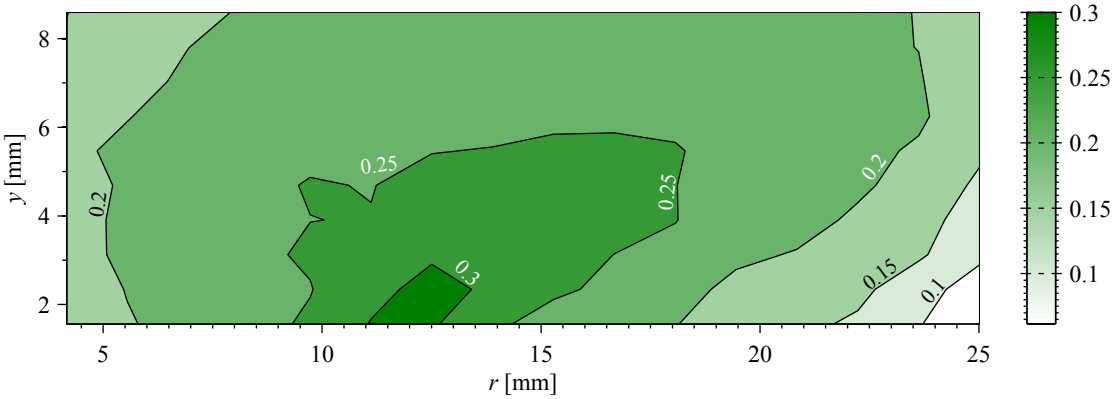

(a) Standard deviation of ξ, σ_ξ, in case P-2.

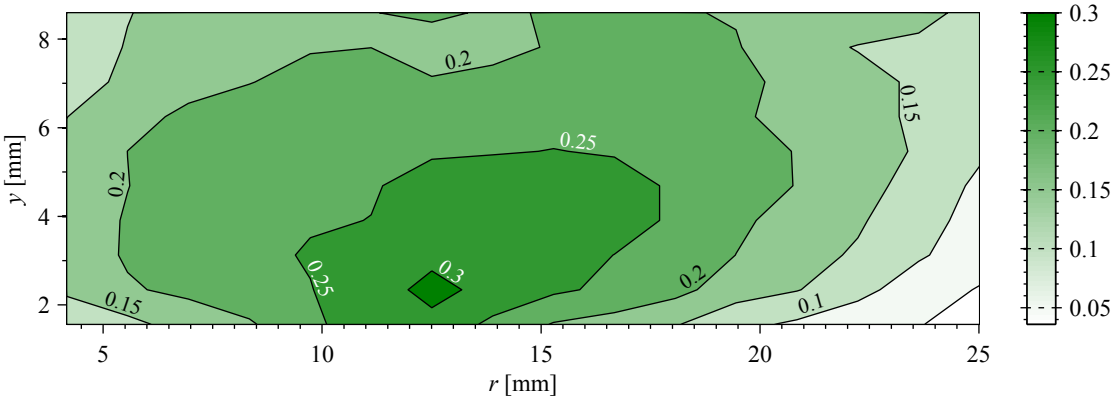

(b) Conditional standard deviation of ξ, $\sigma_{\langle\xi|\xi\neq 0\rangle}$, in case P-2.

Figure C.19: For case P-2, the standard deviation derived from (a) the average of ξ, σ_ξ, and (b) the conditional average of ξ, $\sigma_{\langle\xi|\xi\neq 0\rangle}$, where all locations without flamelets were ignored.

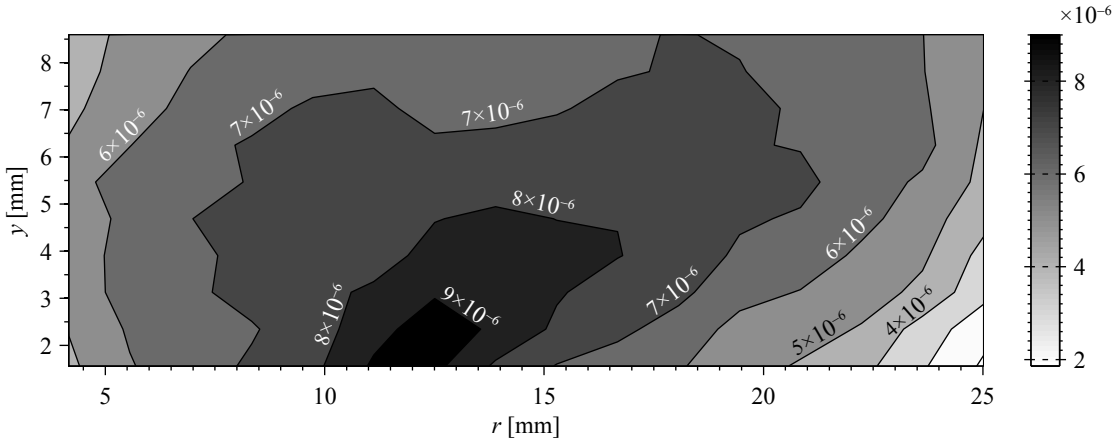

(a) Statistical uncertainty of the average flame index, $\langle \xi \rangle$, in case P-2.

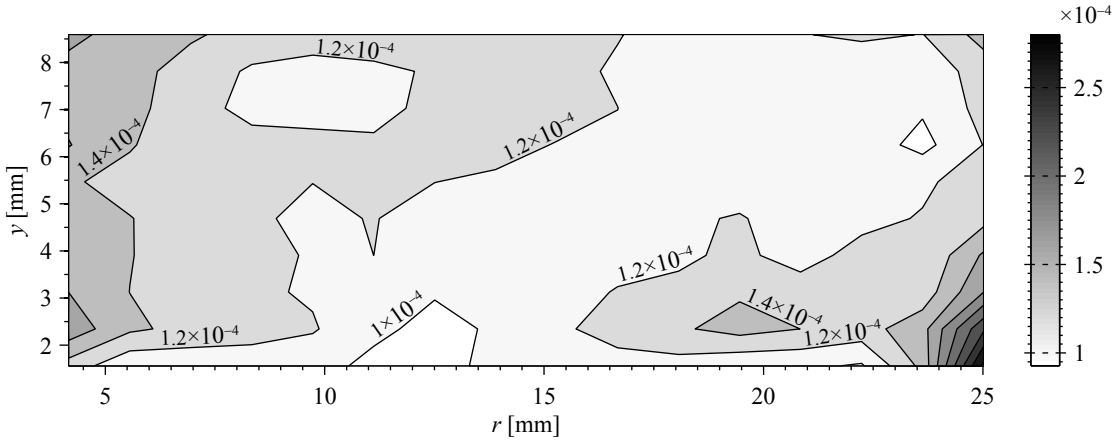

(b) Statistical uncertainty of the conditionally averaged flame index, $\langle \xi \,|\, \xi \neq 0 \rangle$, which ignores locations with no flamelets, in case P-2.

Figure C.20: For case P-2, (a) the uncertainty of the average flame index $\langle \xi \rangle$ and (b) the uncertainty of the conditionally averaged flame index, $\langle \xi \,|\, \xi \neq 0 \rangle$, where all locations without flamelets were ignored. Uncertainties are to a 95 % confidence level.

C.6 Case P-3: Low Flowrate Propane Turbulent Flame

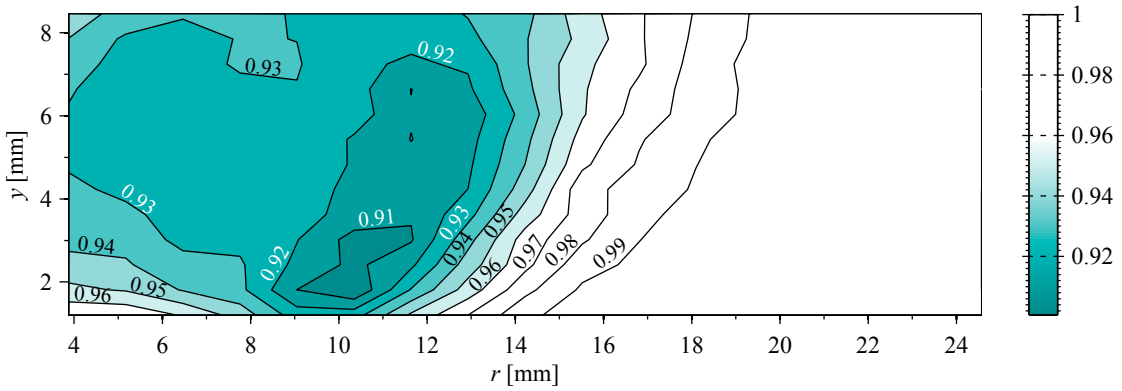

(a) Probability that $\xi = 0$ (B) in case P-3.

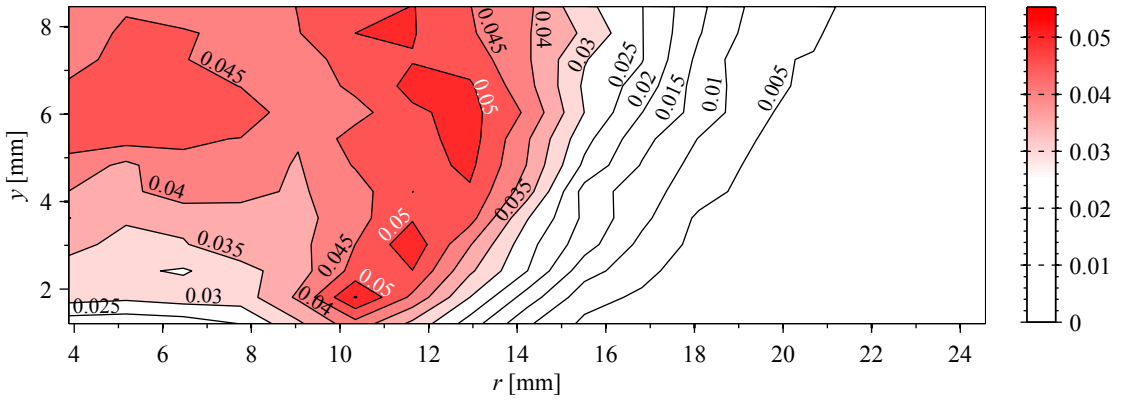

(b) Probability that $\xi = +1$ (C) in case P-3.

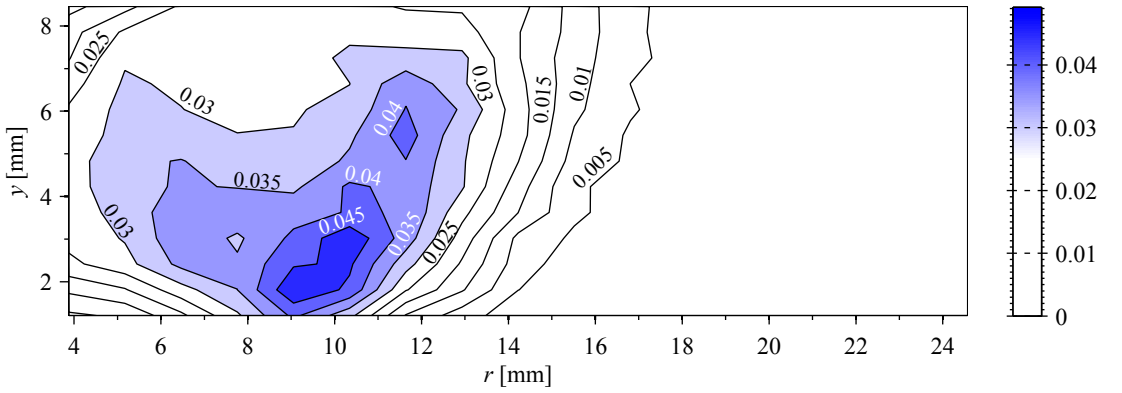

(c) Probability that $\xi = -1$ (A) in case P-3.

Figure C.21: The probability mass function for ξ in case P-3.

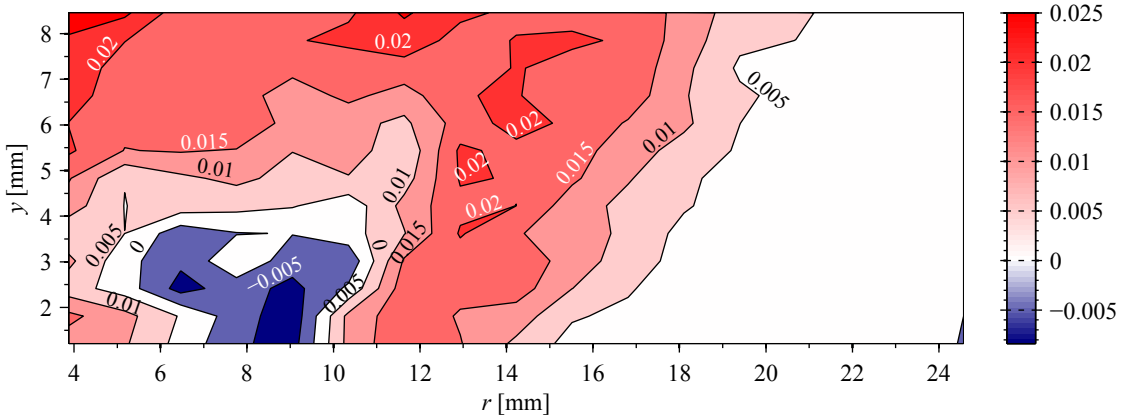

(a) Averaged flame index, $\langle \xi \rangle$ in case P-3.

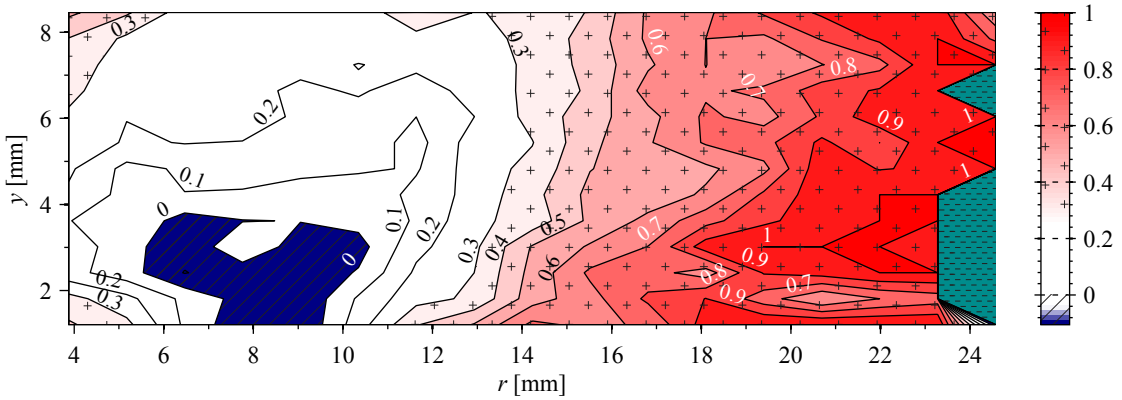

(b) Conditionally averaged flame index, ignoring locations with no flamelets, $\langle \xi \mid \xi \neq 0 \rangle$, in case P-3. Regions that are, on average, more non-premixed are marked with shades of blue and a hatching of diagonal lines while regions that are, on average, highly premixed are marked with shades of red and a hatching of crosses. Regions that never have a flamelet are marked with dark cyan and a hatching of short horizontal lines.

Figure C.22: For case P-3, (a) the average flame index $\langle \xi \rangle$ and (b) the conditionally averaged flame index $\langle \xi \mid \xi \neq 0 \rangle$, where locations without flamelets were ignored.

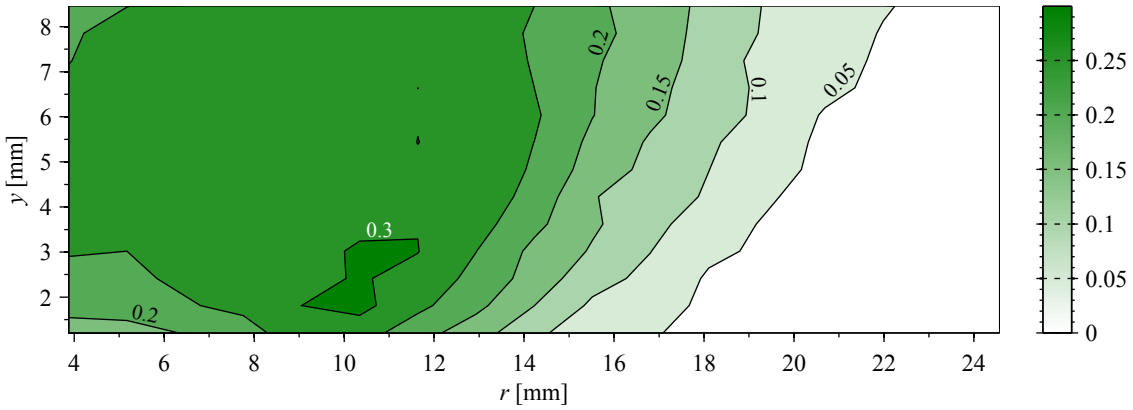

(a) Standard deviation of ξ, σ_ξ, in case P-3.

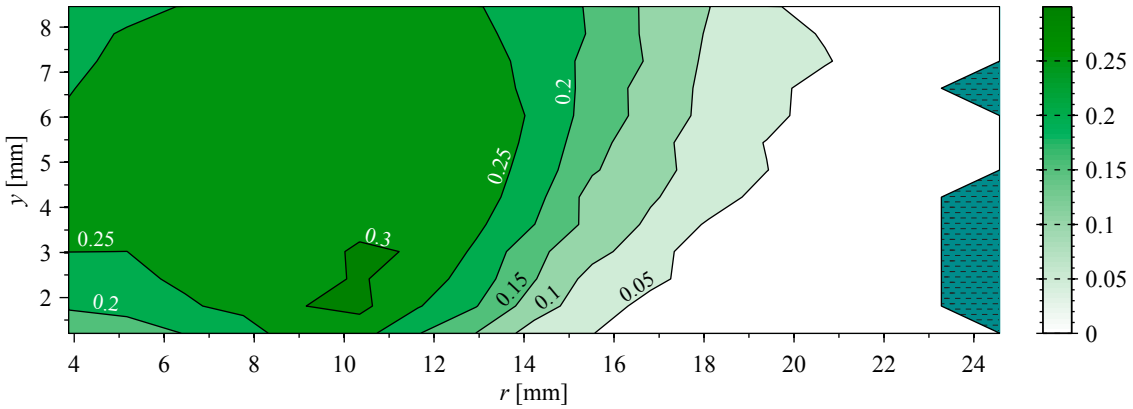

(b) Conditional standard deviation of ξ, $\sigma_{\langle\xi|\xi\neq 0\rangle}$, in case P-3. Regions that never have a flamelet are marked with dark cyan and a hatching of short horizontal lines.

Figure C.23: For case P-3, the standard deviation derived from (a) the average of ξ, σ_ξ, and (b) the conditional average of ξ, $\sigma_{\langle\xi|\xi\neq 0\rangle}$, where all locations without flamelets were ignored.

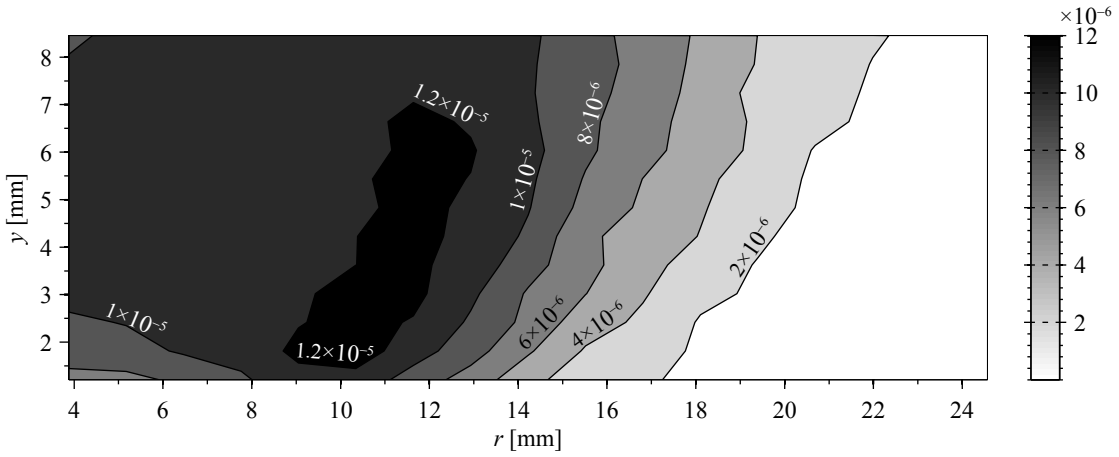

(a) Statistical uncertainty of the average flame index, $\langle \xi \rangle$, in case P-3.

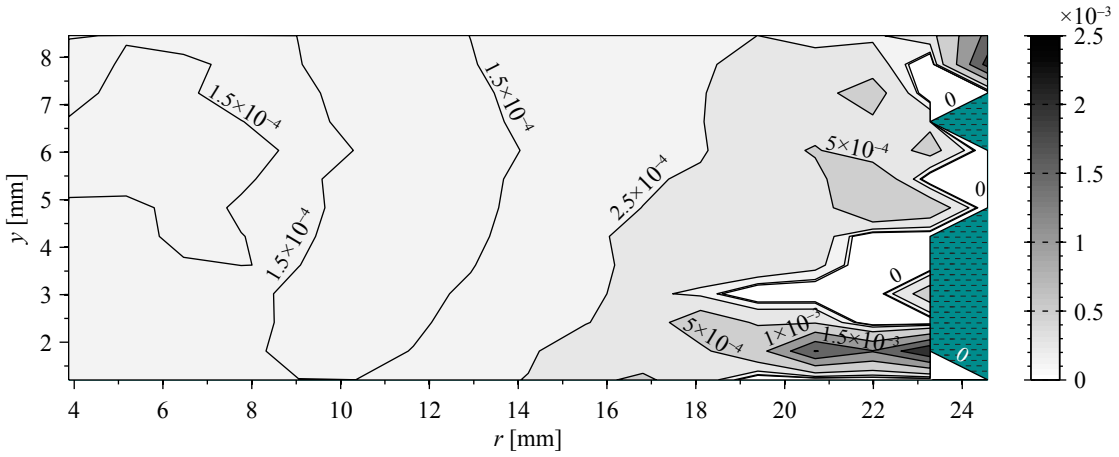

(b) Statistical uncertainty of the conditionally averaged flame index, $\langle \xi \,|\, \xi \neq 0 \rangle$, which ignores locations with no flamelets, in case P-3. Regions that never have a flamelet are marked with dark cyan and a hatching of short horizontal lines.

Figure C.24: For case P-3, (a) the uncertainty of the average flame index $\langle \xi \rangle$ and (b) the uncertainty of the conditionally averaged flame index, $\langle \xi \,|\, \xi \neq 0 \rangle$, where all locations without flamelets were ignored. Uncertainties are to a 95 % confidence level.

C.7 Case S-1: Syngas Turbulent Flame

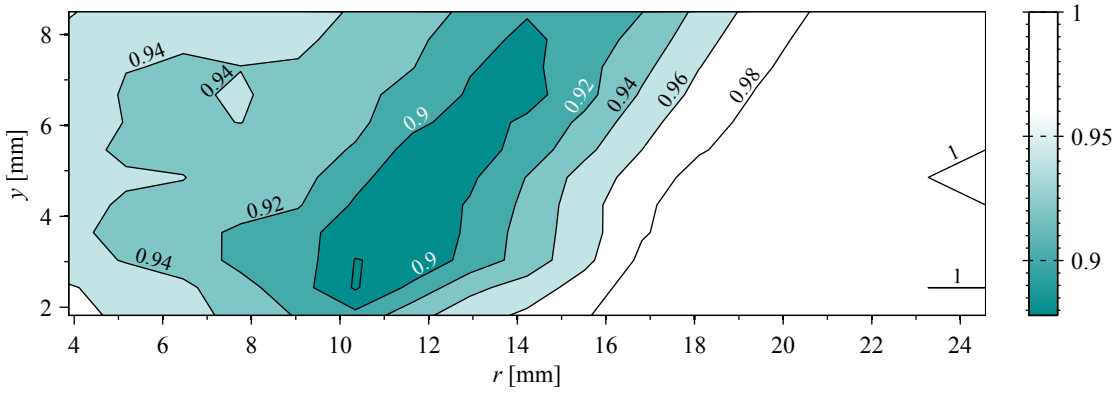

(a) Probability that $\xi = 0$ (B) in case S-1.

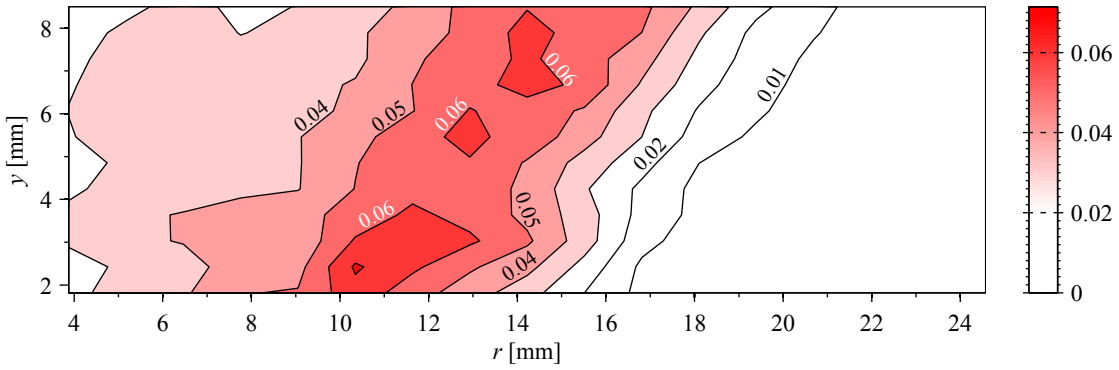

(b) Probability that $\xi = +1$ (C) in case S-1.

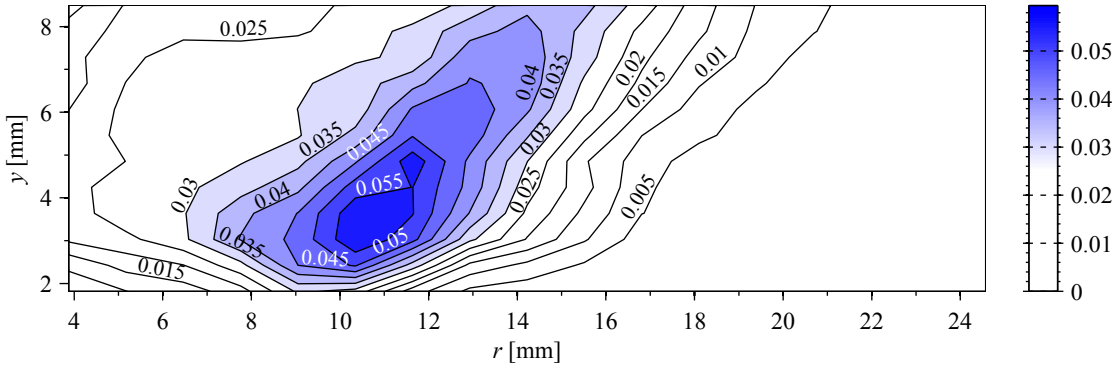

(c) Probability that $\xi = -1$ (A) in case S-1.

Figure C.25: The probability mass function for ξ in case S-1.

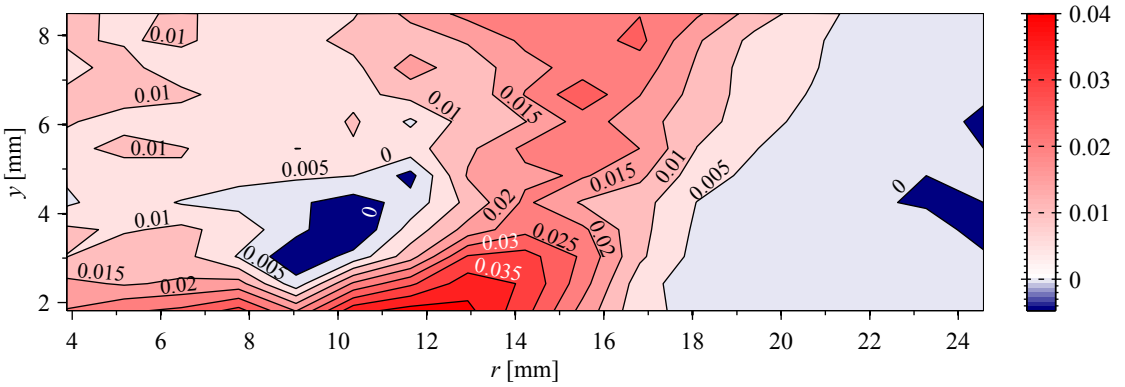

(a) Averaged flame index, $\langle \xi \rangle$ in case S-1.

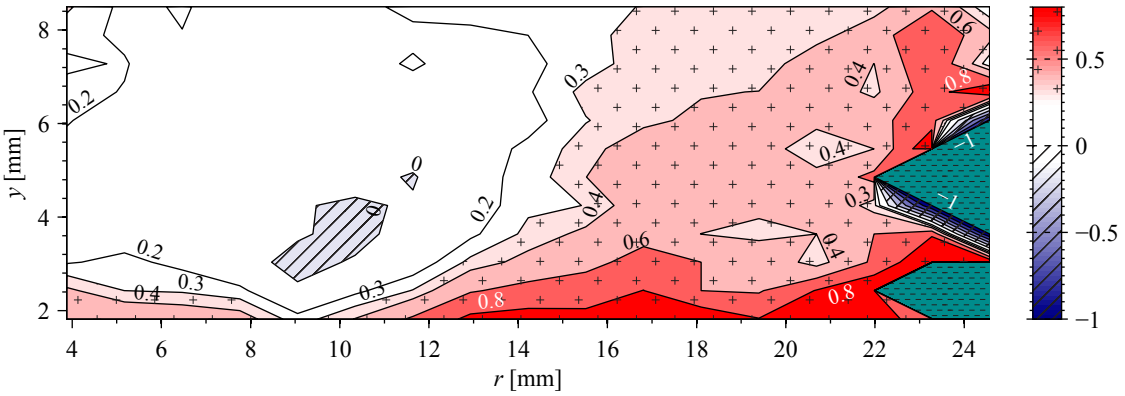

(b) Conditionally averaged flame index, ignoring locations with no flamelets, $\langle \xi \mid \xi \neq 0 \rangle$, in case S-1. Regions that are, on average, more non-premixed are marked with shades of blue and a hatching of diagonal lines while regions that are, on average, highly premixed are marked with shades of red and a hatching of crosses. Regions that never have a flamelet are marked with dark cyan and a hatching of short horizontal lines.

Figure C.26: For case S-1, (a) the average flame index $\langle \xi \rangle$ and (b) the conditionally averaged flame index $\langle \xi \mid \xi \neq 0 \rangle$, where locations without flamelets were ignored.

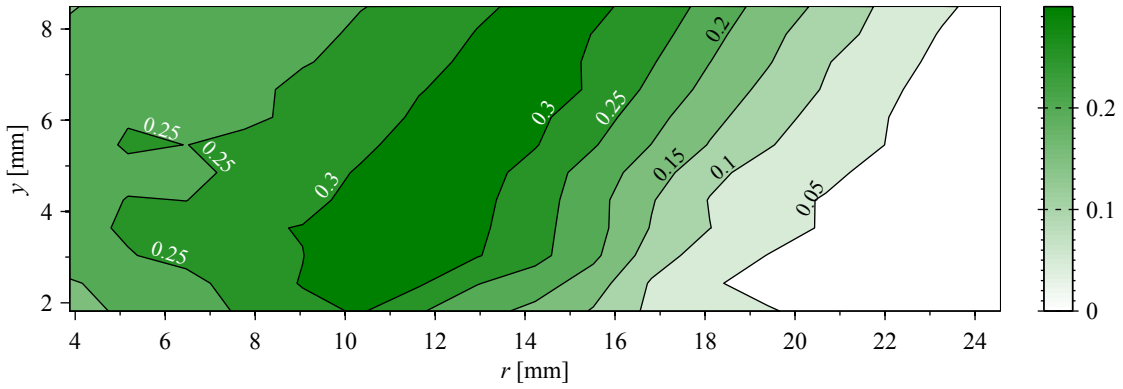

(a) Standard deviation of ξ, σ_ξ, in case S-1.

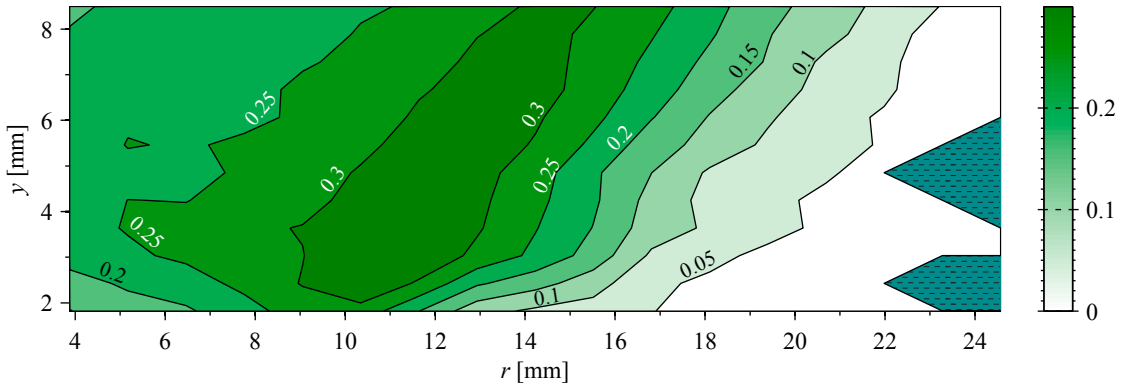

(b) Conditional standard deviation of ξ, $\sigma_{\langle\xi|\xi\neq 0\rangle}$, in case S-1. Regions that never have a flamelet are marked with dark cyan and a hatching of short horizontal lines.

Figure C.27: For case S-1, the standard deviation derived from (a) the average of ξ, σ_ξ, and (b) the conditional average of ξ, $\sigma_{\langle\xi|\xi\neq 0\rangle}$, where all locations without flamelets were ignored.

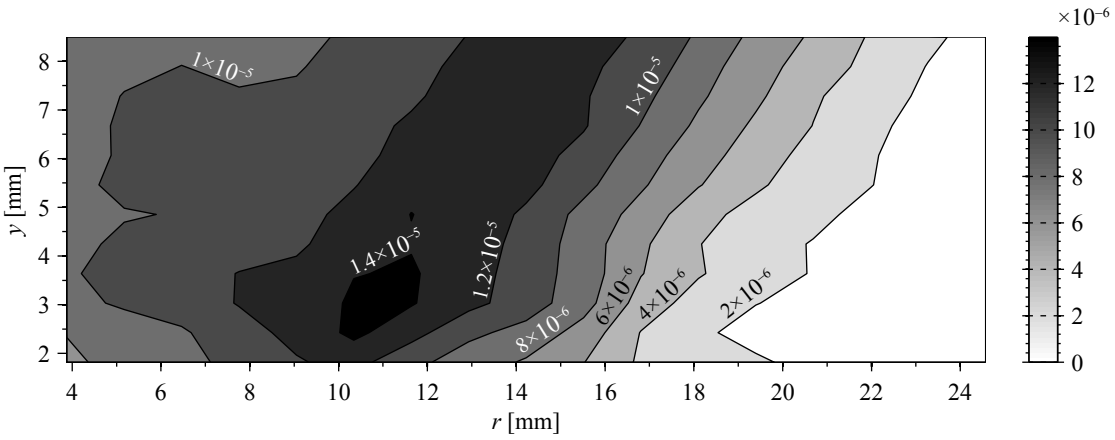

(a) Statistical uncertainty of the average flame index, $\langle \xi \rangle$, in case S-1.

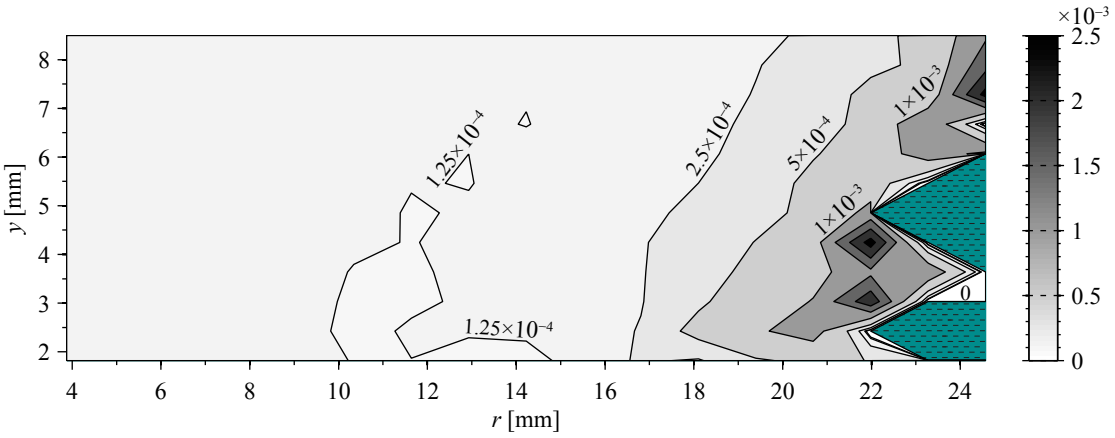

(b) Statistical uncertainty of the conditionally averaged flame index, $\langle \xi \,|\, \xi \neq 0 \rangle$, which ignores locations with no flamelets, in case S-1. Regions that never have a flamelet are marked with dark cyan and a hatching of short horizontal lines.

Figure C.28: For case S-1, (a) the uncertainty of the average flame index $\langle \xi \rangle$ and (b) the uncertainty of the conditionally averaged flame index, $\langle \xi \,|\, \xi \neq 0 \rangle$, where all locations without flamelets were ignored. Uncertainties are to a 95 % confidence level.

BIBLIOGRAPHY

[1] Peters, N., *Turbulent Combustion*, Cambridge University Press, Cambridge, UK, 2000. 1

[2] Yamashita, H., Shimada, M., and Takeno, T., "A numerical study on flame stability at the transition point of jet diffusion flames," *Proceedings of the Combustion Institute*, Vol. 26, No. 1, 1996, pp. 27–34. 1

[3] Bray, K., Domingo, P., and Vervisch, L., "Role of the progress variable in models for partially premixed turbulent combustion," *Combustion and Flame*, Vol. 141, No. 4, 2005, pp. 431–437. 2, 3

[4] Mizobuchi, Y., Tachibana, S., Shinio, J., Ogawa, S., and Takeno, T., "A numerical analysis of the structure of a turbulent hydrogen jet lifted flame," *Proceedings of the Combustion Institute*, Vol. 29, No. 2, 2002, pp. 2009–2015. 2, 3

[5] Knudsen, E. and Pitsch, H., "A general flamelet transformation useful for distinguishing between premixed and non-premixed modes of combustion," *Combustion and Flame*, Vol. 156, No. 3, 2009, pp. 678–696. 2, 3

[6] Knudsen, E. and Pitsch, H., "Capabilities and limitations of multi-regime flamelet combustion models," *Combustion and Flame*, Vol. 159, No. 1, 2012, pp. 242–264. 2, 3

[7] Domingo, P., Vervisch, L., and Bray, K., "Partially premixed flamelets in LES of non-premixed turbulent combustion," *Combustion Theory and Modelling*, Vol. 6, No. 4, 2002, pp. 529–551. 3

[8] Domingo, P., Vervisch, L., and Réveillon, J., "DNS analysis of partially premixed combustion in spray and gaseous turbulent flame-bases stabilized in hot air," *Combustion and Flame*, Vol. 140, No. 3, 2005, pp. 172–195. 3

[9] Fiorina, B., Gicquel, O., Vervisch, L., Carpentier, S., and Darabiha, N., "Approximating the chemical structure of partially premixed and diffusion counterflow flames using FPI flamelet tabulation," *Combustion and Flame*, Vol. 140, No. 3, 2005, pp. 147–160. 3

[10] Ferraris, S. A. and Wen, J. X., "Large eddy simulation of a lifted turbulent jet flame," *Combustion and Flame*, Vol. 150, No. 4, 2007, pp. 320–339. 3

[11] Hanson, R. K., Seitzman, J. M., and Paul, P. H., "Planar laser-fluorescence imaging of combustion gases," *Applied Physics B: Lasers and Optics*, Vol. 50, No. 6, 1990, pp. 441–454. 3

[12] Eckbreth, A. C., *Laser Diagnostics for Combustion Temperature and Species*, Vol. 3 of *Combustion Science and Technology Book Series*, Gordon and Breach Publishers, Amsterdam, 2nd ed., 1996. 3

[13] Partridge, Jr., W. P. and Laurendeau, N. M., "Formulation of a dimensionless overlap fraction to account for spectrally distributed interactions in fluorescence studies," *Applied Optics*, Vol. 34, No. 15, 1995, pp. 2645–2647. 3, 68

[14] Gulati, A. and Warren, Jr., R. E., "NO_2-based laser induced fluorescence technique to measure cold-flow mixing," *Journal of Propulsion and Power*, Vol. 10, No. 1, 1994, pp. 54–61. 4, 72, 74

[15] Agarwal, Y., Hadeishi, T., and Robben, F., "Measurement of NO_2 concentration in combustion using fluorescence excited by an argon-ion laser," *14th AIAA Aerospace Sciences Meeting*, AIAA 76-0136, Washington, DC, 1976. 4

[16] Cattolica, R. J., "Visualization of flame propagation by laser-fluorescence imaging of nitrogen dioxide," *Combustion Science and Technology*, Vol. 54, No. 1-6, 1987, pp. 61–67. 4, 5, 55, 59

[17] Cattolica, R. J., "Combustion-torch ignition: fluorescence imaging of NO_2," *Proceedings of the Combustion Institute*, Vol. 21, No. 1, 1988, pp. 1551–1559. 4, 55

[18] Schofield, K., "Atomic and molecular fluorescence as a stratospheric species monitor," *Journal of Quantitative Spectroscopy and Radiative Transfer*, Vol. 17, No. 1, 1977, pp. 13–51. 4

[19] Vandaele, A. C., Hermans, C., Simon, P. C., Carleer, M., Colin, R., Fally, S., Mérienne, M. F., Jenouvrier, A., and Coquart, B., "Measurements of the NO_2 absorption cross-section from 42 000 cm^{-1} to 10 000 cm^{-1} (238–1000 nm) at 220 K and 294 K," *Journal of Quantitative Spectroscopy and Radiative Transfer*, Vol. 59, No. 3-5, 1998, pp. 171–184, Atmospheric Spectroscopy Applications 96. 4

[20] Myers, G. H., Silver, D. M., and Kaufman, F., "Quenching of NO_2 fluorescence," *The Journal of Chemical Physics*, Vol. 44, No. 2, 1966, pp. 718–723. 4

[21] Abe, K., "Laser excited fluorescence spectrum of nitrogen dioxide," *Journal of Molecular Spectroscopy*, Vol. 48, No. 2, 1973, pp. 395–408. 4

[22] Gillispie, G. D., Khan, A. U., Wahl, A. C., Hosteny, R. P., and Krauss, M., "The electronic structure of nitrogen dioxide. I. Multiconfiguration self-consistent-field calculation of the low-lying electronic states," *The Journal of Chemical Physics*, Vol. 63, No. 8, 1975, pp. 3425–3444. 4

[23] Gillispie, G. D. and Khan, A. U., "The electronic structure of NO_2. II. The $\tilde{A}^2B_2 \leftarrow \tilde{X}^2A_1$ and $\tilde{B}^2B_1 \leftarrow \tilde{X}^2A_1$ absorption systems," *The Journal of Chemical Physics*, Vol. 65, No. 5, 1976, pp. 1624–1633. 4

[24] Chen, P. C., "High resolution coherent 2D spectroscopy," *Journal of Physical Chemistry A*, Vol. 114, No. 43, 2010, pp. 11365–11375. 4

[25] Hsu, D. K., Monts, D. L., and Zare, R. N., *Spectral Atlas of Nitrogen Dioxide, 5530 to 6480 Å*, Academic Press, New York, 1978. 4

[26] Herzberg, G., *Infrared and Raman Spectra of Polyatomic Molecules*, Vol. 2 of *Molecular Spectra and Molecular Structure*, Van Nostrand, Princeton, NJ, 1945. 4

[27] Herzberg, G., *Electronic Spectra and Electronic Structure of Polyatomic Molecules*, Vol. 3 of *Molecular Spectra and Molecular Structure*, Van Nostrand, Princeton, NJ, 1966. 4

[28] Mihalcea, R. M., Baer, D. S., and Hanson, R. K., "Tunable diode-laser absorption measurements of NO_2 near 670 and 395 nm," *Applied Optics*, Vol. 35, No. 21, 1996, pp. 4059–4064. 4

[29] Donnelly, V. M. and Kaufman, F., "Fluorescence lifetime studies of NO_2. I. Excitation of the perturbed $^2B_2$ state near 600 nm," *The Journal of Chemical Physics*, Vol. 66, No. 9, 1977, pp. 4100–4110. 4

[30] Donnelly, V. M. and Kaufman, F., "Fluorescence lifetime studies of NO_2. II. Dependence of the perturbed $^2B_2$ state lifetimes on excitation energy," *The Journal of Chemical Physics*, Vol. 69, No. 4, 1978, pp. 1456–1460. 4

[31] Donnelly, V. M., Keil, D. G., and Kaufman, F., "Fluorescence lifetime studies of NO_2. III. Mechanism of fluorescence quenching," *The Journal of Chemical Physics*, Vol. 71, No. 2, 1979, pp. 659–673. 4

[32] Keil, D. G., Donnelly, V. M., and Kaufman, F., "Fluorescence lifetime studies of NO_2. IV. Temperature dependence of fluorescence spectra and of collisional quenching of fluorescence," *The Journal of Chemical Physics*, Vol. 73, No. 4, 1980, pp. 1514–1520. 4

[33] Baulch, D. L., Drysdale, D. D., Horne, D. G., and Lloyd, A. C., *Homogeneous Gas Phase Reactions of the H_2-N_2-O_2 System*, Vol. 2 of *Evaluated Kinetic Data for High Temperature Reactions*, Butterworths, London, 1973. 5

[34] Schulz, C. and Sick, V., "Tracer-LIF diagnostics: quantitative measurement of fuel concentration, temperature and fuel/air ratio in practical combustion systems," *Progress in Energy and Combustion Science*, Vol. 31, No. 1, 2005, pp. 75–121. 5, 55

[35] Thurber, M. C., Grisch, F., Kirby, B. J., Votsmeier, M., and Hanson, R. K., "Measurements and modeling of acetone laser-induced fluorescence with implications for temperature-imaging diagnostics," *Applied Optics*, Vol. 37, No. 21, 1998, pp. 4963–4978. 5, 23

[36] Thurber, M. C. and Hanson, R. K., "Pressure and composition dependences of acetone laser-induced fluorescence with excitation at 248, 266, and 308 nm," *Applied Physics B: Lasers and Optics*, Vol. 69, No. 3, 1999, pp. 229–240. 5, 76, 77

[37] Lozano, A., Yip, B., and Hanson, R. K., "Acetone: a tracer for concentration measurements in gaseous flows by planar laser-induced fluorescence," *Experiments in Fluids*, Vol. 13, No. 6, 1992, pp. 369–376. 5, 76

[38] Bryant, R. A., Donbar, J. M., and Driscoll, J. F., "Acetone laser induced fluorescence for low pressure/low temperature flow visualization," *Experiments in Fluids*, Vol. 28, No. 5, 2000, pp. 471–476. 5, 76, 77

[39] Yuen, L. S., Peters, J. E., and Lucht, R. P., "Pressure dependence of laser-induced fluorescence from acetone," *Applied Optics*, Vol. 36, No. 15, 1997, pp. 3271–3277. 5, 77

[40] Ernst, J., Spindler, K., and Wagner, H. G., "Untersuchungen zum thermischen zerfall von acetaldehyd und aceton," *Berichte der Bunsengesellschaft für physikalische Chemie*, Vol. 80, No. 7, 1976, pp. 645–650. 5

[41] Yip, B., Miller, M. F., Lozano, A., and Hanson, R. K., "A combined OH/acetone planar laser-induced fluorescence imaging technique for visualizing combusting flows," *Experiments in Fluids*, Vol. 17, No. 5, 1994, pp. 330–336. 5

[42] Sato, K. and Hidaka, Y., "Shock-tube and modeling study of acetone pyrolysis and oxidation," *Combustion and Flame*, Vol. 122, No. 3, 2000, pp. 291–311. 5

[43] Chong, C. T. and Hochgreb, S., "Measurements of laminar flame speeds of acetone/methane/air mixtures," *Combustion and Flame*, Vol. 158, No. 3, 2011, pp. 490–500. 5, 6, 62

[44] Aldén, M., Bood, J., Li, Z., and Richter, M., "Visualization and understanding of combustion processes using spatially and temporally resolved laser diagnostic techniques," *Proceedings of the Combustion Institute*, Vol. 33, No. 1, 2011, pp. 69–97. 6

[45] Ludwig, H. R., Whalen, J. J., and Cairelli, S. G., "Documentation for Immediately Dangerous To Life or Health Concentrations (IDLHs)," Tech. Rep. NTIS PB94-195047, National Institute for Occupational Safety and Health, Cincinati, OH, 1994, http://www.cdc.gov/niosh/idlh/10102440.html. 11

[46] Schumaker, S. A., *An experimental investigation of reacting and nonreacting coaxial jet mixing in a laboratory rocket engine*, Ph.D. thesis, University of Michigan, 2009. 13

[47] Weigand, P., Meier, W., Duan, X. R., Stricker, W., and Aigner, M., "Investigations of swirl flames in a gas turbine model combustor: I. Flow field, structures, temperature, and species distributions," *Combustion and Flame*, Vol. 144, No. 1-2, 2006, pp. 205–224. 15, 16, 20, 23

[48] Giezendanner, R., Weigand, P., Duan, X. R., Meier, W., Meier, U., Aigner, M., and Lehmann, B., "Laser-based investigations of periodic combustion instabilities in a gas turbine model combustor," *Journal of Engineering for Gas Turbines and Power*, Vol. 127, No. 3, 2005, pp. 492–496. 15

[49] Meier, W., Duan, X. R., and Weigand, P., "Investigations of swirl flames in a gas turbine model combustor: II. Turbulence-chemistry interactions," *Combustion and Flame*, Vol. 144, No. 1-2, 2006, pp. 225–236. 15

[50] Allison, P. M., Driscoll, J. F., and Ihme, M., "Acoustic characterization of a partially-premixed gas turbine model combustor: Syngas and hydrocarbon fuel comparisons," *Proceedings of the Combustion Institute*, Vol. 34, No. 2, 2013, pp. 3145–3153. 20, 125

[51] Design Institute for Physical Property Research/AIChE, "DIPPR Project 801," 2010. 21, 22

[52] Clemens, N. T., "Flow Imaging," *Encyclopedia of Imaging Science and Technology*, edited by J. P. Hornak, John Wiley & Sons, Inc., New York, 2002, pp. 390–419. 27, 42, 48, 74, 79

[53] Roberts, W. L., Driscoll, J. F., Drake, M. C., and Goss, L. P., "Images of the quenching of a flame by a vortex—To quantify regimes of turbulent combustion," *Combustion and Flame*, Vol. 94, No. 1-2, 1993, pp. 58–69. 31

[54] Incropera, F. P., DeWitt, D. P., Bergman, T. L., and Lavine, A. S., *Fundamentals of Heat and Mass Transfer*, John Wiley, Hoboken, NJ, 6th ed., 2007. 31

[55] Meier, W., Duan, X. R., and Weigand, P., "Reaction zone structures and mixing characteristics of partially premixed swirling CH_4/air flames in a gas turbine model combustor," *Proceedings of the Combustion Institute*, Vol. 30, No. 1, 2005, pp. 835–842. 32

[56] Duan, X. R., Meier, W., Weigand, P., and Lehmann, B., "Phase-resolved laser Raman scattering and laser Doppler velocimetry applied to periodic instabilities in a gas turbine model combustor," *Applied Physics B: Lasers and Optics*, Vol. 80, No. 3, 2005, pp. 389–396. 32

[57] Smith, W. J., *Modern Optical Engineering: The Design of Optical Systems*, McGraw Hill, New York, 4th ed., 2008. 43

[58] Pawley, J. B., "More Than You Ever Really Wanted to Know About Charge-Coupled Devices," *Handbook of Biological Confocal Microscopy*, edited by J. B. Pawley, Springer, New York, 3rd ed., 2006, pp. 918–931. 48

[59] Janesick, J. R., Elliott, T., Collins, S., Blouke, M. M., and Freeman, J., "Scientific charge-coupled devices," *Optical Engineering*, Vol. 26, No. 8, 1987, pp. 692–714. 49

[60] Perona, P. and Malik, J., "Scale-space and edge detection using anisotropic diffusion," *IEEE Transactions on Pattern Analysis and Machine Intelligence*, Vol. 12, No. 7, 1990, pp. 629–639. 50, 79, 91

[61] Gerig, G., Kübler, O., Kikinis, R., and Jolesz, F. A., "Nonlinear anisotropic filtering of MRI data," *IEEE Transactions on Medical Imaging*, Vol. 11, No. 2, 1992, pp. 221–232. 52

[62] Weickert, J., ter Haar Romeny, B. M., and Viergever, M. A., "Efficient and reliable schemes for nonlinear diffusion filtering," *IEEE Transactions on Image Processing*, Vol. 7, No. 3, 1998, pp. 398–410. 52

[63] Malm, H., Sparr, G., Hult, J., and Kaminski, C. F., "Nonlinear diffusion filtering of images obtained by planar laser-induced fluorescence spectroscopy," *Journal of the Optical Society of America A: Optics and Image Science*, Vol. 17, No. 12, 2000, pp. 2148–2156. 52

[64] Canny, J., "A computational approach to edge detection," *IEEE Transactions on Pattern Analysis and Machine Intelligence*, Vol. PAMI-8, No. 6, 1986, pp. 679–698. 53, 80, 95

[65] Smith, G. P., Golden, D. M., Frenklach, M., Moriarty, N. W., Eiteneer, B., Goldenberg, M., Bowman, C. T., Hanson, R. K., Song, S., Gardiner, Jr., W. C., Lissianski, V. V., and Qin, Z., "GRI-Mech 3.0," 1999, http://www.me.berkeley.edu/gri_mech. 55

[66] Vandooren, J., de Guertechin, L. O., and Tiggelen, P. J. V., "Kinetics in a lean formaldehyde flame," *Combustion and Flame*, Vol. 64, No. 2, 1986, pp. 127–139. 56

[67] Böckle, S., Kazenwadel, J., Kunzelmann, T., Shin, D.-I., and Schulz, C., "Single-shot laser-induced fluorescence imaging of formaldehyde with XeF excimer excitation," *Applied Physics B: Lasers and Optics*, Vol. 70, No. 5, 2000, pp. 733–735. 56

[68] Li, Z. S., Li, B., Sun, Z. W., Bai, X. S., and Aldén, M., "Turbulence and combustion interaction: High resolution local flame front structure visualization using simultaneous single-shot PLIF imaging of CH, OH, and CH_2O in a piloted premixed jet flame," *Combustion and Flame*, Vol. 157, No. 6, 2010, pp. 1087–1096. 56

[69] Buschmann, A., Dinkelacker, F., Schäfer, T., Schäfer, M., and Wolfrum, J., "Measurement of the instantaneous detailed flame structure in turbulent premixed combustion," *Proceedings of the Combustion Institute*, Vol. 26, No. 1, 1996, pp. 437–445. 56

[70] Kaminski, C. F., Bai, X. S., Hult, J., Dreizler, A., Lindenmaier, S., and Fuchs, L., "Flame growth and wrinkling in a turbulent flow," *Applied Physics B: Lasers and Optics*, Vol. 71, No. 5, 2000, pp. 492–496. 56

[71] Massman, W. J., "A review of the molecular diffusivities of H_2O, CO_2, CH_4, CO, O_3, SO_2, NH_3, N_2O, NO, and NO_2 in air, O_2 and N_2 near STP," *Atmospheric Environment*, Vol. 32, No. 6, 1998, pp. 1111–1127. 59

[72] Pichon, S., Black, G., Chaumeix, N., Yahyaoui, M., Simmie, J. M., Curran, H. J., and Donohue, R., "The combustion chemistry of a fuel tracer: measured flame speeds and ignition delays and a detailed chemical kinetic model for the oxidation of acetone," *Combustion and Flame*, Vol. 156, No. 2, 2009, pp. 494–504. 62

[73] Matsumi, Y., Murasawa, Y., Obi, K., and Tanaka, I., "The Schumann-Runge O_2 emission, following visible multiphoton excitation of NO_2," *Laser Chemistry*, Vol. 1, No. 2, 1983, pp. 113–130. 72

[74] Jusinski, L. E., Sharpless, R. L., and Slanger, T. G., "Multiphoton dissociation in NO2 at 532 nm and the generation of vibrationally excited O_2 and NO," *The Journal of Chemical Physics*, Vol. 86, No. 10, 1987, pp. 5509–5514. 72

[75] Hsu, A. G., Srinivasan, R., Bowersox, R. D. W., and North, S. W., "Two-component molecular tagging velocimetry utilizing NO fluorescence lifetime and NO_2 photodissociation techniques in an underexpanded jet flowfield," *Applied Optics*, Vol. 48, No. 22, 2009, pp. 4414–4423. 72

[76] Hsu, A. G., Srinivasan, R., Bowersox, R. D. W., , and North, S. W., "Molecular tagging using vibrationally excited nitric oxide in an underexpanded jet flowfield," *AIAA Journal*, Vol. 47, No. 11, 2009, pp. 2597–2604. 72

[77] Sánchez-González, R., Srinivasan, R., Bowersox, R. D. W., and North, S. W., "Simultaneous velocity and temperature measurements in gaseous flow fields using the VENOM technique," *Optics Letters*, Vol. 36, No. 2, 2011, pp. 196–198. 72

[78] Syred, N., "A review of oscillation mechanisms and the role of the precessing vortex core (PVC) in swirl combustion systems," *Progress in Energy and Combustion Science*, Vol. 32, No. 2, 2006, pp. 93–161. 125

[79] Boxx, I., Stöhr, M., Carter, C., and Meier, W., "Temporally resolved planar measurements of transient phenomena in a partially pre-mixed swirl flame in a gas turbine model combustor," *Combustion and Flame*, Vol. 157, No. 8, 2010, pp. 1510–1525. 125

[80] Wheeler, A. J. and Ganji, A. R., *Introduction to Engineering Experimentation*, Pearson Higher Education, Upper Saddle River, NJ, 3rd ed., 2010. 126

[81] Grout, R. W., Gruber, A., Yoo, C. S., and Chen, J. H., "Direct numerical simulation of flame stabilization downstream of a transverse fuel jet in cross-flow," *Proceedings of the Combustion Institute*, Vol. 33, No. 1, 2011, pp. 1629–1637. 133

[82] Rosenberg, D. A. and Driscoll, J. F., "A method to image flame index in partially premixed flames," *50st AIAA Aerospace Sciences Meeting*, AIAA 2012-0972, Nashville, TN, 2012. 145